ATOMISATION OF LIQUIDS IN HOT ATMOSPHERES

A Thesis Submitted to the University of Leeds

for the Degree of Doctor of Philosophy

by

C.J. Clark. B.Sc.

PAGE NUMBERS CLOSE TO

THE EDGE OF THE PAGE.

SOME ARE CUT OFF

ABSTRACT

An investigation has been performed into the dynamics of thin
liquid sheets.   Observation by high speed photography has revealed a
new mechanism of sheet instability, electrohydrodynamic in origin,
when water is injected into hot combustion gases.   An estimation
has been made of the charge transferred to a liquid sheet from an
ionised gas and a first order solution of the resulting coupled
surface wave has been derived.

General first order solutions of wave-growth on finite viscosity
liquid sheets have been made, while a second order solution has been
obtained for the growth of inviscid sinuous waves.   The results of
the latter analysis have been used to satisfactorily correlate the
coherent sheet length.

ACKNOWLEDGEMENTS

Contents

List of Tables

List of Figures

Chapter 1.   Introduction

The atomisation of liquids is an essential feature of a wide-spread range of industrial equipment and has important applications in combustion (1), chemical (2) and agricultural engineering (3).

In many cases it is desirable to control the quality of atomisation within well-defined limits. For example, in combustion a proportion of very small drops is necessary to assist ignition and promote flame stability, although the size range and relative proportion of bigger drops must be kept within suitable limits in order to achieve complete combustion. On the other hand, in agricultural usage, where it is common practice to spray concentrated solutions of toxic selective materials, it is essential for the proportion of fine drops within the spray to be reduced to a minimum in order to avoid contamination of the surrounding areas by "drift". No successful solution to this problem has been found, although it has been mitigated by the use of additives to control the physical properties of the liquids and by the use of specially designed atomisers for specific purposes.

Few advances can, however, be expected in the control of the spray characteristics until a fuller understanding is achieved of the complex processes of drop formation.

While there is a growing knowledge of the factors influencing the disintegration of liquid streams under normal atmospheric conditions (4), little is known of the performance characteristics of spray nozzles in more extreme environments. The purpose of this research has been to study the mechanisms of drop formation in high temperature gases, and apparatus has been designed to enable visual and photographic observation of water sprays to be made in combustion gases at temperatures ranging up to 1000°C. The single-orifice fan

spray pressure nozzle was used for most of the work since it produces
a flat sheet which is convenient for both analytical and experimental
study, and on which there is a good background of information (5-11).

Former investigations (6) at normal atmospheric temperature and
pressure have established a mechanism of drop formation by rapidly
growing sinuous aerodynamic waves, as a result of which fragments of
liquid are detached at regular intervals and contract into unstable
ligaments from which drops are formed.   On the basis of a simplified
model, expressions were developed which related   the mean drop size
to the operating conditions.

It has been found in this work that hot gases above 300 $^{\circ}$C cause
high frequency capillary waves to be superimposed on the sheet and
disintegration then occurs by the combined action of aerodynamic
waves and perforations, the contribution of the latter predominating
with increase in temperature.   Measurements have shown a critical
dependence of break-up length and drop size upon the nature of the
disintegration process.   It is demonstrated that the new wave
system is electrohydrodynamic in origin, the electric field being
generated by the charged particles present in the gas.

An analysis has been performed of the electrical boundary layer
flow characteristics around a liquid sheet and first order expressions
derived for the criterion of stability and wavelength of the neutral
wave.   Calculated and observed wavelengths are found to differ
appreciably and this is attributed to unknown turbulent motion around
the sheet.

Previous first order theories provide a basis upon which sheet
break-up lengths and average drop sizes may be correlated, but no
information is provided on the actual mechanism by which the sheet
disintegrates.   In this thesis further insight has been obtained by

extending the analysis to include second order terms, and it has
been shown that for low viscosity liquids a critical amplitude exists
at which the sheet breaks down,disintegration occurring at positions
corresponding to ¼ and ¾ of the wavelength. Break-up lengths have
been shown to be a function of the amplitude of the initial disturbance
and experiments have demonstrated its value to be critically
dependent on a Reynolds number, based upon the nozzle orifice
dimensions.

The first order theory has been extended to include real
liquids, and expressions are derived which show the effect of viscosity
on wave growth for both sinuous and dilational waves.

The mechanism of disintegration of the edge of a fan spray sheet
has been explained as a combination of both Rayleigh and Taylor
instability ,and expressions have been developed for the trajectory
of the rim and for the size of drops formed from disintegration.

A critical assessment has been made of the commonly accepted
procedure for analysing photographs of sprays. It is shown that,
because of the periodic nature of drop formation, unsteady state
conditions may persist which give rise to unpredictable errors and
it is therefore concluded that accurate drop size frequency
distributions can only be obtained from an analysis of single flash
photographs taken near the atomiser.

Chapter 2.   Theoretical Considerations
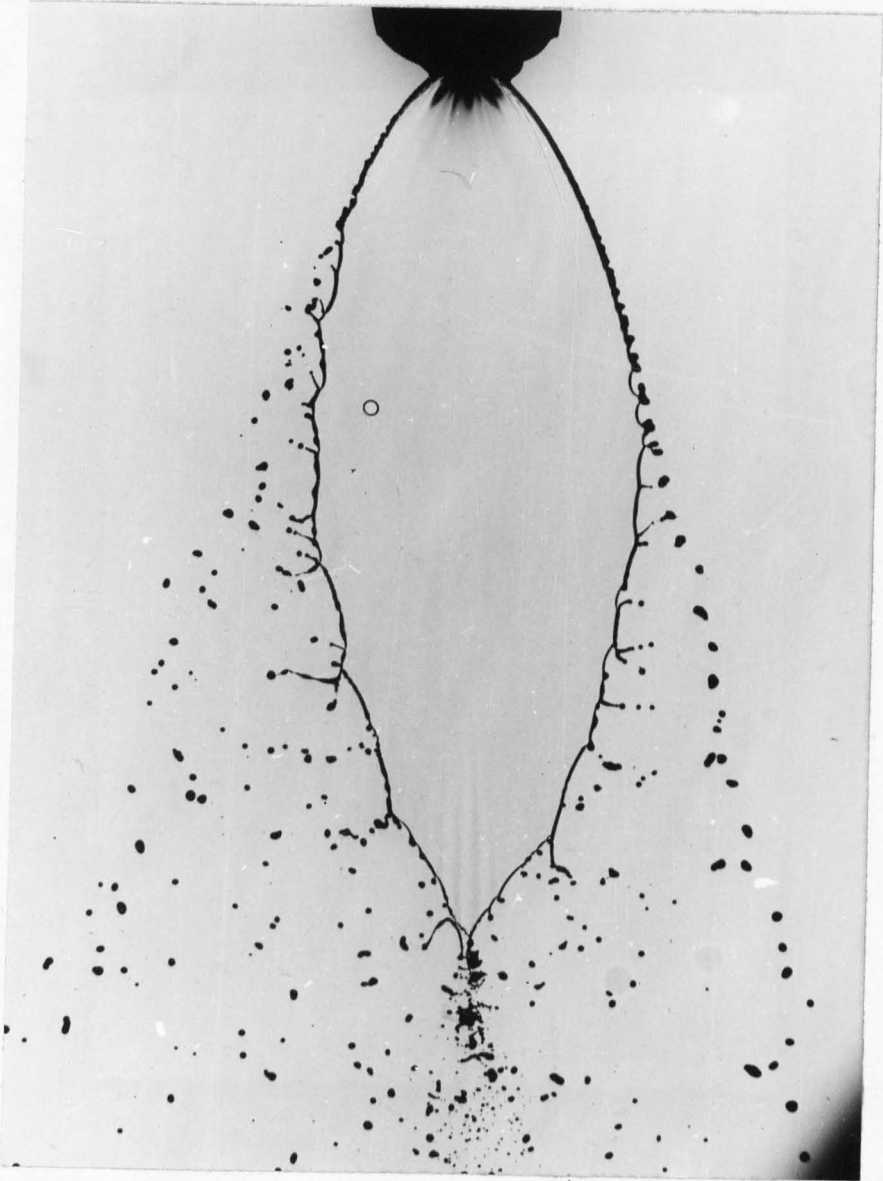
Magnification:- x 3.6

Nozzle:- Bray Unijet Y

Differential Injection Pressure:- 0.69 bar (10 p.s.i.g.)

Fig.2.1a. Formation of a Fan Spray Water Sheet
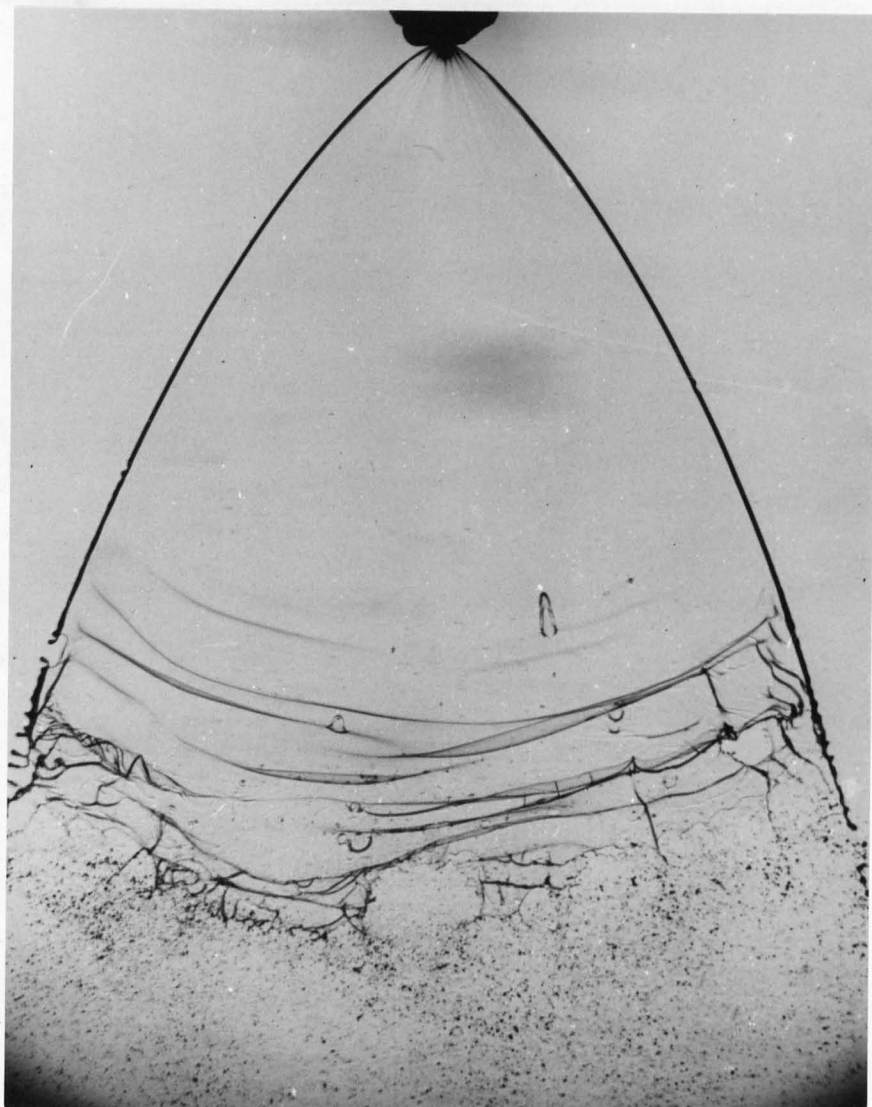
Magnifications: x 2

Nozzle: Bray Unijet X

Differential Injection Pressure:-   2.41 bar (35 psig)

Fig.2.1b. Formation of a Fan Spray Water Sheet
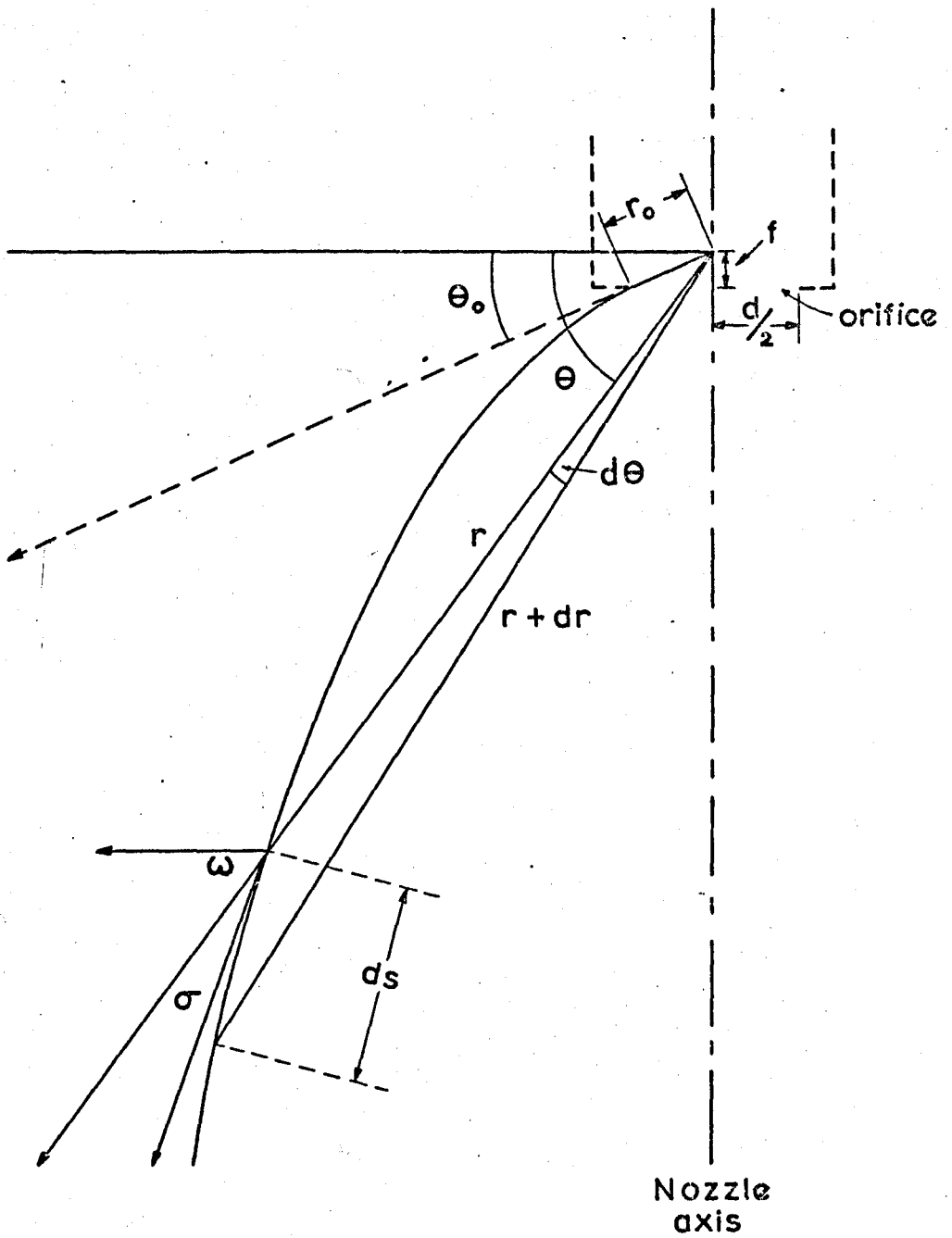
FIG. 2.2   TRAJECTORY OF A SHEET EDGE

2.1. Dynamics of the Rim of a Fan Spray Sheet

The flow characteristics of fan-shaped liquid sheets have been subjected to much study (see for example Ref. 4.), but little attention seems to have been directed towards the factors influencing their development. A typical photograph of a low viscosity fan spray sheet issuing from a single orifice fan spray nozzle is shown in Fig.(2.1a) and it is seen that as a result of surface tension the edges contract and a curved boundary is produced as the sheet extends from the origin. The rims initially thicken as liquid accumulates from the contracted sheet, but, as a result of disturbances which simultaneously appear on the outer surface, rapidly break down into drops. Dombrowski at al (10) derived an approximate expression for the trajectory of the rims by neglecting the effect of accumulated mass and they found that it could be used to correlate results for low viscosity liquids over a wide range of conditions for cases where disintegration occurred close to the origin.

At relatively low ejection velocities the coherent rim may persist some considerable distance before break-up and thus effectively control the sheet area Fig.(2.1b). In this section, an analysis is carried out of its path and its stability.

2.1.1 Trajectory of the Rim of a Fan Spray Sheet

The equilibrium system considered, Fig.(2.2) comprises an attenuating inviscid liquid sheet bounded by liquid rims of cylindrical cross-section.

Conservation of momentum normal to a rim element of length, ds, gives

$$2T = \left(\rho U_t^2\right) \frac{A \, d\psi}{ds} + \rho \frac{d(AU_t)}{ds} \, U_0 \sin \sigma \qquad (2.1)$$

where σ is the angle between the tangent and radius vectors, while conservation of momentum along the rim element gives,

$$\rho \frac{d(AU_t^2)}{ds} = \rho \frac{d(AU_t)}{ds} \, U_0 \cos \sigma \qquad (2.2)$$

For conservation of mass, the net change of flux, within the element is balanced by liquid entering from the liquid sheet i.e.

$$\rho \frac{d(AU_t)}{ds} = \rho U_0 \, h \, r \, \frac{d\theta}{ds} \qquad (2.3)$$

In the absence of external forces, the thickness of a fan spray sheet varies inversely with distance from the origin.*[10] viz.

$$h = \frac{K_0}{r}$$

and hence equation (2.3) may be re-written as,

$$\rho \frac{d(AU_t)}{ds} = \rho U_0 K_0 \frac{d\Theta}{ds} \qquad (2.4)$$

Eliminating $d\frac{(AU_t)}{ds}$ from equation (2.2) and (2.4)

$$AU_t^2 = U_0^2 K \int_{\Theta_0}^{\Theta} \cos\delta \, d\Theta \qquad (2.5)$$

Thus combining equations (2.1), (2.4) and (2.5) and noting that

$\sin\delta = r\frac{d\Theta}{ds}$ we get,

$$N = \frac{dw}{ds} \int_{\Theta_0}^{\Theta} \cos\delta \, d\Theta + \frac{\sin^2\delta}{r} \qquad (2.6)$$

where $N = \frac{2T}{\rho U_0^2 K_0}$ \qquad (2.7)

and, $\frac{dw}{ds}$, the radius of curvature of the rim, is given by

$$\frac{dw}{ds} = \frac{1 + 2\left(\frac{1}{r}\frac{dr}{d\Theta}\right)^2 - \left(\frac{1}{r}\frac{d^2r}{d\Theta^2}\right)}{r\left[1+\left(\frac{1}{r}\frac{dr}{d\Theta}\right)^2\right]^{3/2}}$$

Inspection of photographs reveals that to a first order of approximation a parabolic relation exists between the dimensionless parameter Nr and $(\Theta - \Theta_0)$ and hence,

$$\frac{1}{2}\left(\frac{1}{r}\frac{dr}{d\theta}\right)^2 \approx \frac{1}{r}\left(\frac{d^2r}{d\theta^2}\right) \gg 1$$

giving,

$$\frac{dw}{ds} = \frac{3}{2}\frac{d\Theta}{dr} \qquad (2.8)$$

Thus, combining equations (2.6) and (2.8) we get,

* Streamlines in a fan-shaped sheet appear to diverge from a centre of pressure behind the orifice [10] and the origin is taken at this point (cf Fig.2.2).

$$\left(\frac{d\Theta}{dr}\right)^2 = \frac{4\ (N-B)^2}{(1-(1-r\ (N-B))^2)} \tag{2.9}$$

where $B = \frac{3}{2}\ \frac{d\Theta}{dr}\ \int_{\Theta_o}^{\Theta} \cos\delta\ d\Theta$

In order to provide a simple analytical expression for the trajectory of the rim, it is assumed that since σ is small over a large portion of the rim, B will vary little over the range of integration and may be replaced by the average value $\bar{B}$ defined by,

$$\bar{B} = \frac{1}{r}\ \int_{r_o}^{r} B\ dr$$

Equation (2.9) may thus be integrated to give,

$$(\Theta - \Theta_o) = \left[\cos^{-1}\ (1- 2r\ (N - \bar{B}))\right]_{r_o}^{r}$$

For the nozzles used in the present work (cf Table 2) r_o covers a range from about 0.4 to 0.75 mm, and thus, except within the vicinity of the orifice, $r_o \ll r$. Hence for $\cos\delta \approx 1$, the shape of the boundary may be described by the following relation.

$$2\ Nr = 1 - \cos\ (\Theta - \Theta_o) + \frac{3}{2}\ (\Theta - \Theta_o)^2 \tag{2.10}$$

The velocity of the rim, U_t, is obtained by integrating equation (2.4) and combining with equation (2.5) viz.

$$U_t = \frac{U_o}{\Theta - \Theta_o}\ \int_{\Theta_o}^{\Theta} \cos\delta\ \ d\Theta$$

For small values of δ, $U_t \approx U_o$.
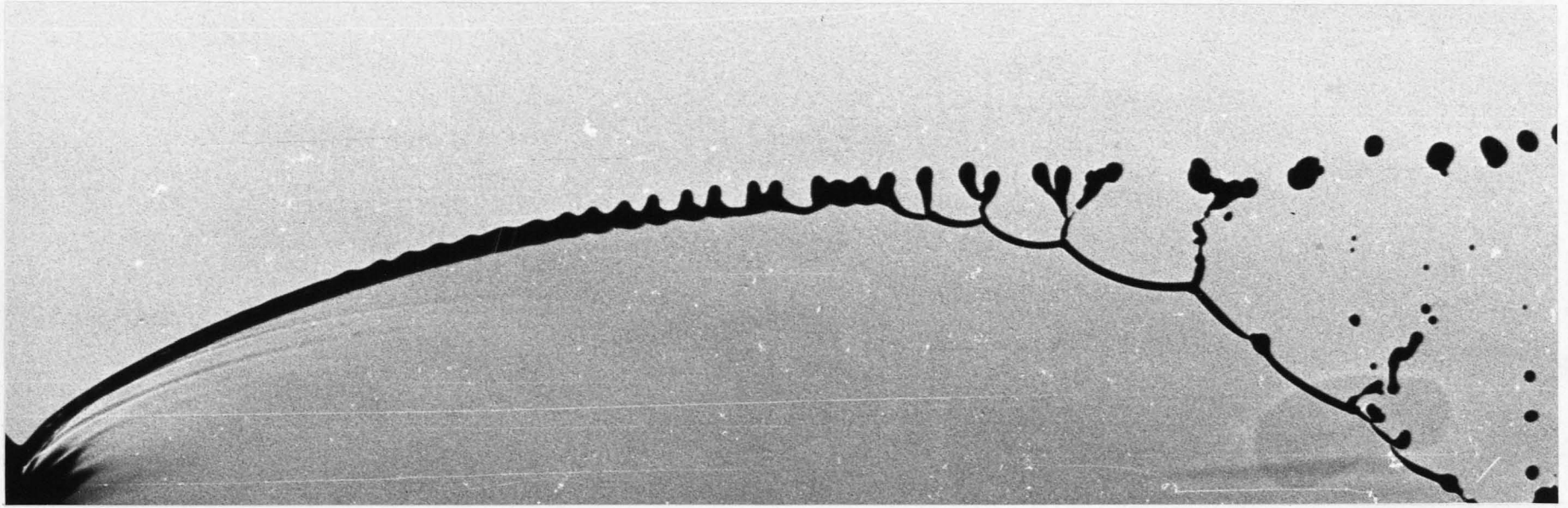
Magnification :-   x 10.7

Nozzle   :-   Bray Unijet Y

Differential Injection Pressure :- 0.69 bar (10 psig)

Fig. 2.3   Growth of Waves on the rim of a Fan Spray Water Sheet.

UNDISTURBED RIM SURFACE

ORIGINAL POSITION OF
SHEET EDGE

I INITIAL
SYMMETRICAL
DISTURBANCE

II ASYMMETRICAL DISTURBANCE
AT LATER STAGE OF GROWTH

III UNDERMINING OF WAVE BY
EXPANDING TROUGHS

IV ACCUMULATION OF LIQUID
AT END OF PROTUBERANCE

V FORMATION OF
DROPS
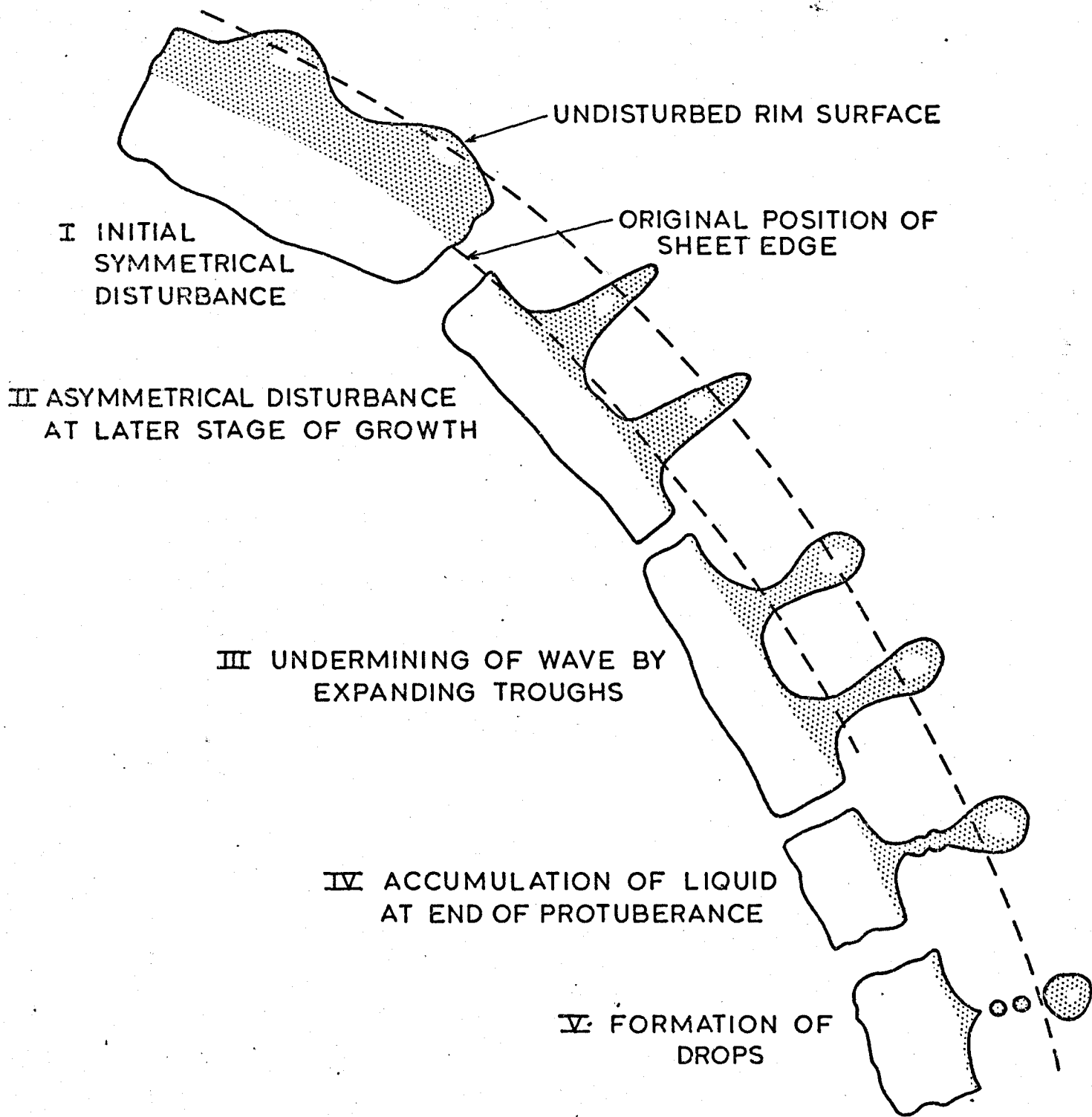
FIG. 24   DISINTEGRATION OF A LIQUID RIM
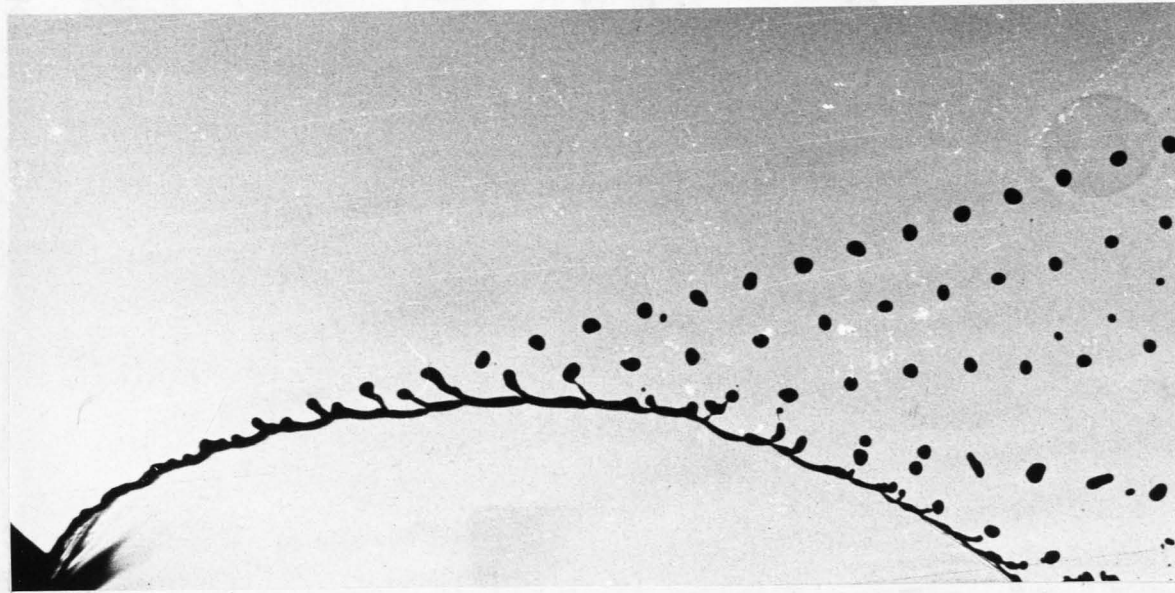
Magnification :- x 6.9

Nozzle :- Bray Unijet Y

Differential Injection Pressure :- 0.69 bar (10 psig)

Fig. 2.5   Formation of Drops from the Rim of a Fan Spray Water Sheet.
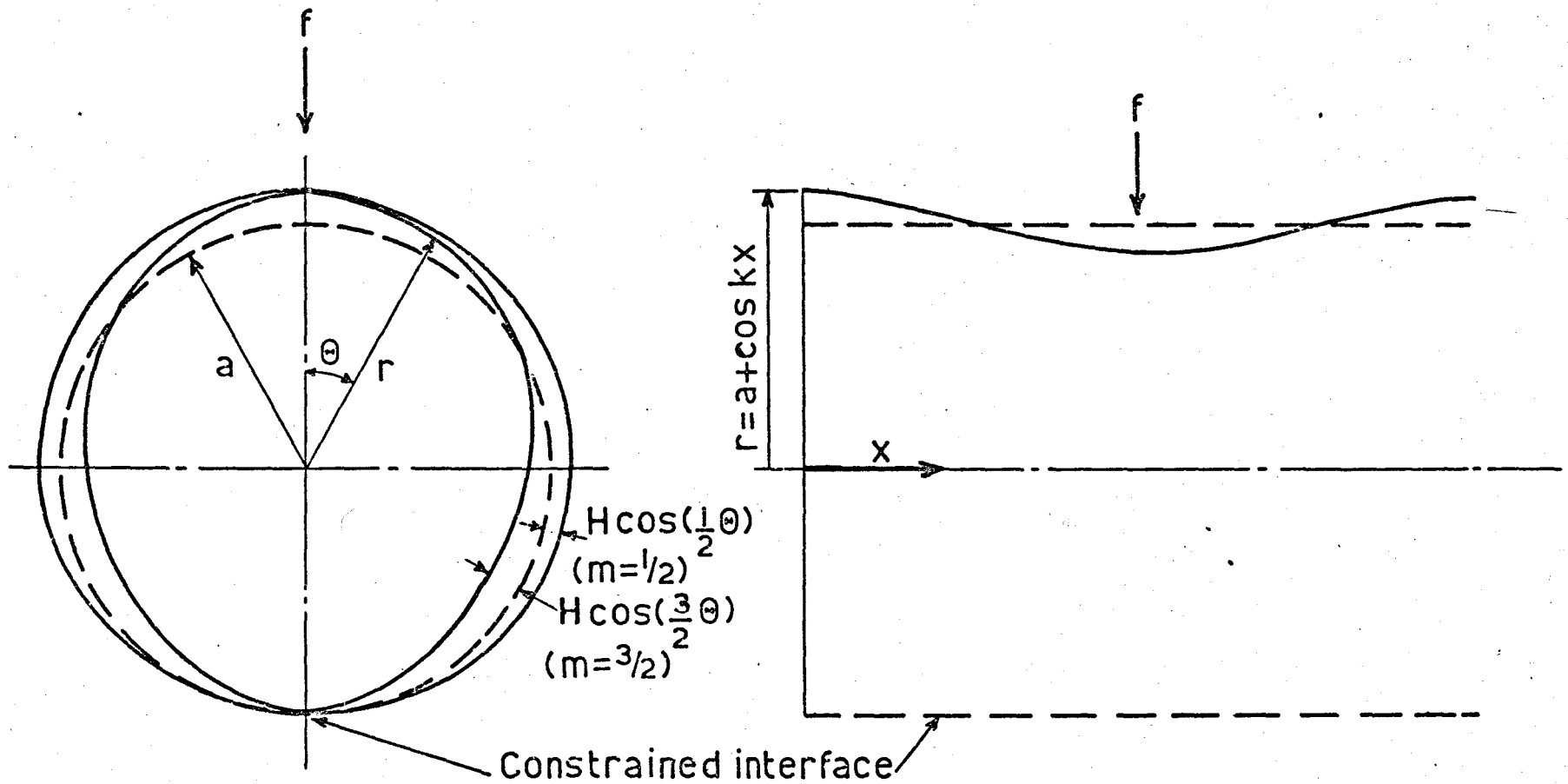
RADIAL DISTURBANCES
ON A JET

LONGITUDINAL DISTURBANCE

Fig. 2.6 Accelerated liquid jet.

2.1.2 Stability of a Liquid Rim Moving along a Curved Path

An enlargement of part of a rim on a sheet of water is shown in
Fig.(2.3) which demonstrates that disintegration occurs as a result of
a high frequency wave motion.   A pictorial representation is given in
Fig.(2.4).   Growth is initially symmetrical, but becomes asymmetrical
at later stages, the waves having the form of spiky projections
separated by shallow troughs.   Eventually the troughs break through
the rim into the thinner sheet where expansion takes place at a con-
siderably accelerated rate.   The base of the wave becomes rapidly
undermined to form a swollen ended protuberance joined to the sheet by
a narrow stem.   The end of the protuberance contracts into a spherical
form and then becomes detached when the stem breaks down, producing
large drops with a few satellites.   It has been found that under
steady flow conditions this mechanism may generate a stream of
regularly sized drops (c.f. Fig.(2.5).   The general appearance of
the waves is characteristic of Taylor instability (12) and the wave
growth can thus be expected to be influenced by the centrifugal forces
generated by a curved trajectory.   A rigorous analysis of the problem
is most complex; it requires solution of the equations of motion in
three dimensions where body forces and equilibrium fluid boundaries
are both time dependent.   However, in most cases the variation of rim
diameter over several wavelengths is very small and the problem can be
reduced to that of a laterally accelerated liquid jet of constant radius.

The system thus considered (Fig.(2.6)) comprises a cylindrical
jet of uniform cross section in which the motion is constrained along
a line formed by the intersection with the surface of a plane passing
through the jet axis.   The liquid is accelerated in a direction from
the gaseous to the liquid phase as shown.   It is assumed that the

cross section of the jet remains sensibly circular under the action of the acceleration.

Instability can be attributed to a combination of two effects, namely, the capillary force generated by a reduction of surface energy and a body force generated by acceleration. The two effects may be studied by Lagrange's method (13) which requires evaluation of the kinetic and potential energies of the jet when subjected to an arbitrary disturbance.

Where viscous dissipation is negligible, conservation of energy gives,

$$(S_1 - S_0) = -(Q_1 - Q_0) \tag{2.11}$$

where S and Q denote respectively total kinetic and potential energies contained in one wavelength, and the subscripts 1 and o denote the disturbed and initial state of the jet. The change in potential energy between these two states, $(Q_1 - Q_0)$, results from a net change in surface area and net force displacement.

In the disturbed state the surface area of the jet along a wave is given by the relation,

$$A_1 = \int_{-\pi}^{+\pi} \int_0^1 \quad r'(1 + (\frac{\partial r'}{\partial x})^2)^{\frac{1}{2}}(1 + \frac{1}{r'^2}(\frac{\partial r'}{\partial \theta})^2)^{\frac{1}{2}} \ d \ (\frac{kx}{2\pi}) \ d\theta \tag{2.12}$$

For an arbitrary harmonic disturbance of the form,

$$r' = a + H \cos kx \cos m\theta$$

where $H = H(t) \ll a$, and a is the effective radius of the disturbed jet (22).

Expansion of the integrand in equation (2.12) to include terms of $O(H^2)$ gives,

$$A_1 = a \iint_{-\pi}^{\pi} \int_0^1 (1 + \frac{H}{a} \cos(kx) \cos(m\,\Theta) + \frac{k^2 H^2}{2} \sin^2(kx) \cos^2(m\,\Theta) +$$

$$\frac{m^2 H^2}{2a^2} \cos^2(kx) \sin^2(m\,\Theta)) \; d(\frac{kx}{2\pi}) \; d\Theta \tag{2.13}$$

Using the identities,

$$\sin^2(x) = \frac{1 - \cos(2x)}{2}$$

and

$$\cos^2(x) = \frac{1 + \cos(2x)}{2}$$

equation (2.13) may be integrated to give,

$$A_1 = 2\pi a + \left\{ \frac{k^2 H^2 a}{2} (\frac{\pi}{2} + \frac{\sin(2m\pi)}{4m}) + \frac{m^2 H^2}{2a} (\frac{\pi}{2} - \frac{\sin(2\pi m)}{4m}) \right\}$$

The net change in surface area between the disturbed and un-
disturbed states is therefore,

$$A_1 - A_0 = 2\pi a - 2\pi a_0 + \frac{k^2 H^2 a}{2} \left\{ (\frac{\pi}{2} + \frac{\sin(2m\pi)}{4m}) \right\} +$$

$$\left\{ \frac{m^2 H^2}{2a} (\frac{\pi}{2} - \frac{\sin(2m\pi)}{4m}) \right\} \tag{2.14}$$

where a_0, the radius of the undisturbed jet is related to a, the
effective radius of the disturbed jet by continuity viz.

$$a_0 = a \left\{ \frac{1}{2\pi} \int_{-\pi}^{+\pi} \int_0^1 (1 + \frac{H}{a} \cos(kx) \cos(m\,\Theta))^2 \; \frac{d(xk)}{2\pi} d\Theta \right\}^{1/2} \tag{2.15}$$

Combining equations (2.14) and (2.15) gives to $C(H^2)$

$$A_1 - A_0 = \frac{a H^2 \pi}{2} \left\{ (\frac{1}{2} + \frac{\sin(2m\pi)}{4m\pi})(k^2 - \frac{1}{a^2}) + \right.$$

$$\left. \frac{m^2}{a^2} (\frac{1}{2} - \frac{\sin(2m\pi)}{4m\pi}) \right\}$$

The surface energy change, $(Q_{A1} - Q_{AO})$ associated with this con-
figuration is

$$(Q_{A1} - Q_{Ao}) = \frac{T a H^2 \pi}{2} \left\{ (\frac{1}{2} + \frac{\sin(2m\pi)}{4m\pi})(k^2 - \frac{1}{a}) + \right.$$

$$\left. \frac{m^2}{a^2} (\frac{1}{2} - \frac{\sin(2m\pi)}{4m\pi}) \right\} \tag{2.16}$$

The energy change associated with the force displacement $(Q_{f1} - Q_{fo})$ is given by,

$$(Q_{f1} - Q_{fo}) = -\frac{\rho_1}{2} \int_{-\pi}^{+\pi}\int_0^1 r'(H \cos(kx) \cos(m \Theta) - (a_o - a))^2$$

$$f \cos \Theta \frac{d(xk)}{2\pi} \, d\Theta \tag{2.17}$$

where f is the centrifugal acceleration.

Using the relation

$$\cos \Theta \, \cos(2m \Theta) = \tfrac{1}{2}(\cos((2m + 1) \Theta) + \cos((2m - 1) \Theta))$$

equation (2.17) can be integrated to give to $C(H^2)$

$$(Q_{f1} - Q_{fo}) = -\rho_1 \frac{afH^2}{8}\left\{ \frac{\sin((2m + 1)\pi)}{(2m + 1)} + \frac{\sin((2m - 1)\pi)}{(2m - 1)}\right\} \tag{2.18}$$

For irrotational flow the kinetic energy can be written as

$$S = \rho_1 \int_{-\pi}^{+\pi}\int_0^1 \frac{r'}{2} \phi \left(\frac{\partial \phi}{\partial r'}\right) \frac{d(xk)}{2\pi} \, d\Theta \tag{2.19}$$

ϕ, the velocity potential is a solution of Laplace's equation which written in cylindrical co-ordinates is,

$$\frac{\partial^2 \phi}{\partial r'^2} + \frac{1}{r'} \frac{\partial \phi}{\partial r'} + \frac{1}{r'^2} \frac{\partial^2 \phi}{\partial \Theta^2} + \frac{\partial^2 \phi}{\partial x^2} = 0$$

and is made unique by the boundary conditions,

$$\frac{\partial \phi}{\partial r} = -\frac{\partial r'}{\partial t}$$

for $r' = a + H \cos(kx) \cos(m \Theta)$ and $-\pi < \Theta < \pi$

and $\frac{\partial \phi}{\partial r'} = 0$

for $r' = a + H \cos(kx) \cos(m \Theta)$ and $\Theta = \pi$

The appropriate solution is,

$$\phi = -H_t \frac{\cos(kx) \cos(m \Theta) \, I_m(kr)}{k \, I_{m,r}(ka)}$$

where I_m is a modified Bessel function; $I_{m,r}'$ is its derivatives with respect to kr', and m may take only the values $\frac{1}{2}$, $\frac{3}{2}$, $\frac{5}{2}$, etc.

Equation (2.19) may now be integrated to give to $O(H^2)$

$$S_1 - S_0 = \frac{H_t^2}{2k} \frac{I_m(ka)\eta}{I_{m,r}'(ka)} \left(\frac{1}{2} + \frac{\sin(2m\pi)}{4\pi m} \right) \tag{2.20}$$

If it is now assumed that the wave amplitude H varies as $H_0 \exp(\beta t)$, then combining (2.16), (2.18) and (2.20) the amplitude growth rate, β, is defined by,

$$\left\{ 1 + \frac{\sin(2m\pi)}{2\pi m} \right\} \frac{H_t^2}{k} \frac{I_m(ka)}{I_{m,r}'(ka)} = \frac{TH^2}{a^2 \rho_1} \left\{ \left(1 + \frac{\sin(2m\pi)}{2\pi m} \right) \right.$$

$$(1 - k^2 a^2) - m^2 \left(1 - \frac{\sin(2m\pi)}{2\pi m} \right) \right\} + \frac{fH^2}{2\pi} \left\{ \frac{\sin((2m+1)\pi)}{(2m+1)} + \right.$$

$$\left. \frac{\sin((2m-1)\pi)}{(2m-1)} \right\} \tag{2.21}$$

Equation (2.21) indicates that the only unstable mode corresponds to $m = \frac{1}{2}$ and the relation may therefore be written,

$$\frac{I_{\frac{1}{2}}(ka)}{I_{\frac{1}{2},r}'(ka)} \frac{\beta^2}{k} = \frac{f}{2} + \frac{T}{a^2 \rho_1} \left(\frac{3}{4} - k^2 a^2 \right) \tag{2.22}$$

and the criterion of instability becomes

$$\left(\frac{f}{2} + \frac{3T}{4a^2 \rho_1} \right) > \frac{Tk^2}{\rho_1} \tag{2.23}$$

For a rim of slowly increasing thickness subjected to a variable normal acceleration, the total growth may be defined in terms of the time average βm, where,

$$\beta_m = \frac{1}{t} \int_0^t \beta(t) \, dt \tag{2.24}$$

It has been shown in Section 2.1 that the shape of the boundary may be described by the following relation,

Nozzle axis
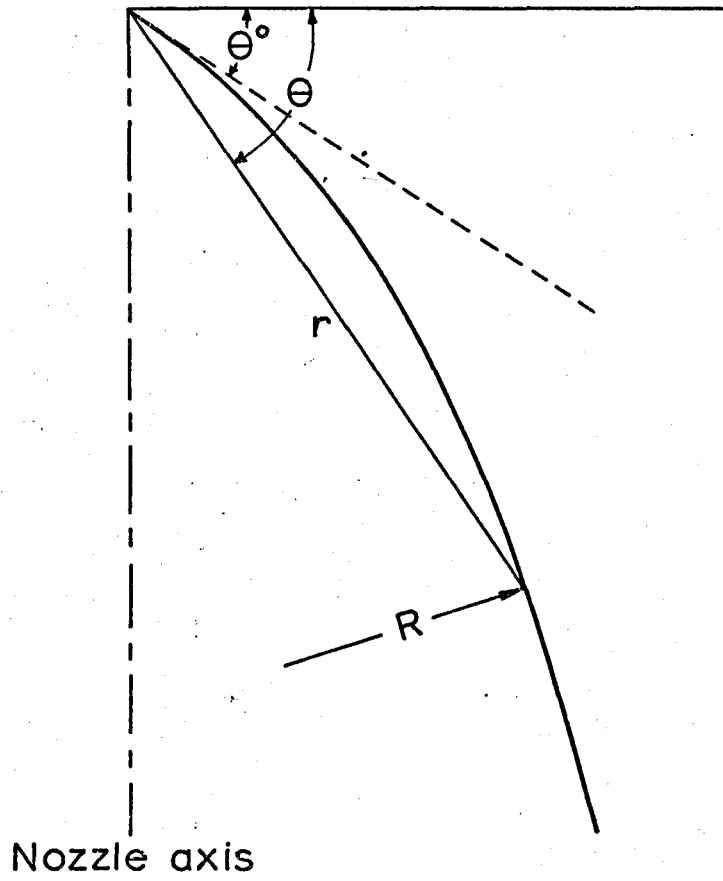
FIG. 2.7   TRAJECTORY OF RIM

$$\frac{4Tr}{\rho_1 K_o U_o^2} = 1 - \cos(\Theta - \Theta_o) + 1.5(\Theta - \Theta_o)^2 \qquad (2.25)$$

where Θ_o defines the direction of the tangent velocity vector at the origin (cf. Fig.(2.7)), the radius of curvature at any point is given by,

$$R = \frac{3}{2} \frac{dr}{d\Theta} \qquad (2.26)$$

and that for the greater part of the rim, U_t is close to the velocity of the sheet U_o. Thus, combining (2.25) and (2.26), and noting that for $(\Theta - \Theta_o) < 1$, $1 - \cos(\Theta - \Theta_o) \simeq \frac{(\Theta - \Theta_o)^2}{2}$, the acceleration experienced by the rim (i.e. $\frac{U_t^2}{R}$) is given as

$$f = \frac{3T}{4 \rho_1 K_o (\Theta - \Theta_o)} \qquad (2.27)$$

whilst the radius at any point is given as

$$a = \left\{ \frac{K_o (\Theta - \Theta_o)}{\pi} \right\}^{\frac{1}{2}} \qquad (2.28)$$

The criterion of stability therefore becomes,

$$\frac{3(\pi + \frac{1}{2})}{4 K_o (\Theta - \Theta_o)} > k^2$$

which is independent of surface tension, density and velocity. Equation (2.24) can only be solved analytically for the limiting case of $ka > 1$, i.e. the diameter $2a > \frac{\lambda}{\pi}$. Inspection of a large number of photographs indicates that this condition corresponds to liquid sheets of low ejection velocity, when the rims are of relatively large curvature. Thus,

$$I_{\frac{1}{2}}(ka) = -\left(\frac{2}{\pi ka}\right)^{\frac{1}{2}} \sinh(ka)$$

and, $\qquad I_{\frac{1}{2}, r}'(ka) = \left\{ -\cosh(ka) + \frac{\sinh(ka)}{2ka} \right\} \left(\frac{2}{\pi ka}\right)^{\frac{1}{2}}$

and hence,

$$\frac{I_{\frac{1}{2}}(ka)}{I_{\frac{1}{2}, r}'(ka)} \simeq 1 \qquad (2.29)$$

Combining equations (2.22), (2.24), (2.27), (2.28) and (2.29) gives;

$$\beta_m = \frac{1}{t} \int_o^t \left(\frac{3(\Uparrow + \frac{1}{2})}{4K_o(\theta - \theta_o)} - k^2 \right)^{\frac{1}{2}} \left(\frac{Tk^2}{\ell_1} \right)^{\frac{1}{2}} dt \qquad (2.30)$$

In principle, the lower limit of integration in equation (2.30) should be taken from the instant at which the rim has thickened sufficiently for the above requirement to be satisfied. However, the growth is initially small and little error will be incurred by taking the limit as zero.

Since ds = $U_o$dt and noting also that ds = $(1 + (\frac{1}{r} \frac{dr}{d\theta})^2)^{\frac{1}{2}} rd\theta$ equation (2.30) may be rewritten in terms of θ viz,

$$\beta_m = \frac{3(\Uparrow + \frac{1}{2})}{4(\theta - \theta_o)} \left(\frac{\ell_1 U_o^2}{T} \right)^{\frac{1}{2}} \int_{\theta_o}^{\theta} \frac{P(\theta - \theta_o)^{\frac{1}{2}}}{k^{\frac{1}{2}}} \left\{ (1 - P^2(\theta - \theta_o))^{\frac{1}{2}} \right.$$

$$\left. (1 + \frac{(\theta - \theta_o)^2}{4})^{\frac{1}{2}} \right\} d\theta \qquad (2.31)$$

where $P = \left\{ \frac{4K_o k^2}{3(\Uparrow + \frac{1}{2})} \right\}^{\frac{1}{2}}$

Under normal operating conditions rim disintegration occurs when $(\theta - \theta_o) < 1$ and since for instability $\frac{4k^2 K_o}{3(\Uparrow + \frac{1}{2})}$ $(\theta - \theta_o) < 1$ equation (2.31) can be simplified to give,

$$\beta_m = \frac{3(\Uparrow + \frac{1}{2})}{4(\theta - \theta_o)} \left(\frac{\ell_1 U_o^2}{T} \right)^{\frac{1}{2}} \int_{\theta_o}^{\theta} \frac{P(\theta - \theta_o)^{\frac{1}{2}}}{k^{\frac{1}{2}}} \left\{ 1 - \frac{P^2}{2} (\theta - \theta_o) - \right.$$

$$\left. \frac{P^4}{8} (\theta - \theta_o)^2 \ldots \ldots \right\} d\theta$$

which on integration gives,

$$\beta_m = \frac{3(\Uparrow + \frac{1}{2})}{4} P \left(\frac{\ell_1 U_o^2}{Tk} \right)^{\frac{1}{2}} \left(\frac{2}{3} (\theta - \theta_o)^{\frac{1}{2}} - \frac{P^2}{5} (\theta - \theta_o)^{3/2} - \right.$$

$$\left. \frac{P^4}{28} (\theta - \theta_o)^{5/2} \ldots \ldots \right) \qquad (2.32)$$

The wave of maximum growth, λ'_d, with wave number k'_d is obtained at any point along the rim by putting $\frac{\partial \beta_m}{\partial k} = 0$. Thus, from equation (2.32)

$$\lambda'_d = 4.74 \ (K_o(\theta - \theta_o))^{\frac{1}{2}} \qquad (2.33)$$

Equation (2.33) shows the wavelength to be independent of sheet velocity and liquid properties and dependent solely on the sheet thickness parameter and the distance from the orifice. However, only the first of these predictions has been verified, the observed (or dominant) wave remaining sensibly constant along the rim. The latter result is not unexpected since the linearized analysis only effectively describes waves during their early stages of growth, higher order terms not being taken into account. Calculated wavelengths for low values of $(\theta - \theta_o)$ where the waves are seen to be in their early stages of growth are about one third of those observed. Measurements of wavelength were made for the range of experiments listed in Table 5 and the resulting relation between the dominant wavelength, λd, and K_o is given by,

$$\lambda d = 2.42 \ K_o^{\frac{1}{2}} \qquad (2.34)$$

Equations (2.32) and (2.34) have been used to estimate the sizes of drops produced when the rim eventually disintegrates, by assuming that the liquid in each drop is derived solely from that contained in one wavelength. By mass balance the drop diameter is given by,

$$D = (6 \ \lambda_d \ a*^2)^{1/3} \qquad (2.35)$$

where a* denotes the effective radius the rim would have at the point of break-up, and is given by,

$$a* = (K_o \ \frac{(\theta* - \theta_o)}{\pi})^{\frac{1}{2}}$$

Break-up occurs when the amplitude of the wave grows to a critical

value, and is defined by the relation,

$$H^* = H_o \exp (\beta_m^* (\Theta^* - \Theta_o))$$

which may be more conveniently written as,

$$\beta_m^* (\Theta^* - \Theta_o) = \ln (\frac{H^*}{H_o}) \qquad (2.36)$$

where the asterisk denotes values at break-up.   From (2.32) and

(2.36)

$$(\Theta^* - \Theta_o)(\frac{\rho_1 U_o^2}{k_d T})^{1/2} \left\{ \frac{2}{3} \rho_d (\Theta^* - \Theta_o)^{1/2} - \frac{P_d^2}{5} (\Theta^* - \Theta_o)^{3/2} - \right.$$

$$\left. \frac{P_d^4}{28} (\Theta^* - \Theta_o)^{5/2} \ldots\ldots\ldots \right\} = \text{Const.} \times \ln (\frac{H^*}{H_o})$$

where $P_d = (\frac{4 K_o k_d^2}{3(\gamma + \frac{1}{2})})^{1/2}$

Since in general $P_d(\Theta - \Theta_o) < 1$ the series may be truncated

after the first term giving,

$$(\Theta^* - \Theta_o)^{3/2} P_d (\frac{\rho_1 U_o^2}{k_d T})^{1/2} = \ln (\frac{H^*}{H_o}) \times \text{Const.} \qquad (2.37)$$

Combining equations (2.34), (2.35) and (2.37)

$$D = \text{const} (\frac{T}{\rho_1})^{1/9} (\frac{K_o^2}{U_o})^{2/9} \ln (\frac{H^*}{H_o}) \qquad (2.38)$$

The term on the right hand side of equation (2.38) contains the

unknown initial and final wave amplitudes.   It is shown in Section (4.3)

that for sheets undergoing aerodynamic wave disintegration $\ln (\frac{\eta^*}{\eta_o})$

has a particular constant value when the orifice Reynolds number is

below 9,000 and another value between Reynolds numbers of 9,000 and

33,000.   In the present study all Reynolds numbers lie below the

former value and since it is reasonable to assume that rim waves will

exhibit similar characteristics under the same flow regime, equation

(2.38) can be written as,

$$D = \text{const } (\frac{T}{\rho_1})^{1/9} (\frac{K_o^2}{U_o})^{2/9} \tag{2.39}$$

Equation (2.39) indicates that the drop size is only weakly determined by the liquid properties and virtually a function of $(\frac{K_o^2}{U_o})$.

2.2 Aerodynamic Instability of Liquid Sheets

The theory of perturbations in liquids has been investigated extensively, the earliest hydrodynamic considerations being connected, naturally, with the tides. Basset (14) presents a comprehensive account of the early history of hydrodynamics, covering the early work of Newton and Laplace. Lamb (15), in order to discriminate between tidal and surface waves, introduced the concept of the capillary wave, with the assumption that it was initiated by a simple harmonic disturbance of low amplitude. Selection of the appropriate velocity potentials led to an expression for the velocity of surface waves of any particular wavelength.

Rayleigh (16), in addition to his well known theoretical analysis of jet disintegration, studied the instability present at the interface of two fluids of differing density and noted that, in cases where the upper fluid is the denser, growth rates were large for small disturbance wavelengths. In similar studies G.I. Taylor (17) examined theoretically the growth of perturbations on an interface accelerated in a direction perpendicular to its plane. . Bellman and Pennington (18) included the effects of surface tension and viscosity and showed that viscosity reduces the rate of growth of surface disturbances, while surface tension reduces the cut-off wave number. Keller and Kolodner (19) further extended the theory by examining the disruption of inviscid sheets by explosion induced acceleration, and estimated, from the most unstable mode, the size of drops which might be obtained as a result of the instability.

Refinements to these theories were carried out by Ingraham (20), who derived a second order approximation, and by Chang et al (21)

who carried the analysis further to a third approximation. Chang notedthat the asymmetric development of an initially sinusoidal disturbance was a non-linear effect and significantly dependent upon the characteristics of the initial disturbance. A similar method of analysis was used by Yuen (22) to study capillary wave growth on liquid jets, and he found that the fundamental frequency and the cut-off wave number were also controlled by the initial amplitude.

Melcher (23) studied the effect of electric and magnetic fields on the growth of waves on conducting liquid surfaces. He applied first order perturbation techniques to Maxwell's equations and developed a criterion of stability for surfaces subject to a stress of electrical origin.

The characteristics of aerodynamic wave growth on parallel-sided inviscid liquid sheets has been studied by Squire (24) and Hagerty and Shea (25). Their analyses have been based upon conventional linearized theory, and first order solutions have been obtained for dilational and sinuous waves. Dombrowski and Johns (11) carried out an approximate analysis for the growth of sinuous waves on viscous sheets by neglecting the tangential component of perturbation velocity and assuming the normal component to be constant throughout the sheet.

In Section 2.2.1 the method of perturbation analysis has been used to provide a more rigorous treatment of the growth of viscous waves. In Section 2.2.2 first order solutions of inviscid flow have been extended to provide a second order solution and, as a result, it has been possible to calculate the critical amplitude at which a sheet breaks down.
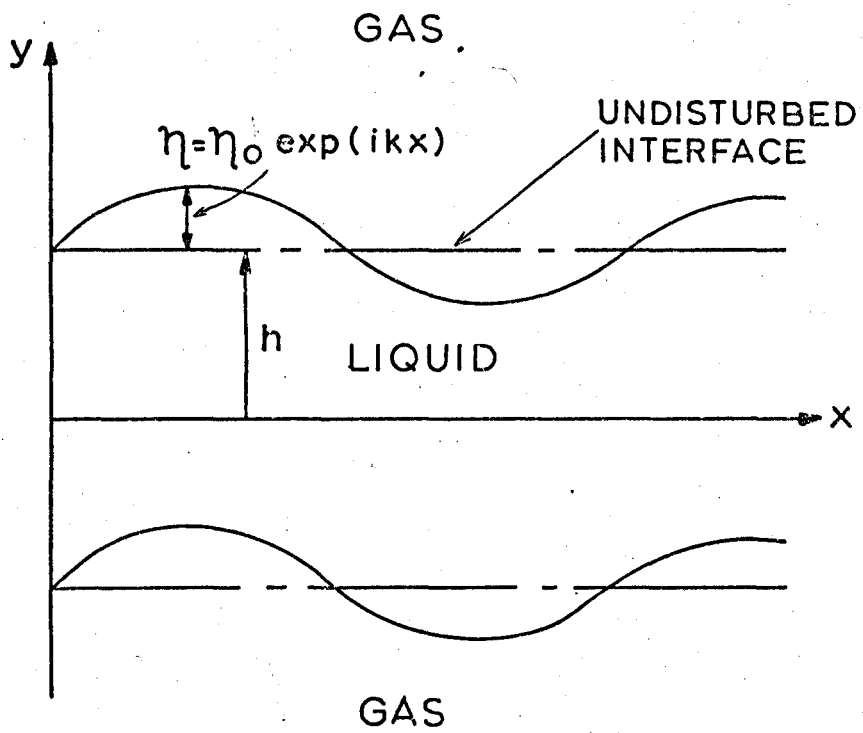
FIG. 2.8 INITIAL SINUOUS DISTURBANCES IMPOSED UPON A PLANE LIQUID SHEET

2.2.1 First Order Solution for Viscous Liquids

The equilibrium system considered, (Fig.(2.8)), comprises a two-dimensional parallel sheet moving with velocity, U_o, through an inviscid stationary gas. The y axis is taken perpendicular to the undisturbed sheet, while the x axis lies along the centre line. The two undisturbed faces are defined by the relation $y = \pm h$.

The system is regarded as having, initially, an arbitrarily small disturbance, the Fourier components of which are assumed dynamically independent. Since each Fourier component is a solution of the linearized equations of motion, it is sufficient to examine the behaviour of a general harmonic disturbance. Zero order acceleration forces are neglected.

For incompressible flow the equations of motion may, therefore, be written as

$$\frac{D u_\alpha}{D t} = - \frac{\partial (p \delta_{\alpha\beta})}{\partial x_\beta} + \frac{\partial \tau_{\alpha\beta}}{\partial x_\beta} \qquad (2.40)$$

and

$$\frac{\partial u_\alpha}{\partial x_\alpha} = 0$$

where $\delta_{\alpha\beta}$ is the symmetric unit tensor and $\tau_{\alpha\beta}$ the shear stress tensor governing Newtonian flow.

The effect of viscosity is to make the flow within the liquid film rotational, and we therefore introduce a perturbation stream function to satisfy the continuity equation.

$$\Psi(x,y,t) = - \Phi(y) \exp (i (kx + nt)) \qquad (2.41)$$

such that the perturbation velocity components are

$$u = -\Psi_y$$

$$v = \Psi_x$$

Combining equations (2.40) and (2.41) and collecting first order terms gives,

$$\nu \, \bar{\Phi}_y^{IV^+} - \bar{\Phi}_y^{II} \, (i(n + U_o k) + 2\nu k^2) + k^2(i(n + U_o k)$$

$$+ \, \nu \, k^2) \, \bar{\Phi} = 0 \tag{2.42}$$

$$-p + \Upsilon_{yy} = 2\rho\nu \frac{\partial v}{\partial y} - \left\{ \bar{\Phi}_y^I \, (\frac{n}{k} + U_o) + \frac{i\nu}{k} (\bar{\Phi}_y^{III} - k^2 \bar{\Phi}_y^I) \right\}$$

$$\rho \, \exp \, i(kx + nt) \tag{2.43}$$

$$\Upsilon_{xy} = \Upsilon_{yx} = -\rho\nu \left\{ \bar{\Phi}_y^{II} + k^2 \bar{\Phi} \right\} \exp \, i(kx + nt) \tag{2.44}$$

where Υ_{xy} and Υ_{yx} are the perturbation components of the tangential and normal stress.

Equation (2.42) is a form of the Orr-Sommerfield equation. Unique solutions are obtained by satisfying the boundary conditions at each interface.

1. The normal velocity of each fluid is given by the relation

$$\Upsilon_x = \frac{\partial \eta}{\partial t} + U_o \frac{\partial \eta}{\partial x} \tag{2.45}$$

for $y = \pm h$ and $\Upsilon_{xj} \to 0$ for $y \to \pm \infty$

2. Shear stress continuity is given by

$$[\![\, \Upsilon_{xy}]\!]^* = \rho\nu \left\{ \frac{\partial v}{\partial x} + \frac{\partial u}{\partial y} \right\} \tag{2.46}$$

for $y = \pm h$

3. Normal stress continuity is given by

$$[\![-p + \Upsilon_{yy}]\!] = -T \frac{\partial^2 \eta}{\partial x^2} \tag{2.47}$$

for $y = \pm h$

where $\eta(x,t)$ is the Fourier component of the initial disturbance and is given by $\eta_1 = \eta_o \, \exp(i \, (kx + nt))$ for the upper interface and $\eta_2 = \eta_o' \, \exp(i \, (kx + nt + \epsilon))$ for the lower interface.

[+] The superscripts I, II, III, and IV denote the degree of differentiation w.r.t. the subscripted variable.

[*] $[\![\,]\!]$ denotes a step change across the interface.

Equations (2.42) through to (2.47) constitute a complete
boundary value problem, and its solution yields a relation between
the properties of primary flow and those of the disturbance. From
this relationship may be deduced the conditions governing instability
of the liquid film.

Equation (2.42) has a solution of the form,

$$\overline{\Phi} = a_1 \exp(ky) + a_2 \exp(-ky) + a_3 \exp(my) + a_4 \exp(-my)$$

where $\quad m^2 = k^2 + i \left(\dfrac{n + U_o k}{\nu_l}\right)$ $\hspace{2cm}$ (2.48)

The stream function then becomes

$$\Psi = (a_1 \exp(ky) + a_2 \exp(-ky) + a_3 \exp(my) + a_4 \exp(-my))$$
$$\exp(i(kx + nt)) \hspace{4cm} (2.49)$$

For the gaseous phase $\nu_a = 0$, and equation (2.49) therefore
reduces to the simple form

$$\Psi_j = (a_1 \exp(ky) + a_2 \exp(-ky)) \exp(i(kx + nt))$$

where the subscript $j = 1$ corresponds to the upper interfaces and
$j = 2$ corresponds to the lower interface.

As $y \to -(-1)^j \infty$, $\Psi_j \to 0$

and therefore

$$\Psi_j = a_1 \exp((-1)^j ky) \exp(i(kx + nt)) \hspace{2cm} (2.50)$$

Solutions of equations (2.49) and (2.50) are obtained for imposed
disturbances of sinuous and dilational form.

2.2.1.1 Sinuous Disturbances

For sinuous disturbances $\eta_1 = \eta_2 = \eta_o \exp(i(kx + nt))$ and
hence combining equations (2.45) and (2.50) and noting that for the
gaseous phase $U_o = 0$

$$a_1 = \eta_c \frac{n}{k} \exp(kh)$$

Therefore,

$$\gamma_j = \eta_0 \frac{n}{k} \exp\left(-(-1)^j ky + kh\right)) \exp\left(i(kx + nt)\right) \qquad (2.51)$$

Combining equations (2.45) and (2.49) and noting that the liquid phase has a finite velocity and viscosity, we get,

$$\eta_0 i (n + U_o k) = ik (a_1 \exp(kh) + a_2 \exp(-kh) + a_3 \exp(mh)$$
$$+ a_4 \exp(-mh)) \qquad (2.52)$$

for $y = +h$

and

$$\eta_0 i (n + U_o k) = ik (a_1 \exp(-kh) + a_2 \exp(kh) + a_3 \exp(-mh)$$
$$+ a_4 \exp(mh)) \qquad (2.53)$$

for $y = -h$

Combining equations (2.49) and (2.46) gives,

$$-2k^2 (a_1 \exp(kh) + a_2 \exp(-kh)) - (m^2 + k^2) (a_3 \exp(mh)$$
$$+ a_4 \exp(-mh)) \qquad (2.54)$$

for $y = +h$

and

$$-2k^2 (a_1 \exp(-kh) + a_2 \exp(kh)) - (m^2 + k^2) (a_3 \exp(-mh)$$
$$+ a_4 \exp(mh)) \qquad (2.55)$$

for $y = -h$

Excluding the trivial case of a_1, a_2, a_3, $a_4 = 0$, the set of equations (2.52) to (2.55) have the following solutions

$$a_1 = a_2$$

$$a_3 = a_4$$

$$a_3 = a_1 \frac{2k^2}{m^2 + k^2} \frac{\cosh(kh)}{\cosh(mh)}$$

$$a_1 = \frac{\eta_0 (n + U_o k)}{k(1 - \frac{2k^2}{m^2 + k^2}) \cosh(kh)}$$

and therefore from equation (2.41) the liquid stream function is given by,
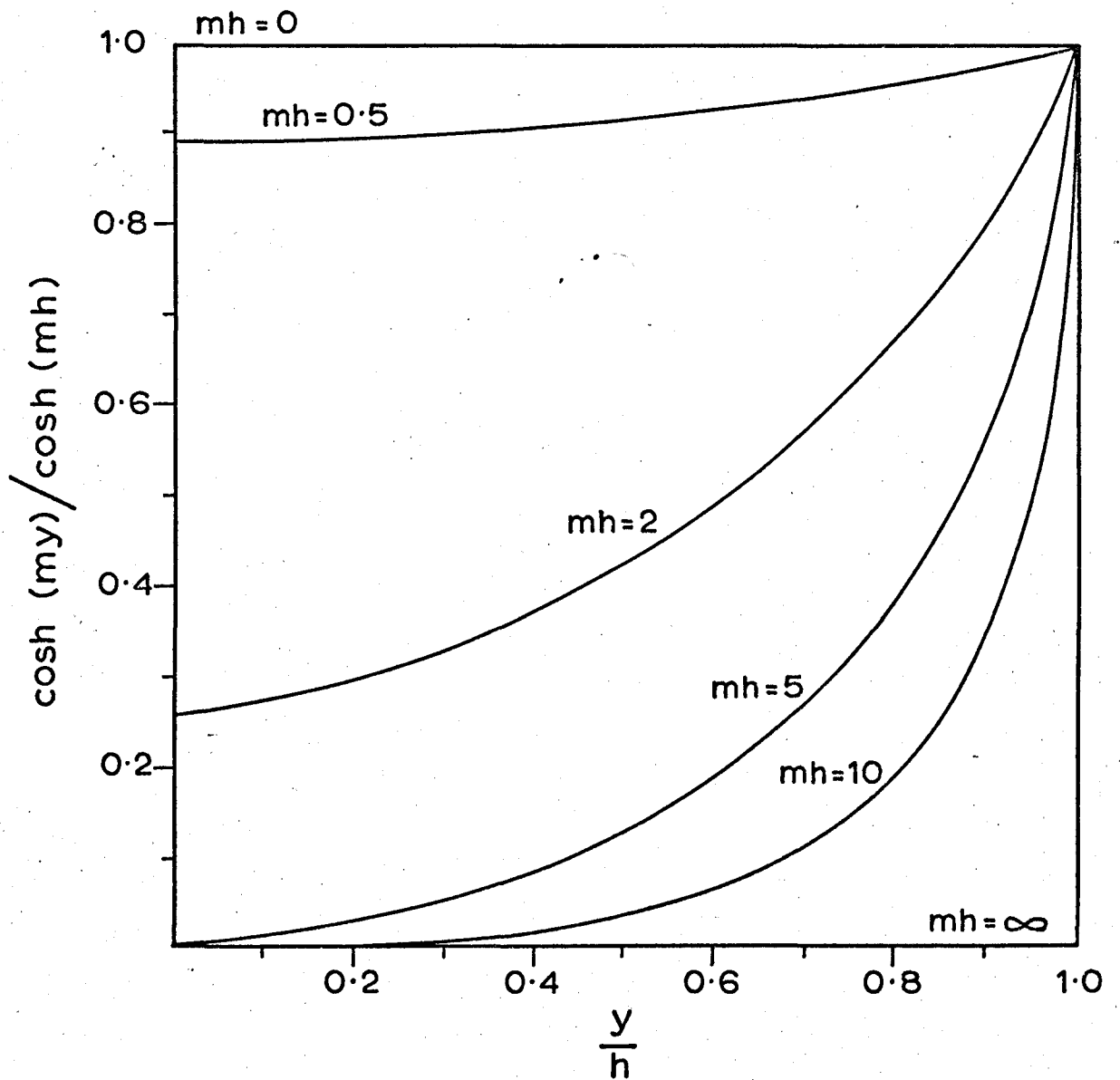
FIG. 2.9   VORTICITY PROFILES FOR SINUOUS WAVES

$$\psi = \frac{\eta_0 \, (n + U_0 k)}{k(1 - \frac{2k^2}{m^2 + k^2})} \left\{ \frac{\cosh(ky)}{\cosh(kh)} - \frac{2k^2}{m^2 + k^2} \frac{\cosh(my)}{\cosh(mh)} \right\}$$

$$\exp(i \, (kx + nt)) \qquad\qquad (2.56)$$

Combining equations (2.51), (2.56) and (2.47) provides an equation governing normal stress continuity, i.e.

$$(2 \nu_{\ell} k^2 + i(n + U_0 k))^2 + \frac{Tk^3 - \rho_a n^2}{\rho_{\ell}} \frac{1}{\tanh(kh)} = 4k^3 m \, \nu_{\ell}^2 \, \tanh(mh)$$

$$\coth(kh) \qquad\qquad (2.57)$$

In order to proceed further and obtain a solution of equation (2.57) it is necessary to gain insight into the nature of the flow within the liquid film by examination of the vorticity function ω, defined as,

$$\omega = \frac{\partial^2 \psi}{\partial x^2} + \frac{\partial^2 \psi}{\partial y^2} \qquad\qquad (2.58)$$

From equation (2.56) equation (2.58) may be re-written as

$$\omega = 2k \, (n + U_0 k) \, f(y) \, \exp(i \, (kx + nt))$$

where $f(y) = \cosh(my)/\cosh(mh)$

The dimensionless parameter $f(y)$ is uniquely determined by mh, the liquid film Reynolds number (c f. equation (2.48)) and provides a measure of the vorticity profile within the liquid film. The function is plotted in Fig.(2.9) for a range of values of mh against the dimensionless thickness parameter y/h^*. The curves indicate that for $mh \gg 1$ the effect of viscosity is essentially to produce a thin boundary layer near the interface in which the flow is rotational. As mh is progressively decreased, the circulatory flow penetrates further into the liquid film until for

---

* It is assumed that waves travel with the sheet velocity so that mh is real (cf. equation (2.48)).

$mh \ll 1$ the vorticity is practically constant throughout. In character with all singular perturbation problems the boundary layer is effectively a region of non-uniformity which must arise following the neglect of the gas phase viscosity and the consequent abolition of the non-slip boundary condition. (26). Solution of equation (2.57) must therefore be restricted to the limiting case of $mh \gg 1$ when the boundary layer is thin and the relation is thus valid over the bulk of the liquid film.

For $mh \gg 1$ $\tanh(mh) \simeq 1$ and hence equation (2.57) reduces to the form

$$(2 \nu_l k^2 + i(n + U_o k))^2 + \frac{Tk^3 - \rho_a n^2}{\rho_l} \tanh(kh) = 4k^3 m \nu_l^2 \coth(kh) \quad (2.59)$$

Using the transformations (15),

$$N^2 = \frac{\rho_a n^2 - Tk^3}{\rho_l} \quad (2.60)$$

$$(i(n + U_o k) + 2 \nu_l k^2) = XN \quad (2.61)$$

and

$$\frac{\nu_l k^2}{N} = M \quad (2.62)$$

equation (2.59) reduces to the form

$$(X^2 \tanh(kh) + 1)^2 = 16M^2(X - M) \quad (2.63)$$

In general $|M| \ll 1$ and hence equation (2.63) becomes

$$(X^2 \tanh(kh) + 1) = 0$$

which, expressed in dimensional variables, is

$$\frac{-\rho_a n^2 + Tk^3}{\rho_l \tanh(kh)} + (i(U_o k + n) + 2 \nu_l k^2)^2 = 0 \quad (2.64)$$

The solution of equation (2.64) gives two roots of the form,

$$n = \alpha - i\beta$$

where α, the wave velocity, is given by the relation

$$\alpha = \frac{-U_o k}{1 + \frac{\rho_a}{\rho_l}\tanh(kh)} \tag{2.65}$$

and β, the rate of wave growth or decay, is given by

$$\beta = -2\nu_1 k^2 \pm$$

$$\left\{ \frac{\frac{\rho_a}{\rho_l}\tanh(kh)(U_o^2 k^2 - 4\nu_1 k^3 U_o i) - \frac{Tk^3}{\rho_l}\tanh(kh)(1 + \frac{\rho_a}{\rho_l}\tanh(kh))}{(1 + \frac{\rho_a}{\rho_l}\tanh(kh))} \right\}^{1/2}$$

where the two roots can be used to specify the initial velocity and initial surface displacement. In general, for a gas liquid system $\frac{\rho_a}{\rho_l}\tanh(kh) \ll 1$ and the criterion of stability is then given by

$$\beta = -2\nu_1 k^2 + \left\{ \frac{\rho_a U_o^2 k^2 - Tk^3}{\rho_l \tanh(kh)} \right\}^{1/2} \tag{2.66}$$

where the term $2\nu_1 k^2$ may be defined as a damping factor. The equation shows that instability arises when energy derived from the flow field is sufficient to overcome viscous dissipation within the sheet.

2.2.2.2 Dilational Disturbances

Solution of equations (2.42) through to (2.47) and (2.28) for dilational disturbances are obtained in a similar way after first noting that $\eta_1 = \eta_o \exp(i(kx + nt))$ and $\eta_2 = \eta_o \exp(i(kx + nt + \pi))$
Thus, for the gaseous phase,

$$\gamma_j = -(-1)^j \eta_o \frac{n}{k}(\exp((-1)^j k \, y + kh)) \exp(i(kx + nt)) \tag{2.67}$$

and for the liquid,
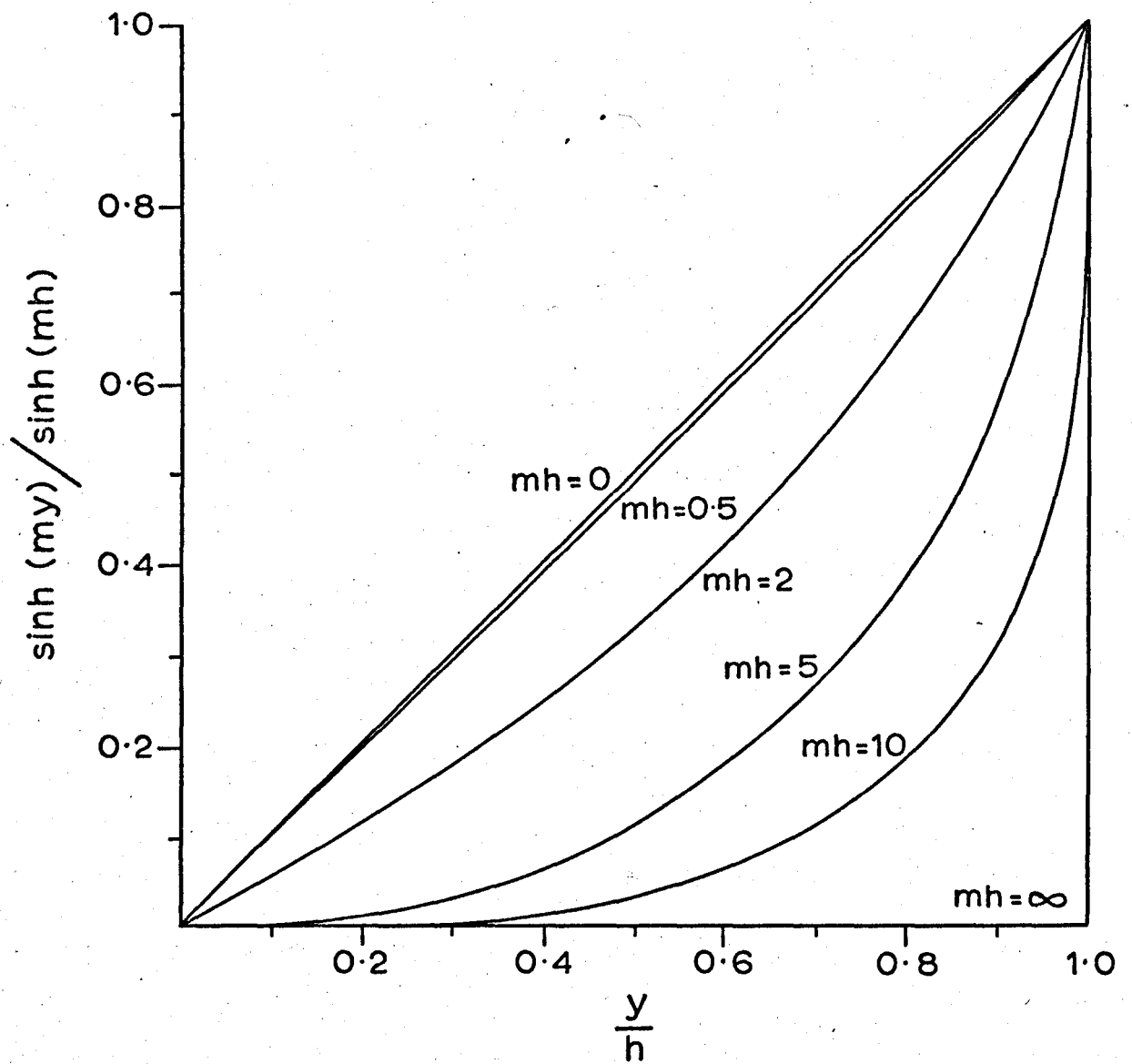
FIG. 2.10 VORTICITY PROFILES FOR DILATIONAL WAVES

$$\gamma = \frac{\eta_o (n + U_o k)}{k \left(1 - \frac{2k^2}{m^2 + k^2}\right)} \left\{ \frac{\sinh(ky)}{\sinh(kh)} - \frac{2k^2}{m^2 + k^2} \frac{\sinh(my)}{\sinh(mh)} \right\} \exp(i(kx + nt)) \tag{2.68}$$

Combining equations (2.47), (2.67) and (2.68) provides the normal stress continuity equation

$$((2\nu_1 k^2 + i(n + U_c k))^2 + \frac{Tk^3 - \rho_a n^2}{\rho_1 \coth(kh)})$$

$$= 4k^3 m \nu_1^2 \tanh(kh) \coth(mh) \tag{2.69}$$

From equations (2.58) and (2.68) the vorticity is given by,

$$\omega = 2k (n + U_o k) f(y) \exp(i (kx + nt))$$

where $f(y) = \sinh(my)/\sinh(mh)$

The function $f(y)$ is plotted in Fig.(2.10) against the dimensionless thickness parameter y/h for a range of mh. For $mh \gg 1$ the vorticity profiles are similar to those obtained for sinuous disturbances and show that the region of non-uniformity is again restricted to a thin layer in the region of the interface. For $mh \ll 1$, however, the function $f(y) \to y/h$ which may be compared with the uniform value attained for a sinuous disturbance (cf. Fig.(2.9)). As before, a valid solution of equation (2.69) can be obtained only for the limiting case of $mh \gg 1$ and hence

$$(2\nu_1 k^2 + i(U_o k + n))^2 + \frac{Tk^3 - \rho_a n^2}{\rho_1 \coth(kh)} = 4k^3 m \nu_1^2 \tanh(kh) \tag{2.70}$$

Using the transformations given by equations (2.60), (2.61) and (2.62) and noting that, in general, $|M| \ll 1$ equation (2.70) reduces to,

$$-\frac{\rho_a n^2 + Tk^3}{\rho_1 \coth(kh)} + (2\nu_1 k^2 + i (n + U_o k))^2 = 0$$

which has the solutions

$$\alpha = -\frac{U_o k}{1 + \frac{\rho_a}{\rho_1} \coth(kh)} \tag{2.71}$$

and,

$$\beta = -2\nu_1 k^2 + \left\{ \frac{\rho_a U_o^2 k^2 - Tk^3}{\rho_1 \coth(kh)} \right\}^{\frac{1}{2}} \qquad (2.72)$$

for $\frac{\rho_a}{\rho_1} \ll 1$

The damping factor is thus similar for both sinuous and dilational waves, and in common with inviscid flow, sinuous waves grow at a greater rate than dilational waves for $kh \ll 1$ and at equal rates when $kh \gg 1$.

The square root terms in (2.66) and (2.72) are identical to the expressions for the growth rates of inviscid waves found by (24) and (25) equation (2.60) and (2.72) may therefore be written as,

$$\beta = \beta' - 2\nu_1 k^2 \qquad (2.73)$$

where β' is the inviscid growth rate. Thus, combining equations (2.48) and (2.73)

$$mh = \left\{ \frac{\beta'}{\nu_1 k^2} - 1 \right\}^{\frac{1}{2}} kh$$

and hence for $mh \gg 1$

$$\frac{\beta'}{\nu_1 k^2} \gg 1 + \frac{1}{k^2 h^2} \qquad (2.74)$$

Inspection of equation (2.74) indicates that the level of viscosity at which the equations may be applied is essentially determined by the sheet thickness, so that wave growth can be examined for either relatively thick sheets of high viscosity or thinner sheets of lower viscosity. Further for $mh \gg 1$ the region of non-uniformity is restricted to a thin layer adjacent to the interface. The flow within the bulk of the film is then irrotational and the potential distribution reduces to that of inviscid flow (cf. equation 2.102). Under these conditions the velocities of both sinuous and dilational waves are independent of viscosity for a gas-liquid system and are effectively equal to that of the sheet (cf. equations (2.65) and (2.71)).

2.2.2   A Second Order Solution of Wave Growth on Inviscid

Liquid Sheets

First order analysis provides a criterion of aerodynamic instability and describes the characteristics of waves in their early stages of growth.   It cannot, however, predict the critical amplitude at which the sheet breaks down, since it shows that during wave growth the two gas-liquid interfaces remain parallel. Thus, to gain further insight into the mechanism of sheet disintegration, the analysis has been extended by a method of successive approximation to take into account non-linear effects.   The approach assumes that the velocity potential and the free surface displacement functions may each be expanded as a series of functions of a small parameter which characterises the wave amplitude.   Sets of linearized boundary value problems are then obtained by arranging for each series to satisfy the equations of motion and the boundary conditions.   The calculations presented have been taken up to the second order terms.

2.2.2.1   Wave Growth on Uniform Sheets

The system considered again comprises a two-dimensional parallel-sided sheet moving with velocity through a stationary gas. The y axis is taken perpendicular to the undisturbed sheet, while the x axis lies along the centre line.   The two undisturbed interfaces are defined by the relation $y = \pm h$.   Zero order acceleration forces are neglected.

At zero viscosity the flow is irrotational and may be described by a velocity potential.   The general equations of continuity are thus:

1.   For the gas phase $\phi'_{xxj} + \phi'_{yyj} = 0$ $\qquad\qquad$ (2.75)

for $\eta_1 + h < y < \infty$, $-\infty < y < -h + \eta_2$, where j

corresponds to the upper ($j = 1$) and lower ($j = 2$) inter-

faces.

Similarly for the liquid phase

$$\phi_{xx} + \phi_{yy} = 0 \tag{2.76}$$

for $\eta_2 - h \leq y \leq h + \eta_1$

Unique solutions are obtained by satisfying the following

boundary conditions:-

1. The surface of the fluid moves with the fluid.

Thus for the gaseous phase,

$$\eta_{tj} - \phi'_{xj}\eta_{xj} + \phi'_{yj} = 0 \tag{2.77}$$

for $y = \eta_j - (-1)^j h$

and for the liquid phase

$$\eta_{tj} - \phi_x \eta_{xj} + \phi_y = 0 \tag{2.78}$$

where each surface is defined by $y = \eta_j(x, t) - (-1)^j h$

2. The component of normal stress is continuous across the

interface.   Thus,

$$(\phi_t \rho_1 - \phi'_{t,j}\rho_a) - \tfrac{1}{2}\rho_1(\phi_x^2 + \phi_y^2) + \tfrac{1}{2}\rho_a(\phi'^2_{x,j} + \phi'^2_{y,j})$$

$$= (-1)^j T(\eta_{xx,j} \cdot (1 + \eta^2_{x,j})^{-3/2}) \tag{2.79}$$

for $y = \eta_j - (-1)^j h$

Following Rosenhead (27) we assume that the surface dis-

turbances and velocity potentials admit expansions of the form,

$$\eta_j = h \cdot \sum_{r=1}^{\infty} \eta_o^r \, {}^r\eta_j^* (x,t) \tag{2.80}$$

* Superscripts preceeding the terms of the series represent

the order of that term

and

$$\phi = \sum_{r=0}^{\infty} \eta_o^r \; {}^r\phi(x,y,t) \quad (2.81) \qquad \phi_j' = \sum_{r=1}^{\infty} \eta_o^r \; {}^r\phi_j'(x,y,t) \quad (2.82)$$

where η_o is a small dimensionless parameter defined as the initial amplitude to sheet thickness ratio,

where $\phi_o = -U_x$ and ${}^r\phi_j'$, ${}^r\phi$ must satisfy equations (2.75) and (2.76) respectively.

The function ϕ can be expressed at $y = \eta \pm h$ in terms of its value and those of its derivatives at $y = h$ by a Taylor series, i.e.

$$ {}^r\phi(\eta_j - (-1)^j h) = {}^r\phi(-(-1)^j h) + \eta_j \left. \frac{\partial \, {}^r\phi}{\partial y} \right|_{y = -(-1)^j h} \quad (2.83)$$

The surface disturbance may be represented as a periodic function by the complex Fourier series of the form,

$$\eta_j = h\left(\eta_o \; {}^1\psi_j(t) \, \exp(ikx) + \sum_{m=2}^{\infty} \sum_{m=1}^{\infty} \eta_o^r \; {}^{m,r}\psi_j(t) \, \exp(im\alpha x) \right) \quad (2.84)$$

where ${}^{mr}\psi(t)$ is a function of time only, and k is a real number representing the spatial frequency. Solutions of ${}^{mr}\psi(t)$ are made unique by the condition that,

$$ {}^{mr}\psi_j(o) = \left. \frac{\partial \, {}^{mr}\psi_j}{\partial t} \right|_{t=0} = 0 \quad r \geqslant 2, \quad m \geqslant 2 \quad (2.85)$$

and $\; {}^1\psi_j(o) = 1, \quad \left. \dfrac{\partial \, {}^1\psi_j}{\partial t} \right|_{t=0} = i\alpha \quad (2.86)$

The set of linear equations thus generated have been successively solved to obtain a solution of the second approximation.

I. Solution of the first order equations

Combining equations (2.75) through to (2.83) and collecting first order terms gives;

$$^1\phi'_{xx,j} + {}^1\phi'_{yy,j} = 0 \ , \ h < y < \infty \ , \ -\infty < y < -h \tag{2.87}$$

$$^1\phi_{xx} + {}^1\phi_{yy} = 0 \quad , \ -h \leq y \leq h \tag{2.88}$$

$$^1\phi'_{y,j} + h{}^1\eta_{t,j} = 0 \quad , \ y = \pm h \tag{2.89}$$

$$^1\phi_y + hU_0{}^1\phi_x + h{}^1\eta_{t,j} = 0 \ , \ y = \pm h \tag{2.90}$$

$$({}^1\phi_t \rho_1 - {}^1\phi'_{t,j} \rho_a) + \rho_1 U_0{}^1\phi_x - (-1)^j hT{}^1\eta_{xx,j} = 0 \ , \ y = \pm h \tag{2.91}$$

Substitution in (2.89) , for $^1\eta_j$ from equation 2.84 gives,

$$^1\phi'_{y,j} = -h\psi_{t,j} \exp(ikx) \quad , \quad y = \pm h \tag{2.92}$$

and $\quad ^1\phi_y = -h\psi_{t,j} \exp(ikx) - iU_0 kh \exp(ikx), \ y = \pm h \tag{2.93}$

From equations (2.88) and (2.87) the solutions for $^1\phi$ and $^1\phi'$ have the form,

$$^1\phi'_j = (A_j \exp(ky) + B_j \exp(-ky))(C_j \exp(ikx) + D_j \exp-(ikx))$$
$$F_j(t) + fj(t) \tag{2.94}$$

$$^1\psi = (E \exp(ky) + F \exp(-ky))(G \exp(ikx) + H \exp(-ikx))$$
$$F_3(t) + f_3(t) \tag{2.95}$$

where A_j, B_j, C_j, D_j and E, F, G, H are constants of integration.

As $y \to -(-1)^j \infty$ then $^1\phi'_j \to 0$ for all t and hence, $A_1 = B_2 = 0$

Also from equations (2.92) and (2.94) ,we get,

$$-^1\psi_{t1} \exp(ikx) = (-k/h) \exp(-kh)F_1(t) (C_1 \exp(ikx) + D_1$$
$$\exp(-ikx))$$

for $y = +h$, and,

$$-^1\psi_{t2} \exp(ikx) = (k/h) \exp(kh)F_2(t) (C_2 \exp(ikx) + D_2$$
$$\exp(-ikx))$$

for $y = -h$

By inspection, $D_j = 0$ and $C_j F_j(t) = \dfrac{-(-1)^j \exp(kh)h \, {}^1\gamma_{tj}}{k}$

Similarly from equations (2.93) and (2.95)

$$F_3(t) \, k \, (E \exp(kh) - F \exp(-kh))(G \exp(ikx) + H \exp(-ikx))$$

$$= -h \, {}^1\gamma_{t1} \exp(ikx) - iU_o kh \exp(ikx) \, {}^1\gamma_1$$

for $y = +h$

$$F_3(t) \, k \, (E \exp(-kh) - F(\exp kh))(G \exp(ikx) + H \exp(-ikx))$$

$$= -h \, {}^1\gamma_{t2} \exp(ikx) - iU_o kh \exp(ikx) \, {}^1\gamma_2$$

for $y = -h$

where by inspection $H = 0$ and thus, by elimination

$$F_3(t) \, EG = \frac{-(h \, {}^1\gamma_{t2} + iU_o kh \, {}^1\gamma_2)(\gamma \exp(kh) - \exp(-kh))}{2k \sinh(2kh)}$$

$$F_3(t) \, FG = \frac{-(h \, {}^1\gamma_{t2} + iU_o kh \, {}^1\gamma_2)(\gamma \exp(-kh) - \exp(kh))}{2k \sinh(2kh)}$$

where $\gamma = \dfrac{{}^1\gamma_1}{{}^1\gamma_2}$

Hence combining equations (2.91), (2.94) and (2.95) the two linear differential equations governing normal stress continuity at each interface are;

$$\rho_1 \left(- \left\{ h \, {}^1\gamma_{tt2} + {}^1\gamma_{t2} \, iU_o kh \right\} \left\{ \frac{\gamma \cosh(2kh) - 1}{k \sinh(2kh)} \right\} \exp(ikx) + \rho_a f_{t,1} \right.$$

$$+ \rho_2 f_{t3} - \rho_a h \frac{{}^1\gamma_{tt2}}{k} \gamma \exp(ikx)) - \rho_1 U_o (\left\{ h \, {}^1\gamma_{t2} + {}^1\gamma_2 \, iU_o kh \right\}$$

$$(ik) \left\{ \frac{\gamma \cosh(2kh) - 1}{k \sinh(2kh)} \right\} \exp(ikx)) - Tk^2 \gamma \, h \, {}^1\gamma_2 = 0 \qquad (2.96)$$

for $y = +h$, and,

$$\rho_1 (-\left\{ h \, {}^1\gamma_{tt2} + {}^1\gamma_{t2} \, iU_o kh \right\} \left\{ \frac{\gamma - \cosh(2kh)}{k \sinh(2kh)} \right\} \exp(ikx) + \rho_1 f_{t3}$$

$$- \rho_a f_{t,1} + (\rho_a h \frac{{}^1\gamma_{tt2}}{k} \exp(ikx)) - \rho_1 U_o (\left\{ h \, {}^1\gamma_{t2} + {}^1\gamma_2 \, iU_o k \right\}$$

$$\left\{ \frac{\gamma - \cosh(2kh)}{k \sinh(2kh)} \right\} \exp(ikx)) + Tk^2 h \, {}^1\gamma_2 = 0 \qquad (2.97)$$

By inspection $\gamma = 1$ and $f_1 f_3 = 0$ and equations (2.96) and (2.97) reduce to the single expression:

$$-\frac{{}^1\psi_{tt}}{k}\{\rho_1 \tanh(kh) + \rho_a\} - 2iU_0\rho_1 \tanh(kh) {}^1\psi_t +$$

$$\{kU_0^2\rho_1 \tanh(kh) - Tk^2\}\,{}^1\psi = 0$$

which has the solution:

$${}^1\psi = A\exp(i(\alpha' + {}_i\beta')t) + B\exp(i(\alpha' - {}_i\beta')t)$$

where α' and β' are the real and imaginary parts of the complex wave frequency n and its conjugate $\bar{n}$, i.e.

$$\alpha' = \frac{-U_0 k}{1 + \dfrac{\rho_a}{\rho_1} \tanh(kh)} \tag{2.98}$$

$$\beta' = \left\{\frac{(\rho_1\rho_a\, U_0^2 k^2 \tanh(kh) - Tk^3(\rho_1\tanh(kh) + \rho_a)}{(\rho_1 \tanh(kh) + \rho_a)^2}\right\}^{1/2} \tag{2.99}$$

Equations (2.98) and (2.99) are identical to those presented by Squire without derivation and identical to equations (2.65) and (2.66) when $\nu = 0$.

For the initial conditions ${}^1\psi(0) = 1$ and $\dfrac{\partial {}^1\psi}{\partial t}\Big|_{t=0} = i\alpha'$

$A = B = \frac{1}{2}$ and therefore ${}^1\psi = \cosh\beta' t\,\exp(i\alpha' t)$ (2.100)

Thus combining equations (2.84), (2.94), (2.95), and (2.100) gives for ${}^1\eta_1, {}^1\phi, {}^1\phi'$ viz.

$${}^1\eta = {}^1\psi \exp(ikx) \tag{2.101}$$

$${}^1\phi = -\left\{h\,{}^1\psi_t/k + hiU_0\,{}^1\psi\right\}\frac{\sinh(ky)}{\cosh(kh)}\exp(ikx) \tag{2.102}$$

$${}^1\phi' = -(-1)^j\,\frac{h\,{}^1\psi_t}{k}\,\exp(kh)\exp((-1)^j ky)\exp(ikx) \tag{2.103}$$

II Solution of 2nd Order Equations

Combining equations (2.75) through to (2.83) and collecting second order terms gives:-

$$^2\phi'_{xx_j} + {}^2\phi'_{yx_j} = 0, \text{ for } h < y < \infty \ , \ -\infty < y < \ -h \tag{2.104}$$

$$^2\phi'_{xx} + {}^2\phi'_{yy} = 0, \text{ for } -h \leq y \leq h \tag{2.105}$$

$$h^2\eta_{t,j} - (h^1\eta_x \ {}^1\phi'_{x,j}) + {}^2\phi'_{y,j} + {}^1\phi'_{yy,j} \ {}^1\eta h = 0, \text{ for } y = \pm h \tag{2.106}$$

$$h^2\eta_{t,j} - (h^1\eta_x \ {}^1\phi_x + h^2\eta_{x,j} \ {}^0\phi_x) + {}^2\phi_y + {}^1\phi_{yy} {}^1\eta^h \tag{2.107}$$
$$= 0, \text{ for } y = \pm h$$

$$(^2\phi_t \ \varrho_1 - {}^2\phi'_{t,j}\varrho_a) - \tfrac{1}{2}\varrho_1({}^1\phi_x^2 + {}^1\phi_y^2 + 2{}^0\phi_x \ {}^2\phi_x) + \tfrac{1}{2}\varrho_a$$

$$(^1\phi'^2_{x,j} + {}^1\phi'^2_{y,j}) - \varrho_a \ {}^1\phi'_{t,y,j} \ {}^1\eta \ h + \varrho_1 \ {}^1\phi_{t,y} \ {}^1\eta^h - \varrho_1 \ {}^0\phi_x$$

$$^1\phi_{xy} \ {}^1\eta \ h = -(-1)^j \ T \ {}^2\eta_{xx}h, \text{ for } y = \pm h \tag{2.108}$$

where ${}^1\phi$, ${}^1\phi'_j$, ${}^1\eta$ and ${}^2\eta_j$ are defined by equations (2.102), (2.103), (2.101) and (2.84) respectively.

Solving equations (2.104) and (2.105) gives,

$$^2\phi'_j = (A_j \exp(2ky) + B_j \exp(-2ky))(C_j \exp(2 ikx) + D_j \exp(-2 ikx))$$
$$F_j(t) + f_j(t) \tag{2.109}$$

$$^2\phi = (E \exp(2ky) + F \exp(-2ky))(G \exp(2 ikx) + H \exp(-2 ikx))$$
$$F_3(t) + f_3(t) \tag{2.110}$$

where A_j, B_j, C_j, D_j, $f_j(t)$ $j = 1$ and 2 and f_3, E, F, G and H are constants of integration.

As $y \to -(-1)^j\infty$ then ${}^2\phi'_j \to 0$ for all t and hence,

$$A_1 = B_2 = 0$$

Also from equations (2.101) to (2.103) and (2.106) we get,

$$h^2 2\psi_{t,1} \exp(2ikx) + {}^2\phi'_{y1} = -k^2 h^2 \left\{ \left(\frac{\beta'}{2k} \sinh(2\beta't) + i\alpha' \right.\right.$$

$$\left.\left. \left(\frac{1 + \cosh(2\beta't)}{2}\right)\right) \exp(2i\alpha't) \exp(2\,ikx)\right\}, \tag{2.111}$$

for y = +h

and

$$h^2 2\psi_{t,2} \exp(2\,ikx) + {}^2\phi'_{y2} = h^2 \left\{ k^2 \left(\frac{\beta'}{2k} \sinh(2\beta't) + i\alpha' \right.\right.$$

$$\left.\left. \left(\frac{1 + \cosh(2\beta't)}{2}\right)\right) \exp(2\,i\alpha't) \exp(2\,ikx)\right\}, \tag{2.112}$$

for y = -h

Similarly from equations (2.101) to (2.103) and (2.107) we get,

$$h^2 2\psi_{t,1} \exp(2\,ikx) + U_o^2 2\psi_1\, 2\,ik \exp(2\,ikx) + {}^2\phi_y = k^2 h^2$$

$$\left\{\frac{\beta'}{2k} \sinh(2\beta't) + i\,(U_o + \alpha'/k)\left(\frac{1+\cosh(2\beta't)}{2}\right)\tanh(kh) \right.$$

$$\left. \exp(2\,i\alpha't) \exp(2\,ikx)\right\}, \tag{2.113}$$

for y = +h

$$h^2 2\psi_{t,2} \exp(2\,ikx) + U_o^2 2\psi_2\, 2\,ik \exp(2\,ikx) + {}^2\phi_y = -k^2 h^2$$

$$\left\{\frac{\beta'}{2k} \sinh(2\beta't) + i(U_o + \alpha'/k)\left(\frac{1+\cosh(2\beta't)}{2}\right)\tanh(kh) \right.$$

$$\left. \exp(2\,i\alpha't)\exp(2\,ikx)\right] \tag{2.114}$$

for y = -h

Combining equations (2.109), (2.111) and (2.112) gives,

$$D_j = 0 \text{ and hence,}$$

$$B_1 F_1(t) = \frac{\exp(+2kh)}{2k} \left\{ h^2 2\psi_{t,1} + kh^2 \left(\frac{\beta'}{2} \sinh(2\beta't) + i\alpha' \right.\right.$$

$$\left.\left. \left(\frac{1+\cosh(2\beta't)}{2}\right)\right) \exp(2\,i\alpha't) \right. \tag{2.115}$$

and

$$A_2 F_2(t) = \frac{\exp(+2kh)}{2k} \left\{ -h^2 2\psi_{t,2} + 2kh^2 \left(\frac{\beta'}{2} \sinh(2\beta't) + i\alpha' \right.\right.$$

$$\left.\left. \left(\frac{1+\cosh(2\beta't)}{2}\right) \exp(2\,i\alpha't) \right.\right. \tag{2.116}$$

Similarly combining equations (2.110), (2.113) and (2.114) gives,

H = 0 and hence,

$$2k\left\{E\exp(2kh) - F\exp(-2kh)\right\}F_3(t) = k^2h\left\{\frac{\beta'}{2k}\sinh\right.$$

$$\left.(2\beta't) + i(U_0 + \alpha'/k)(\frac{1 + \cosh(2\beta't)}{2})\right\}\exp(2i\alpha't)\tanh(kh)$$

$$-h^{22}\psi_{t1} - U_0^{22}\psi_1 2\,ikh \tag{2.117}$$

and

$$2k\left\{E\exp(-2kh) - F\exp(2kh)\right\}F_3(t) = -k^2h\left\{\frac{\beta'}{2k}\sinh(2\beta't)\right.$$

$$\left.+ i(U_0 + \alpha'/k)(\frac{1 + \cosh(2\beta't)}{2})\right\}\exp(2i\alpha't)\tanh(kh) - h^{22}\psi_{t2}$$

$$-U_0^{22}\psi_2 2\,ikh \tag{2.118}$$

Elimination of $EF_3(t)$ between (2.117) and (2.118) gives

$$FF_3(t) = \frac{1}{4k\sinh(4kh)}\left\{\left\{(2k^2h^2(\frac{\beta'}{2k}\sinh(\beta'2t) + i(U_0 + \alpha'/k)\right.\right.$$

$$\left.(\frac{1 + \cosh(2\beta't)}{2}))\tanh(kh)\cosh(2kh))\exp(2i\alpha't)\right\} + \left\{h^{22}\psi_{t2}\right.$$

$$\left.+ U_0 2\,ikh^{22}\psi_2\right\}\exp(2kh) - \left\{h^{22}\psi_{t1} + U_0 2kh^{22}\psi_1\right\}\exp(-2kh)\right\}$$

Similarly eliminating $FF_3(t)$ between (2.117) and (2.118) gives

$$EF_3(t) = \frac{1}{4k\sinh(4kh)}\left\{\left\{2k^2h^2(\frac{\beta'}{2k}\sinh(2\beta't) + i(U_0 + \alpha'/k)\right.\right.$$

$$\left.(\frac{1 + \cosh(2\beta't)}{2}))\cosh(2kh)\tanh(kh)\exp(2i\alpha't)\right\} + \left\{h^{22}\psi_{t2}\right.$$

$$\left.+ U_0 2\,ikh^{22}\psi_2\right\}\exp(-2kh) - \left\{h^{22}\psi_{t1} + U_0 2kh^{22}\psi_1\right\}\exp(2kh)\right\}$$

From equations (2.109) and (2.110), the velocity potentials may then be written as

$$2\phi_1' = \frac{\exp(2kh)}{2k}\left\{\left\{h^{22}\psi_{t2}\gamma + kh^2(\frac{\beta'}{2}\sinh(2\beta't) + i\alpha'(\frac{1 + \cosh(2\beta't)}{2}))\right.\right.$$

$$\left.\exp(2i\alpha't)\right\}\exp(2ikx)\exp(-2ky)\right\} + f_1(t) \tag{2.119}$$

$$2\varphi_2' = \frac{\exp(-2kh)}{2k} \left\{\left\{-h^2{}^2\gamma_{t2} + \left\{kh^2(\frac{\beta'}{2}\sinh(2\beta't) + i\alpha'\right.\right.\right.$$

$$\left.\left.(\frac{1+\cosh(2\beta't)}{2})\right\} \exp(2i\alpha't)\right\} \exp(2ikx)\exp(2ky)\right\} \quad (2.120)$$
$$+ f_2(t)$$

$$2\varphi = \left\{EF_3(t)\exp(2ky) + FF_3(t)\exp(-2ky)\right\}\exp(2ikx)$$

$$+ f_3(t) \qquad\qquad (2.121)$$

where

$$EF_3(t) = \frac{+1}{4k\sinh(4kh)}\left\{2k^2h^2\left\{(\frac{\beta'}{2k}\sinh(2\beta't) + i(U_o + \alpha'/k)\right.\right.$$

$$(\frac{1+\cosh(2\beta't)}{2}))\exp(2i\alpha't)\tanh(kh)\cosh(2kh)\right\} + h^2{}^2\gamma_{t2}$$

$$+ U_o 2ikh^2{}^2\gamma_2\right\}\left\{\exp(-2kh) - \gamma\exp(2kh)\right\} \qquad (2.122)$$

and

$$FF_3(t) = \frac{+1}{4k\sinh(4kh)}\left\{2k^2h^2\left\{(\frac{\beta'}{2k}\sinh(2\beta't) + i(U_o + \alpha'/k)\right.\right.$$

$$(\frac{1+\cosh(2\beta't)}{2}))\exp(2i\alpha't)\tanh(kh)\cosh(2kh)\right\} + \left\{h^2{}^2\gamma_{t2}\right.$$

$$+ U_o 2ikh^2{}^2\gamma_2\right\}\left\{\exp(2kh) - \gamma\exp(-2kh)\right\}\right\} \qquad (2.123)$$

From equations (2.84), (2.108) and (2.119) through to (2.123) we get the following simultaneous linear differential equations which satisfy the requirement of stress continuity at each interface, i.e.

$$-2\rho_1 U_o ki\left\{\frac{1}{2k}\left\{\frac{h^2{}^2\gamma_{t2} + U_o^2{}^2\gamma_2 2ikh}{2\sinh(4kh)}\right\}\left\{2\gamma\cosh(4kh) - 2\right\}\right\}$$

$$-\rho_2\left\{\frac{1}{2k}\left\{\frac{h^2{}^2\gamma_{tt2} + U_o^2{}^2\gamma_2 2ikh}{2\sinh(4kh)}\right\}\left\{2\gamma\cosh(4kh) - 2\right\}\right\} - \rho_a$$

$$\left\{\frac{\gamma}{2}(\frac{h^2{}^2\gamma_{tt2}}{k})\right\} - 4Tk^2h^2{}^2\gamma_2\gamma = h^2R(t) + h^2P(t) - \frac{\rho_2 f_{t,3} + \rho_a f_{t,1}}{\exp(2ikx)}$$

$$+\left\{\frac{\rho_1}{4}\left\{(\beta^2(3+\tanh^2(kh)) - (\alpha+U\kappa)^2(1-\frac{\tanh^2(kh)}{2}))\cosh(2\beta t)\right.\right.$$

for $y = +h$ 　$\left.+(\beta^2-(\alpha+U\kappa)^2)(1-\frac{\tanh^2(kh)}{2})\right\} - \frac{\rho_a}{4}(2\beta^2\cosh(2\beta t))\right\}/\exp(2ikx)$ (2.124)

and

$$+ 2\rho_1 U_o ki\left\{\frac{1}{2k}\left\{\frac{h^2{}^2\gamma_{t2} + U_o^2{}^2\gamma_2 2ikh}{2\sinh(4kh)}\right\}\left\{2\cosh(4kh) - 2\gamma\right\} + \rho_2\right.$$

$$\left\{\frac{1}{2k}\left\{\frac{h^2{}^2\gamma_{tt2} + U_o^2{}^2\gamma_2 2ikh}{2\sinh(4kh)}\right\}\left\{2\cosh(4kh) - 2\gamma\right\}\right\} + \rho_a\left\{\frac{h}{2}\right.$$

$$(\frac{{}^2\gamma_{tt2}}{k})\right\} + 4Tk^2h^2{}^2\gamma_2 = h^2R(t) + h^2P(t) - \frac{\rho_2 f_{t,3} + \rho_a f_{t,2}}{\exp(2ikx)}$$

$$+\left\{\frac{\rho_1}{4}\left\{(\beta^2(\frac{3+\tanh^2(kh)}{2})) - (\alpha+U\kappa)^2(1-\frac{\tanh^2(kh)}{2}))\cosh(2\beta t)\right.\right.$$

for $y = -h$ 　$\left.+(\beta^2-(\alpha+U\kappa)^2)(1-\frac{\tanh^2(kh)}{2})\right\} - \frac{\rho_a}{4}(2\beta^2\cosh(2\beta t))\right\}/\exp(2ikx)$ (2.125)

where R(t) is given by,

$$2R(t) = \left\{ \rho_1 k^2 \left\{ \cosh(2\beta't)\left(\frac{\beta'^2}{k^2} - (U_o + \alpha'/k)^2\right) + \sinh(2\beta't) \right. \right.$$
$$\left. \left(\frac{2i\beta'}{k}(U_o + \alpha'/k)\right) - (U_o + \alpha'/k)^2 \right\} \tanh(kh)\coth(2kh)$$
$$+ \rho_a\left(2\alpha'\beta'i\,\sinh(2\beta't) + (\beta'^2 - \alpha'^2)(\cosh(2\beta't)) - \alpha'^2\right\}\exp(2i\alpha't)$$

and P(t) by ,

$$2P(t) = \left\{\rho_1\frac{k^2}{2}\left\{\cosh(2\beta't)\left(\frac{\beta'^2}{k^2} - (U_o + \alpha'/k)^2\right)\left(\frac{3-\tanh^2(kh)}{2}\right)\right.\right.$$
$$+(\sinh(2\beta't))\left(\left(\frac{2i\beta'}{k}\right)(U_o + \alpha'/k)\right)\left(\frac{3-\tanh^2(kh)}{2}\right) + \frac{\beta'^2}{k^2}$$
$$(1 + \tanh^2(kh)) - (U_o + \alpha'/k)^2\left(\frac{3-\tanh^2(kh)}{2}\right)\right\}$$
$$-\rho_a\left\{2i\alpha'\beta'\sinh(2\beta't) + (\beta'^2 - \alpha'^2)(\cosh(2\beta't) + 1)\right\}\right\}\exp(2i\alpha't)$$

By inspection of equations (2.124) and (2.125) $\gamma = -1$ and $f_1 = f_2 = \frac{1}{4}\beta\sinh(2\beta t)$
$f_3 = \frac{1}{4}\{(\beta(\frac{3+\tanh^2(kh)}{4}) - (\alpha + Uk)^2(\frac{1-\tanh^2(kh)}{4}))\sinh(2\beta t) + (\beta^2 - (\alpha + Uk)^2(1-\tanh^2(kh))t\}$
. The equations then become identical and using the

relations ,

$$\sinh(4kh) = 2\cosh(2kh)\sinh(2kh)$$

and

$$\frac{1+\cosh(4kh)}{\sinh(4kh)} = \coth(2kh), \text{ reduce to the form,}$$

$$^{22}\psi_{tt2} + ^{22}\psi_{t2}b + ^{22}\psi_2 c = h\left\{P\cosh(2\beta't) + Q\sinh(2\beta't) + R\right\}$$
$$\exp(2\alpha't) \tag{2.125a}$$

where,

$$b = \frac{4\rho_1 U_o ki\coth(2kh)}{\rho_1\coth(2kh) + \rho_a}$$
$$c = -\frac{4\rho_1 U_o^2 k^2\coth(2kh) + 8Tk^3}{\rho_1\coth(2kh) + \rho_a}$$

$$Q = \left\{\rho_1 k^3\left(\frac{2i}{k}\beta'(U_o + \alpha'/k)\left(\frac{3-\tanh^2(kh)}{2}\right) - 2\tanh(kh)\right.\right.$$
$$\left.\coth(kh)\right) + \rho_a k(\alpha'\beta'i)\right\}/2(\rho_1\coth(2kh) + \rho_a)$$

$$P = \rho_1 k^3\left(\frac{\beta'^2}{k^2} - (U_o + \alpha'/k)^2\left(\frac{3-\tanh^2(kh)}{2} - 2\tanh(kh)\coth(2kh)\right.\right.$$
$$+ \rho_a(k(\beta'^2 - \alpha'^2))\ /2(\rho_1\coth(2kh) + \rho_a)$$

and,

$$R = \left\{ \rho_1 k^3 \left\{ \left(\frac{\beta'^2}{k^2}\right) \left(\frac{1 + \tanh^2(kh)}{2}\right) - (U_0 + \alpha'/k)^2 \left(\frac{3 - \tanh^2(kh)}{2}\right) \right. \right.$$

$$\left. \left. - 2\tanh(kh)\coth(2kh) \right\} - \rho_a k (\beta'^2 + \alpha'^2) \right\} / 2(\rho_a + \rho_1 \coth(2kh))$$

Equation (2.125) may be conveniently solved by Laplace transformation giving the auxillary equation,

$$Y(s) = \frac{h}{(s^2 + bs + c)} \left\{ \frac{P+Q}{2(s - 2i(\alpha' - i\beta'))} + \frac{P-Q}{2(s - 2i(\alpha' + i\beta'))} \right.$$

$$\left. + \frac{R}{(s - 2i\alpha')} \right\}$$

for the initial conditions $,^{22}\gamma_2(0) = 0$ and $\left.\frac{\partial^{22}\gamma_2}{\partial t^2}\right|_{t=0} = 0$

Defining the roots of the quadric group $,s^2 + bs + c$, as $s = a$ and $s = \bar{a}$ equation (2.126) may be split into partial fractions as follows,

$$-\frac{P+Q}{2} \left\{ \frac{1}{(s-a)(s-\bar{a})(s - 2i(\alpha' - i\beta'))} \right\} = \frac{A_1}{(s-a)}$$

$$+ \frac{A_2}{(s-\bar{a})} + \frac{A_3}{(s - 2i(\alpha' - i\beta'))}$$

$$\frac{P-Q}{2} \left\{ \frac{1}{(s-a)(s-a)(s - 2i(\alpha' + i\beta'))} \right\} = \frac{A_4}{(s-a)}$$

$$+ \frac{A_5}{(s-\bar{a})} + \frac{A_6}{(s - 2i(\alpha' + i\beta'))}$$

$$\frac{R}{(s-a)(s-\bar{a})(s - 2i\alpha')} = \frac{A_9}{(s - 2i\alpha')} + \frac{A_7}{(s-a)} + \frac{A_8}{(s-\bar{a})}$$

where $A_1 = \frac{(P+Q)}{2} \left(\frac{1}{(a-\bar{a})(a - 2i(\alpha' - i\beta'))} \right)$

$$A_2 = -\frac{(P+Q)}{2} \left(\frac{1}{(a-\bar{a})(\bar{a} - 2i(\alpha' - i\beta'))} \right)$$

$$A_3 = (\frac{P + Q}{2}) \left(\frac{1}{(a - 2i(\alpha - i\beta'))(\overline{a} - 2i(\alpha' - i\beta'))}\right)$$

$$A_4 = (\frac{P - Q}{2}) \left(\frac{1}{(a - \overline{a})(a - 2i(\alpha' + i\beta'))}\right)$$

$$A_5 = - (\frac{P - Q}{2}) \left(\frac{1}{(a - \overline{a})(\overline{a} - 2i(\alpha' + i\beta'))}\right)$$

$$A_6 = (\frac{P - Q}{2}) \left(\frac{1}{(a - 2i(\alpha' + i\beta'))(\overline{a} - 2i(\alpha' + i\beta'))}\right)$$

$$A_7 = R \left(\frac{1}{(\overline{a} - 2i\alpha)(a - \overline{a})}\right)$$

$$A_8 = -R \left(\frac{1}{(\overline{a} - 2i\alpha)(a - \overline{a})}\right)$$

$$A_9 = R \left(\frac{1}{(\overline{a} - 2i\alpha)(a - 2i\alpha)}\right)$$

Inverse transformation of equation (2.126) gives the general second order solution as follows.

$$^{22}\gamma_2(t) = h\left\{\left[(A_1 + A_4 + A_7) \exp at + (A_2 + A_5 + A_8) \exp(\overline{a}t)\right.\right.$$
$$\left.\left. + (A_3 \exp(2\beta't) + A_6 \exp(- 2\beta't) + A_9)\right] \exp(2 i\alpha't)\right\} \quad (2.127)$$

where the roots of the equation $s^2 + bs + c$ are given in terms of the actual parameters as:-

$$a = \frac{i\left\{(2\rho_1 U_0^k \coth(2kh)) + 2i\left\{(\rho_a\rho_1 U_0^2 k_\lambda^2 {}^{\coth(2kh)} - 2Tk^3(\rho_1 \coth(2kh) + \rho_a))\right\}^{\frac{1}{2}}\right\}}{(\rho_1 \coth(2kh) + \rho_a)} \quad (2.128)$$

$$\overline{a} = \frac{i\left\{(2\rho_1 U_0^k \coth(2kh)) - 2i\left\{(\rho_a\rho_1 U_0^2 k_\lambda^2 {}^{\coth(2kh)} - 2Tk^3(\rho_1 \coth(2kh) + \rho_a))\right\}^{\frac{1}{2}}\right\}}{(\rho_1 \coth(2kh) + \rho_a)} \quad (2.129)$$

In general $kh \ll 1$, so that $\tanh(kh) = kh$ and $\coth(2kh) = \frac{1}{2kh}$, and for a gas-liquid system $\rho_a < \rho_1$ and hence equation (2.127) may be simplified. Since the complex wave frequency a and its conjugate $\overline{a}$ may be written as,

$$a = i(\alpha'' + i\beta'')$$

$$\overline{a} = i(\alpha'' - i\beta'')$$

and examination of equations (2.98) and (2.128) shows that

$$\alpha'' = 2\alpha' = -2U_0 k$$

and thus equation (2.127) becomes

$$^{22}\gamma_2 = \left\{ \frac{Ph}{(2\beta' + \beta'')(2\beta' - \beta'')} \left\{ \cosh(2\beta't) - \cosh(\beta''t) \right\} \right.$$

$$\left. + \frac{Rh}{\beta''^2} \left\{ \cosh(\beta''t) - 1 \right\} \right\} \exp(2i\alpha't) \qquad (2.130)$$

where

$$P = R = \frac{\beta'^2 k^2 h}{2}$$

Combining equations (2.84), (2.119), (2.120), (2.121) and (2.130) gives the 2nd

order solutions for $^2\eta_j$, the wave amplitude, $^2\phi'$ and $^2\phi$ the

velocity potentials, i.e.

$$^2\eta_j = h^{22}\gamma_j \exp(2ikx) \qquad (2.131)$$

where $^{22}\gamma_j = (-1)^j \left\{ \frac{Ph}{(2\beta' + \beta'')(2\beta' - \beta'')} \left\{ \cosh(2\beta't) - \cosh(\beta''t) \right\} \right.$

$$\left. + \frac{Rh}{(\beta'')^2} \left\{ \cosh(\beta''t) - 1 \right\} \right\} \exp(2i\alpha't)$$

$$^2\phi = \frac{\cosh(2ky)}{2k \sinh(2kh)} \left\{ \left\{ \left\{ \frac{k^2 h^2}{2} \left(\frac{\beta'}{k} \sinh(2\beta't) + i(U_0 + \alpha'/k) \right. \right. \right. \right.$$

$$(1 + \cosh(2\beta't)) \tanh(kh) \exp(2i\alpha't) \right\} + h^{22}\gamma_{t2} + 2iU_0 kh^{22}\gamma_2 \right\}$$

$$\exp(2ikx) \left\} + \frac{1}{4} \left\{ \left(\beta \left(\frac{3+\tanh^2(kh)}{4} \right) - \frac{(\alpha+Uk)^2}{\beta} \left(\frac{1-\tanh^2(kh)}{4} \right) \right) \right) \sinh(2\beta t) \right. \qquad (2.132)$$

$$\left. + \left(\beta^2 - (\alpha+Uk)^2 \right) \left(\frac{1-\tanh^2(kh)}{2} \right) t \right\},$$

for $-h \leq y \leq h$

$$^2\phi'_1 = \frac{\exp(-2k(h-y))}{2k} \left\{ -h^{22}\gamma_{t2} + kh^2 \left(\frac{\beta'}{2} \sinh(2\beta't) + i\alpha' \right. \right.$$

$$\left. \left(\frac{1 + \cosh(2\beta't)}{2} \right) \right) \exp(2i\alpha't) \right\} \exp(2ikx) + \frac{1}{4}\beta\sinh(2\beta t), \qquad (2.133)$$

for $h < y < \infty$

$$^2\phi'_2 = \frac{\exp(2k(y+h))}{2k} \left\{ -h^{22}\gamma_{t2} + kh^2 \left(\frac{\beta'}{2} \sinh(2\beta t) + i\alpha' \right. \right.$$

$$\left. \left(\frac{1 + \cosh(2\beta't)}{2} \right) \right) \exp(2i\alpha't) \right\} \exp(2ikx) + \frac{1}{4}\beta\sinh(2\beta t) \qquad (2.134)$$

for $-\infty < y < -h$
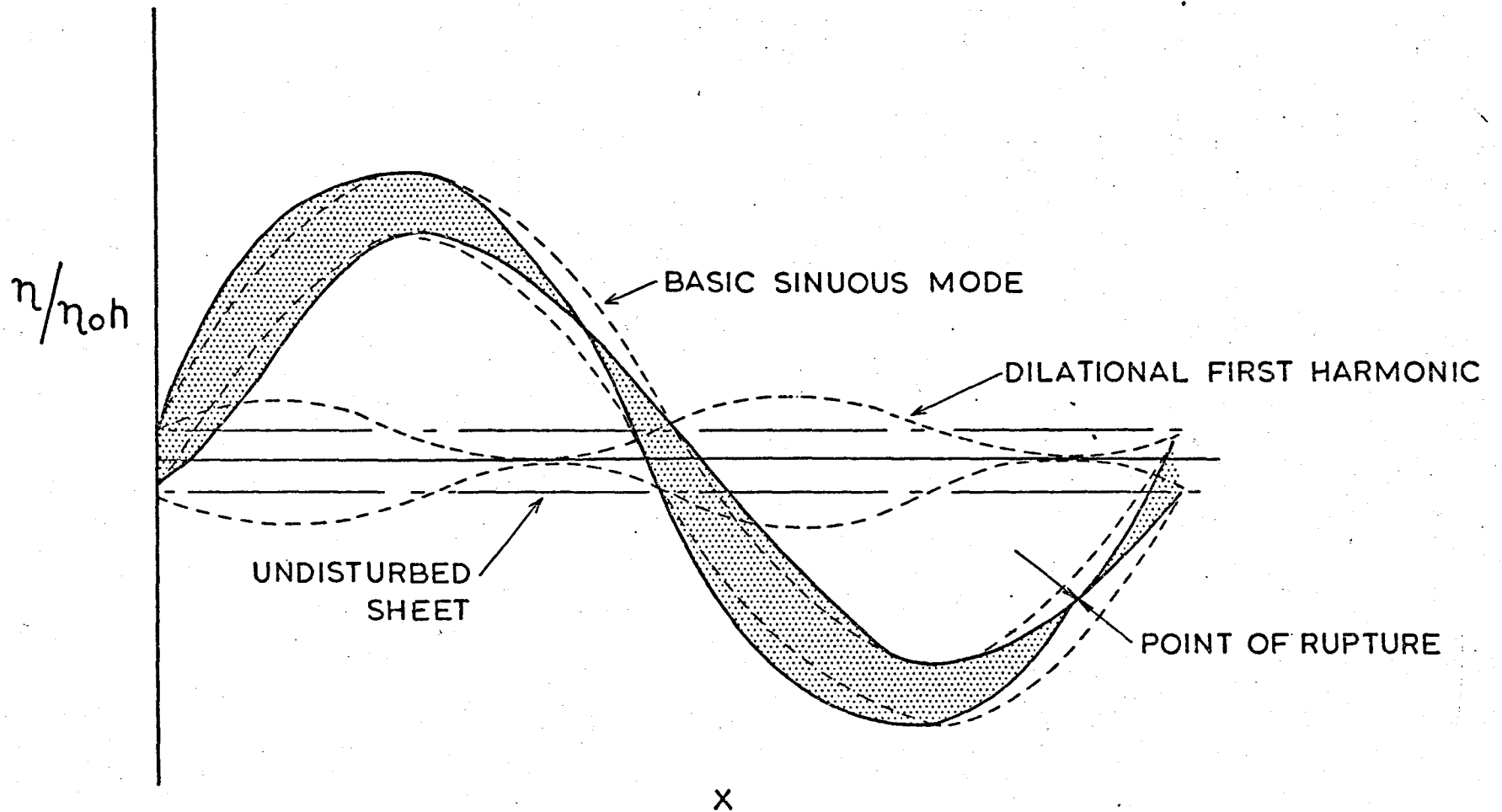
FIG. 2.11   PICTORIAL REPRESENTATION OF A SINUOUS WAVE AT BREAK-UP

where $\beta' = \left\{ \dfrac{(\rho_a U_o^2 k - Tk^2)}{\rho_1^h} \right\}^{\frac{1}{2}}$

$\beta'' = \left\{ \dfrac{(\rho_a U_o^2 k^2 - 2Tk^3)2kh}{\rho_1} \right\}^{\frac{1}{2}}$

The second order solution describes some new features of aerodynamic wave growth. Equations (2.131) and (2.101) which describe the interfacial disturbances, shows that wave growth corresponds to a combination of a basic sinuous mode and a dilational first harmonic. As a result wave growth is asymmetric and the sheet progressively diminishes in thickness at points equal to $\frac{3}{8}\lambda$ and $\frac{7}{8}\lambda$ of the fundamental mode. The sketch shown in Fig.(2.11) demonstrates the wave profile at the point of rupture. Equations (2.132) and (2.133) show that the growth of the first harmonic is due to two effects, namely, the energy addition derived solely from the fundamental and the inherent instability of the first harmonic itself when the wave number $k < \dfrac{\rho_a U^2}{2T}$.

Inspection of the series expansion of the liquid phase velocity potential obtained by combining equations (2.102) and (2.132) i.e.

$$\phi = -U_o x + \eta_o h \left\{ -\left\{ (^1\psi_{t/k} + iU_o^1\psi)\dfrac{\sinh(ky)}{\cosh(kh)} \exp(ikx)\right\}\right\} + \eta_o^2 h^2 \left\{ \right.$$

$$\dfrac{\cosh(2ky)}{2k \sinh(2ky)}) \left\{ \dfrac{k^2}{2}(\dfrac{\beta'}{k} \sinh(2\beta't) + i(U_o + \dfrac{\alpha'}{k})(1 + \cosh(2\beta't))) \right.$$

$$\tanh(kh)\exp(2 i\alpha t) + {}^{22}\psi_{t2} + 2iU_o k^2 {}^{22}\dot\psi_2 \exp(2 ikx)\left. \right\} + f_3 \left. \right\}..$$

shows that at large values of time the series becomes invalid when

$^1\phi = {}^2\phi \not> O(\eta_o^{-1})$

2.2.2.2 Break-up Length of an Attenuating Sheet

Equation (2.131), shows that on a parallel sided sheet thinning and eventual rupture occur at half wavelength intervals. The break-up length may therefore be defined by the implicit equation:-

$$\eta_2(x^*, t^*) - \eta_1(x^*, t^*) = 2h$$

where x^* denotes the break-up length, t^* denotes the break-up time and the interfacial disturbances η_2 and η_1 are given by equations (2.101) and (2.131). Since the second order growth rate β'' is negligible, $\cosh(\beta'' t) \simeq 1$ and thus, the point of rupture occurs when

$$\left\{ \eta_0^2 \frac{1}{4} k^2 h^3 \left\{ \cosh(2\beta' t^*) - 1 \right\} \right\} = 2h \tag{2.135}$$

Equation (2.135) can be applied to an attenuating sheet, if the effect of surface curvature is neglected and if it is assumed that the wave growth at any point depends solely upon the values of the local parameters. The growth rate then becomes time dependant and the total growth can be defined by a time average. Thus, equation (2.135) may be re-written as

$$\left\{ \eta_0^2 \frac{1}{4} k^2 h^3 \left\{ \cosh(2\beta'_m t) - 1 \right\} \right\} = 2h \tag{2.136}$$

where $\quad \beta'_m = \frac{1}{t^*} \int_0^t \beta'(t)\, dt$

In the absence of external forces the thickness of an attenuating sheet at any point is inversely proportional to its distance from the orifice[**]

i.e. $\quad 2h = \dfrac{Ko}{x} = \dfrac{Ko}{U_0 t}$

Hence, from equations (2.93) and (2.136)

$$\beta'(t) = \left\{ \frac{2(\rho_a U_0^2 k - Tk^2) U_0 t}{\rho_1 Ko} \right\}^{1/2}$$

and $\quad \beta'_m = \left\{ \dfrac{8(\rho_a U_0^2 k - Tk^2) U_0 t}{9 \, \rho_1 Ko} \right\}^{1/2} \tag{2.137}$

[**] When an attenuating sheet is formed from an orifice the streamlines

Since $x^{*} = U_o t^{*}$ equations (2.136) and (2.137) give the break-up length of the sheet i.e.

$$x^{*} = \left\{ \frac{9 \rho_1 K_o U_o^2}{32(\rho_a U_o^2 k - Tk^2)} U_o t^{*} \right\}^{1/2} \cosh^{-1}\left\{ 8(\eta_o kh)^{-2} + 1 \right\} \qquad (2.138)$$

appear to diverge from a source situated behind it. Since the distance between this 'origin' is negligible compared to the length of the sheet, x can effectively be measured from the orifice.

2.3 The Electrohydrodynamic Instability of Liquid Sheets

in an Ionised Gas

The behaviour of liquid streams in an applied electric field has received much attention (28-31) and it has been shown that for conducting jets, charge, under certain limiting conditions, has the effect of extending the range of instability.

In Appendix I a description is given of the characteristics of a liquid sheet injected into a hot ionised gas, and the following analysis provides approximate expressions for the early stages of growth of field-coupled waves, where the surface charge is derived solely by diffusion from the surrounding gas in the absence of an applied field.

The system considered comprises an isolated parallel-sided inviscid liquid sheet of perfect electrical conductivity supporting an equilibrium charge and moving through a stationary gas. The y axis is taken perpendicular to the plane of the undisturbed sheet and the x axis lies along the centre line. The interfaces are defined by the relation $y = \eta \pm h$, where $\eta = \eta(x,t)$ is a small imposed periodic disturbance.

For incompressible flow the equations of motion may therefore be written as,

$$\rho \frac{Du_\alpha}{Dt} = -\frac{\partial(\rho \delta_{x\beta})}{\partial x_\beta} + \frac{\partial M_{x\beta}}{\partial x_\beta} \qquad (2.139)$$

and

$$\frac{\partial u_x}{\partial x_x} = 0 \qquad (2.139)$$

where $\delta_{x\beta}$ is the symmetric unit tensor and $M_{x\beta}$ is the Maxwell stress tensor defined as,

$$M_{x\beta} = D\epsilon_o \left\{ E_x E_\beta - \frac{1}{2} \delta_{x\beta} (E_\gamma E_\gamma) \right\} \qquad (2.140)$$

where D is the dielectric constant and ϵ_o the permittivity of free space.

The flow is implicitly irrotational and hence,

$$\epsilon_{\alpha\beta\gamma} \frac{\partial u_\alpha}{\partial u_\beta} = 0 \qquad (2.140)$$

where $\epsilon_{\alpha\beta\gamma}$ is the alternating unit tensor.

For zero magnetic field strength Maxwells equations reduce to,

$$\epsilon_{\alpha\beta\gamma} \frac{\partial E_\alpha}{\partial x_\beta} = 0 \qquad (2.141)$$

and

$$\frac{\partial E_\alpha}{\partial x_\alpha} = \frac{\rho_f}{D \epsilon_0} \qquad (2.142)$$

for $\eta + h < y < \infty$ and $\infty - < y < - h + \eta$
and

$$E_\alpha = 0 \qquad (2.143)$$

for $\eta - h < y < \eta + h$

As a consequence of equations (2.140) and (2.141) both the field strength and fluid velocity can be written in terms of their respective potential functions viz.

$$E_\alpha = - \frac{\partial \phi_e}{\partial x_\alpha} \qquad (2.144)$$

$$u_\alpha = - \frac{\partial \phi}{\partial x_\alpha} \qquad (2.145)$$

Combining (2.138 and (2.145); (2.142) and (2.144) and (2.143) and (2.145) gives respectively

$$\nabla^2 \phi = 0 \qquad (2.146)$$

$$\nabla^2 \phi_e = \frac{\rho_f}{D \epsilon_0} \qquad (2.147)$$

and

$$\phi_e = \text{const} \qquad (2.148)$$

for $\eta - h < y < \eta + h$

Unique solutions of equations (2.146) and (2.147) are obtained by satisfying the following boundary conditions

1) For $y \to \pm\infty$ $\qquad \phi \to 0$ $\hfill$ (2.149)

For $y = \eta \pm h$, the normal velocity of each fluid is given

by the relation

$$\phi_y + \eta_t + \phi_x \eta_x = 0 \hfill (2.150)$$

2) Normal stress continuity is given by

$$\eta_\beta \left[-p \, \eta_\beta + M_{\alpha\beta} \, \eta_\alpha \right]^- = T \eta_{xx} \left\{ 1 + \eta_x^2 \right\}^{-3/2} \hfill (2.151)$$

where η_α is a unit vector normal to the interface.

3) For $y \to \pm\infty$ $\quad \phi_e \to 0$ $\hfill$ (2.152)

Further, the electrical boundary conditions at the interface are

found by integrating equations (2.142) and (2.139) over the volume of

a normal cylinder which instantaneously includes the interface, i.e.

$$\int_V \frac{\partial (D\epsilon_0 E_x)}{\partial x_\alpha} \, dv \; = \; \int_V \rho_f \, dv \hfill (2.153)$$

$$\int_V \epsilon_{\beta s} \frac{\partial E_\alpha}{\partial x_\beta} \, dv \; = \; 0 \hfill (2.154)$$

If the dimensions of the cylinder are diminished such that in

the limit it becomes a disc lying in the interface equations (2.153)

and (2.154), using Gauss's theorem, reduce to a form which describes

the "electrical" boundary conditions, i.e.

$$\eta_x \left[D\epsilon_0 E_x \right] = \sigma_f \hfill (2.155)$$

$$\epsilon_{\alpha\beta\delta} \eta_\beta \left[E_\alpha \right] = 0 \hfill (2.156)$$

where σ_f denotes the charge per unit area at the interface.

Equations (2.146) through to (2.152), and (2.155) and (2.157)

define a complete boundary value problem for the velocity and electrical

potentials and may be solved assuming that for small perturbations

the charge density, electrical potential, velocity potential and

surface disturbance functions may be expanded in the form

$$\rho_f = \sum_{r=0}^{\infty} \eta_o^r \, {}^r\rho_f \, (x, \, y, \, t) \tag{2.157}$$

$$\phi_e = \sum_{r=0}^{\infty} \eta_o^r \, {}^r\phi_e \, (x, \, y, \, t) \tag{2.158}$$

$$\phi = \sum_{r=0}^{\infty} \eta_o^r \, {}^r\phi \, (x, \, y, \, t) \tag{2.159}$$

and

$$\eta = \sum_{r=0}^{\infty} h \, \eta_o^r \, {}^r\eta \, (x, t) \tag{2.160}$$

where the first term of the series defines the equilibrium state and η_o is the dimensionless parameter a/h.

Combining equations (2.147), (2.157) and (2.158) and collecting first order terms we get

$$\nabla^2 \, {}^1\phi_e = - \, {}^1\rho_f \Big/ \mathcal{D} \epsilon_o \tag{2.161}$$

for $h < y < \infty$ and $-\infty < y < -h$

Equation (2.161) is solved in the region $h < y \, \infty$, the solution for the lower region being given by symmetry.

The charged particle density in the region adjacent to the surface is a function of the potential and may be expressed by the relation

$$\rho_f = \rho_f(\phi_e)$$

The first order perturbation term can therefore be written as

$$\rho_f = \frac{d\rho_f}{d\phi_e} \cdot {}^1\phi_e$$

For a disturbance of the form ${}^1\eta_{1,2} = \gamma(t) \exp(ikx)$, equation (2.151) therefore has a solution of the form,

$${}^1\phi_e = {}^1Y(y) \, \overline{\Phi} \, (t) \exp(ikx)$$

where $^1Y(y)$ is a solution of the second order differential equation

$$\frac{d^2\,^1Y}{dy^2} + \left\{\frac{1}{D\epsilon_c}\frac{d\rho_f}{d\phi_e} - k^2\right\}\,^1Y = 0 \qquad (2.162)$$

The solution of equation (2.162) depends upon the value of the bracketed function. For $\left\{\frac{d\rho_f}{d\phi_e}\frac{1}{D\epsilon_c} - k^2\right\} > 0$

the equation has an oscillating solution and for

$$\left\{\frac{d\rho_f}{d\phi_e}\frac{1}{D\epsilon_o} - k^2\right\} < 0$$

it has an exponential solution. Using the transformation of variables given on page A7 Appendix I and noting that $(y-h)/\xi_o = t$, $k' = k\xi_o$ and $x' = x/\xi_o$ equation (2.162) can be written as,

$$\frac{d^2\,^1R}{dt^2} - \left\{p^2\,q(t) + k'^2\right\}\,^1R = 0 \qquad (2.163)$$

where $q(t) = \dfrac{d(n_i - n_e)}{d\,^1R}$

p^2 is a large parameter and k' is $\leqslant O(1)$ over the whole range of t. The form of the equation is therefore similar to that considered by Langer (32) and assuming $q(t)$ has a root of order 1 at $t = t_o$* then the solution of equation (2.163) which is finite over the whole range of t is

*In the analysis performed in Appendix I it has been assumed that the positive and negative charge densities are zero at the interface and equal and finite at large distances from it. Under these conditions it is found that the electrical potential increases monotonically on moving away from the interface, while the charge separation passes through a maximum value. The parameter q therefore has a zero at this point.

$$
{}^1_R = \frac{\left\{\frac{3}{2}\int_{t_0}^{t} q^{1/2}\, dt\right\}^{1/6}}{q^{1/4}} \left\{A.\mathrm{Ai}\,(p^{2/3}z\ ) + B\,\mathrm{Bi}\,(p^{2/3}z\ )\right\} \tag{2.164}
$$

where $z = (\frac{3}{2}\int_{t_0}^{t} q^{1/2}\, dt)^{2/3}$, and $\mathrm{Ai}\,(p^{2/3}z\ )$ and $\mathrm{Bi}\,(p^{2/3}z\ )$

are Airy functions of the first and second kind.

Invoking the boundary condition of equation (2.152), equation
(2.164) has a bounded solution provided that $B = 0$. The perturbation
distribution therefore becomes

$$
-{}^1\phi_e = \frac{K\Theta}{e}\frac{G}{q^{1/4}}\left\{\int_{t_0}^{t} q^{1/2}\, dt\right\}^{1/6}\mathrm{Ai}\,(p^{2/3}z\ )\overline{\phi}(t)\exp\,(ikx) \tag{2.165}
$$

G is found by utilizing the boundary conditions of equation
Combining (2.144), (2.148) and (2.156) and noting that to a first order
of approximation $\bar{n} = \bar{a} - \eta_0\frac{\partial^1\eta}{\partial x}\bar{b}$ where $\bar{a}$ and $\bar{b}$ are unit vectors
in the y and x directions respectively, we get,

$$
\frac{\partial \phi_e}{\partial x_\alpha} = 0
$$

i.e. the interface remains at constant potential so that

$$
\phi_e(\eta + h) = {}^0\phi_e(h) \tag{2.166}
$$

Expanding $\phi_e(\eta + h)$ by means of a Taylor expansion to include all
first order terms, gives,

$$
\phi_e(\eta + h) = {}^0\phi_e(h) + \eta_0\,{}^1\phi_e(h) + \eta_0\,{}^1\eta\ h\frac{\partial\,{}^0\phi_e(h)}{dy}
$$

and hence from equation (2.166).

$$
{}^1\phi_e(h) = -\,h\exp(ikx)\,\Psi(t)\frac{\partial\,{}^0\phi_e(h)}{dy} \tag{2.167}
$$

From equation (2.165)

$$
{}^1\phi_e = \frac{G.K\Theta}{eq^{1/4}}\left\{\int_{t_0}^{0} q^{1/2}\, dt\right\}^{1/6}\mathrm{Ai}(z\,p^{2/3})\,\overline{\phi}(t)\exp\,(ikx) \tag{2.168}
$$

Thus, combining equations (2.167) and (2.168) and noting that

$$\frac{\partial \,^{o}\varphi_e}{\partial y} = -\,^{o}E$$

$$^{1}\varphi_e = \,^{o}Eh \; \frac{F}{F_o} \, \psi(t) \, \exp(ikx) \tag{2.169}$$

where $F = \dfrac{\left\{ \displaystyle\int_{t_o}^{t} q^{\frac{1}{2}} \, dt \right\}^{1/6} Ai(\cancel{z} \, p^{2/3})}{q^{\frac{1}{4}}}$ (2.170)

and the subscript o indicates the function to be evaluated at the interface.

By symmetry the solution for the lower region is,

$$^{1}\varphi_e = \,^{o}_{-E} h \; \frac{F}{F_o} \, \psi(t) \, \exp(ikx)$$

where in the corresponding expression for F and F_o, t is replaced by $-t$.

Comparing first order terms in equation (   ) gives

$$-\,^{1}p_1 + \,^{i}p_a + D\,c_o \; ^{o}E^1E = (-1)^{j} \, T \,^{1}\eta_{xx} h \tag{2.171}$$

for $y = \pm h$

where $j = 1$ denotes the upper interface and $j = 2$ the lower interface.

In this research the nature of wave growth in ionised gases has been examined at temperatures of about $1000^{o}C$. Under these conditions aerodynamic effects are negligible for velocities

3,000 cm/sec (ref. Section 4.1   ) and hence the perturbation value of gas pressure may be omitted from equation (2.171).

It was shown in Section 2.2.2.1 that for sinuous disturbances the velocity potential may be written as

$$^{1}\varphi = -h \left\{ \frac{\psi t}{k} + i \, U_o \psi \right\} \frac{\sinh(ky)}{\cosh(kh)} \, \exp(ikx) \tag{2.172}$$

where $\dfrac{\partial^1\phi}{\partial t} + U_o\dfrac{\partial^1\phi}{\partial x} = -^1p_1$

Combining equations (2.169), (2.171) and (2.172) gives two identical expressions for each interface, i.e.

$$\gamma_{tt} + 2iU_ok\gamma_t - \gamma U_o^2k^2 = \left\{\dfrac{(-D\epsilon_o{}^oE^2\frac{F_{t,o}}{F_o})k - Tk^3\xi_o}{\ell_1\tanh(kh)\xi_o}\right\} \qquad (2.173)$$

Equation (2.173) has a solution of the form exp(int) where for temporally growing waves,

$$n = U_ok \pm i\left\{\dfrac{(-D\epsilon_o{}^oE^2\frac{F_{t,o}}{F_o})k - Tk^3\xi_o}{\ell_1\tanh(kh)\xi_o}\right\}^{\frac{1}{2}}$$

A dilational disturbance of the form $\eta_1 = h\gamma(t)\eta_o\exp(ikx)$ and $\eta_2 = h\gamma(t)\eta_o\exp(i(kx+\pi))$ similarly yields the growth rate of dilational waves i.e.

$$n = U_ok \pm i\left\{\dfrac{(-D\epsilon_o{}^oE^2\frac{F_{t,o}}{F_o})k - Tk^3\xi_o}{\ell_1\coth(kh)\xi_o}\right\}^{\frac{1}{2}}$$

The criterion of stability of both types of disturbance reduces to the form,

$$\left\{(-D\epsilon_o{}^oE^2\frac{F_{t,o}}{F_o})/T\xi_o\right\}^{\frac{1}{2}} > k$$

giving the cut-off wave number as,

$$k_c = \left\{(-D\epsilon_o{}^oE^2\frac{F_{t,o}}{F_o})/T\xi_o\right\}^{\frac{1}{2}} \qquad (2.174)$$

The optimum wave numbers are, however, only similar for kh>1 when,

$$k_{opt} = \left\{(-D\epsilon_o{}^oE^2\frac{F_{t,o}}{F_o})/3T\xi_o\right\}^{\frac{1}{2}} \qquad (2.175)$$

while for kh<1

$$k_{opt} = 0$$

for sinuous waves

and

$$k_{opt} = \left\{(-D\epsilon_o{}^oE^2\frac{F_{t,o}}{F_o})/2T\xi_o\right\}^{\frac{1}{2}}$$

for dilational waves

k_c and k_{opt} can be evaluated for any set of operating conditions provided ^OE and F_o are known. Approximate values of the latter may be obtained by assuming that the sheet has reached its floating potential. This approximation is valid when the relaxation time of the ionised gas is at least an order of magnitude less than the break-up time of the sheet. In the present work the hot gases contain sodium as an impurity and electron concentrations 10^{18} electron m^{-3} can be expected (33). The corresponding value of relaxation time is 10^{-6} secs, which is significantly greater than the sheet break-up time of 10^{-3} secs.

A partial analysis of the characteristics of the momentum and electrical boundary layers surrounding a conical liquid sheet is carried out in Appendix I. It is shown that the dimensionless electric field strength, G, arising at the gas-liquid interface as a result of charge separation in a non-convective sheath adjacent to the sheet is determined by the equation

$$\frac{1}{p^2} \frac{G^{II}}{G} = \frac{G^2}{2p^2 x} + \left\{ J_i + \frac{J_e}{x} \right\} \left\{ t - ts \right\} - \frac{(J_i - J_e)}{G}$$

$$- \frac{G^I}{p^2} \left\{ \frac{1}{x} - 1 \right\} \tag{A.35}$$

with boundary conditions

$G^I = 0$, $G^{II} = -p^2(J_i - J_e)$ and $G = Gw$ when $t = 0$

$$G \rightarrow 0 \quad \frac{(J_i - J_e)}{(J_i + \frac{J_e}{x})(t - ts)} \qquad \text{as } t \rightarrow 1$$

where p^2, x, J_i and J_e are dimensionless parameters, and G is related to its dimensional value by the expression

$$G = - \varsigma_c \frac{^cE_e}{K\theta_e} \tag{2.176}$$

where ξ_o is the thickness of the non-convective sheath.

Since the parameter q is defined as,

$$q = \frac{d(n_i - n_e)}{dR} \tag{2.177}$$

where,

$$dR = -G dt$$

and from equation (A.34)

$$(n_i - n_e) = -\frac{G I}{p^2}$$

Equations (A.35) and (2.177) can be combined to give,

$$q = \frac{G II}{p^2 G} = \frac{G^2}{2p^2 *} + \left\{ J_i + \frac{J_e}{*} \right\} \left\{ t - ts \right\} - \frac{(J_i - J_e)}{G}$$

$$- \frac{G I}{p^2} \left\{ \frac{1}{*} - 1 \right\}$$

For the case where the surface potential is negative with respect to the free stream gas (i.e. charging results from more mobile negative ions or electrons) q is negative and hence arg $q = \pi$. The ratio $\frac{F_{t,o}}{F_o}$ can be obtained from equation (2.170) as,

$$\frac{F_{t,o}}{F_o} = \frac{\frac{d}{dt}(Ai(p^{2/3} e^{i\pi} z_o))}{Ai(p^{2/3} e^{i\pi} z_o)} \left\{ \frac{|q_o|^{1/2} p^{2/3}}{(\int_{t_o}^{o} |q|^{1/2} dt)^{1/3}} \right\}$$

$$+ \left\{ \frac{1}{6} (\int_{t_o}^{o} |q|^{1/2} dt)^{-1} \cdot |q_c|^{1/2} + \frac{1}{4} \frac{d|q|}{dt}\Big|_{t=0} \cdot |q_o|^{-1} \right\} \tag{2.178}$$

where $z_o = (\frac{3}{2} \int_{t_o}^{o} |q|^{1/2} dt)^{2/3}$

and from equation

$$\int_{t_o}^{o} |q|^{1/2} dt = \int_{t_o}^{o} |\left\{ p^2(ts - t)(J_i + J_e/*) - \frac{G^2}{2*} - \frac{(J_i - J_e)}{G} \right.$$

$$\left. \frac{G I}{p^2} (1 - \frac{1}{*}) \right\}|^{1/2} dt \tag{2.179}$$

and $\dfrac{d\ q}{dt}\bigg|_{t=0} = J_i + \dfrac{J_e}{x} + (J_i - J_e)(\dfrac{1}{x} - 1)$

For any set of operating conditions the dimensionless parameters p^2, t_s, J_i, J_e and G_w, and the parameter ξ_o has been determined using the matching procedure described in Appendix I, part 3. With these data available equation (A.35) has then been solved numerically using an RKM procedure, the point t_o being given by the zero of $-\dfrac{G^{II}}{p^2 G}$ and the resulting values of G and G^I used to evaluate equation (2.179) by quadrature. The ratio $\dfrac{F_{t,o}}{F_o}$ has then been obtained from equation (2.178) using tabulated values of the Airy functions, while ^oE has been obtained from equation (2.176) using the calculated values of G_w and G_o.

Chapter 3.   Experimental Procedure
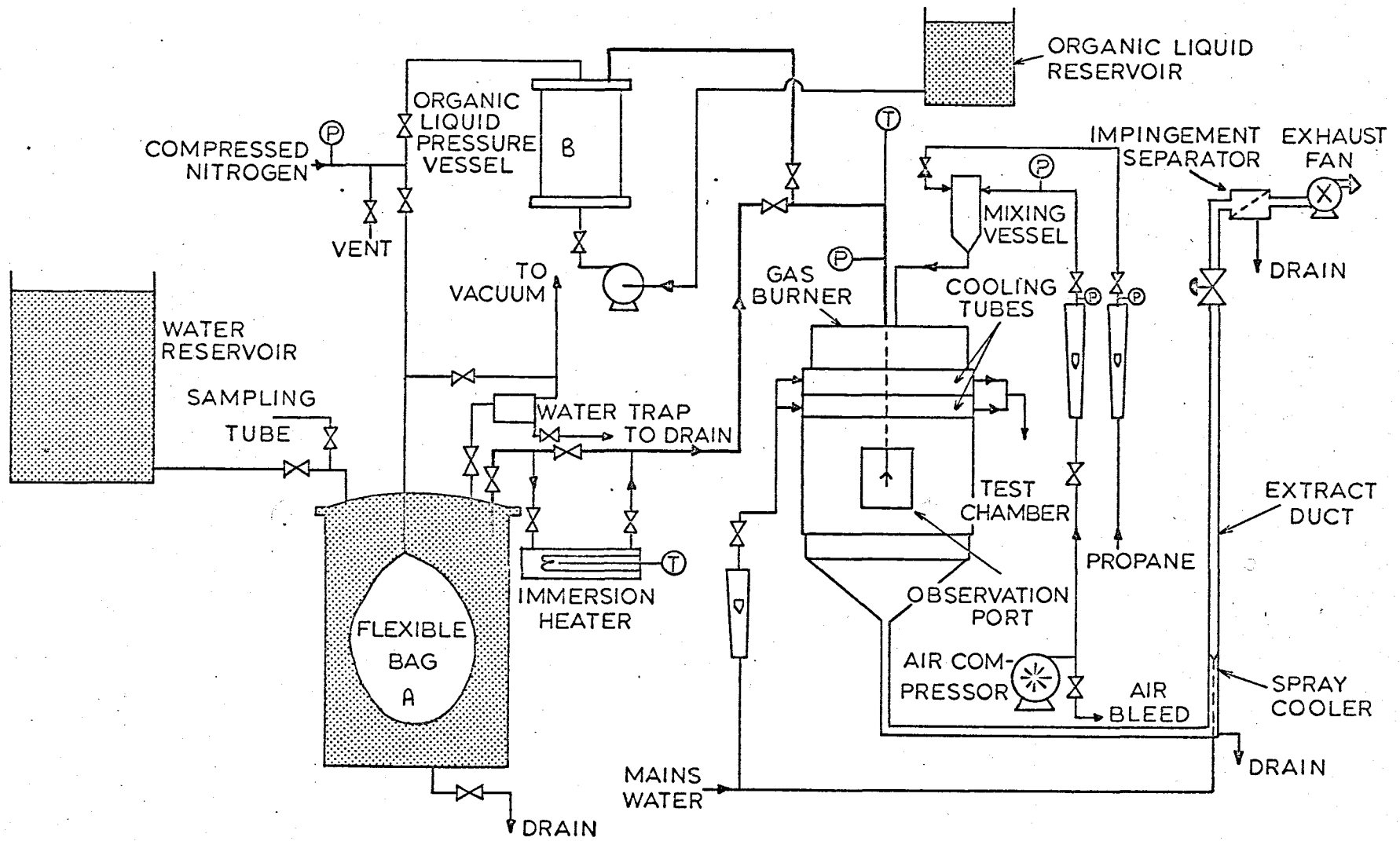
FIG. 3.1   GENERAL ARRANGEMENT OF APPARATUS

3.1 Layout of Apparatus

The apparatus has been designed for the purpose of studying the performance characteristics of pressure spray nozzles in gaseous environments ranging up to $1,000^{\circ}C$. The flow diagram is shown in Fig.(3.1). The nozzle is positioned in the test chamber to spray vertically downwards into a conical funnel, which removes most of the spray by impingement. An exhaust fan draws the remainder through an internally spray cooled duct, and through an impingement separator.

All the work was carried out with water apart from a short series of experiments in which organic liquids were used. Water is fed to the nozzle from a 5.46×10 1 (12 gallon) pressure vessel, A, by means of compressed nitrogen isolated from the liquid in a flexible bag. Provision is made for de-aerating the liquid by applying a vacuum to the vessel, and for heating the liquid by means of a 2 Kw manually controlled immersion heater operating on a by-pass. Other experimental liquids are fed from a 6.85 1 (1½ gallon) cadmium plated pressure vessel, B, the pressure being applied by means of oxygen-free nitrogen.

The hot gas is supplied by a specially designed 1.78×10^{-1} m (7 in) square propane-air flat flame burner, attached to a 4.57×10^{-1} m (18 in) high asbestos-lined chamber. The fuel and oxidant, metered separately by variable area flow meters, are injected tangentially into a mixing vessel and then fed to the burner. Rectangular ports cut in the sides of the chamber afford access to the interior for photographic observation and temperature measurement. Provision is made for cooling the gases by inserting one or two sets of water-cooled tubes between the burner body and test chamber.

The liquid temperature at the nozzle is measured by a copper-constanton thermocouple placed just upstream of the orifice, while the hot gas temperature is measured by a Platinum-Platinum 13% Rhodium thermocouple. The output from each thermocouple is displayed upon separate chart recorders.

3.2 Design of the Burner

The basis of design of the gas burner is to produce an environment with uniform temperature and velocity profiles. These requirements are best satisfied by an enclosed flat-flame burner whose characteristics approximate to a one-dimensional system.

The operation of a flat-flame burner necessitates a balance between the approach gas and flame velocities at all points in the combustion plane. In practice this can only be achieved by burning the gases upon a stabilising grid. Gas is passed through the grid at a velocity lower than that of the free space flame, which, as a result, tends to burn back. As the latter approaches the grid, loss of heat by conduction lowers the flame velocity until the required balance is reached between the velocity of the flame and that of the incoming gas. A flame maintained under such conditions is extremely stable and unaffected by transient disturbances. To maintain a uniform temperature profile it is necessary to ensure that combustion takes place only at the surface of the grid, and the gas mixture must therefore be homogeneous and uniformly distributed.

Fig.(3.2) shows a diagram of the gas burner and mixing vessel finally adopted, which implements the above requirements. The apparatus has been designed to burn an 85% lean stoichiometric mixture of propane and air, which corresponds to an approximate flame speed of 0.43 m/sec at atmospheric pressure (34).

Fig.3.2.   Sketch of Gas Burner

and Mixing Vessel

'SIAPS' blocks

Adjustable feed
tube ¼" I.D.

Test chamber

Dowel pins

SIDE
VIEW

Wire gauze

¾"

¼"

3"

¼" I.D. pipe

64 x ¹⁄₃₂" equispaced
holes

Premixed gases

Gas distributor ½" I.D

'O'-ring

Liquid feed

7"

5½"

1⅛"

PLAN
VIEW

7"

Gas burner

Thread to suit ½" L.H.
B.O.C. hose connection

16 holes on 2¾"
P.C.D. to suit ¼"
B.S.F. bolts

⅜" I.D. pipe

Tangential
gas inlet

16 holes (as above)

⅛" × ³⁄₁₆" spigot
on 1½" P.C.D.

6·35 × 10⁻³ mm.
aluminium foil

60°

2"

2"

¾"

½"

⅛

Mixing vessel

FIG. 3.3 TEMPERATURE PROFILES ADJACENT TO A FLAT
WATER SHEET IN A HOT GAS
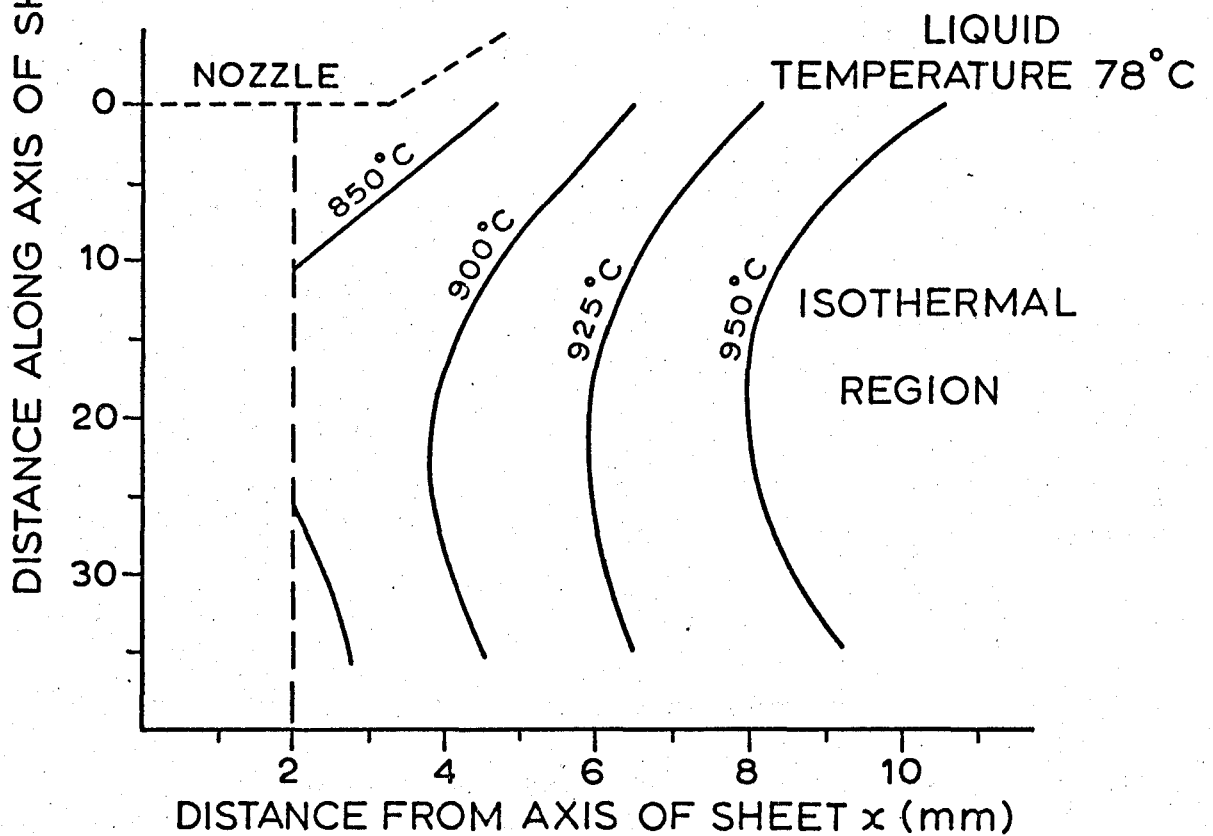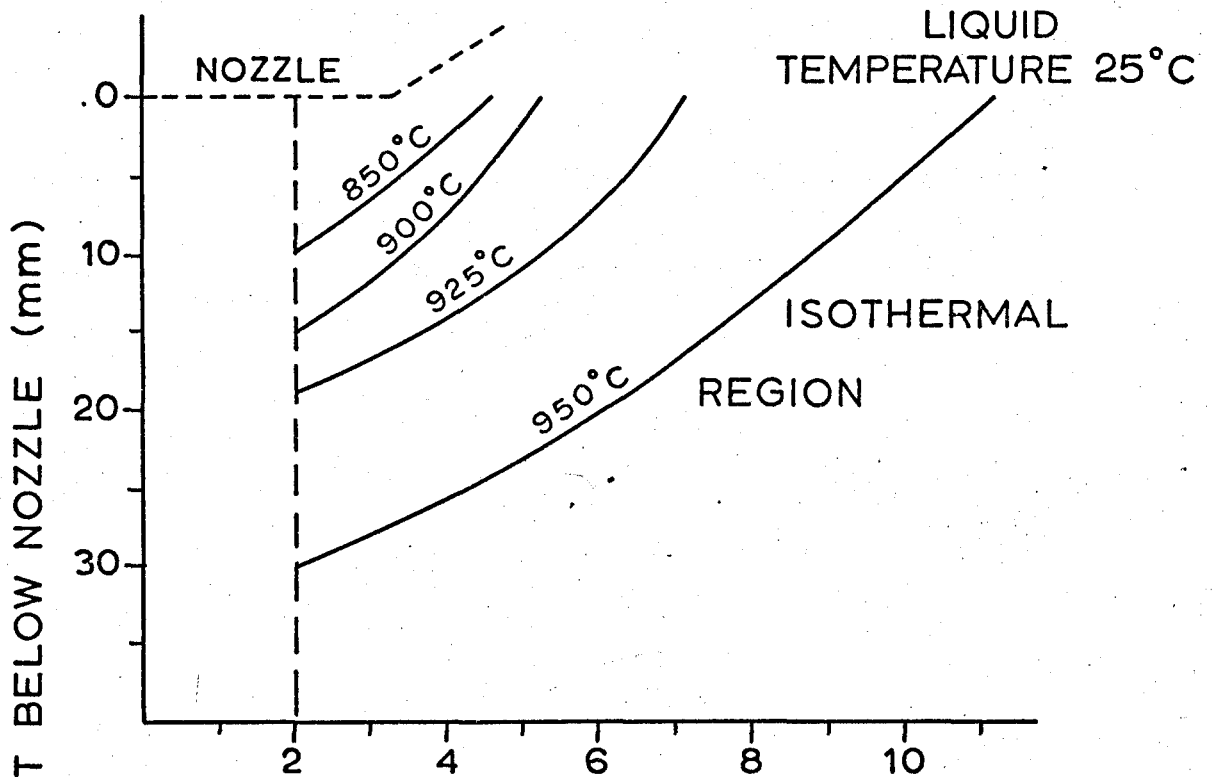
NOZZLE :- BRAY UNIJET Y
DIFFERENTIAL INJECTION PRESSURE, 1·74 bar (25 psig)

FIG.3.4 ISOTHERMS ADJACENT TO A FLAT WATER SHEET IN A HOT GAS

NOZZLE :- BRAY UNIJET Y
DIFFERENTIAL INJECTION PRESSURE, 1·72 bar (25 psig)

The mixing vessel has a capacity of approximately 5×10^{-1} l.
The propane and air enter respectively through diametrically opposed
6.35 mm (0.25 in) tangential ports let into the cylindrical walls,
and leave through a 12.7 mm (0.5 in) outlet at the top. A bursting
disc clamped between a spigot and flange forms the base of the
vessel. Preliminary tests indicated that the required propane and
air flow rates of 1.65×10^{4} and 6×10^{2}l /sec respectively gave a
pressure drop of 0.276 bar (4 psi) over the whole system, and con-
sequently a bursting disc fabricated from 6.35×10^{-3}mm (2.5×10^{-4} in)
aluminium foil which ruptures under a differential pressure of
0.552 bar (8 psi) was used.

The premixed gases are distributed initially at the top of the
burner by a perforated toroidal pipe and subsequently by 23 gauge wire
gauze, before passing through a ceramic stabilising grid. The grid
comprises a number of 9.5 mm (0.375 in) thick ceramic blocks pinned
and cemented together to form a 1.78×10^{-1}m (7 in) square. The
blocks, which have been kindly supplied by Messrs. Siaps*, have a
free area of flow equal to half the total area. In order that the
nozzle may be rotated about the axis and located at any desired
height below the combustion zone, a 6.35 mm (0.25 in) I.D. pipe is
inserted along the axis of the burner. The nozzles may be clamped
at any position by means of a gland with an O-ring seal.

Fig.(3.3) shows typical axial temperature profiles normal to
the liquid sheet when water at 25°C and 78°C respectively is injected
into hot gases at a bulk temperature of $1,000^{\circ}$C. The results are
also plotted in Fig.(3.4) as isotherms.

*Siaps Gas Radiants Ltd., Grand Buildings, Trafalgar Sq.,
London W.C.1

3.3 Temperature Measurement

3.3.1 Gas Temperature

The most convenient method of measuring gas temperature of not more than about 1000°C is by thermocouple probe, although these must be fabricated from fine wires in order to afford good spatial resolution which can be in the order of 10x the wire diameter and to minimise both aerodynamic and thermal disturbances. Catalytic effects at the hot junction which give rise to spuriously high readings can be eliminated by a coating of non-catalytic material such as silica (34). Low readings due to conduction losses can be neglected if fine wires less than 0.25 mm diameter with an exposed surface to diameter ratio of about 50 are used (35), whilst those due to radiation may be estimated by making a balance between the energy received by convection and that lost by radiation.

Thus, for a small spherical body within a large enclosure at constant temperature we have,

$$h(T_t - T_j) = e_j \sigma (T_j^4 - T_w^4) \qquad (3.1)$$

where h, the heat transfer coefficient, is determined from the expression, (36)

$$Nu = 0.42 \, Pr^{0.2} + 0.57 \, Pr^{0.33} \, Re^{0.5} \qquad (3.2)$$

for $0.01 \leqslant Re \leqslant 10,000$

Gas properties in equation (3.2) are evaluated at the mean of the junction temperature T_j, and the true gas temperature T_t.

The emittance, e_j, of the coated junction has been taken as being equal to 0.22 (34) since microscopic examination of the thermocouple used in the present work indicated the thickness of the silica to be small in comparison to the total diameter of the junction

The wall temperature, T_w, has been estimated by equating the heat lost by convection from the outer surface of the test section with that flowing through it by conduction, i.e.

$$T_w = (h_2(T_o - T_a) + \frac{T_o}{R}) R \qquad (3.3)$$

In equation (3.3) the heat transfer coefficient, h_2 is given by the relation, (37)

$$h_2 = 1.82 \, (\frac{\Delta T}{L})^{\frac{1}{4}} \qquad (W \, m^{-2} \, {}^{o}C^{-1}) \qquad (3.4)$$

The thermal resistance of the test chamber, R, is $4.19 \, m^2 \, {}^{o}C \, W^{-1}$. The outer wall temperature, T_o, and the ambient gas temperature, T_a, were measured directly.

In this research temperatures have been measured of the bulk flow from the burner and that adjacent to fan shaped sheets of water. Water has an absorption spectrum with a peak of $3 \, \mu m$ (38) corresponding closely to the peak in the radiation from a black body at $900^{o}C$. It can therefore be expected that the sheet will tend to act as a heat sink and thus make additional corrections necessary. However, the maximum radiation loss that could occur would correspond to an enclosure maintained at a room temperature. Under these conditions equation (3.1) predicts a positive correction of $40^{o}C$ for a thermocouple reading of $920^{o}C$. At a gas temperature of $960^{o}C$ the walls of the test chamber have a temperature of $570^{o}C$ which results in a correction of $30^{o}C$. The presence of a water sheet will produce a correction lying between these two values, but since the maximum possible difference of $10^{o}C$ lies well within the experimental error of $\pm15^{o}C$, its effect can be neglected.

Temperatures have been measured over a range of 100-1000°C
and a Platinum-Platinum 13% Rhodium thermocouple has been used.
The thermocouple assembly is shown in Fig.(3.5a). The wires,each
of 0.125 mm diameter,were supported in a twin bore ceramic tube
and welded at the hot junction to form a bead of approximately
0.5 mm diameter. Further support and rigidity is given by a con-
centric 3 mm O.D. single bore ceramic tube and a 6.35 mm (0.25 in)
O.D. brass tube. A terminal block clamped to the former provides
electrical contact with the B.S. compensating cables. Extraneous
temperature effects at this junction are minimized by enclosing it in
a glass wool filled cardboard case. The hot junction was coated
with silica by passing it slowly (about 1 pass per second) through
a flame containing particles of silica from the decomposition of
dimethyl siloxane, and then examining the junction under a microscope
for possible flaws. The thermocouple is supported by a system of
micrometer screw slides, so that it can be traversed at any plane
around the nozzle.

Fig.3.5.   Thermocouple Assemblies for

the Measurement of Liquid and

Gas Temperatures
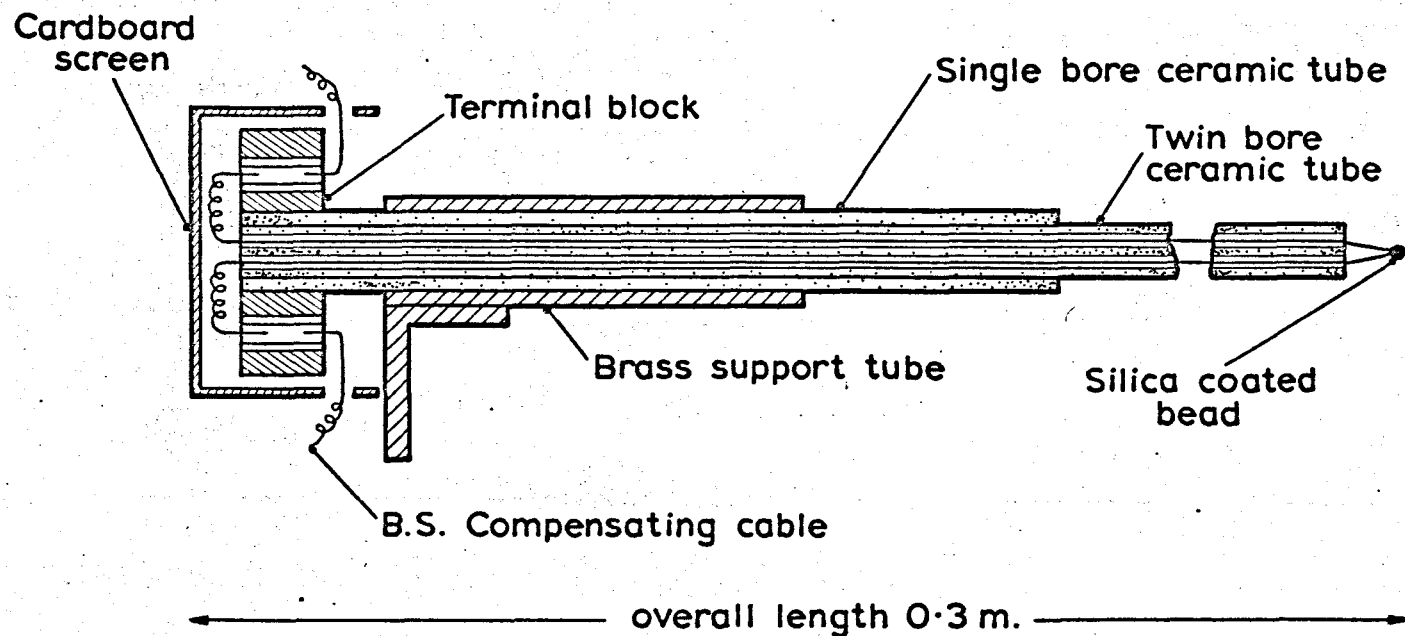
(b) Pt.–Pt. 13% Rh. Thermocouple assembly.
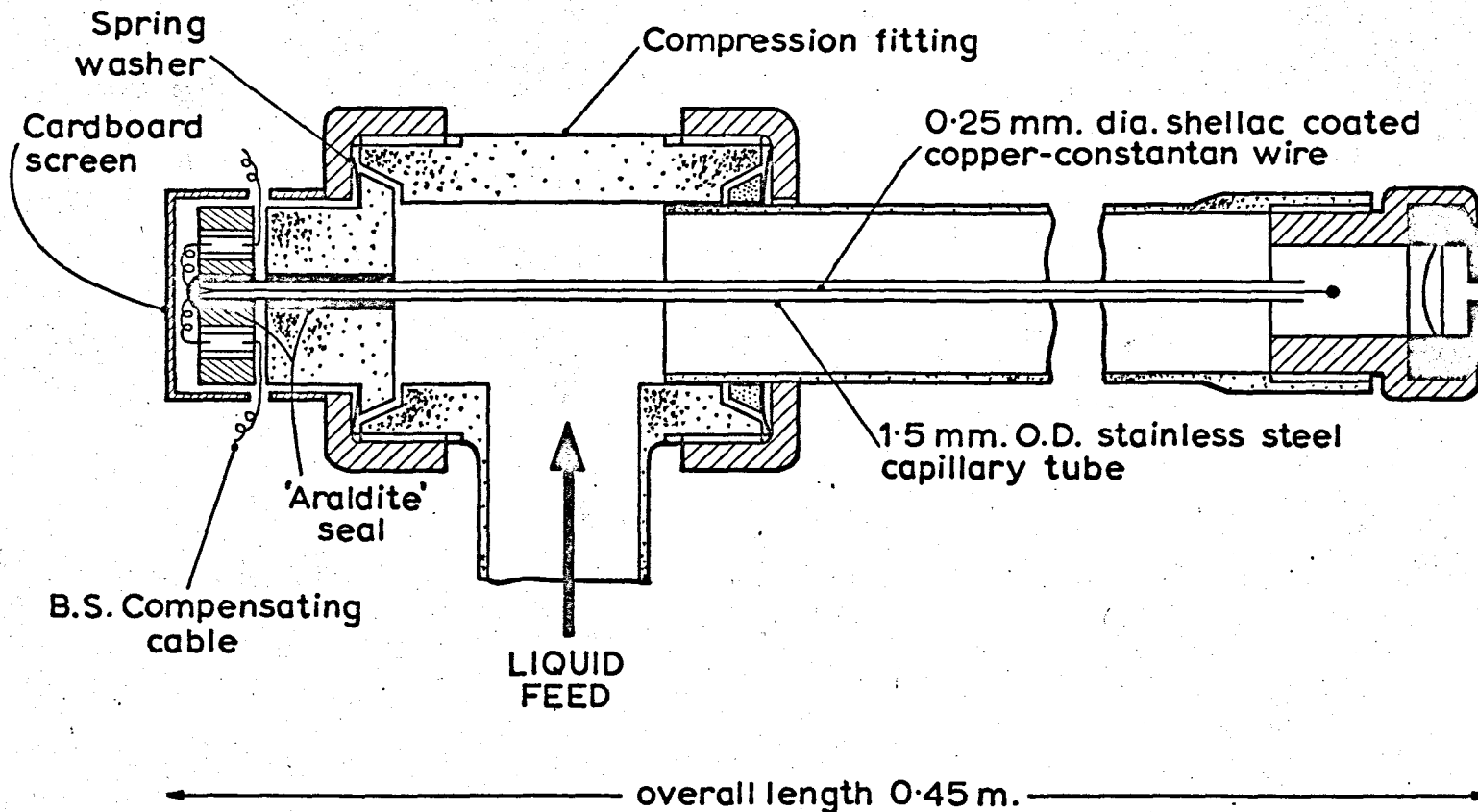
(a) Nozzle assembly.
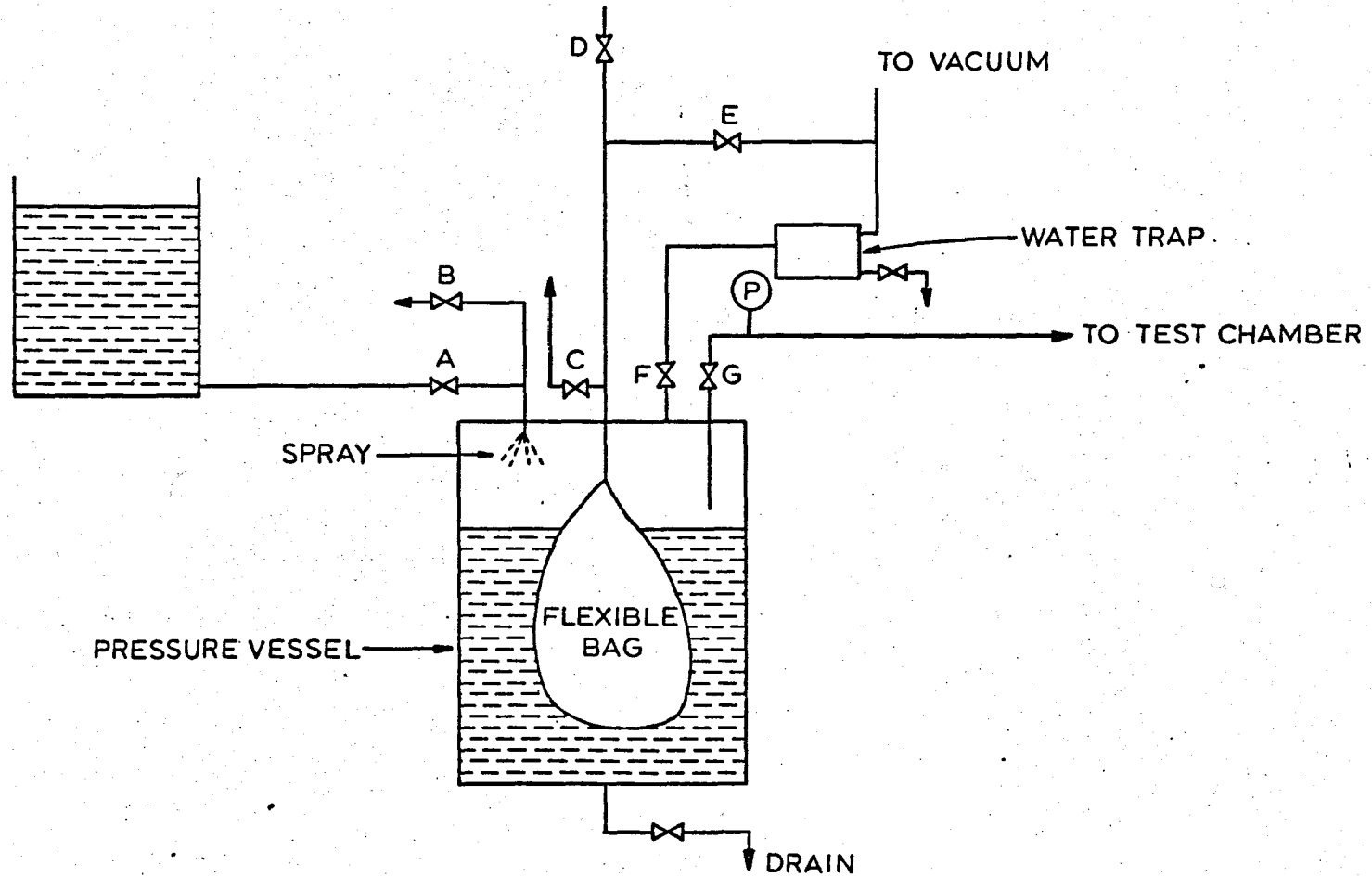
FIG. 3.6 GENERAL ARRANGEMENT OF APPARATUS FOR PRODUCING
DEAERATED WATER.

3.3.2 Liquid Temperature

In order to evaluate temperature dependent properties of the
liquid as it is injected into a gaseous atmosphere a 0.25 mm diameter
Shellac covered Copper-Constantan thermocouple was positioned just
upstream of the orifice.   A diagram of the assembly is shown in
Fig.(3.5b).   The thermocouple wires are supported in a stainless
steel tube, which passes down the centre of the feed pipe.
Effective sealing is provided by plugging the top end of the thermo-
couple tube with "Araldite" and attaching it to the feed pipe with a
tapered compression fitting.

3.4 De-aeration of Liquid Feed

In order to investigate the effect of dissolved air on the
mechanism of sheet disintegration in hot atmospheres, the equipment
shown in Fig.(3.6) was used to obtain de-aerated water and inject
it into the test chamber by applying compressed nitrogen, yet
avoiding gas to liquid contact.

To prepare a batch of distilled water, the first step was the
evacuation of the pressure vessel and also the flexible bag which
would otherwise expand and prevent the entry of water.

Vacuum was applied to the system through a water trap by means
of a water ejector.   During the evacuation A, B, C, D, G and H were
closed while E and F were open.   When the minimum pressure was
reached, A was opened to admit distilled water from a 50 litre
reservoir.   It entered through a Bray miniature Unijet Y nozzle.
Water accumulating in the water trap indicated that the pressure
vessel had been filled and it was then isolated by closing A, E and
F.   Finally, D was opened to connect the flexible bag with the
compressed nitrogen supply and the de-aerated water was now ready
for injection into the test chamber by opening G.

Samples of water were withdrawn through B after each batch was produced. The air current in the samples was analysed by the method due to Winkler (39), which depends on the chemical estimation of the amount of dissolved oxygen.
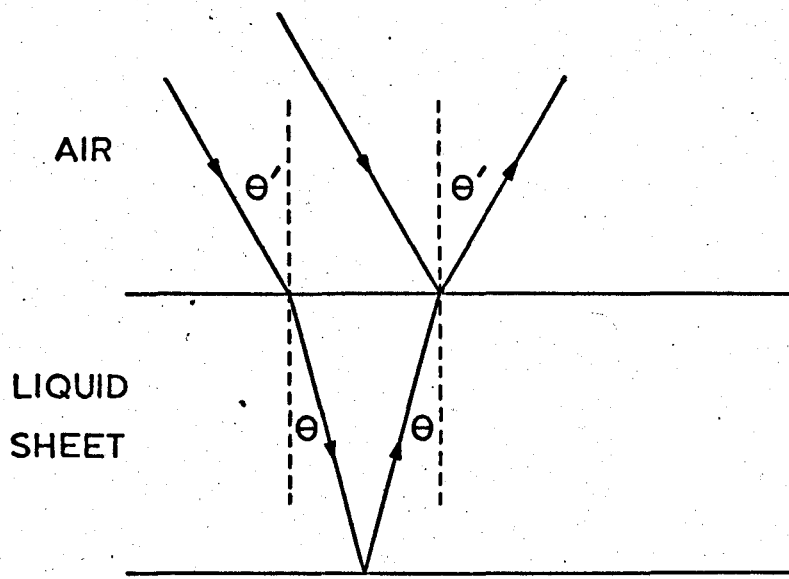
FIG. 3.7   INTERFERENCE OF LIGHT RAYS IN A THIN SHEET
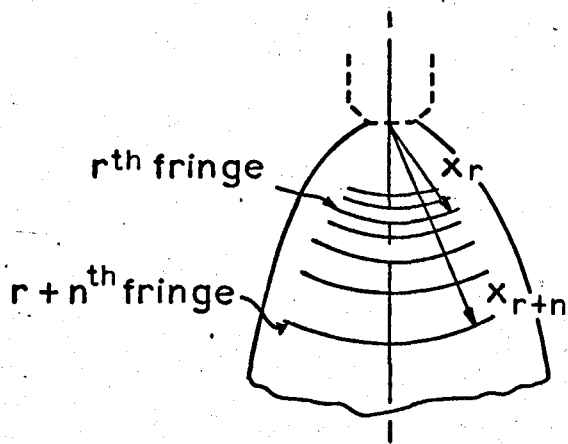
FIG. 3.8   PATTERN OF FRINGES ON A SHEET

3.5 Determination of Sheet Thickness and Sheet Length

The thickness of spray sheets has been measured by an interferometric technique developed by Dombrowski, Hasson and Ward (10), since it enables thickness variations over the entire sheet to be determined from a single photograph.

The break-up length of spray sheets has been measured directly from sub-microsecond flash photographs which have been obtained employing an optical system identical to that in Section 3.6

Theory

When a monochromatic parallel beam of light falls upon a film, reflection takes place at both the front and rear surfaces.(3.7). Because of the difference in the light paths, the reflections mutually interfere or reinforce to produce a system of fringes, Fig.(3.8). If the light paths between two adjacent light fringes are D_r and D_{r+1}, then

$$Dr = (2n + 1) \ w/2 = 2S_r \mu \cos \theta$$

$$D_{r+1} = (2n + 3) \ w/2 = 2S_{r+1} \mu \cos \theta$$

where w is the wavelength of light

μ is the refractive index of the film

θ is the angle of refraction of the light beam in the film

S_r and S_{r+1} are the sheet thicknesses corresponding to the light path lengths D_r and D_{r+1}.

$$(S_{r+1} - S_r) = \frac{w}{2 \mu \cos \theta} \tag{3.5}$$

since for a spray $S = \dfrac{K_o}{x}$, equation (3.5) gives:

$$K_o \left(\frac{1}{x_r} - \frac{1}{x_{r+1}} \right) = \frac{w}{2 \mu \cos \theta}$$

or more generally,

$$K_o \left(\frac{1}{x_r} - \frac{1}{x_{r+n}} \right) = \frac{wn}{2 \mu \cos \theta}$$

MERCURY VAPOUR
LAMP
J

CONDENSING
LENS SYSTEM
I

FILTER
K

FRONT
SILVERED
MIRROR

PLANE OF SHEET
FOR SPARK PHOTOGRAPHY

PLANE OF SHEET FOR
RECORDING FRINGES

SHORT FOCAL
LENGTH LENS

SPARK SOURCE A

NEUTRAL DENSITY
FILTER

CONDENSING
LENS
F

CAMERA
D

18°
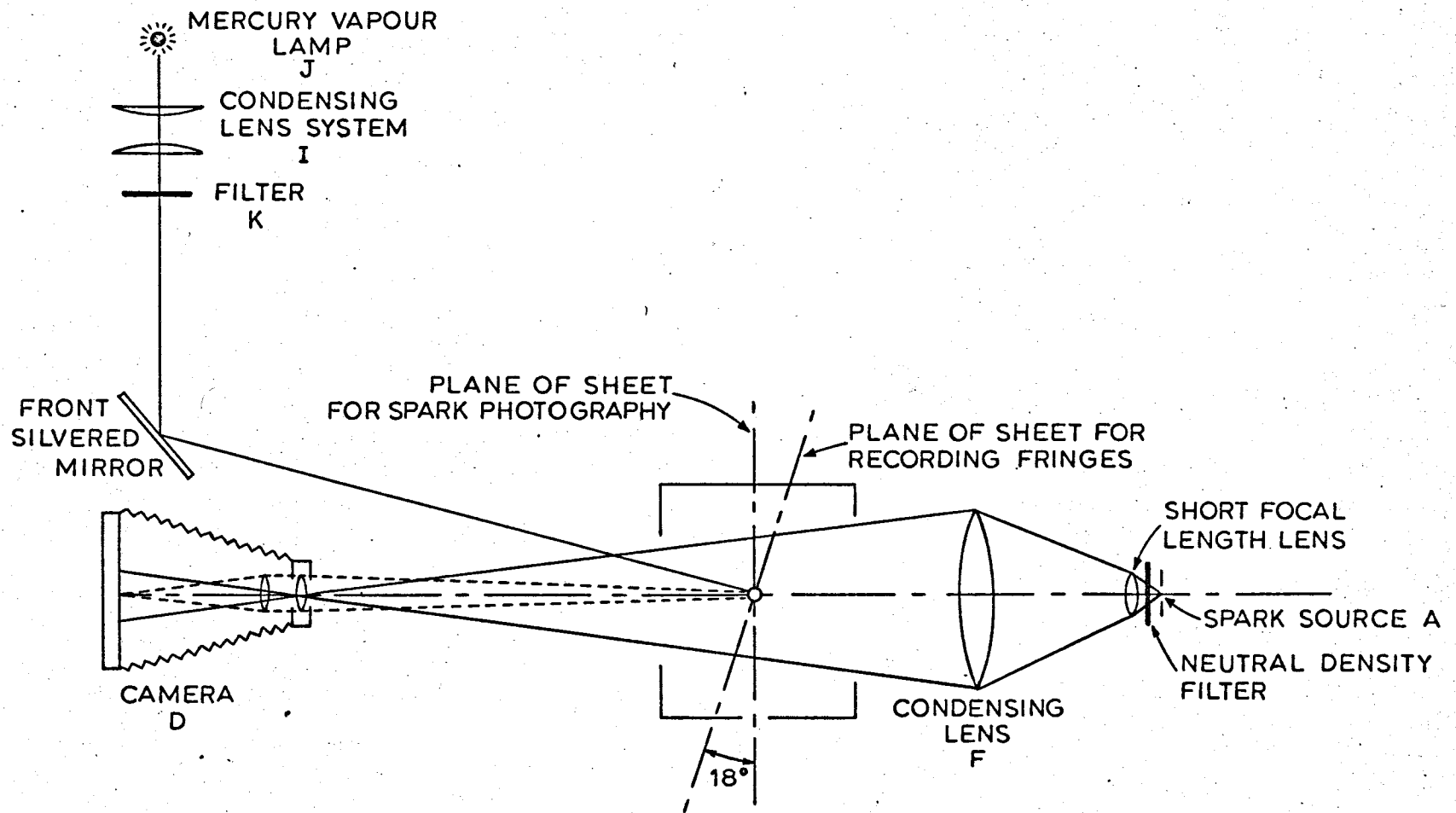
FIG. 3.9 OPTICAL ARRANGEMENT FOR MEASUREMENT OF SHEET LENGTH
AND SHEET THICKNESS.

A linear relation therefore exists between n and $\dfrac{1}{x_{r+n}}$. If the slope is given by m, then

$$K_o = \frac{w}{2m\mu} \left(1 - \frac{\sin^2\Theta'}{\mu^2}\right)^{1/2} \tag{3.6}$$

where Θ' is the angle of incidence.

Experimental

For convenience the optical system was combined with that employed for recording sheet length by submicrosecond-spark photography (Fig.(3.13) Section 3.6), a common camera being used for both sets of experiments. The arrangement is shown in Fig.(3.9). Light from a 250 watt mercury vapour lamp (J) is condensed by a pair of 1.52×10^{-1} m (6 in) plane convex lenses (I) into an approximately parallel beam and transmitted through a mercury yellow filter (K) onto the liquid sheet by a front aluminized mirror. The reflected light is directed back to the camera (D) by appropiately rotating the plane of the sheet about the nozzle axis. Equation (3.6) shows that the value of K_o depends upon the value of $\sin^2\Theta'$. The error in determining Θ' has been reduced by placing the mirror and camera as close together as possible and under these conditions the angle Θ' was about 9° so that any error in measurement was negligible.

Because the plane of the sheet is disturbed by waves, relatively long exposures and a wide aperture are required to ensure that light is reflected from every part of the sheet as the latter moves past the lens. The best arrangement embodied a shutter setting of 1/30 sec at an aperture of f5.6 with PanF film reversally processed to give high contrast.
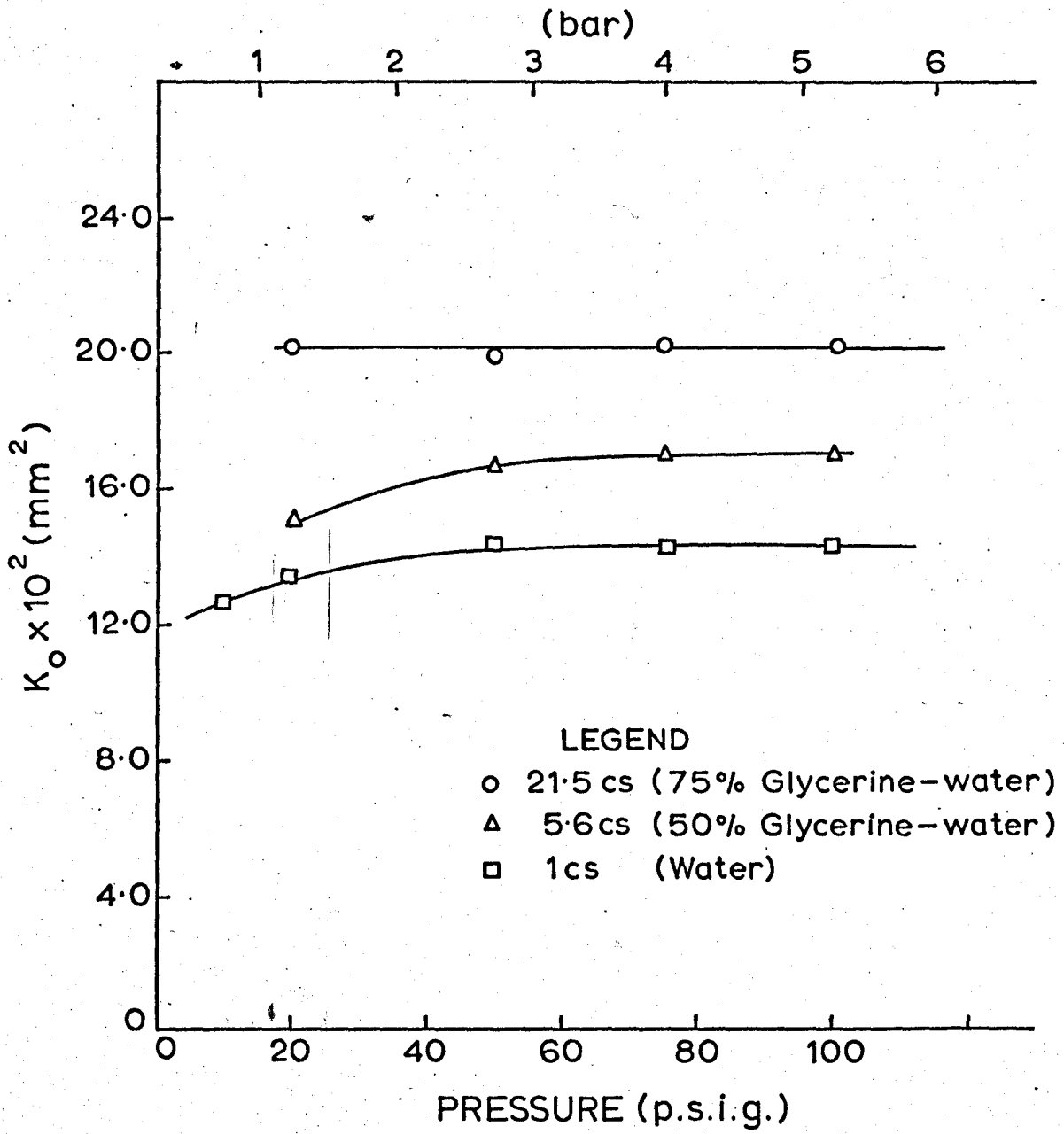
FIG. 3.10 VARIATION OF SHEET THICKNESS PARAMETER,
K_O, WITH PRESSURE AND VISCOSITY FOR
BRAY MINIATURE UNIJET W NOZZLE.
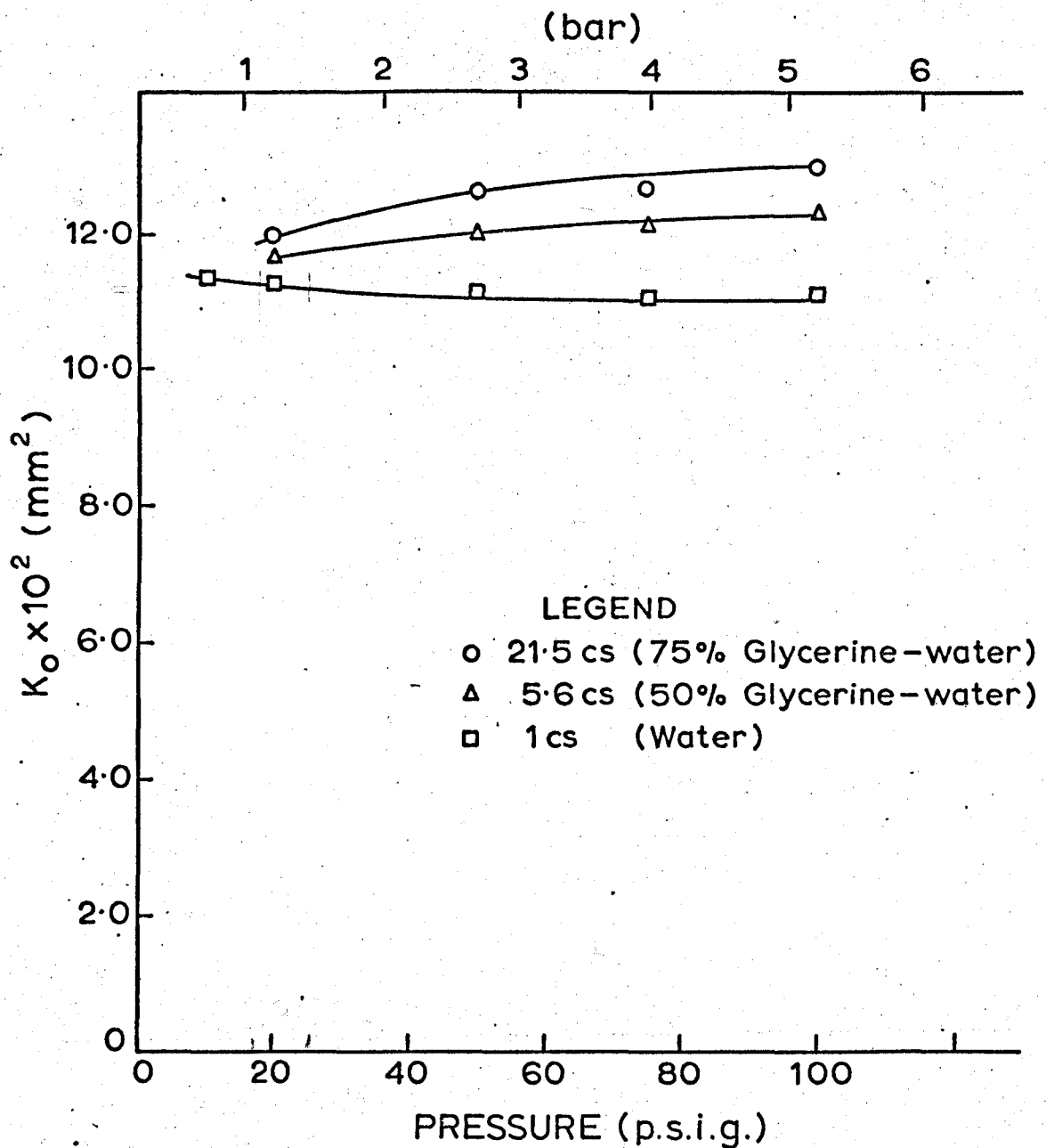
FIG. 3.11 VARIATION OF SHEET THICKNESS PARAMETER, K_O, WITH PRESSURE AND VISCOSITY FOR BRAY MINIATURE UNIJET X NOZZLE.
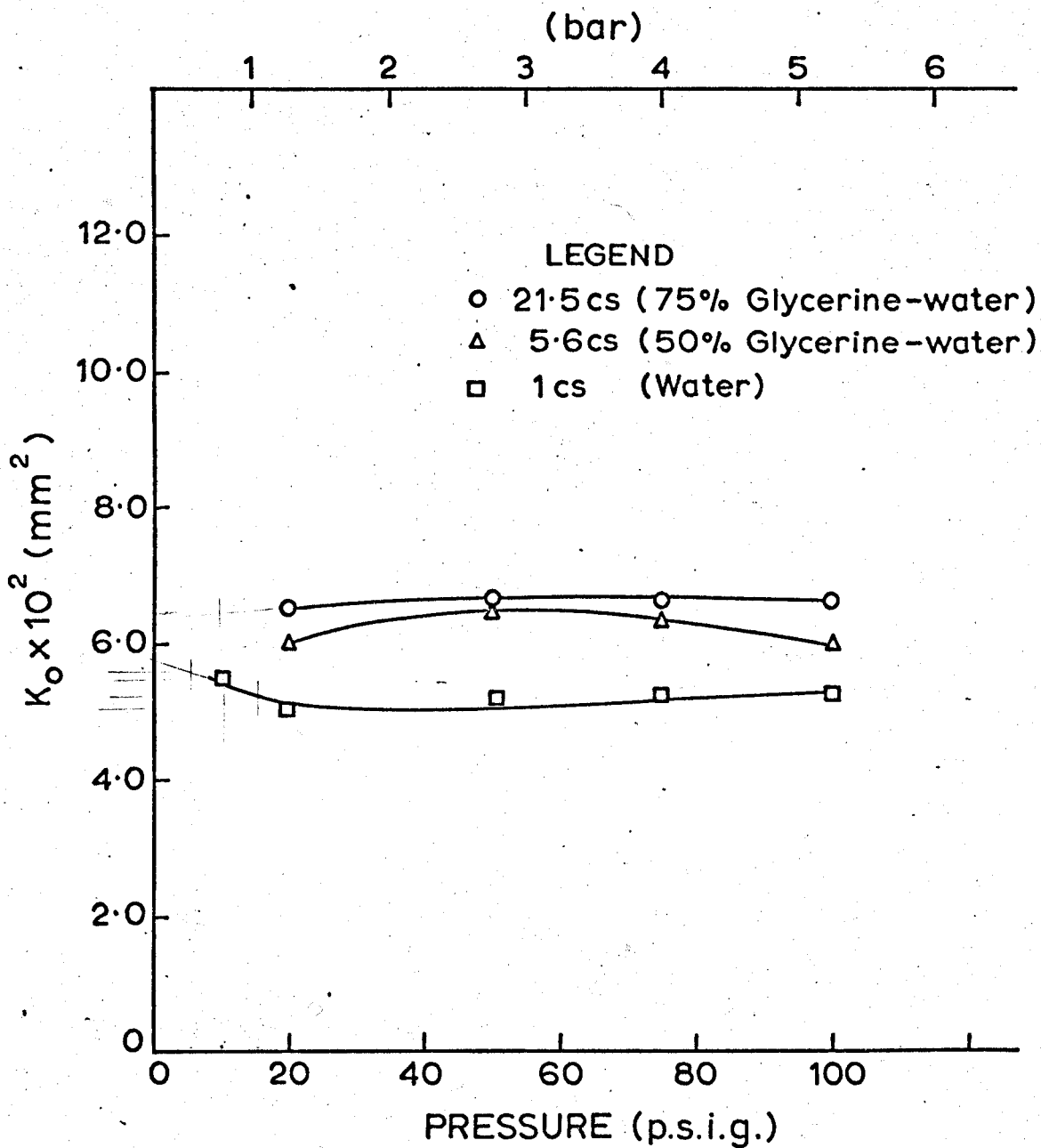
FIG. 3.12 VARIATION OF SHEET THICKNESS PARAMETER, K_o, WITH PRESSURE AND VISCOSITY FOR BRAY MINIATURE UNIJET Y NOZZLE.
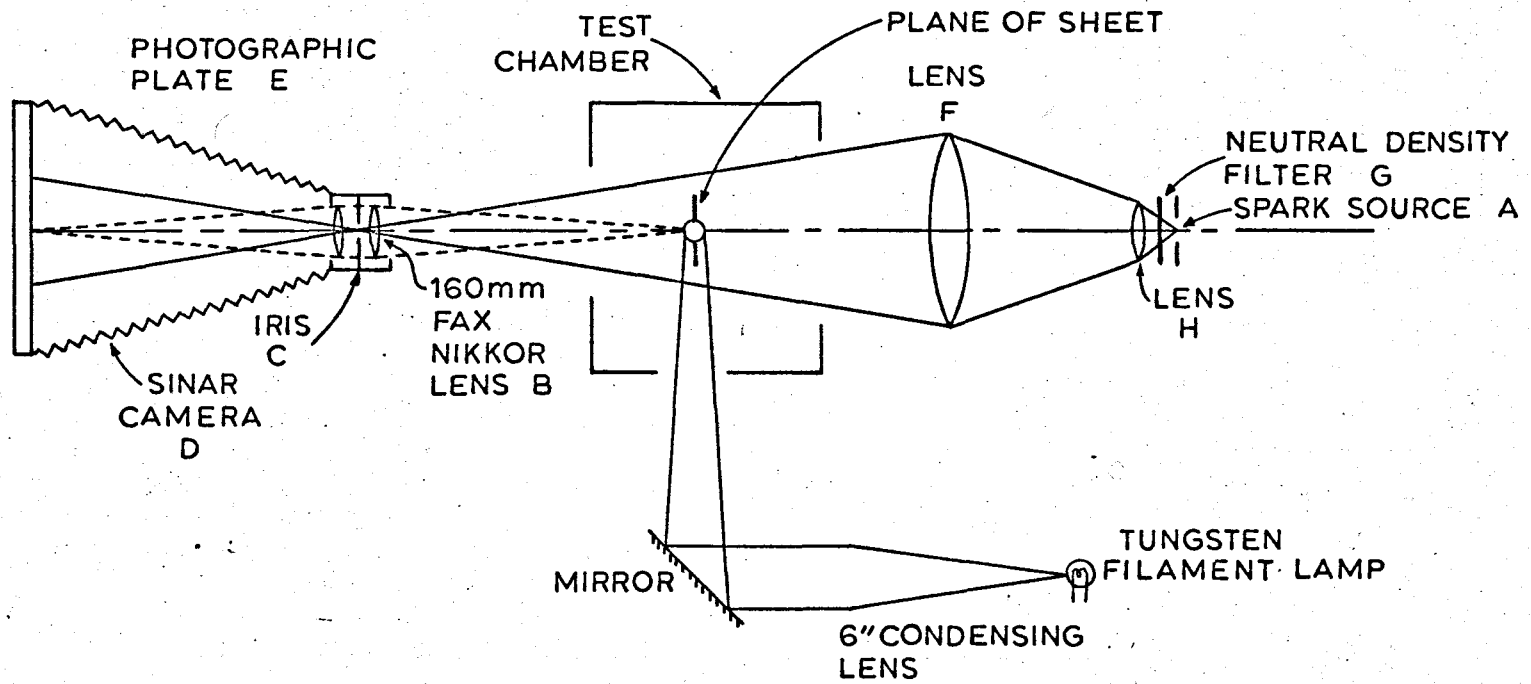
FIG. 3.13 OPTICAL ARRANGEMENT FOR MEASUREMENT OF DROP SIZE (PLAN VIEW)

Experimental Results

The thickness parameter, K_o, has been measured for the three sizes of Bray miniature unijet nozzle listed in Table 3 over a range of injection pressures. Since it has been established by previous workers that K_o is independent of surface tension, measurements have only been made with water and aqueous glycerine mixtures. Figs.(3.10) (3.11)and (3.12) show the results obtained for W, X and Y nozzles using water, 50% and 75% glycerine water mixtures respectively, for an injection pressure range of 0.69 - 6.91 bar (10-100 psig).

3.6 Measurement of Drop Size

High speed flash photography was chosen as the means for assessing the drop size distributions. It is a relatively simple technique and has a further advantage in that measurements can be made without affecting the dynamics of the spray.

It is shown in Appendix III that, because of the periodic nature of drop formation, accurate results can only be assured by measurements of the spatial size distribution within the vicinity of the atomiser. Double-flash photography, usually employed for obtaining temporal size distribution, was thus unnecessary, and a single-exposure electronic flash unit has been used.

A diagram of the plan view of the optical system is given in Fig.(3.13) Light from a spark source (A) is focussed by means of a condensing lens system, comprising a 1.52×10^{-1}m (6 in) single element convex lens (H) and a 1.72×10^{-1}m (7 in) Aero Ektar lens (F), into the centre of the camera iris (B). A 1:1 object/image magnification at an aperture of f/16 was chosen to provide the best compromise between a good depth of field and high resolution. Because of the limitations

of the optical components the field of view could not always incorporate the region of drop formation and the nozzle, and, in order to ascertain the position of the nozzle on the photograph, it was illuminated by an auxilliary light source. This was carried out by focussing the light from a Pointolight lamp onto the nozzle tip by a condensing lens-mirror system.

The light flashes, of sub-microsecond duration, were provided by an open electrode spark discharge system comprising a 0.02μF rapid discharge condenser charged to 15 Kv. The electric gap was set to 8 mm and the light intensity adjusted to the required value by a 0.1 natural density filter (G). Kodak Kodaline KS5 film, giving high resolution and contrast, was used; the optimum developing conditions were found to be 390 secs (6½ mins) in Ilford I.D.11 developer. The minimum size of drop that could be resolved was 10μm with a depth of field of 4 mm.

3.7 Drop Sizing and Counting

To avoid the difficulties of counting and sizing drops by microscopic techniques the negatives were examined at a magnification of x60 by rear projection on a screen covered with tracing paper; the size groups chosen were $0-30\mu$m, $30-45\mu$m, $45-60\mu$m, etc., in intervals of 15μm.

The minimum number of drops to be counted in a sample to give a reasonable estimate of mean drop size is difficult to determine. Hooper (40) has shown that a drop count of 1,000 gives the mean diameter to an accuracy of $\pm 10\%$. The normal counting rate of samples ranging in size from 800-1200 drops was about 2,000 per hour and the total number counted per day by dictation into a tape recorder was 10,000.

It is shown in Appendix III that the true drop size distribution of a spray can only be accurately determined if the drops are measured close to the region of disintegration. Thus, for each photograph the section analysed covered the first band of drops formed. For consistency, drops were measured within 5.0 mm on either side of the nozzle axis.

Calculation of Sauter Mean Diameter

The mean drop size was expressed in terms of the volume-surface mean diameter, D_{32}, defined as:-

$$D_{32} = \int_0^{D_{max}} D^3 \frac{dn}{dD} \, dD \bigg/ \int_0^{D_{max}} D^2 \frac{dn}{dD} \, dD \qquad (3.7)$$

In equation (3.7) D is the drop diameter and $\frac{dn}{dD}$ is the frequency distribution. Since

$$\int_0^{D_{max}} D^3 \frac{dn}{dD} \, dD = \text{Total drop volume}$$

suitable rearrangement of equation (3.7) gives

$$D_{32} = 1 \bigg/ \int_0^{D_{max}} \frac{1}{D} \frac{dU^*}{dD} \, dD \qquad (3.8)$$

where U* is the fractional volume oversize.

For discrete drop sizes the equation may be written as

$$D_{32} = 1 \bigg/ \sum_0^{D_{max}} \left\{ \frac{D^3_m \Delta N}{D} \bigg/ \sum_0^{D_{max}} D^3_m \Delta N \right\} \qquad (3.9)$$

In equation (3.9) Dm is the median drop size in any group, N is the number of drops in a group, D_{max} is the maximum drop diameter in the spray.

Table 1.   Calculation of Volume-surface

Mean Diameter

Nozzle:- Bray Unijet Y

Injection Pressure:- 50 psig

Liquid Temperature:- 26°C

Ambient Gas Temperature: 675°C

A.   Calculation of Cumulative Fraction Oversize

Group	Size Range μm	Median Dia. μm	$D^3 \times 10^{-6}$	ΔN	$D^3 \times \Delta N \times 10^{-6}$	$D^3 \times \Delta N / \Sigma D^3 \times N$	Cumulative Fraction Vol. Oversize
1	0-30	15	0.0034	110	0.062	0.00013	1.00000
2	30-45	37.5	0.0535	526	27.878	0.05967	0.99987
3	45-60	52.5	0.1455	320	46.400	0.09932	0.94020
4	60-75	67.5	0.3085	122	37.576	0.08034	0.84088
5	75-90	82.5	0.5675	66	37.092	0.07940	0.76045
6	90-105	97.5	0.9275	64	59.328	0.12699	0.68105
7	105-120	112.5	1.4245	32	45.568	0.09754	0.55406
8&9	120-150	135	2.460	54	132.840	0.28435	0.45652
10&11	150-180	165	4.492	8	35.936	0.07692	0.17217
12&13	180-210	195	7.415	6	44.490	0.09523	0.09523
Totals					467.170	0.99989	

B.   Calculation of D_{32} Using Smoothed Data from Fig

Size Range μm.	Median Dia. μm.	Cumulative Fraction Vol. Range	Cumulative Fraction Vol. in Each Group	$(D^3 \times \Delta N) / D \Sigma D^3 \times \Delta N$
0-20	10	1.00-0.992	0.008	0.00080
20-40	30	0.992-0.954	0.046	0.00153
40-60	50	0.954-0.865	0.089	0.00178
60-80	70	0.865-0.735	0.130	0.00185
80-100	90	0.735-0.592	0.143	0.00158
100-120	110	0.592-0.455	0.137	0.00124
120-140	130	0.455-0.308	0.147	0.00113
140-160	150	0.308-0.175	0.133	0.00086
160-180	170	0.175-0.081	0.094	0.00053
180-200	190	0.081-0.015	0.066	0.00035
200-220	210	0.015-0.000	0.015	0.00007
220-240	230	-		

$$D_{32} = \frac{1}{D^3 \times N/D \quad D^3 \times N} = 85 \, \mu m.$$

FIG. 3.14 CUMULATIVE FRACTION OVERSIZE CURVE.

CUMULATIVE VOL. FRACTION OVERSIZE

DROP SIZE, D_L, (μ)
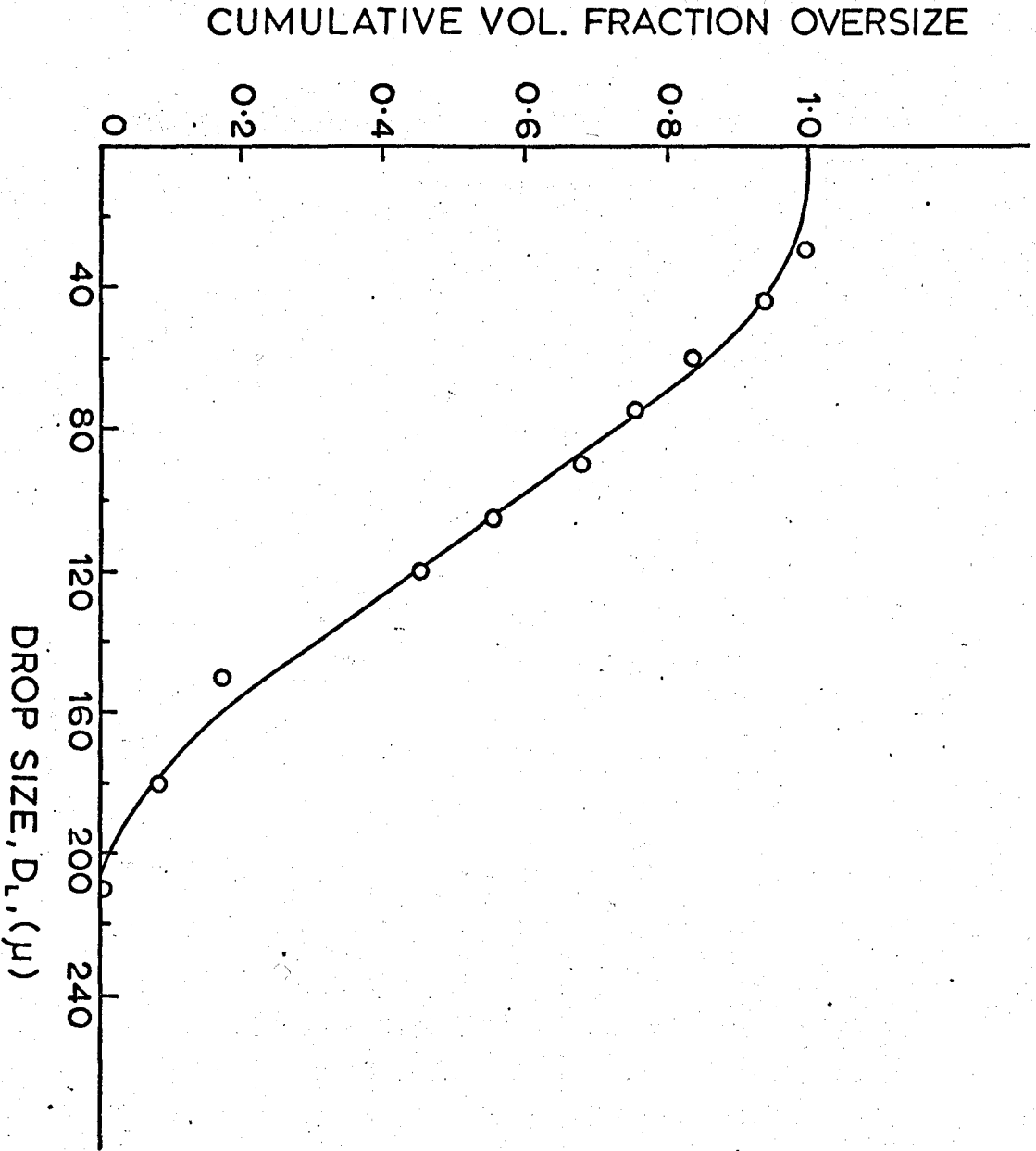
Following Heywood (41) the data is first smoothed by plotting

$$\sum_{D_L}^{D_{max}} D^3_m \Delta N \Bigg/ \sum_{0}^{D_{max}} D^3_m \Delta N$$

against D_L, the lower limit of the size groups (cf. Fig.(3.14).

The abscissa is divided into $20 \mu m$ intervals and the volume for each is read from the curve, and divided by its median diameter.

The summation of all these quantities gives

$$\sum_{0}^{D_{max}} \frac{D^3_m \Delta N}{D} \sum_{0}^{D_{max}} D^3_m \Delta N \qquad (3.9)$$

the reciprocal of which (i.e. equation (3.9)) gives the mean drop size D_{32}. A sample calculation is given in Table 1.

Table 2

(i) List of Fan Spray Nozzles

Nozzle Catalogue Designation	Orifice[+] Dimensions (mm)	Water Flow Number (FN) x 10^5	Velocity Coefficient (Cv)
W	0.85 x 0.395	0.403 (0.84)	0.85
X	0.745 x 0.311	0.275 (0.57)	0.84
Y	0.46 x 0.247	0.124 (0.26)	0.81

(ii) List of Swirl Spray Nozzles

Manufacturer's Designation	Water Flow Number (FN) x 10^5	Velocity Coefficient (Cv)*	Sheet Thickness Parameter (K_0) mm^2 x 10^2
D8/30*	0.072 (0.15)	0.79	2.8
D8/45 *	0.077 (0.16)	0.79	2.8
D25/45*	0.288 (0.6)	0.84	8.5
D100/80	1.2 (2.5)	0.84	23.7

[+]These figures are based upon the dimensions of a rectangle of equivalent area.

*The number appearing after the solidus signifies the nominal spray angle.

Table 3

List of Liquid Properties

Liquid	Distilled Water	Acetone	Carbon Tetra-chlcride	50% Glycerine -water	75% Glycerine -water
Density, ρ_1, ($Kg m^{-3}$) x 10^{-3}	1.0	0.79	1.595	1.13	1.2
Surface Tension, T, at $20^\circ C$ x 10^3 (Nm^{-1})	72.8	23.7	26.95	70	69
Viscosity, at $20^\circ C$ x 10^6, ($m^2 s^{-1}$)	1.0	0.405	0.6C6	5.65	31
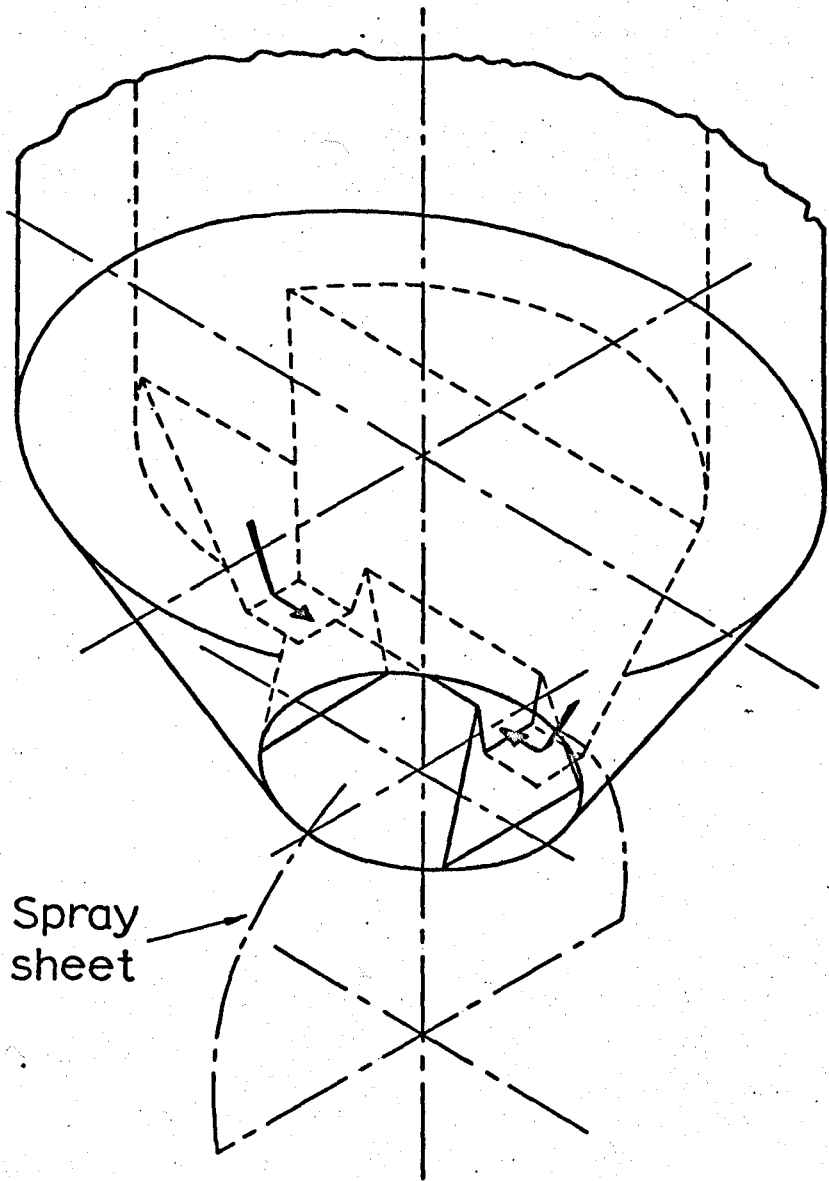
Spray
sheet

FIG. 3.15   SINGLE-HOLE FAN SPRAY NOZZLE
BRAY MINIATURE UNIJET

3.8 Liquids Studied in Present Work

The majority of the work was carried out with distilled water, while a short series of experiments were conducted on sheet length determination with acetone, carbon tetrachloride and 50% glycerine solution. The physical properties of the four liquids are given in Table 3.

3.9 Spray Nozzles used in Present Work

Experiments were performed with both single hole fan sprays and swirl spray nozzles.

3.9.1 Fan Sprays

The single hole fan spray nozzles used were Bray miniature unijets, manufactured by Geo. Bray and Co. Ltd. The functional part of the nozzle is a porcelain moulding in a brass frame (cf. Fig. 3.15). Table 2 gives the dimensions of the rectangular orifices of the nozzle, measured with a microscope, and the flow characteristics. The flow number, FN, is defined as the ratio

$$FN = \frac{Q}{P^{1/2}}$$

where Q is the injection flow rate and P the differential injection pressure. For convenience the value of flow number is presented both in S.I. units and conventional units $(gph/(psig)^{1/2})$, the latter appearing in brackets. The velocity coefficient (C_v) has been taken equal to the discharge coefficient (C_Q), which has been obtained from volumetric flow measurements. Since it has been shown (2) that the area coefficient (C_A) is approximately equal to unity for flow through fan spray nozzles.

3.9.2 Swirl Sprays

The swirl sprays used were manufactured by Danfoss Ltd. (London), Greenford, Middlesex. Table 2 gives their flow characteristics (42). The sheet thickness parameter K_o is

defined as

$$K_o = \frac{Q}{2\pi U_o \sin \phi_o}$$

where Q is the volume flowrate, U_o is the sheet velocity and $2\phi_o$ is the cone angle.

Chapter 4.   Results

Differential injection (a) 1.72 bar   (b)   3.44 bar   (c)   6.2 bar
pressure   (25psig)   (50 psig)   (90 psig)

Magnificstion   :   x 2
Nozzle   :   Bray Unijet Y
Ambient has temperature : 20°C
Liquid temperature   : 20°C

Fig. 4.1 Typical Photographs of Fan Spray Water Sheets formed at Room Temperature.
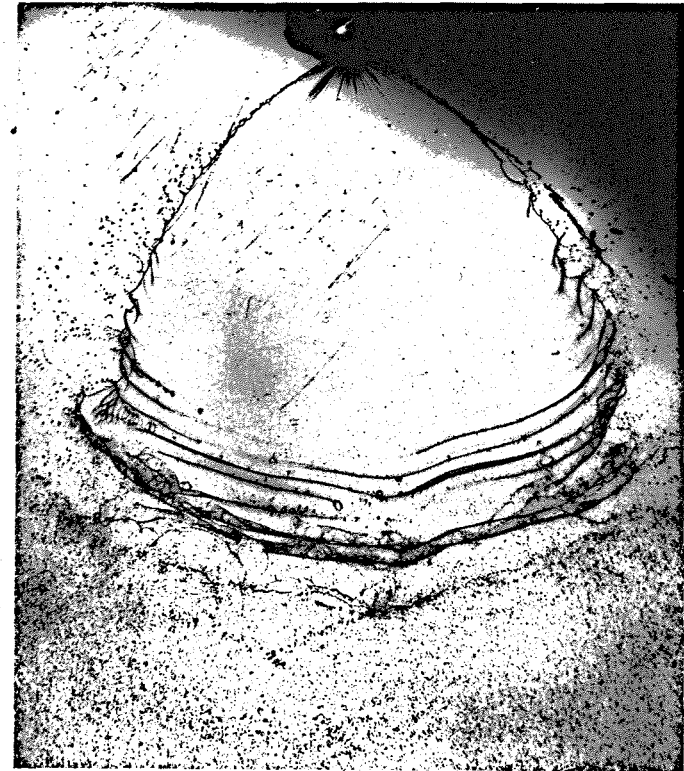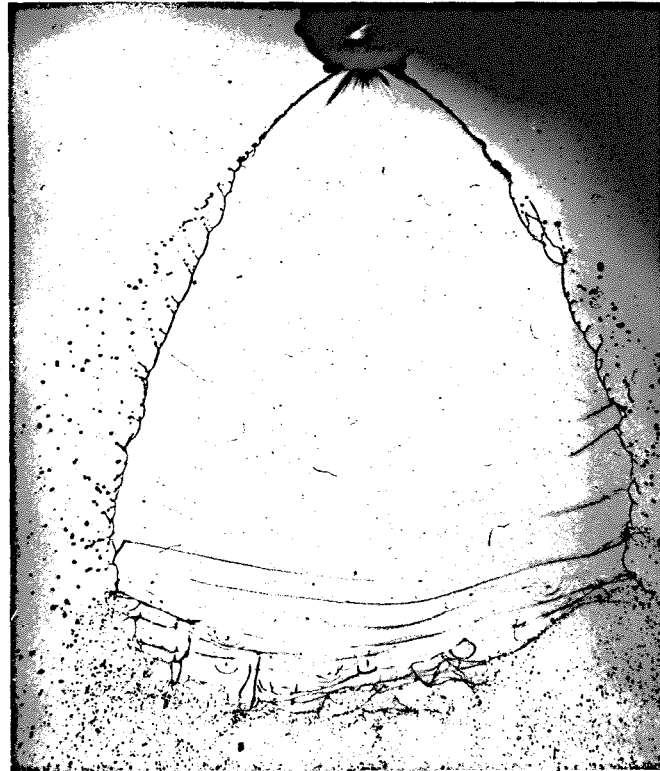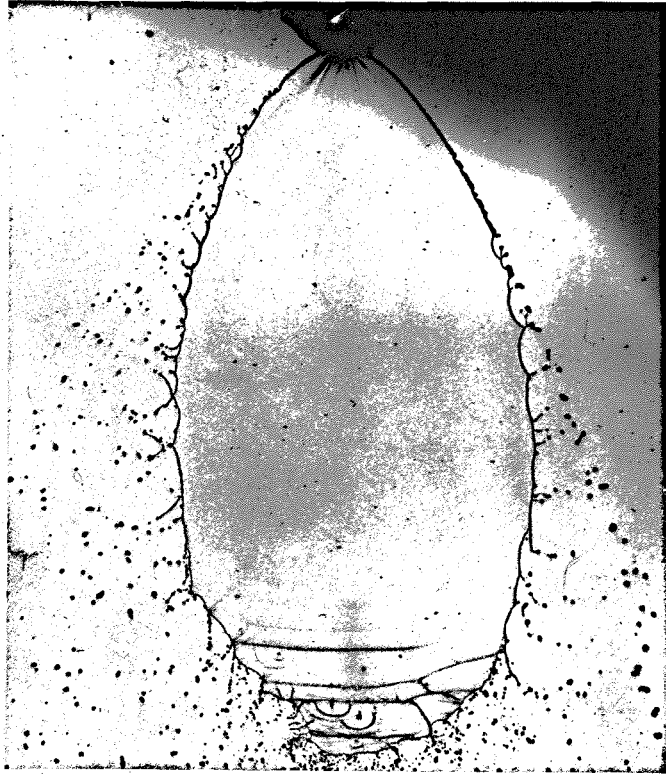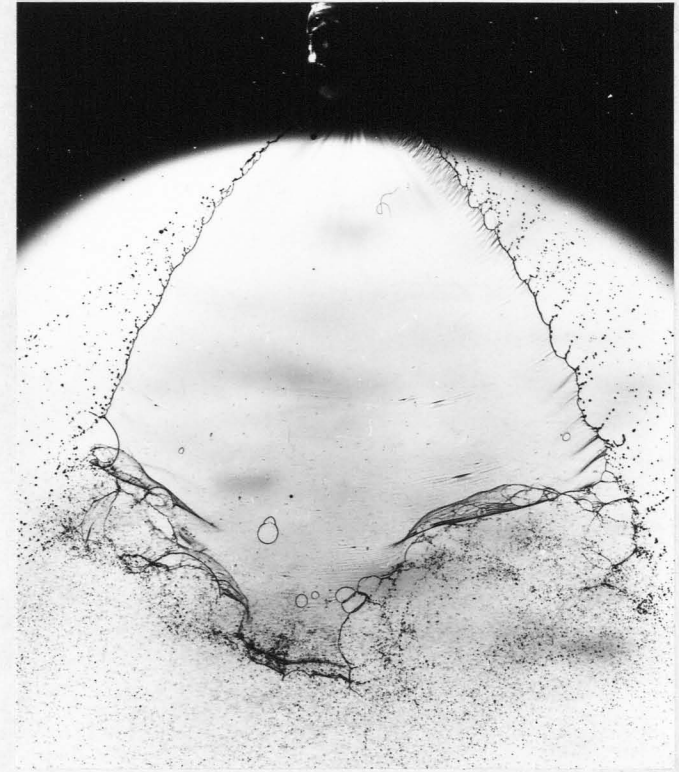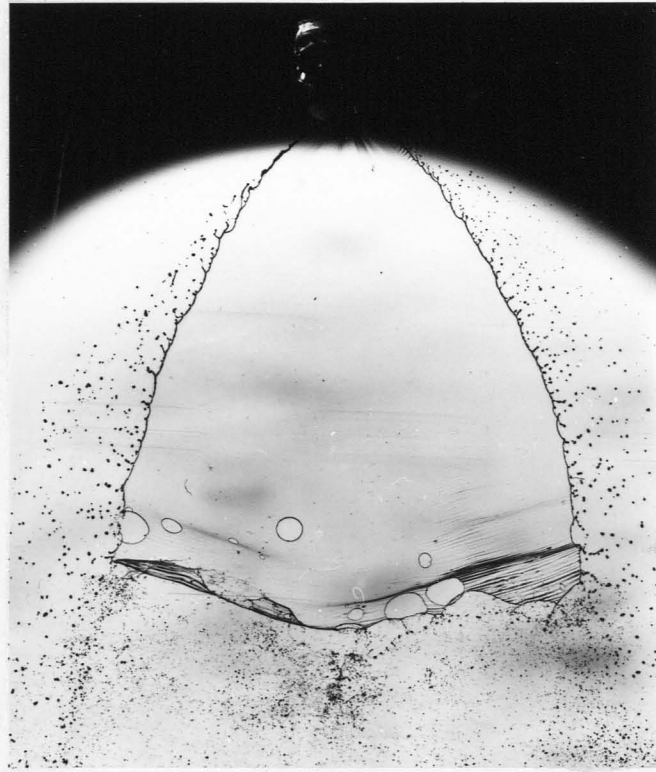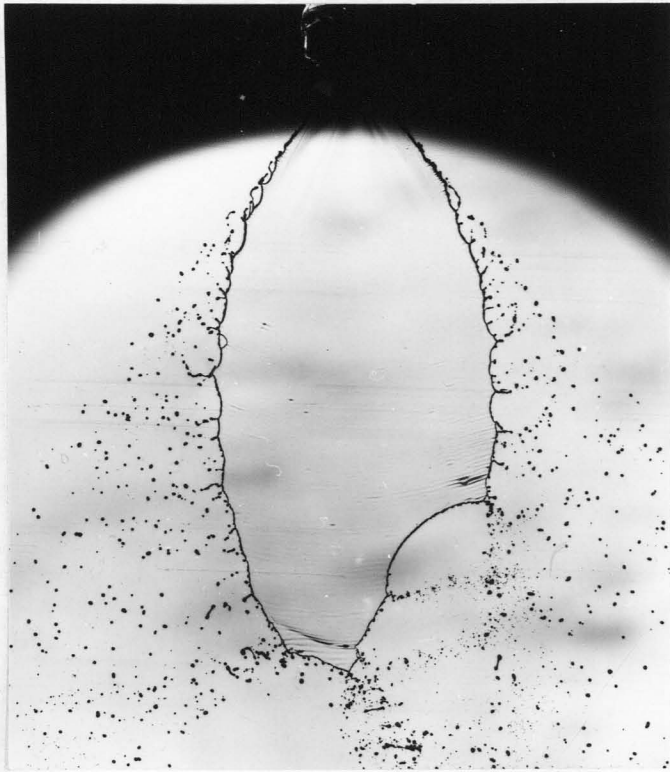
Differential injection   a)   1.72   bar
pressure   (25 psig)

(b)   3.58   bar
(52 psig)

(c)   6.35   bar
(92 psig)

Magnification   :   x 2

Nozzle   :   Bray Unijet   Y

Ambient gas temperature   : $380^{\circ}C$

Liquid temperature   : $24 - 28^{\circ}C$

Fig. 4.2   Typical Photographs of Fan Spray Water Sheets formed in a Hot Gas.

Differential injection (a) 1.72 bar   (b)   3.58 bar   (c)   6.35 bar
    pressure   (25psig)   (52psig)   (92psig)

Magnification : x 2

Nozzle   : Bray Unijet Y

Ambient gas temperature : 675°C

Liquid temperature   : 24 - 26°C

Fig. 4.3 Typical Photographs of Fan Spray Water Sheets formed in a Hot Gas.
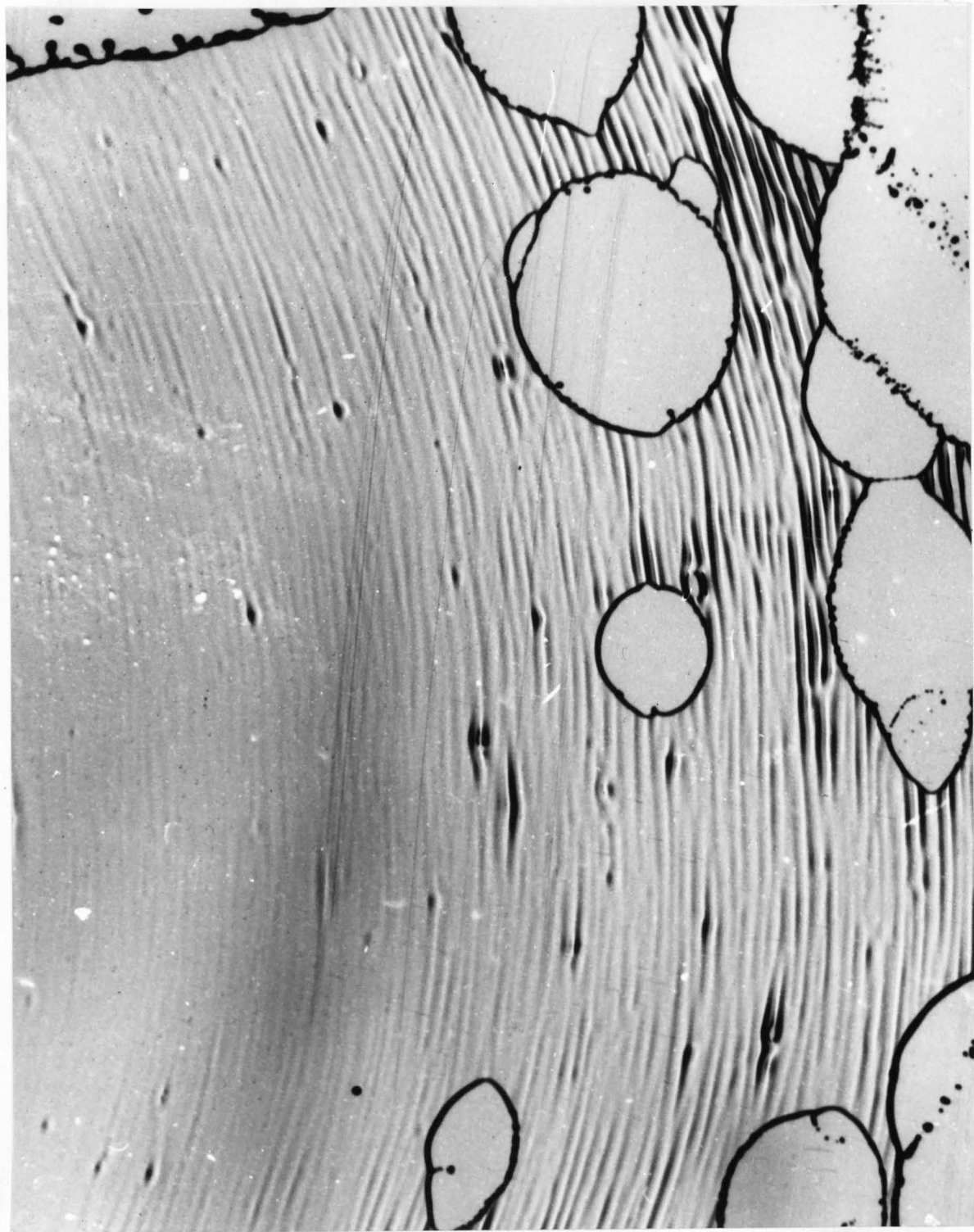
Magnification: x 10.4

Nozzle: Bray Unijet Y

Differential Injection Pressure: 3.44 bar (50 psig)

Ambient Gas Temperature: 675°C

Liquid Temperature: 25°C

Fig.4.4.   The Region of Disintegration of a Flat Water
            Sheet in a Hot Gas

4.1   The Mechanism of Drop Formation in Hot Atmospheres

The effect of ambient gas temperature on the mechanism of sheet disintegration was examined at temperatures of $20^{\circ}C$, $380^{\circ}C$, $675^{\circ}C$ and $950^{\circ}C$. Some results are demonstrated in Figs.(4.1), (4.2) and (4.3) for a range of injection pressures. Fig.(4.1) shows typical photographs of sheets formed at room temperature with aerodynamic waves being clearly visible and causing break-up at the higher pressures. Fig.(4.2) demonstrates that, as expected, the aerodynamic wave motion becomes less pronounced when the temperature is raised to $380^{\circ}C$. The photographs also reveal, however, the presence of a series of high frequency capillary waves over a large portion of the sheet, and that sheet disintegration occurs as a result of aerodynamic wave motion and random perforations. At $675^{\circ}C$ (Fig.(4.3)) aerodynamic waves are only apparent at the highest pressure and capillary wave motion predominates throughout. Perforations become more frequent and the region of disintegration recedes back towards the nozzle. The mechanism of drop formation now follows more closely the simple model employed for wave disintegration, the liquid trapped within the network of holes contracting into ligaments which subsequently break down into a corresponding network of drops. Fig.(4.4) shows part of the sheet illustrated in Fig.(4.3b). Inspection of the edges of the larger perforations reveals varicose profiles which indicate the ripples to be dilational waves. This conclusion may also be drawn from the highly eccentric elliptical shape of the perforations which can be assumed to result from the relatively high rate of expansion along the wave troughs where the sheet is thinnest. The enlargement also reveals the presence of numerous point disturbances where the waves have high local growth rates. Examination of a large number of similar photographs

shows the disturbances always to be present and randomly distributed about the sheet. This phenomenon was examined further with the aid of a high speed cine camera* operated at a rate of 10,000 pictures per second. The resulting film demonstrated that the disturbances became apparent only at some distance from the orifice and that they were eventually the sole cause of sheet break down.

A series of experiments was undertaken to ascertain the cause of these phenomena. Initially, in order to determine whether the presence of dissolved air affected the behaviour of the sheet, experiments were carried out with tap water, which was generally found to be super-saturated with air, and with distilled water in which the air content was reduced to a value of 1 ppm by means of the method described in Section 3.4. No difference could be detected. Experiments were then carried out in the open laboratory with a Meker burner to examine the sheet more closely. It was discovered that the perforations were produced only when the luminous gases came into contact with the sheet. Since they are a rich source of charged particles, figures in the range 10^{13} - 10^{15} ions/m^3 being reported for bunsen flames (42), 10^{15} - 10^{18} ions/m^3 for hydrocarbon-air flames (43-44) and 10^{17}-10^{19} ions/m^3 for flames containing traces of alkali metals[+](33), it was postulated that the phenomena were associated with the electrical properties of the flame gases.

* The high speed film was taken with a Hitachi Hymac 16 mm camera synchronised with an Ernest Turner 86/AV sub-microsecond repetitive spark light source.

[+] The burners used in the work incorporated ceramic stabilising grids and produced predominantly yellow flames typical of the coloration of sodium traces.
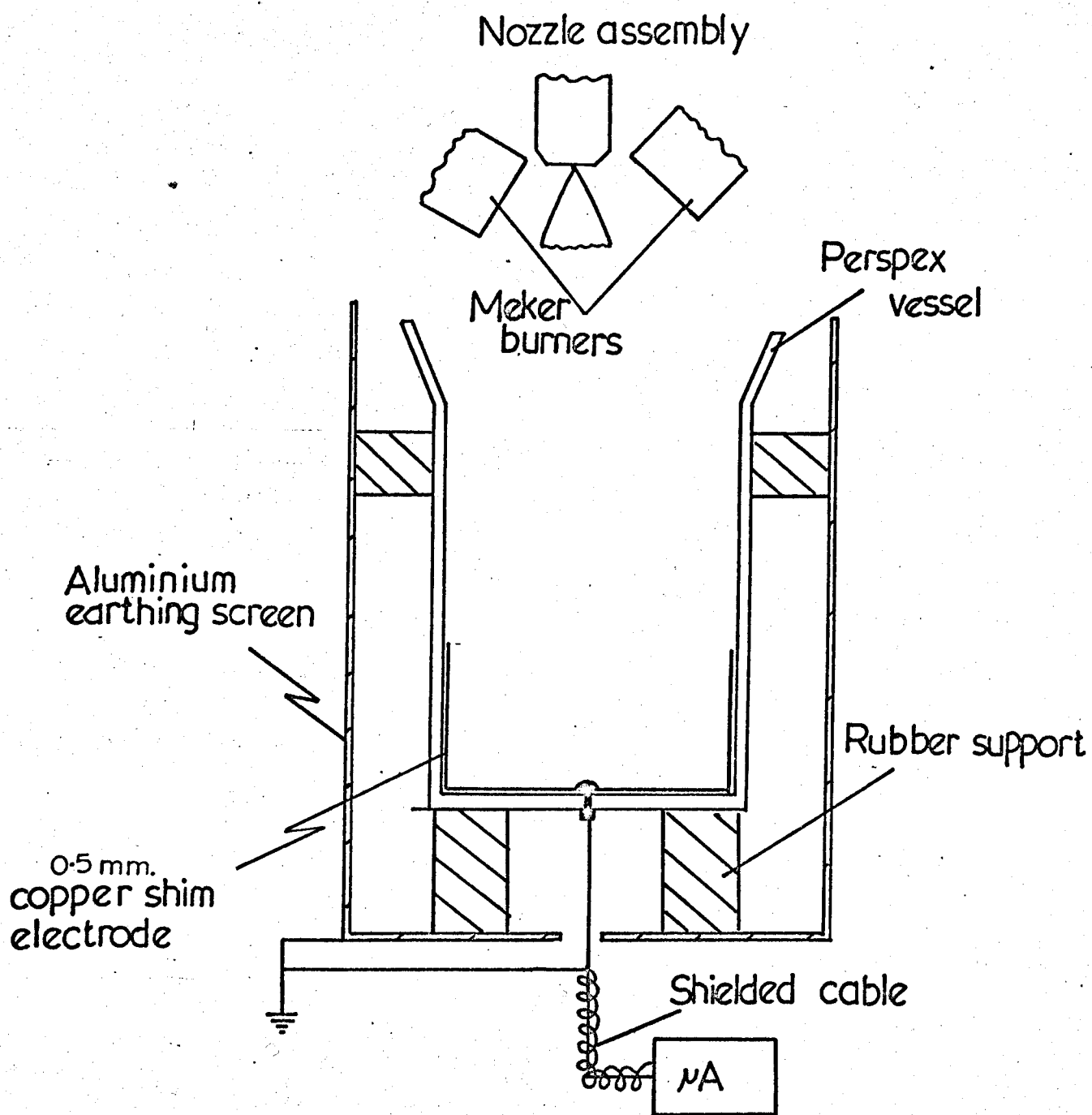
FIG. 4.5 APPARATUS FOR DETECTING CHARGE ON A LIQUID SHEET

In order to determine whether charge transference could take place in the relatively short lifetime of the sheet (i.e. 10^{-3} secs), a simple apparatus was constructed to determine approximate values of the charge collected by the liquid. A schematic diagram of the apparatus is shown in Fig.(4.5). Water from a swirl spray nozzle operated at a low pressure of about 0.69 bar (10 psig) to minimise droplet dispersion, was passed through the impinging interconal gases of two meker burners and then collected in a perspex container. The bottom half of the latter was covered with a thin copper electrode which was connected through a microammeter to earth. The whole apparatus was surrounded by an earthed aluminium screen. It was observed that, in the absence of the flame, the spray produced a small positive current of approximately 10^{-2} µA. When the burners were ignited a negative current of the order of 1-3 µA was recorded. The negative polarity was not unexpected since it has been previously demonstrated that non-emitting surfaces placed in an ionised gas accumulates charge as a result of the high mobility of electrons. However, at this stage, evidence for the waves being electrohydrodynamic in origin was inconclusive, since the possibility of temperature effects could not be excluded. Further experiments were therefore performed to isolate these two properties. The first series was devised to study the behaviour of sheets in hot gases with the surface charge reduced to negligible proportions, while the second was performed to examine the effect of surface charge at room temperature. All experiments were performed with a Bray miniature unijet Y nozzle.

Two approaches were adopted to reduce the surface charge. The first was concerned with reducing the electron mobility and promoting recombination by introducing a material with a high collision cross-section into the boundary layer. The most convenient method of
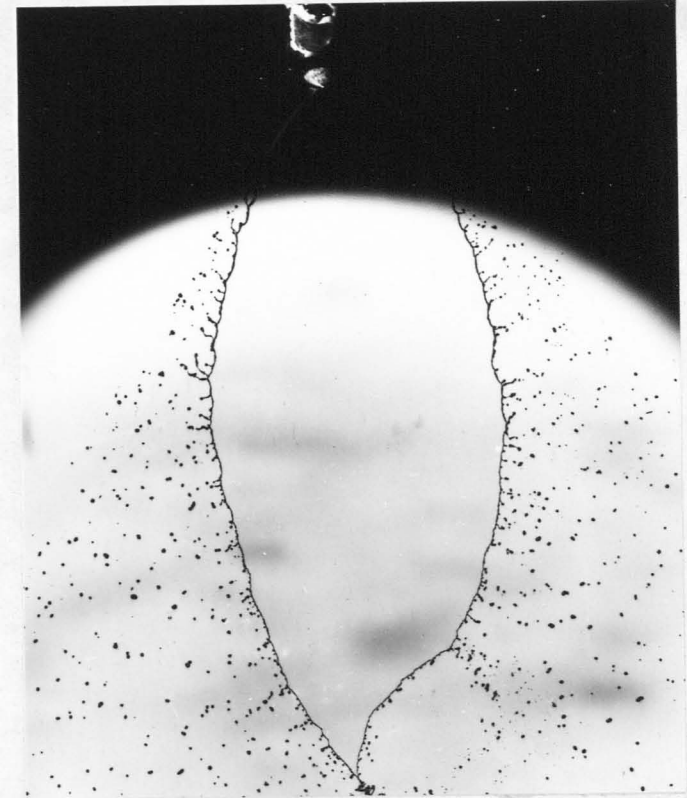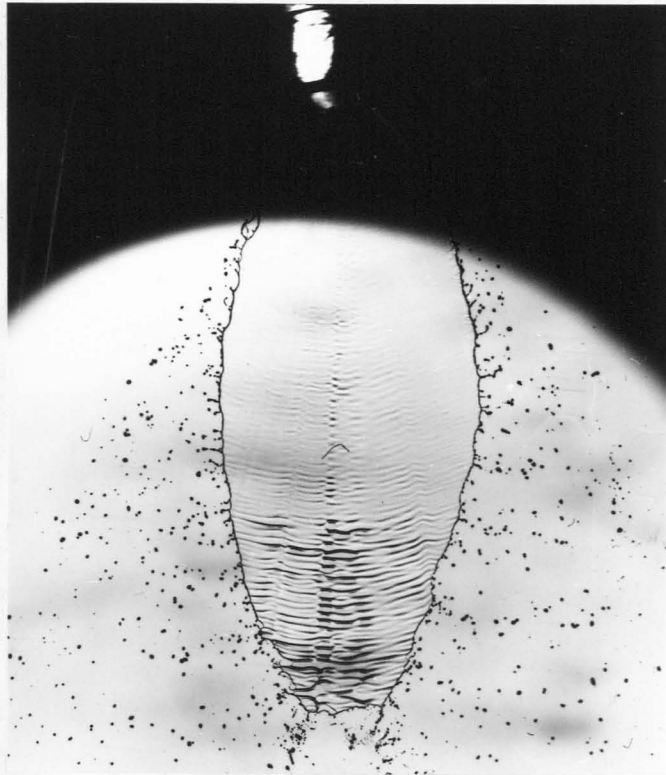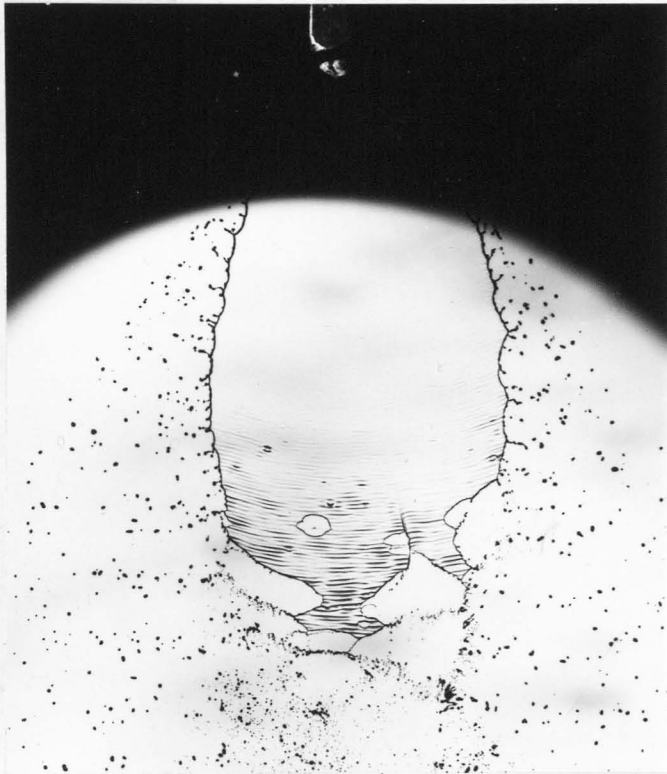
Liquid Temperature :   (a)   56°C   .   (b)   67°C   (c)   78°C

Differential Injection Pressure : 1.72 bar (25psig)   1.59   bar   (23psig)   1.72   bar   (25psig)

          Magnification : x 2

          Nozzle   : Bray Unijet Y

          Ambient gas temperature : 940°C

Fig. 4.6 Typical Photographs showing the effect of Liquid Temperature on the Mechanism of Water Sheet disintegration in Hot Atmospheres.

accomplishing this is, in fact, to raise the partial pressure of water vapour adjacent to the surface by heating the liquid, and a series of photographs were taken of sheets at various temperatures in a gas stream of 950°C. The partial pressure of water vapour in the combustion gas was estimated to be about 0.133 bar (103 mm Hg) and it was therefore expected that significant effects in sheet stability were only likely to be observed at liquid temperatures _giving vapour pressures_ above this value. Fig.(4.6) shows photographs of sheets of water with temperatures ranging from 56°C to 78°C*. Fig. (4.6a) (56°C equilibrium vapour pressure 0.165 bar (124 mm Hg)) demonstrates capillary wave motion and disintegration typical of that observed at low liquid temperatures. As the liquid temperature is raised above 56°C the incidence of perforations becomes less, until at 67°C, Fig (4.6b) (equilibrium vapour pressure 2.72 bar (205 mm Hg)), they cease. Capillary waves are, however, still evident although the wavelength is increased. As the temperature is raised still further the waves become less pronounced until, at a temperature of 78°C (Fig.(4.6c), equilibrium partial pressure 0.432 bar (327 mm Hg)), they disappear. Under these conditions the sheet remains plane and dis-integration occurs at the edges in a manner similar to that observed by Hooper at low gas densities (40). Temperature profiles in the test chamber (Fig.(3.3)) show that the temperatures adjacent to the sheet are not significantly different from those at liquid injection temperatures of 20°C. Confirmation of these measurements is afforded by the fact that, at gas temperatures below 300°C, where capillary waves have disappeared, the gas density is sufficiently high for aerodynamic waves to re-appear.

* The maximum temperature attainable at the nozzle was 85°C.
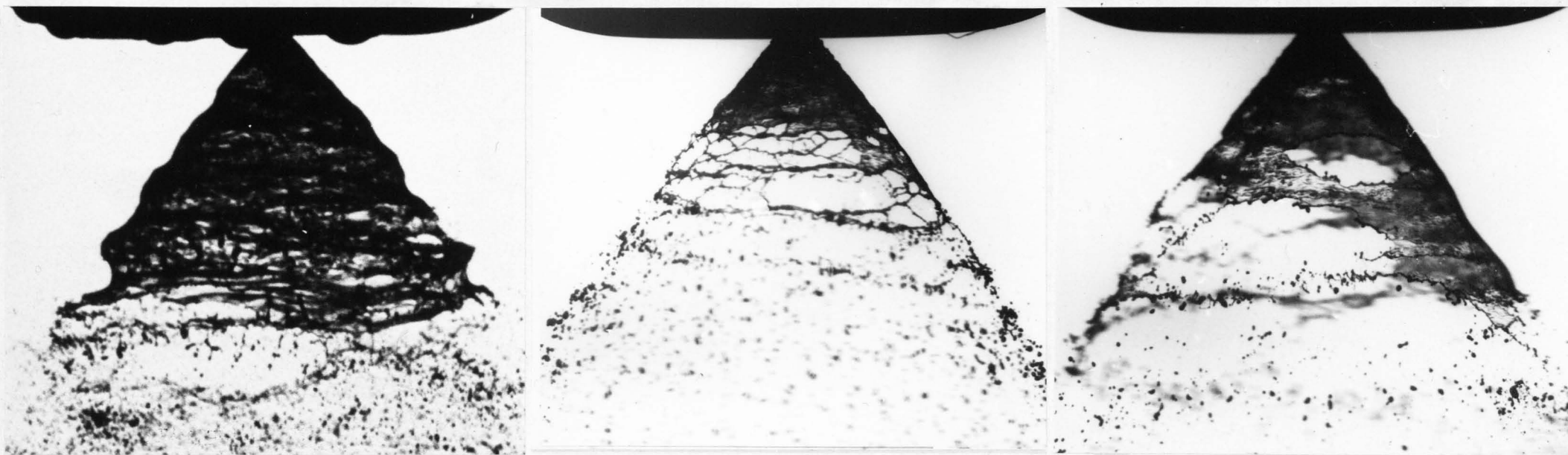
| Ambient gas temperature | (a) 20°C | (b) 940°C | (c) 940°C |
| Liquid temperature | 20°C | 26°C | 82°C |

Magnification : X 7.9

Differential Injection Pressure : 3.44 bar (50psig)

Nozzle : Danfoss D8/45

Fig. 4.7   Typical Photographs showing the effect of both liquid and gas temperature upon the mechanism of conical water sheet disintegration.

The second approach took advantage of the fact that ionisation in hydrogen-air flames is several orders of magnitude less than that of hydrocarbon-air mixture. A meker burner was modified to burn premixed hydrogen and air by first removing the ceramic grid and placing a fine mesh stainless steel gauze in the mouth of the burner. High purity Air Products Ltd. hydrogen and air were used, great care being taken to ensure that all surfaces were free from contaminants. The flame was directed to impinge on both sides of the sheets and temperatures of 1300°C were recorded adjacent to the surface. Stroboscopic illumination showed the sheet to be plane; devoid of both aerodynamic and capillary wave motion. The two free surfaces contracted by surface tension and a sheet similar to that shown in Fig.(4.6c) was produced. Capillary waves could, however, be induced by seeding the flame with small amounts of sodium bicarbonate.

Some observations were also made of the behaviour of conical sheets under the same set of operating conditions, and a few typical results are given in Fig.(4.7). Similar effects were found to occur at low liquid temperatures, but differences were noted at higher temperatures.

At low gas temperatures (Fig.(4.7a))* disintegration takes place through aerodynamic wave motion. At high temperatures (Fig.(4.7b) the sheet length is markedly decreased by the onset of perforations, and capillary waves may readily be identified.

*No significant differences were observed for sheets ranging in temperature from 18° to 82°C and Fig.(4.7a) is used to represent sheets produced both at 20°C and 82°C when injected into air at room temperature.
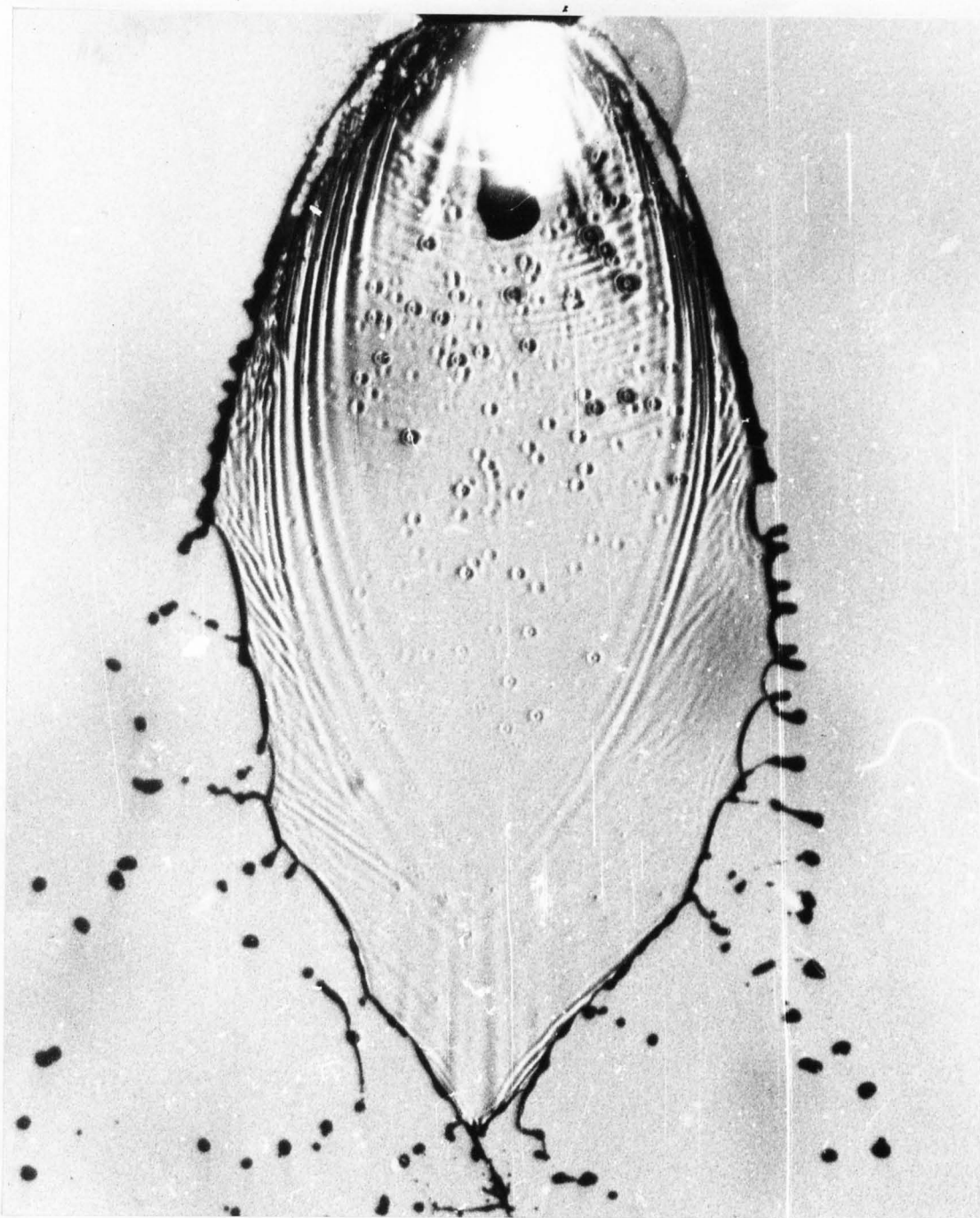
Magnification:- x **5.9**
Nozzle:- Bray Unijet **Y**
Differential injection pressure:- 0.69 bar (10 p.s.i.g)
Ambient gas temperature:- 20°C
Liquid temperature:- 20°C

Fig. **4.8**   Typical photograph of a flat water spray sheet showing the
              disturbances arising from a high frequency spark discharge.

It has been shown (45) that when a conical sheet, produced by a swirl spray nozzle, is injected into an environment of sufficiently low density, aerodynamic wave motion disappears. The sheet length increases, but premature breakdown by perforations occurs as a result of ripples originating at the origin (cf. Section 4.3) before the leading edge attains at equilibrium position. In the light of the findings for fan sprays it was therefore expected that at high liquid temperatures conical sheets would exhibit similar phenomena. However, although Fig.(4.7b) demonstrates the absence of aerodynamic waves and the presence of perforations, the latter occur relatively close to the nozzle. Inspection of the sheet again reveals the presence of associated capillary waves. The reason for this is not clear, although it is likely that the boundary layers around conical sheets are comparatively thinner as a result of their more turbulent nature and hence a higher temperature and thus higher vapour pressure is required to reduce charge diffusion to the surface.

The effect of surface charge at room temperature was studied by placing an electrode near the sheet and causing a high frequency, high voltage discharge to take place between it and the metal pressing surrounding the nozzle tip. The power source consisted of an Ernest Turner HSS/4/8 stroboscope operating at 4,000 flashes/sec with the standard flash lamp replaced by a pair of electrodes. The charging mechanism is not directly comparable with that occurring in hot gases, since surface charge will result from both induction and diffusion. However, it was expected that the general characteristics would be similar. A typical result is shown in Fig.(4.8). The photograph demonstrates a similar pattern of waves and local disturbances, although they differ in detail, the disturbances taking on the form of craters.

Table 4

Data used to calculate the surface charge, and cut-off and optimum wave numbers on liquid sheets

Nozzle	Flat Sheets Bray Unijet Y	Conical Sheets Danfoss D8/45
θ_a, (Ambient gas temperature) ($^\circ$K)	1220	
θ_l, (Liquid temperature) ($^\circ$K)	300	
Gas composition	H_2O = 0.133 CO_2 + A = 0.100 O_2 = 0.032 N_2 = 0.735	
N_{fo} (Charge particle density) (m^{-3})	10^{18}	
Sc_a (Ambipolar schmidt number)	1	
θ_i (Ion temperature) ($^\circ$K)	760	
ν_g (Gas phase kinematic viscosity) (m^2sec^{-1})	5.7×10^{-4}	
k_i (Ion mobility) (m^2sec^{-1})	0.7×10^{-4}	
*	0.62	
J_i/J_e	10^3	
U_o (Liquid velocity) ($m\ sec^{-1}$)	14	8.1
A (eq.A.48)	1.72×10^{-4}	8.2×10^{-4}
p^2 (eq. A.32)	1.2×10^2	1.0×10^{2}*
η_o (eq. 12c)	0.38	0.67
G_w (eq. A.42)	18.2	17.4
k_{opt} (m^{-1})	0.85×10^2	0.64×10^2
k_c (m^{-1})	1.47×10^2	1.21×10^2
k measured (m^{-1})	1.2×10^4	3.3×10^4
$^\circ$E calculated (Vm^{-1})	2.99×10^4	2.38×10^4
$^\circ$E observed (Vm^{-1})	–	2.07×10^6

*Although these values of p^2 and η_o do not satisfy the requirements given on page A.12 they are sufficiently close to provide reasonable estimates of the charge and field distributions.

It is well known (28-31) that liquid streams become more unstable under the influence of an applied electric field and it was therefore reasonable to conclude that the small waves are electrohydrodynamic in origin, while the localized disturbances are a result of random fluctuations in the charged particle distribution in the surrounding gas. An analysis was then performed of the electrical boundary layer characteristics around a continuously expanding liquid sheet assuming laminar flow (Appendix I) and expressions were developed for the criterion of stability, and the cut-off and optimum wave-numbers of the field coupled waves (cf. equations (2.174) and (2.175) Section 2.3).

Values of cut-off and optimum wave-numbers have been calculated for flat sheets and conical sheets and compared with observed values. Typical sets of operating conditions and calculations are given in Table 4. It is assumed that the gas composition corresponds to that obtained from complete combustion of an 85% stoichiometric mixture of propane and air to carbon dioxide and water and that the ionization results from sodium impurities of low electronegativity, which at the theoretical flame temperature of $2140^{\circ}K$ give rise to a free stream charge particle density, N_{fo}, of 10^{18} electrons m^{-3}.

Little information is available on the values of ambipolar Schmidt numbers in ionized* gases and recourse was made to estimation[+] taking average values of the temperature dependent properties in the gas boundary layer (θ_i, ν_g and k_i) based upon the arithmetic mean temperature $(\theta_a + \theta_i)/2$.

*Talbot(46) has reported values of 1.3 for ions in Argon at low temperature.

[+]The ambipolar Schmidt number is given by $Sca = \frac{1}{2} \left(\frac{\nu_g \acute{e}}{K\theta_i k_i} + \frac{\nu_g e}{K\theta_e k_e} \right)$ and since the ion mobility k_i is much less than the electron mobility k_e the expression reduces to $Sca = \nu_g e / 2K\theta_i k_i$.

θ_i, the ion temperature, was then assumed to be equal to the mean temperature since ions are generally in thermal equilibrium with the neutral carrier gas, while η_g, the viscosity of the boundary layer, has then been taken to be that of air under the same conditions.

k_i, the ion mobility, is dependent upon the nature of the carrier gas, particularly its permittivity. For example, the presence of water molecules over a wide range of conditions reduces the ion mobility as a result of ion-molecule cluster formation. Preliminary calculations using the approach of Bloom and Margenau (47) indicated that, for the proportions of water and carbon dioxide present in the ionized gases, appreciable clustering will occur at temperatures below $400^{\circ}K$ for CO_2 and $1000^{\circ}K$ for water. Munson and Hoselitz (48) have measured the mobility of sodium ions in Argon in the presence of varying amounts of water vapour at a temperature of $293^{\circ}K$, and calculated the corresponding cluster sizes by means of the classical Langevin equation in the small ion limit (49). Their results indicated that at zero field strength the cluster attains a maximum of six water molecules. The maximum field strength/gas pressure ratio was of the order of 1.52×10^6 volts $(m \cdot bar)^{-1}$, and for 2.8% by volume water vapour the cluster was estimated to contain four molecules, corresponding to 0.7 of the maximum. Loeb (50) has noted that a field of this magnitude corresponds to an increase in the gas temperature to about $550^{\circ}K$. Since Munson and Hoselitz have also shown that cluster stability increases with increase in water vapour content, it is reasonable to assume that for the present work where the mean temperature is $750^{\circ}K$ and the water vapour content is 13%, the cluster size will be near to its maximum value throughout the boundary layer. For this cluster size the

Langevin equation gives a value of mobility of $5.7 \times 10^{-4} \, m^2 \, (\text{sec volt})^{-1}$ at $700^{\circ}K$ in N_2^+ at 1 bar (760 mm Hg)*, compared to a value of $7.7 \times 10^{-4} \, m^2 \, sec^{-1} \, volt^{-1}$ for the unclustered ion.   Using this value of mobility gives the ambipolar Schmidt number a value of   1.

The parameter, A, defined by equation (A.48) is dependent upon the surface radius $y(s)$ (cf. equation (A.54)) For simplicity, an average value based upon half the sheet length has been used.

In determining the value of $\varkappa$, the ratio of ion to electron temperature to be used in the calculations, it has been assumed that because of the relatively small size of electrons little momentum transfer occurs as they pass through the boundary layer.   Their temperature thus remains close to that of the ambient gas (θ_a), giving a value of $\varkappa$ of 0.62.   The ratio J_i/J_e given by equation (A.29b) is equal to the ratio of ion and electron diffusivities at their respective temperatures.

Using the Einstein relations, $D_i = k_i \dfrac{K \, \theta_i}{e}$ the ratio becomes $k_e/\varkappa k_i$. k_e has been determined by utilizing the Compton equation with tabulated values of collision cross section.   Since k_e is also a function of $^{\circ}E$, the interfacial field strength, an iterative procedure was adopted using equations (A.47) and (A.48) to obtain the appropriate value.

+Although nitrogen constitutes only 73% of the gas mixture, Blancs Law (49) shows that little error is incurred by treating the gas as pure nitrogen.

*For convenience Loeb's computed values of mobility at $293^{\circ}K$ have been utilized and the required values at $750^{\circ}K$ determined from the approximate relation $k_i \, \theta_i = \text{const}$ (49).

Examination of the numerical results shows the theory to predict cut-off and optimum wave-numbers to be of approximately two orders of magnitude smaller for both flat and conical sheets. These differences are most likely to be due to the implicit assumption in the boundary layer analysis that the mode of charge transfer is independent of the nature of the surface. In practice it would be expected that the onset of wave motion would induce local turbulence and thus enhance diffusion rates. This effect would be particularly marked for conical sheets, which show the greatest discrepancies, since, compared to flat sheets, the photographs (e.g. Fig.(4.7)) reveal the presence of a basic irregular wave pattern caused by flow disturbances within the nozzle.

An alternative method of testing the electrohydrodynamic theory of wave-growth derived in Section 2.3 could in principle be carried out by using known values of the charge distributions on and adjacent to the surface of the sheet. It is not possible, however, to make direct measurements from moving liquid sheets, but an indirect estimate of the surface charge on conical sheets can be made from its effect upon the sheet profile. This is discussed in detail in Appendix II where it is shown that the field is much greater than that estimated above, being 2.07×10^6 volts/m compared to the theoretical value of 2.38×10^4.
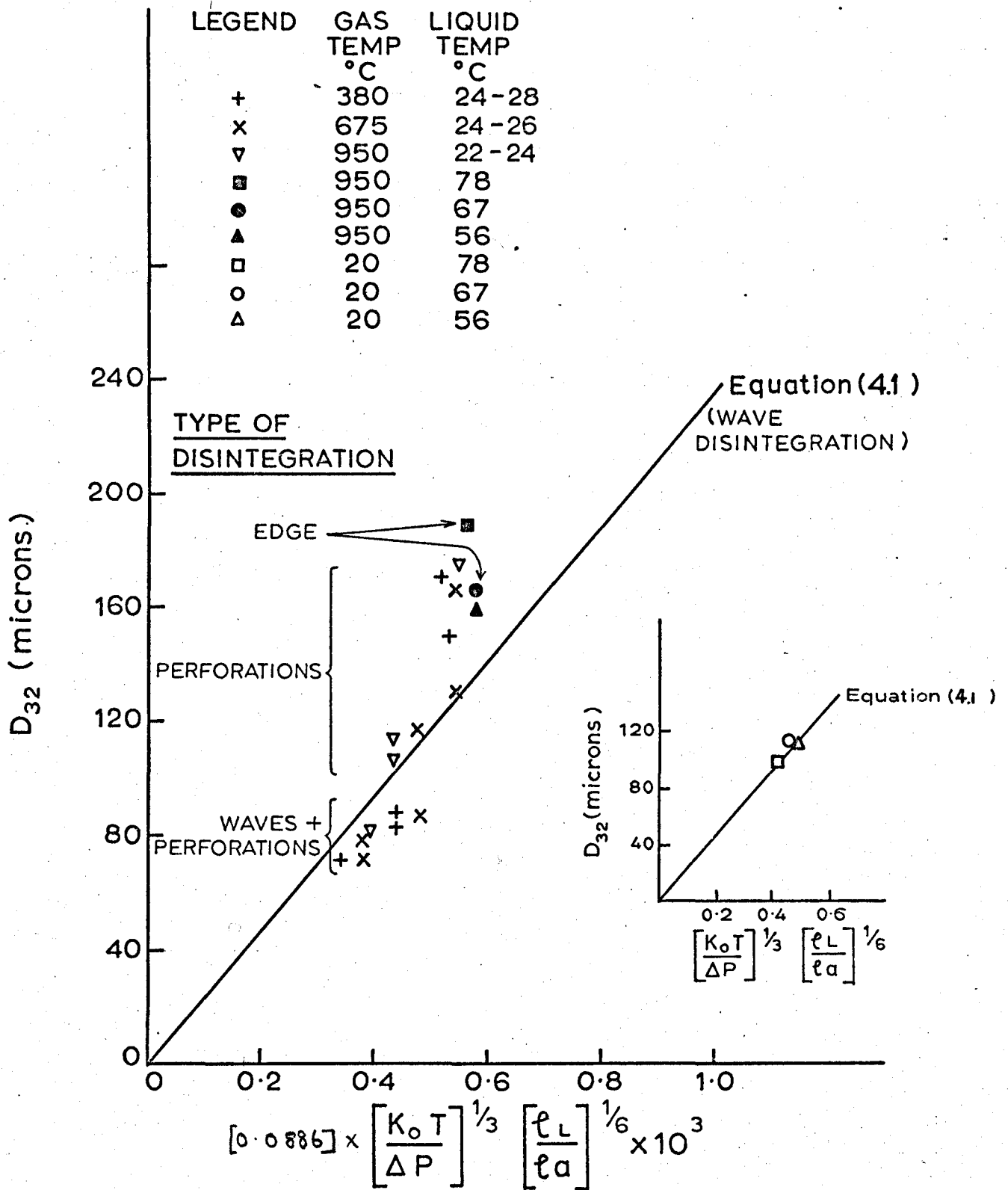
FIG. 4.9 CORRELATION OF DROP SIZE DATA FOR FLAT WATER SHEETS AT VARYING GAS TEMPERATURES (BRAY UNIJET Y NOZZLE)
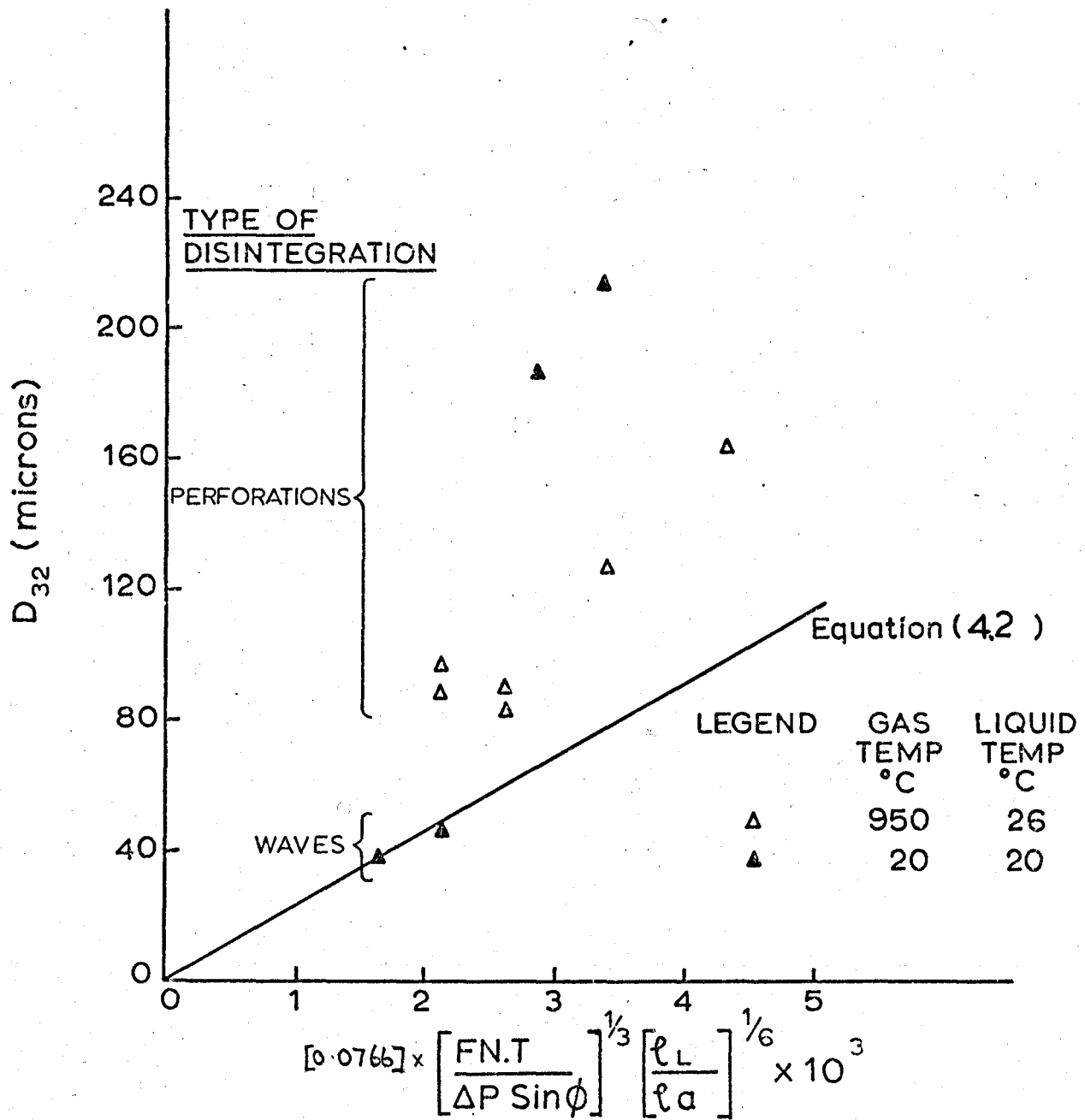
FIG.4.1O CORRELATION OF DROP SIZE DATA FOR CONICAL
WATER SHEETS AT VARYING GAS TEMPERATURES
(DANFOSS D8. 45 NOZZLE)

4.2 Effect of Gas and Liquid Temperature upon Drop Size

Drop size distributions as produced by both fan and swirl spray nozzles have been determined for a range of gas temperatures and injection velocities using Bray unijet Y and Danfoss D8/45 nozzles. In general two measurements were made for each set of operating conditions using the technique described in Section (3.6).

For sheets disintegrating through aerodynamic wave motion the volume surface mean diameter, D_{32}, can be related to the operating conditions, and relations are available for both fan and swirl sprays. For liquids of low viscosity, Hooper (40) and Briffa (53) have shown that

$$D_{32} = 236 \ (\frac{K_o T}{\Delta P})^{1/3} \ (\frac{\rho_1}{\rho_a})^{1/6} \ (\mu m) \tag{4.1}$$

for fan sprays, while Wolfsohn (54) has shown that

$$D_{32} = 22.7 \ (\frac{FN \cdot T}{\Delta P \ \sin\phi})^{1/3} \ (\frac{\rho_1}{\rho_a})^{1/6} \ (\mu m) \tag{4.2}$$

for swirl sprays.

The results for all operating conditions are plotted in Figs. (4.9) and (4.10) on the basis of equations with the corresponding mechanisms of sheet disintegration identified. In Fig. (4.9), in order to avoid confusion due to a multiplicity of points, some of the data are plotted separately on the inset graph. The figures show that, where drop formation occurs through aerodynamic wave motion, the results compare favourably with those obtained by previous workers. It is also seen that the superimposition of perforations on the waves has no significant effect. However, where disintegration occurs solely by perforations the resulting drop size tends to be higher than that predicted by equation (4.1) to an extent inversely related to the pressure and independent of gas and liquid temperature. This decrease

in drop size with pressure may be explained by a close examination of photographs such as those in Fig.(4.3), which indicate that the number of perforations increases with pressure.   The size of the ligaments are consequently reduced, resulting in relatively smaller drop sizes. The increased frequency is probably due to a greater number of flow disturbances which act as sites of high local growth rate, and it is therefore likely that higher pressures may lead to even smaller drop sizes.

The figures also show that, as found previously (40) for both types of sheet, edge disintegration causes larger drop sizes than the other mechanisms.

4.3 Comparison of Measured and Theoretical Break-up Lengths

of Attenuating Sheets

Break-up lengths have been determined for attenuating sheets

as produced by fan and swirl spray nozzles*.   The measurements

were made using flash photography, the initial point of rupture

being clearly delineated by using a "focussed shadowgraph" lighting

technique (Section 3.6).   It was found that break-up lengths

fluctuated by $\pm 20\%$ about a mean, and at least a dozen readings were

taken in each case.   The average values are listed in Table   7.

In order to compare these values with those predicted by

equation (2.138), it is necessary to determine the value of

dominant wavelength, λdom, and initial disturbance η_oh character-

istic of the operating conditions.

Previous workers have taken the dominant wave as the optimum,

i.e. the wave of maximum theoretical growth according to first order

theory viz. $\lambda_{opt} = 4\pi T/\rho_a U_o^2$.   However, there is no real

justification for this choice, as it implicitly assumes a uniformly

distributed wave spectrum in which each component grows independ-

ently of the others.   Hooper (40) found that the dominant wave-

length is significantly greater than the optimum, although, for a

limited range of conditions, the values may be correlated.   Second

order theory does not provide any further information on the

relation between optimum and dominant wavelength.

*Application of equation (2.138) to liquid sheets issuing from

orifices is not strictly valid since disturbances are unlikely to

be instantaneously imposed at the origin and, as a result, spatially

growing waves are generated which may be described by the relation

$$\eta = \eta_o h \exp(i ((k_r + i\, k_i)\, x + \alpha t))$$
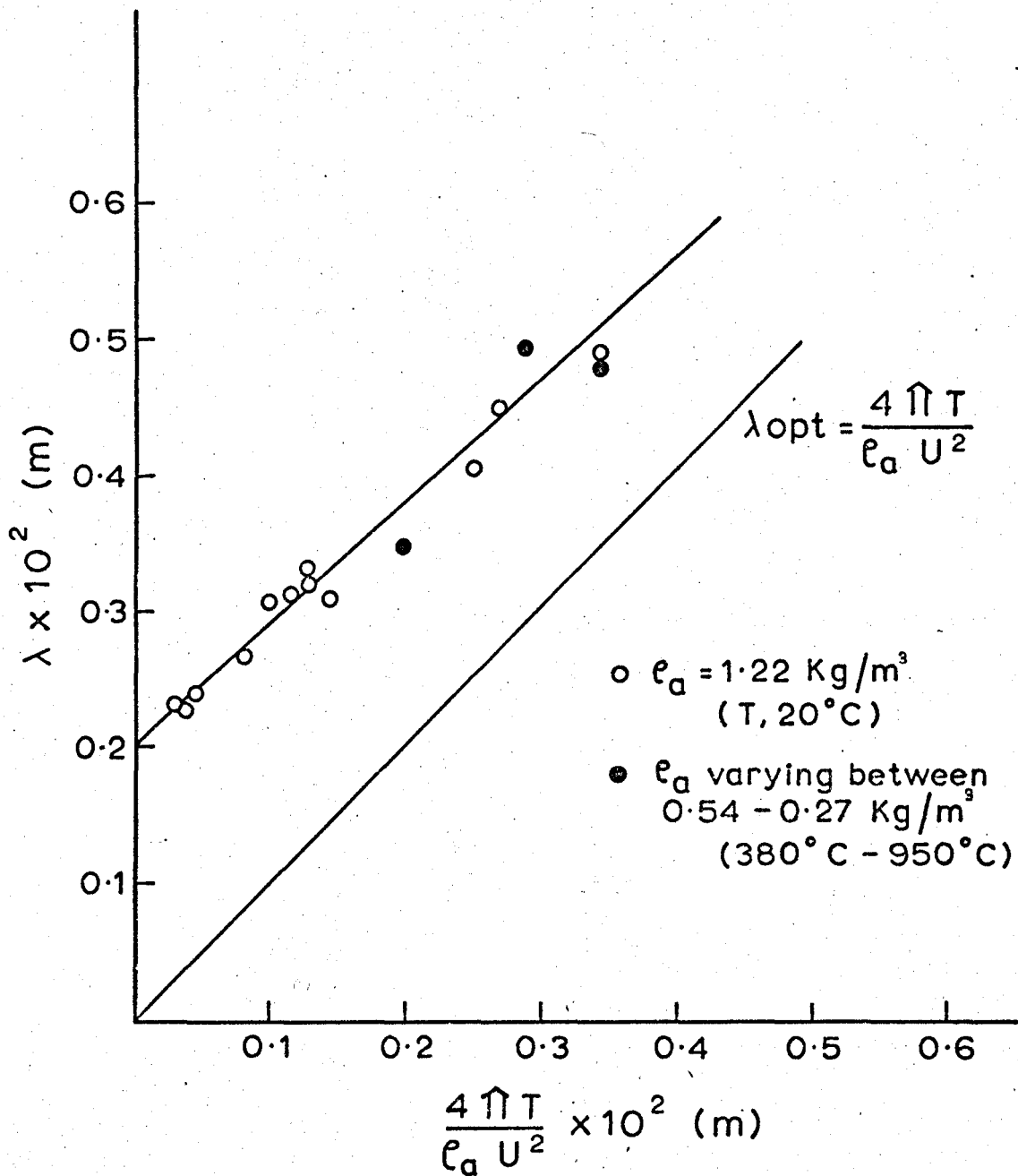
FIG. 4.11 COMPARISON OF THEORETICAL OPTIMUM
AND MEASURED WAVELENGTH

Indeed, since equation (2.132) demonstrates that energy for wave growth is essentially derived from the fundamental, the optimum wavelength is identical to that given by equation (2.99).

Values of dominant wavelength as observed directly from the photographs have therefore been used, and for ease of handling the data have been correlated with λ_{opt}. A plot of the two wavelengths is shown in Fig.4.11 and a linear regression gives

$$\lambda_{dom} = 0.9 \frac{4\pi T}{\rho_a U_o^2} + 0.002 \pm 0.00018$$

While some theoretical background exists for predicting characteristic wavelengths, the unknown nature of the random molecular or turbulent motions at the interfaces makes it impossible to specify the amplitude of disturbances initiating wave growth.   In principle, therefore, recourse has to be made to direct measurement. This was readily achieved for the conical sheets by examining the profile at the orifice and it was found that the initial values of amplitude were approximately 10^{-4} m[+]. It was not possible, however, to measure initial amplitudes on fan spray sheets, since the presence of the rims precludes observations along the plane of the sheet. It was therefore necessary to make an estimation of this value. Disturbances observed on conical sheets are most likely caused by wave motions within the air core upstream of the orifice.   These values cannot be used as a working basis for estimations for fan sprays, since the orifice runs full, and disturbances can only be propagated upstream of the outlet.

[+]Because $\eta_o h$ occurs as a logarithmic term in equation (2.138) accurate measurements are unnecessary.
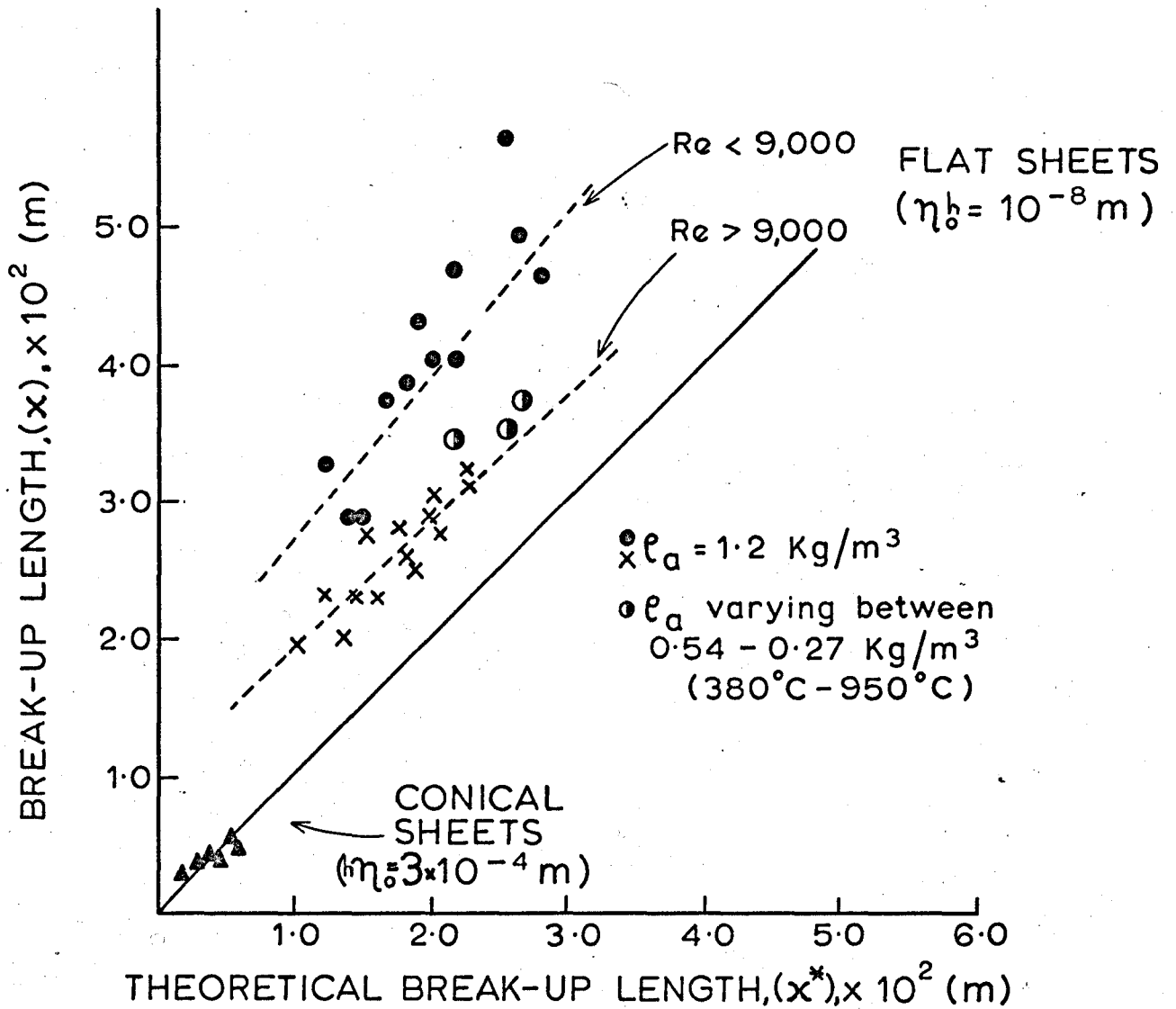
FIG. 4.12 COMPARISON OF THEORETICAL AND
MEASURED BREAK-UP LENGTHS
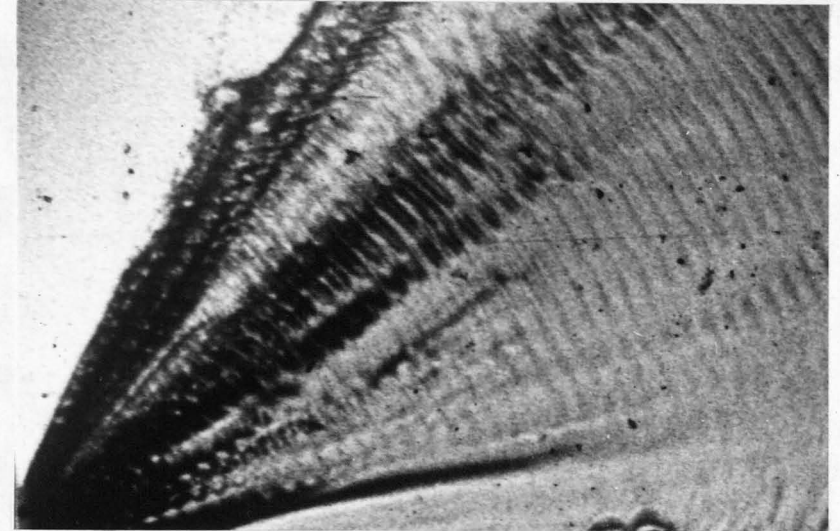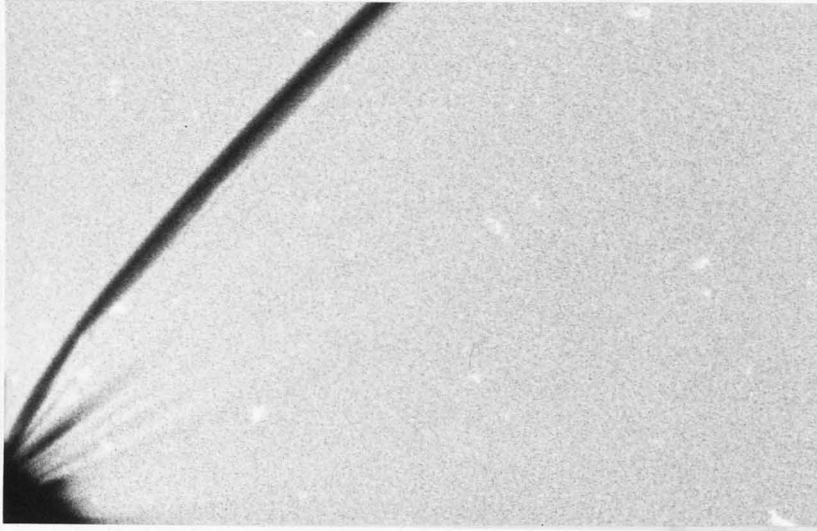
a)   Re = 8,150

Liquid :   Distilled water
Differential Injection
Pressure :   2.41 bar
                (36 psig)

Magnification   x 11.1

Nozzle   Bray Unijet X

b)   Re = 23,800

                Acetone

                2.75 bar
                (40 psig)

Fig. 4.13 Typical Photographs of a Fan Spray Sheet Taken of the Region near the Nozzle Orifice.

It is reasonable to postulate, however, that the minimum value is likely to be of the order of molecular dimensions, i.e. 10^{-8}m. This value was therefore used for calculating break-up lengths from equation (2.138). Measured values of break-up lengths, and those calculated, are plotted in Fig.(4.12). The figure shows that the results for conical sheets fall about the theoretical line, while those for fan sheets are scattered above it. This ostensibly implies that smaller values of initial disturbances should be used as a basis for calculation and a figure of 10^{-12} m would be necessary to perform their appropriate adjustments. Little significance can, however, be attached to this value and the discrepancies are more likely to be understood in the light of approximations incurred in the derivation of the equations. The satisfactory agreement for conical sheets may well, therefore, be fortuitous as a result of additional thinning caused by surface ripples which are probably generated in the swirl chamber. However, the 'fan sheet' data were re-examined in conjunction with the corresponding photographs to establish the cause of the wide scatter, and it was observed that, for the results nearest the theoretical line, regular non-growing capillary waves were visible at the orifice, while the sheet remained plane for the others. Typical enlarged photographs of the regions within the vicinity of the orifices for these two cases are shown respectively in Figs.(4.13a) and (4.13b). On this basis it was found that the experimental points could be separated into two distinct bands. This suggested differences in the nature of flow in the nozzles and it was established, in fact, that the onset of ripples occurs at a critical value of Re. No.* which lies around 9,CCC.

*Based upon the hydraulic mean diameter of the orifice.
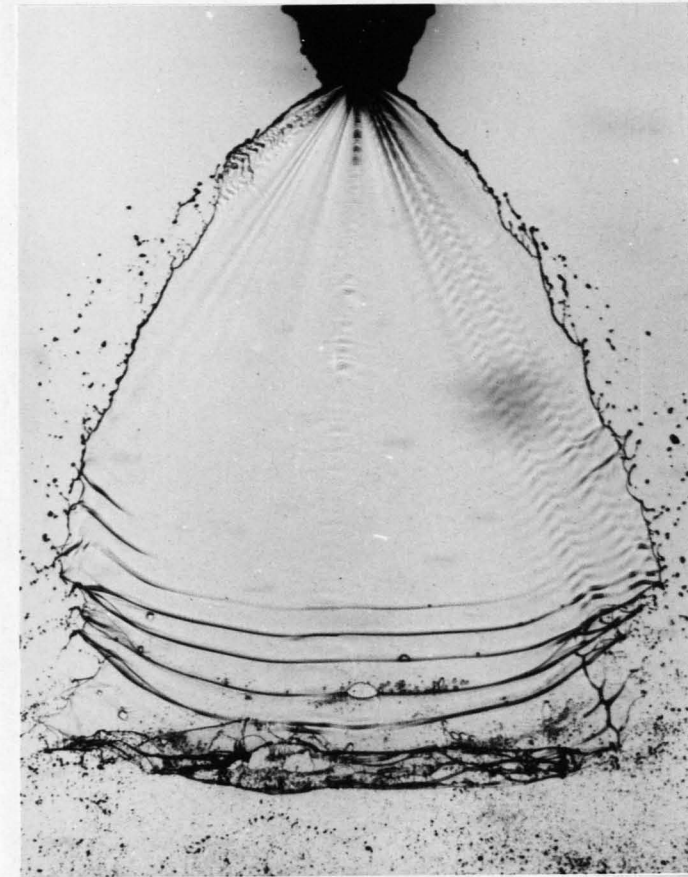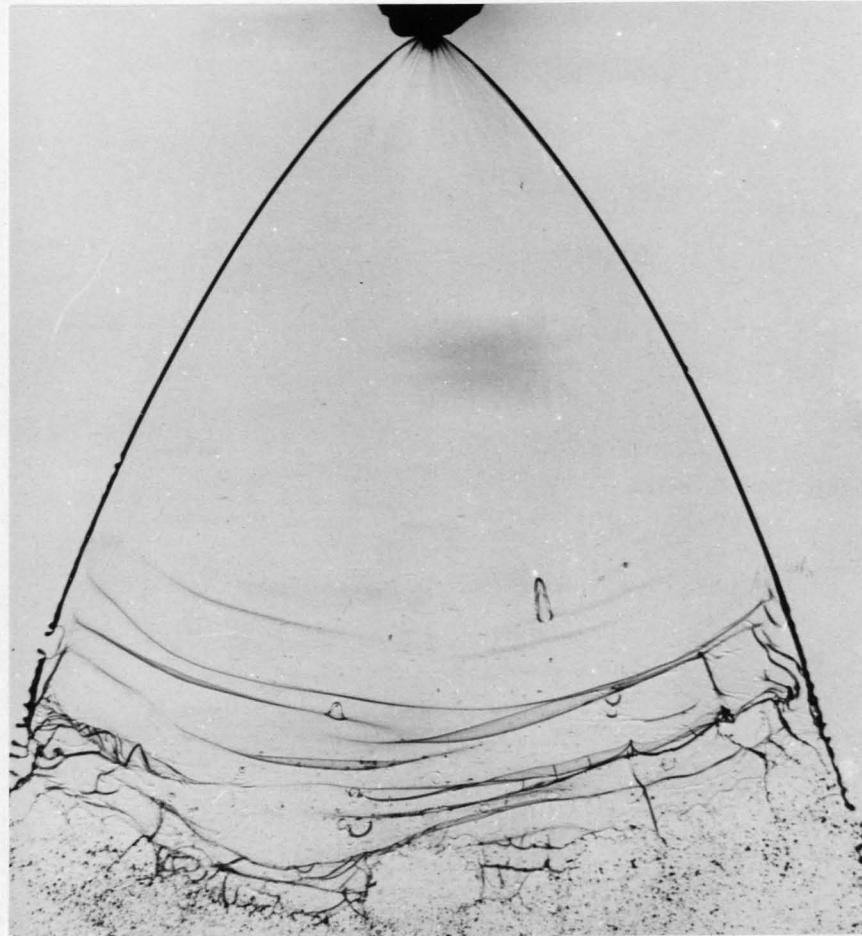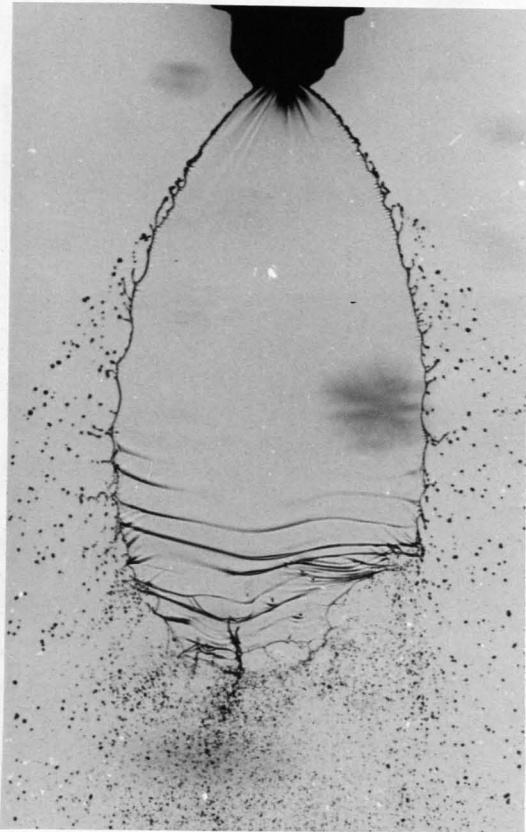
Nozzle :-	(a) Bray Unijet Y	(b) Bray Unijet X	(c) Bray Unijet W
Reynolds number	4,250	8,000	10,400
Magnification	x 2.		

Differential Injection Pressure : 241 bar (35psig)

Fig. 4.14   Typical Photographs of Water Spray Sheets showing the effect of Reynolds number upon the break-up length.
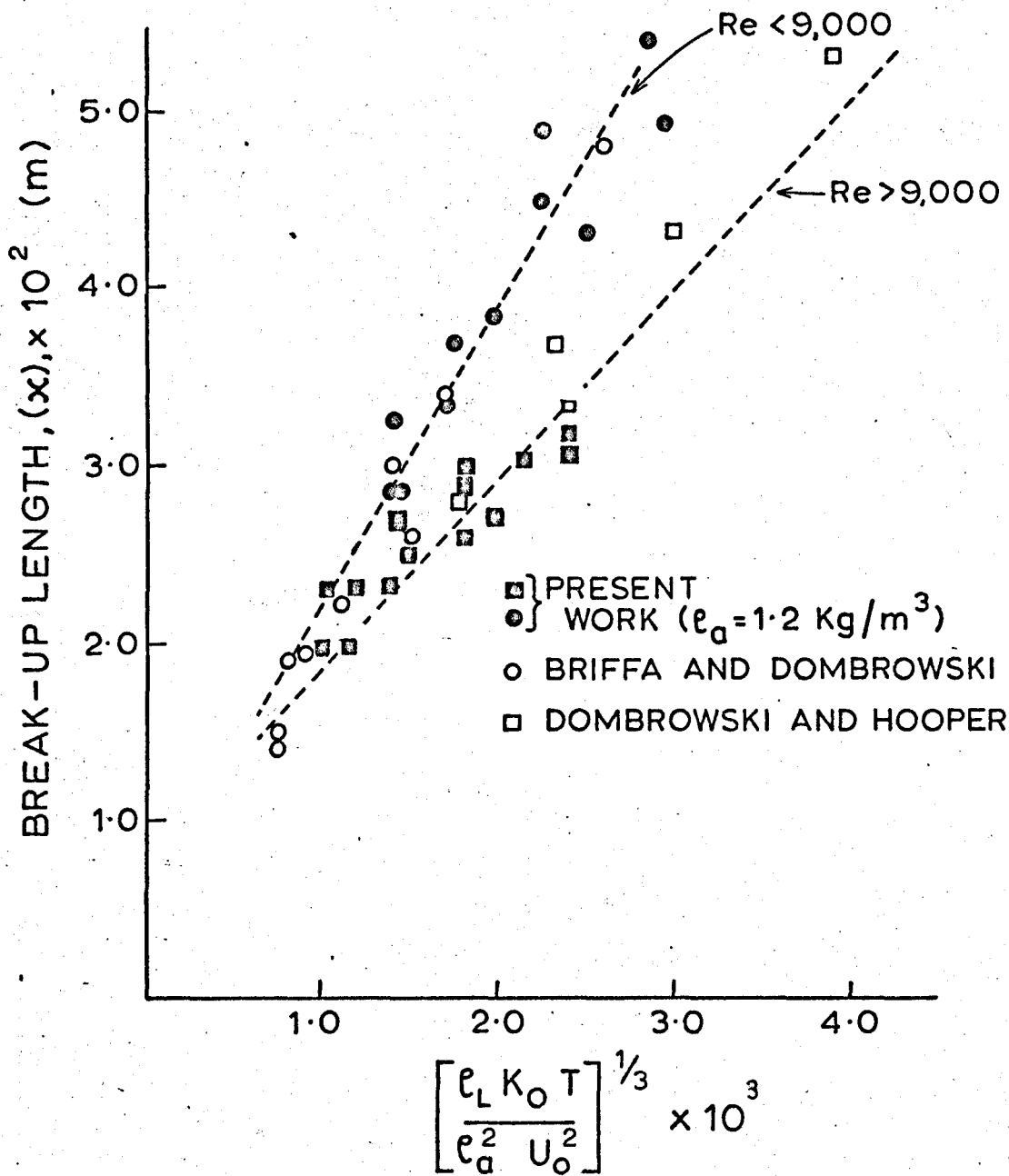
FIG. 4.15 CORRELATION OF MEASURED
BREAK-UP LENGTHS

The effect is demonstrated in Fig. (4.14) which shows photographs of water sheets produced from the nozzles at constant ejection velocity. The nozzle orifices increase in size from left to right, the first two, (a and b), operating at Reynolds numbers below 9,000, whilst the third (c) operates above. Comparison of photographs (a and b) clearly shows the expected increase of sheet length with nozzle size. A further increase, however, photograph (c), results in a Reynolds number of 10,400 ripples are therefore propagated, and the sheet markedly diminishes in length.

These findings can be used to explain the apparent anomalous results of Dombrowski and Hooper (9) and Briffa (52), who correlated sheet lengths on the basis of a theoretical relation developed from the first order theory of Squire,[+] viz.

$$x^* = \text{Const} \left\{ \frac{\rho_1 \, K_o T \ln \eta_{/h} \eta_o}{\rho_a^2 \, U_o^2} \right\}^{1/3}$$

Ln $\eta_{/h} \eta_o$ was taken to be constant and evaluated from the 'best line' relation between x^* and $\left\{ \frac{\rho_1 K_o T}{\rho_a^2 U_o^2} \right\}^{1/3}$. Dombrowski and Hooper found the value to be 12, while Briffa and Dombrowski found it to be 50, i.e. sheet lengths predicted by the latter were greater than the former.

Re-examination of their data reveals that the former worked at Reynolds numbers in excess of 9,000, while the latter worked below the value. Fig. 4.15, which shows a plot of these parameters, indicates that the present data compares favourably with those of the other workers.

[+] The previous published results cannot be plotted according to Fig. (4.12) since no details were given of the operating conditions for each experimental point.
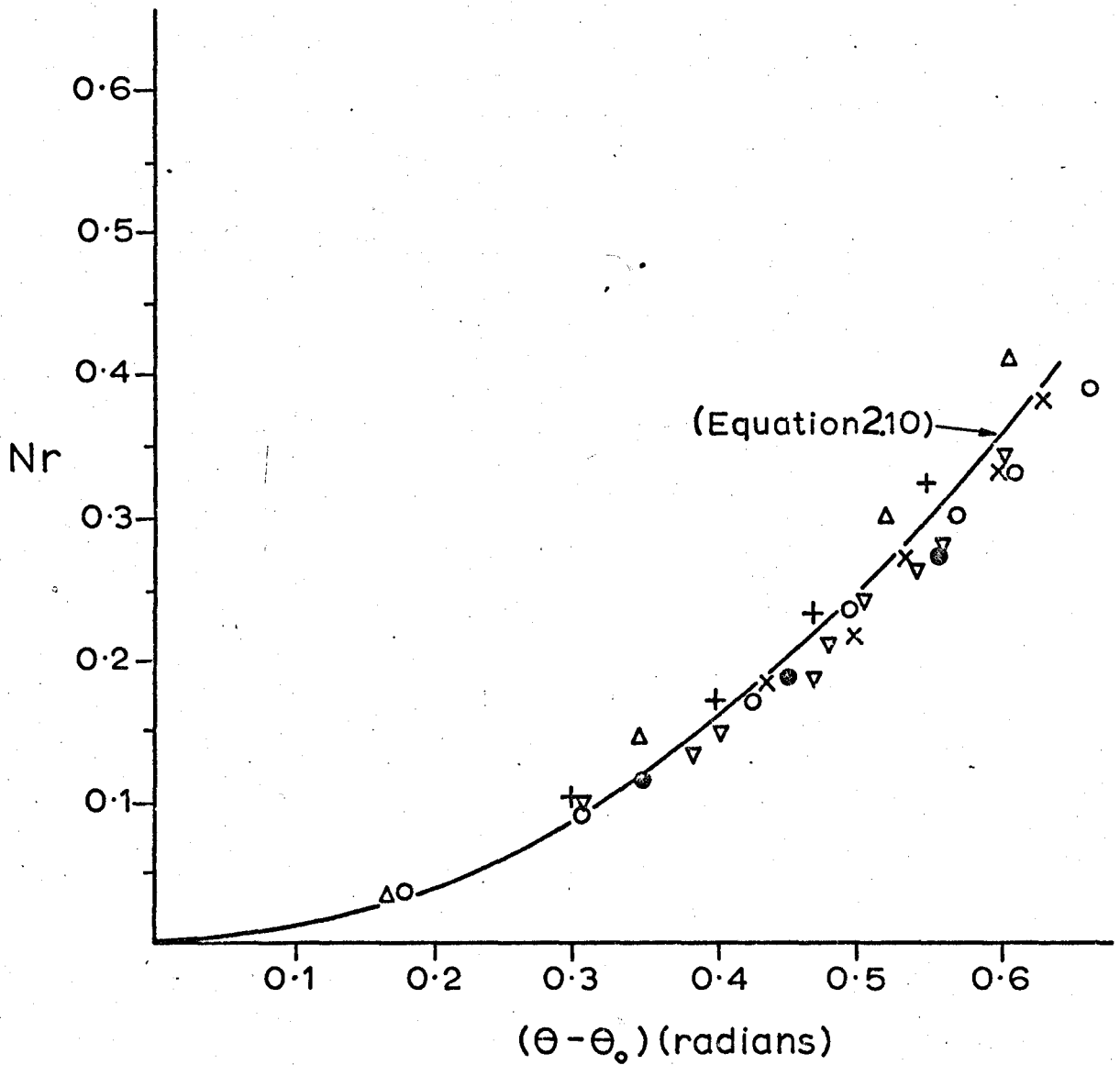
FIG. 4.16 COMPARISON OF THEORETICAL AND MEASURED
RIM TRAJECTORIES (FOR LEGEND SEE TABLE 5)

Table 5.   Range of Experiments

Legend (Fig.4.16 and 4.17)	Liquid	Nozzle	Injection Pressure Range (bar)
∇	Water	Y	0.69 – 1.38 (K_o, 5.5×10^{-2} mm^2)
o	Water	X	0.69 – 2.41 (K_o, $11.3 - 11.1 \times 10^{-2}$ mm^2)
$\overset{+}{\bullet}$	Acetone	Y	0.69 (K_o, 11.3×10^{-2} mm^2)
$\overset{+}{+}$	50% Glycerine-Water	X	1.38 (K_o, 11.6×10^{-2} mm^2)
x	Water	W	0.69 – 1.38 (K_o, $12.5 - 13.5 \times 10^{-2}$ mm^2)
$\overset{+}{\Delta}$	50% Glycerine-Water	W	1.38 (K_o, 15×10^{-2} mm^2)
$\overset{*}{\bullet}$	Carbon Tetrachloride	Y	2.41 (K_o, 5.0×10^{-2} mm^2)

+ Fig.4.16 only

* Fig.4.17 only

4.4 Comparison of Theoretical and Measured Rim Trajectories

Equation (2.10) has been tested by plotting the dimensionless parameters Nr and $(\theta - \theta_o)$ for a range of Bray miniature fan spray nozzles and liquids as listed in Tables (2) and (3).

The streamline velocity, U_o, is given by (10)

$$U_o = C_Q \ (2\Delta P/\rho_1)^{\frac{1}{2}}$$

while from continuity

$$\theta_o = \pi/2 - \frac{Q}{2U_o K_o}$$

The distance of the sheet origin from the orifice is then given by,

$$f = 2d \tan \theta_o$$

where d is the width of the orifice. The distance r is then measured from this point.

The results are shown in Fig.4.16 . It is seen that for the lower viscosity liquids the experimental points lie very close to the theoretical line, but tend to fall below it with increase of $(\theta - \theta_o)$. This divergence is not unexpected, because of the initial assumption $\cos\sigma \simeq 1$. While this simplification is justified near to the origin discrepancies become progressively magnified further away (cf. equation (2.6))

Viscous forces can be expected to oppose contraction of the rim so that corresponding points should lie above the inviscid line. This is demonstrated in Fig.(4.16) for a viscosity of 5.65 cs, although it should be borne in mind that the apparent differences have been minimised by the inherent theoretical errors described above.
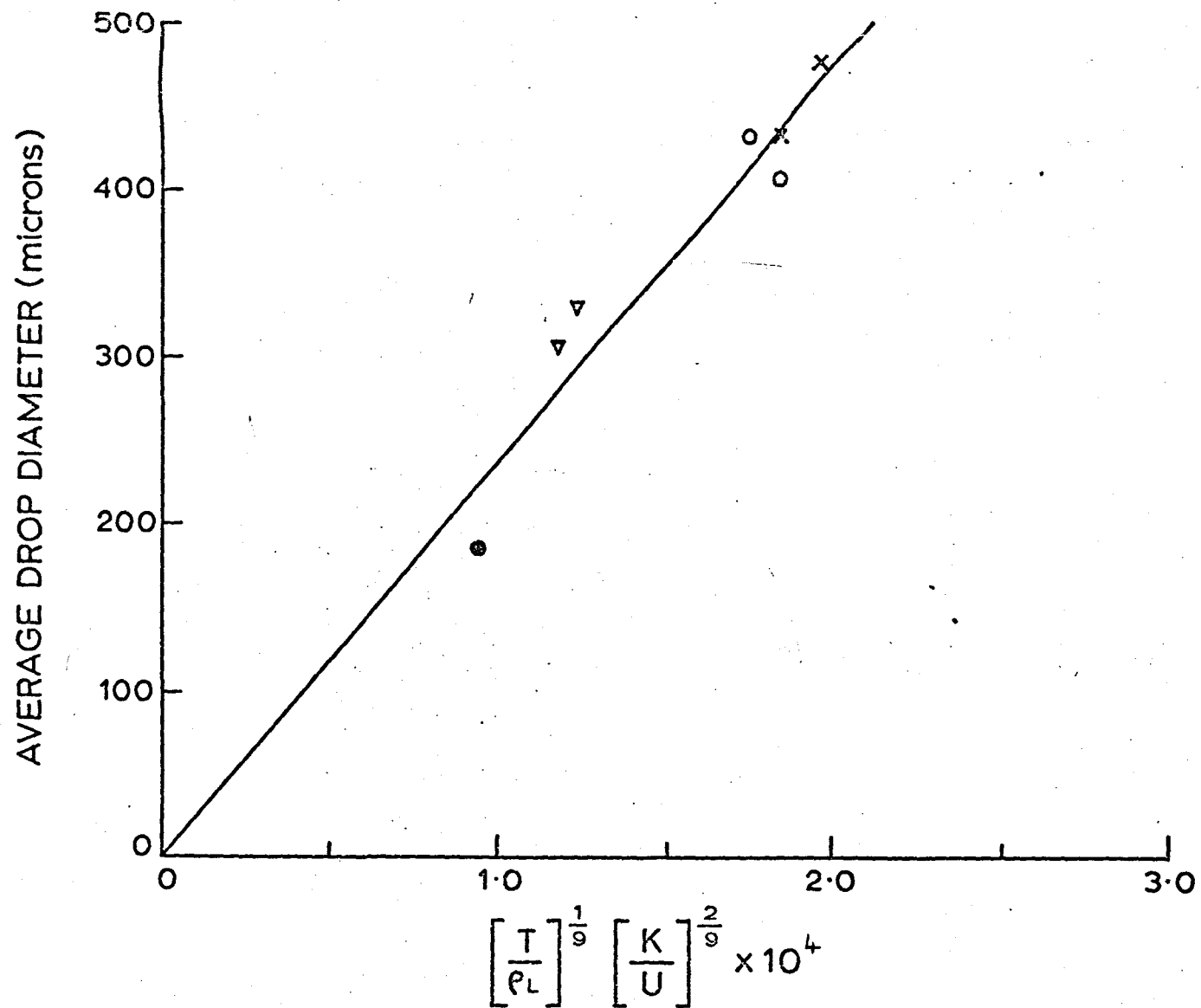
FIG. 4.17   DROP SIZE CORRELATION (FOR LEGEND SEE TABLE 5)

The y-axis is labeled: AVERAGE DROP DIAMETER (microns)

The x-axis is labeled: $\left[\dfrac{T}{\rho_L}\right]^{\frac{1}{9}} \left[\dfrac{K}{U}\right]^{\frac{2}{9}} \times 10^4$

4.5   Sizes of Drops Formed from a Liquid Rim

Some measurements have been made of the main drops produced at
the edges of sheets ejected from the range of Bray miniature fan spray
nozzles listed in Table 2.   It was noticed in some photographs that,
because of initial random disturbances, adjacent waves occasionally
tended to merge (cf. Fig.(2.3)) producing relatively large drops and
these were neglected.   Between 10 and 20 measurements were made for
each set of operating conditions and the arithmetic mean values each
with a scatter of approximately ±11% are listed in Table 9.   The data
have been correlated on the basis of equation (2.39) and the results
shown in Fig.(4.17), where it is seen that the experimental points
fall close to a straight line passing through the origin.

It should be noted that apart from one experiment with Carbon
tetrachloride, all the work was carried out with water and the equation
therefore requires further experimental confirmation.

Chapter 5.   Summary of Conclusions

1. Theoretical and experimental studies have been made of the flow instabilities of liquid sheets under a wide range of conditions.

2. An analysis has been carried out of the trajectory of the rim of a fan spray sheet of liquid and a theoretical relation derived which shows satisfactory agreement with experimental values (c.f. Sections 2.1.1 and 4.4).

3. It is postulated that the subsequent break down of the rim is due to both Rayleigh and Taylor instability, the latter resulting from centrifugal forces generated by a curved trajectory. A semi-empirical relation is developed which satisfactorily correlates the sizes of drops formed from the disintegrating rim with operating conditions for a limited number of experimental data (c.f. Sections 2.1.2 and 4.5).

4. The early stages of aerodynamic wave growth have been analysed for both sinuous and dilational waves using first order perturbation theory, and it has been shown that the velocities of both forms of wave are independent of viscosity and effectively equal to that of the sheet. The viscous damping factor is found to be similar for both types of wave, and, in common with inviscid flow, long sinuous waves grow at a greater rate than dilational waves, whilst short waves grow at an equal rate (c.f. Section 2.2.1).

5. In order to gain insight into the mechanism of aerodynamic wave disintegration a second order analysis has been made of the growth of waves on parallel-sided inviscid liquid sheets. It is shown that the wave profile comprises a basic sinuous mode and a dilational first harmonic. Wave growth is consequently asymmetric and the sheet progressively diminishes in thickness at points equal to $\frac{1}{4}\lambda$ and $\frac{3}{4}\lambda$ of the fundamental mode, where it subsequently breaks down.

6. The results of the above analysis have been applied to attenuating liquid sheets and a relation has been derived which relates the lengths of sheets produced by fan and swirl spray nozzles to the operating conditions (c.f. Section 2.2.2.2).

7. The derived relations show that break-up lengths are a function of the amplitude of the initial disturbance and experiments have suggested that its value is critically dependent upon the nature of the flow within the orifice (c.f. Section 4.3).

8. An experimental study has been made of the stability of liquid sheets in hot combustion gases, and a new form of instability has been discovered in which high frequency capillary waves are superimposed upon the sheet. This has been shown experimentally to be caused by the charging of the sheet by ionised particles present in the gas. The sheet subsequently perforates, giving a larger drop size than is produced in otherwise comparable conditions (c.f. Sections 4.1 and 4.2).

9. Perturbation analysis has been used to study wave stability and characteristics of sheets subjected to electrohydrodynamic instability, but insufficient physical data are available to verify the findings completely (c.f. Section 2.3).

10. An estimation of the charge diffusing to the sheet surface has been obtained by examining the profile of a conical sheet in both the presence and absence of hot gases (c.f. Appendix II).

11. Theoretical analyses of charge transfer using laminar boundary layer theory have been carried out, the results of which predict the value of the equilibrium surface charge to be approximately two orders of magnitude less than that observed. It has been postulated that this discrepancy arises from neglecting turbulent diffusion around the sheet (c.f. Appendix I).

12. A critical appraisal has been made of the commonly used high speed
     photographic techniques for measuring drop size in sprays, and it
     is shown that, because of the periodic nature of drop formation,
     unsteady state conditions may persist near the atomiser which give
     rise to unpredictable errors.   In these circumstances, correct
     size-frequency distributions can be obtained only from the analysis
     of single flash photographs taken of the region of drop formation
     (c.f. Appendix III).

SHEET ORIGIN

$\frac{s}{s}v$

s,u

ξ_0

$v=0$

$u=U_0$
$N_i=N_e=0$

$v=u=0$
$N_i=N_e=N_{r0}$

$N_i=N_e<N_{r0}$

REGION I

REGION II

FREE GAS STREAM
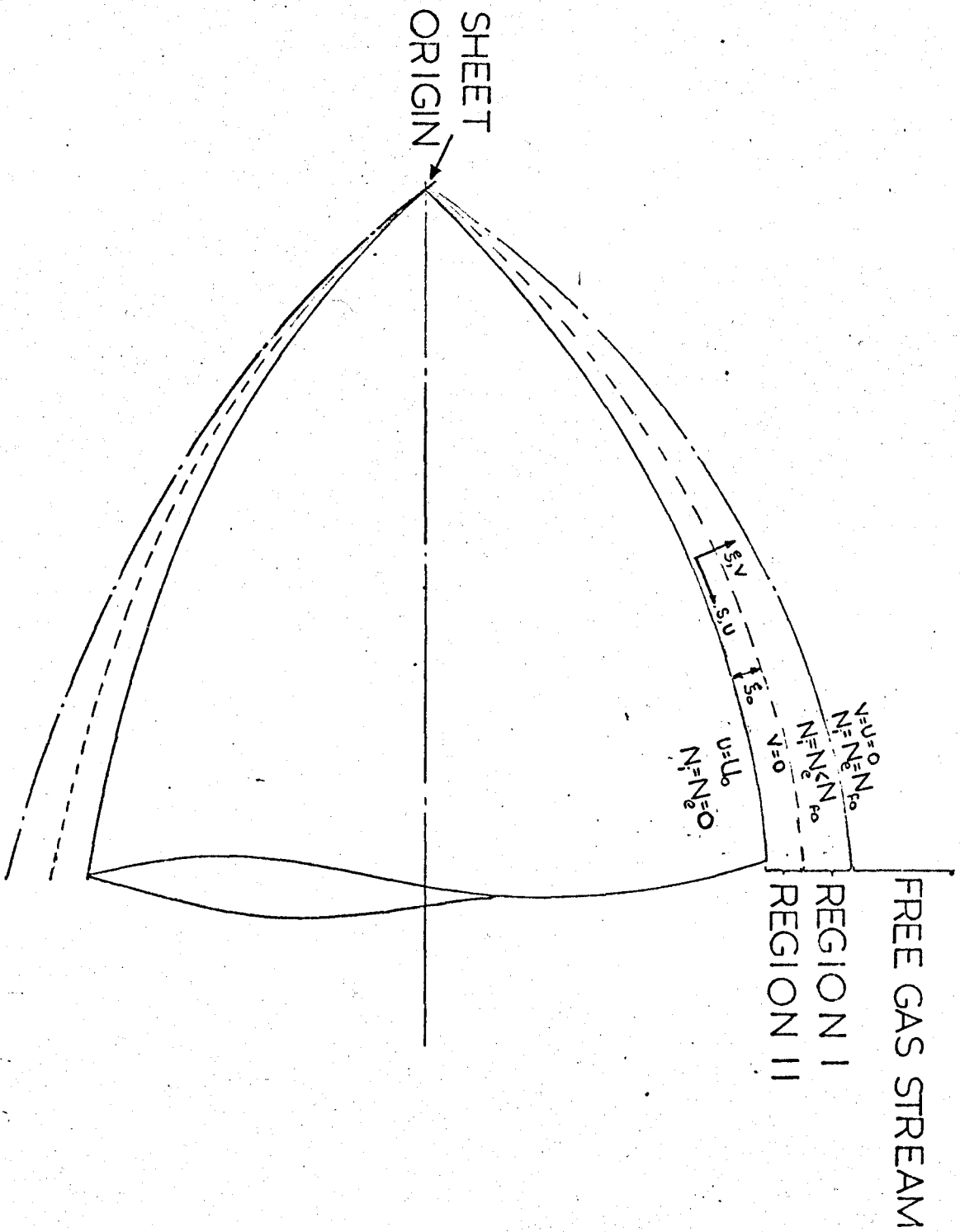
FIG.A1 PICTORIAL REPRESENTATION OF THE ELECTRICAL BOUNDARY
LAYER AROUND A LIQUID SHEET.

Appendix I

The Electrical Characteristics of Laminar Boundary Layers around Liquid

Sheets Flowing in an Ionised Gas

As a liquid sheet flows through an ionised gas, an electrical
boundary layer is developed in which interaction occurs between the
gas and the surface as a result of the transference of charged particles.
In particular, when the charge carriers exhibit a difference in mobility
charge separation occurs giving rise to a field of significant effect,
which for an isolated liquid becomes a maximum at ambipolar diffusion.
Under such conditions, the system is similar to that considered by
Chung . (55) ., who analysed the boundary layer characteristics for
flow past two dimensional and axisymmetric solids. It was found that
for a weakly ionised gas the diffusion boundary layer could be divided
into two regions, as shown in Fig. Al . Region I is electrically
neutral throughout and particle flux results from ambipolar diffusion
which is described oy the classical boundary layer similarity equations.
Region II defines a thin sheath adjacent to the wall of the conductor
in which charge separation occurs effectively in the absence of
convective diffusion.

In Section Al.1 and Al.2 analyses are made of the charged particle
and field strength distributions in Regions I and II respectively for
the case of a conical liquid sheet in which the liquid flows in the
.direction of the meridian.

In Section Al.3 expressions are derived to determine the thickness
of the non-convective sheath.

Al.1   Analysis of the Charged Particle and Field Strength Distributions
       in the Neutral Boundary Layer
       In the analysis the free stream gas is considered to contain only
           ions and electrons and it is assumed that negligible ion-

electron recombination occurs in the boundary layer. For a weakly ionised gas the electrical properties have no effect upon the macroscopic equations of charge transfer, and in general the equations of continuity for ions and electrons throughout both regions become respectively,

$$U_\alpha \frac{\partial N_i}{\partial x_\alpha} + \frac{\partial \Gamma_{i\alpha}}{\partial x_\alpha} = 0 \qquad (A1)$$

$$U_\alpha \frac{\partial N_e}{\partial x_\alpha} + \frac{\partial \Gamma_{e\alpha}}{\partial x_\alpha} = 0 \qquad (A2)$$

where N_i and N_e are the number densities of ions and electrons and $\Gamma_{i\alpha}$ and $\Gamma_{e,\alpha}$ their flux densities, are given by,

$$-\Gamma_{i\alpha} = D_i e \frac{\partial N_i}{\partial x_\alpha} + \frac{N_i D_i e}{K \Theta_i} \frac{\partial \phi_e}{\partial x_\alpha} \qquad (A3)$$

$$-\Gamma_{e\alpha} = D_e e \frac{\partial N_e}{\partial x_\alpha} - \frac{N_e D_e e}{K \Theta_e} \frac{\partial \phi_e}{\partial x_\alpha} \qquad (A4)$$

where ϕ_e, the electrical potential, is determined by,

$$\nabla^2 \phi_e = \frac{-e}{D \epsilon_o} (N_i - N_e) \qquad (A5)$$

and where $N_i = N_e = N_{fo}$ and $\phi_e = 0$ in the free gas stream and $N_i = N_e = 0$ and $\phi_e = \phi_{ew}$ at the surface.

Because of surface tension the profile of a conical sheet is curved (Appendix II). However, the boundary layers will generally be small in comparison to the radius of curvative and the neutral boundary layer approximation of equations (A1 - A5) becomes

$$u \frac{\partial N}{\partial s} + v \frac{\partial N}{\partial \xi} = D_a \frac{\partial^2 N}{\partial \xi^2} \qquad (A6)$$

The equations of motion and continuity may be written as (Meskyn (57))

$$u \frac{\partial u}{\partial s} + v \frac{\partial u}{\partial \xi} = \nu_3 \frac{\partial^2 u}{\partial \xi^2} \qquad (A7)$$

$$y(s)u = \frac{\partial \psi}{\partial \xi} \qquad (A8)$$

$$\text{and} \quad y(s)v = \frac{-\partial \psi}{\partial s} \qquad (A9)$$

where D_a is the ambipolar diffusion coefficient, s and ξ are general orthogonal co-ordinates respectively, measured along and normal to the meridian, and where $y(s)$ is the radius of the surface.

The boundary conditions for equations (A6 to A9) are,

$$u = U_o, \quad v = 0, \quad \text{when} \quad \xi = 0$$

$$u = U_s, \quad v \to 0, \quad N = N_o \quad \text{when} \quad \xi = \xi_o$$

and $\quad u \to 0, \quad N \to N_{fo}$ as $\quad \xi \to \infty$

Equations (A6 to A9) can be reduced to a form which is identical with those for plane flow using Manglers transformation (57).

Letting,

$$x = \int_0^s (y(s))^2 ds, \qquad \eta = \left\{ \frac{U_o}{2 \nu_g x} \right\}^{1/2} \xi \, y(s),$$

$$\Psi = (2 \nu_g U_o x)^{1/2} f(\eta)$$

and $\quad m = \dfrac{N}{N_{fo}} \quad$ gives

$$U = U_o \frac{\partial f}{\partial \eta} \tag{A10}$$

and $\quad V = -U_o \left(\dfrac{\nu_g}{2x \, U_o} \right)^{1/2} y(s) \left\{ f - \eta \dfrac{\partial f}{\partial \eta} \right\} \tag{A11}$

Combining equations (A10), (A11) with their respective differential coefficients, equations (A6), (A7), (A8) and (A9) are transformed into

$$f''' + ff'' = 0 \tag{A12a}$$

and $\quad m'' + Sca \, m'f = 0 \tag{A12b}$

with the corresponding boundary conditions

$$f' = 1, \quad f = 0 \text{ at } \eta = 0$$

$$m = m_o \text{ at } \eta = \eta_o \tag{A12c}$$

and $\quad f' \to 0, \quad m \to 1$ as $\eta \to \infty$

where Sca is the ambipolar Schmidt number defined as $\dfrac{\nu_g}{D_a}$

To solve equation (A4) which defines the velocity distribution, we put,

$$f(\eta) = \eta + \sum_{2}^{\infty} \frac{a_n \eta^n}{n!}$$

where $f(\eta)$ satisfies the boundary conditions at $\eta = 0$. Substituting the expansion into (A12) we find the coefficients a_n in terms of $a_2 = a$, whence,

$$f(\eta) = \eta + \frac{a\eta^2}{!2} - \frac{a\,\eta^4}{!4} - \frac{a^2\eta^5}{!5} + \frac{3a\eta^6}{!6}$$

$$+ \frac{11a^2\eta^7}{24!7} \qquad \text{(A13)}$$

The unknown parameter, a, is found by integrating equation (A12), i.e.

$$-(f^{1}(\infty) - f^{1}(0)) = a \int_{0}^{\infty} \exp - F(\eta)\,d\eta = -1 \qquad \text{(A14)}$$

(A14) is evaluated with the following substitution

$$F(\eta) = \eta^2 \sum_{n=0}^{\infty} C_n \eta^n = \tau \qquad \text{(A15)}$$

and

$$\eta = \sum_{m=0}^{\infty} A_m /(m+1)\,\tau^{\frac{1}{2}(m+1)} \qquad \text{(A16)}$$

where by comparison with (A13)

$$C_o = \tfrac{1}{2}, \; C_1 = a/!3, \; C_2 = 0, \; C_3 = a/!5, \; C_4 = -a^2/!6,$$

$$C_5 = 3a/!7, \; C_6 = 11/24!8\,a^2 \;\ldots\ldots$$

Combining equations (A14) and (A15) we get,

$$a \int_{0}^{\infty} e^{-\tau} \sum_{m=0}^{\infty} \frac{A_m}{2} \tau^{\frac{1}{2}(m-1)} \, d\tau = -1 \qquad \text{(A17)}$$

Integrating (A17) in Gamma functions we obtain

$$\frac{a}{2}\left[A_o \; \Gamma(\tfrac{1}{2}) + A_1 \; \Gamma(1) + A_2 \; \Gamma(3/2) + A_3 \; \Gamma(2) \right. \qquad \text{(A18)}$$

$$\left. + A_4 \; \Gamma(5/2) \;\ldots\ldots\ldots\ldots = -1 \right.$$

To evaluate the coefficients we differentiate (A16) to give,

$$d\eta = \sum_{m=0}^{\infty} \frac{A_m}{2} \tau^{\frac{1}{2}(m-1)} \, d\tau$$

when it follows that,

$$\int^{0+} \frac{d\eta}{\tau^{\frac{1}{2}(m+1)}} = \frac{A_m}{2} \int^{0+,0+} \frac{d\tau}{\tau} = 2\pi i \, A_m \qquad (A19)$$

where o+ denotes a circuit in the positive direction around the zero point, the single circuit around $\eta = 0$ corresponds to a double circuit round $\tau = 0$ in the plane. This integration path is necessary to dispose of the fractional powers of τ. It follows, therefore, from (A19) that A_m is the coefficient of η^{-1} in the expansion of $\tau^{-\frac{1}{2}(m+1)}$ in ascending powers of η.

Now from (A15)

$$\tau^{-\frac{1}{2}(m+1)} = \eta^{-(m+1)} (c_0 + c_1 \eta + c_2 \eta^2 \ldots\ldots)^{-\frac{1}{2}(m+1)} \qquad (A20)$$

Expanding (A20) by the binomial expansion we find,

$$A_0 = c_0^{-\frac{1}{2}} \quad , \quad A_1 = -c_1 c_0^{-2} \quad , \quad A_2 = c_1^2 c_0^{-7/2} \frac{15}{4}$$

$$A_3 = -c_0^{-5}(2c_0^2 c_3 + 4c_1^3) \quad ,$$

$$A_4 = c_0^{-13/2}(-5/2 c_0^3 c_4 + \frac{35}{4} c_0^2 c_3 c_1 + \frac{5.7.9.11 c_1^4}{16!4})$$

$$A_5 = c_0^{-8}(-3c_5 c_0^4 + 12 c_0^3 c_1 c_4 - \frac{3.3.4.5.}{!3} c_0^2 c_1^2 c_3$$
$$\quad \frac{3.4.5.6.7}{!5} c_1^5)$$

The value of the parameter, a, can now be found by substituting for the coefficients A_m in equation (A18) and then determining the roots of the generated power series by successive approximation. The series converges rapidly for a < 1 and, truncating after the first four terms, gives a value of a equal to -0.625. This agrees well with the

exact value of -0.627 obtained by Howarth (58) who obtained a numerical solution of equation (A12).

Equation (A26) which defines the charged particle distribution may be solved to give,

$$\frac{m - m_o}{1 - m_o} = \frac{\int_{\eta_o}^{\eta} \exp(-F)\,d\eta}{\int_{\eta_o}^{\infty} \exp(-F)\,d\eta} \qquad (A21)$$

where $F = Sca \int_{\eta_o}^{\eta} f\,d\eta$

From (A12) $f = \dfrac{-f'''}{f''}$ and equation (A21) may be written more simply as,

$$\frac{m - m_o}{1 - m_c} = \frac{\int_{\eta_o}^{\eta} |f''|^{Sca}\,d\eta}{\int_{\eta_o}^{\infty} |f''|^{Sca}\,d\eta} \qquad (A22)$$

The denominator on the R.H.S. equation (A22) may be written as,

$$\int_{\eta_o}^{\infty} f''^{Sca}\,d\eta = \int_{0}^{\infty} |f''|^{Sca}\,d\eta - \int_{0}^{\eta_o} |f''|^{Sca}\,d\eta \qquad (A23)$$

The first term on the R.H.S. of equation (A23) is solved using equations (A17) and (A18) to give,

$$\int_{0}^{\infty} |f''|^{Sca}\,d\eta = \frac{1}{2}\left[\frac{A_o\,\Gamma(\frac{1}{2})}{Sca^{\frac{1}{2}}} + \frac{A_1\,\Gamma(1)}{Sca} + \frac{A_2\,\Gamma(\frac{3}{2})}{Sca^{3/2}} \dots\dots \right. \qquad (A24)$$

The last term may be integrated by the mean value theorem to give,

$$\int_{0}^{\eta_o} |f''|^{Sca}\,d\eta = \eta_o |f''_m|^{Sca} \qquad (A25)$$

where f''_m denotes the mean value of f'' in the range $0 \leqslant \eta \leqslant \eta_c$.

Examination of equation (A13) shows that for $\eta \ll 1$, f'' is approximately constant and we may therefore put $f''_m = f''(o) = a$.

Thus, after substituting for the values of A_m, found above, in equation (A24) and combining with equation (A25), equation (A23) becomes,

$$\int_{\eta_o}^{\infty} |f''|^{Sca} \, d\eta = |a|^{Sca} \left[\left[1.26 \, Sca^{-\frac{1}{2}} + 0.209 \, Sca^{-1} + 0.206 \right. \right.$$
$$\left. Sca^{-3/2} - 0.114 \, Sca^{-2} + 0.028 \, Sca^{-5/2} \right.$$
$$\left. \left. -0.002 \, Sca^{-3} \ldots \right] - \eta_o \right] \quad (A26)$$

A1.2 Analysis of the Normal Charged Particle and Field Strength
      Distributions in a Non-convective Sheath

Omitting convective terms from equations (A1) and (A2) and considering transport only in the direction normal to the interface we get,

$$e \, D_i \left(\frac{dN_i}{d\xi} + \frac{N_i}{k\theta_i} \frac{d\phi_e}{d\xi} \right) = I_i \quad (A27)$$

and

$$e \, D_e \left(\frac{dN_e}{d\xi} - \frac{N_e}{k\theta_e} \frac{d\phi_e}{d\xi} \right) = I_e \quad (A28)$$

where I_i and I_e are constants of integration and denote respectively ion and electron currents which are identical ($I_i = I_e = I$) for ambipolar diffusion.

Equation (A5) is then,

$$\frac{d^2\phi_e}{d\xi^2} = \frac{-e}{D\epsilon_o} (N_i - N_e) \quad (A29a)$$

Introducing the dimensionless variables,

$$R = -\frac{e\phi_e}{k\theta_e} \quad , \quad t = \frac{\xi}{\xi_o} \quad , \quad n_i = \frac{N_i}{N_o} \quad , \quad n_e = \frac{N_e}{N_o} \quad (A29b)$$

$$x = \frac{\theta_i}{\theta_e} \quad , \quad J_i = \frac{I\xi_o}{eN_o D_i} \quad , \quad J_e = \frac{I\xi_o}{eN_o D_e} \quad \text{and}$$

$$h_e^2 = \frac{k\theta_e D\epsilon_o}{N_c e^2}$$

where ξ_o denotes the thickness of the sheath, equations (A27), (A28) and (A29) reduce to the form,

$$\varkappa \frac{dn_i}{dt} - n_i \frac{dR}{dt} = \varkappa J_i \tag{A30}$$

$$\frac{dn_e}{dt} + n_e \frac{dR}{dt} = J_e \tag{A31}$$

and

$$\frac{1}{p^2} \frac{d^2 R}{dt^2} = n_i - n_e \tag{A32}$$

where $p^2 = h_e^2 / \xi_o^2$

with the transformed boundary conditions

$$R_{(o)} = R_w \text{ and } R_{(1)} = 0$$

$$n_{i(o)} = n_{e(o)} \text{ and } n_{i(1)} = n_{e(1)} = 1$$

Replacing $-\frac{dR}{dt}$ in equations (A30), (A31) and (A35) by G and eliminating n_i and n_e, a differential equation describing the dimensionless field strength is obtained viz.

$$\frac{1}{p^2} \left[\frac{G^{II}}{G} \right]^I - \frac{GG^I}{p^2 \varkappa} + \frac{G^{II}}{p^2} \left[\frac{1}{\varkappa} - 1 \right] = \left[J_i + \frac{J_e}{\varkappa} \right] + \frac{G^I}{G} (J_i - J_e)$$

Integration gives

$$\frac{G^{II}}{p^2} - \frac{G^3}{2p^2 \varkappa} + \frac{G^I G}{p^2} \left[\frac{1}{\varkappa} - 1 \right] = \left[J_i + \frac{J_e}{\varkappa} \right] Gt - (J_i - J_e) + GC_1 \tag{A33}$$

where C_1 is a constant of integration.

The four boundary conditions required to solve equation (A33) can be found using equations (A30), (A31) and (A32) together with the conditions imposed upon the charged particle densities at $t = 0$ and $t = 1$.

i.e. $G^I = 0$ and $G^{II} = -p^2 (J_i - J_e)$ at $t = 0$

and $G^I = C$ and $G^{II} = -p^2 \left[G(1 + \frac{1}{\varkappa}) + (J_i - J_e) \right]$ at $t = 1$

We are, however, only interested in solutions of equation (A33) for which G is small and $n_i \simeq n_e$ in the neighbourhood of $t = 1$. Examination of equation (A33) shows that for large p^2 it tends to the asyptotic form

$$G = \frac{J_i - J_e}{t(J_i + J_e/x) + C_1} \qquad \text{as } t \to 1$$

Invoking the boundary conditions $n_{e(1)} = n_{i(1)} = 1$ equations (A30) and (A31) give $G = x \frac{(J_i - J_e)}{1 + x}$ at $t = 1$ and hence,

$$C_1 = 1 + \frac{1}{x} - (J_i + \frac{J_e}{x})$$

The boundary conditions for equation (A33) when p^2 is large may therefore be written

$$G^I = 0 \text{ and } G^{II} = -p^2 (J_i - J_e) \text{ at } t = 0$$

$$\text{and} \qquad G \longrightarrow \frac{xJ_i - J_e}{(xJ_i + J_e)(t - ts)} \qquad \text{as } t \to 1 \qquad (A34)$$

$$\text{where} \quad ts = \frac{xJ_i + J_e - 1 + x}{(xJ_i + J_e)}$$

The self consistency of equation (A34) in the neighbourhood of $t = 1$ may be examined by using it to evaluate the order of the neglected terms. It can be shown by this method that the errors involved are $< O(p^{-2/3})$. Thus, for $p^2 = 10^3$ the error is in the order of less than 10%.

Introducing the scaling variables

$$s = p^{2/3} \left[-(J_i + \frac{J_e}{x}) \right]^{1/3} \left[ts - t \right] \qquad (A35)$$

$$\text{and} \qquad G = p^{2/3} \left[-(J_i + \frac{J_e}{x}) \right]^{1/3} F \qquad (A36)$$

equation (A33) reduces to the form,

$$-\frac{F''}{F} + \frac{F^2}{2x} + F' (\frac{1}{x} - 1) = -s - \frac{\lambda}{F} \qquad (A37)$$

Table 6

Summary of Cohen's Numerical Results

s_w	λ	$\frac{1}{x}$	s_w	λ	$\frac{1}{x}$
-3.334	0.9990	1.00	-6.263	0.990	5.00
-2.364	0.9900	"	-4.599	0.9900	"
-2.000	0.9785	"	-2.495	0.9000	"
-1.176	0.9000	"	-1.245	0.7000	"
-0.521	0.7000	"	-0.627	0.5000	"
-0.500	0.6890	"			
-0.232	0.5000	"			
-4.456	0.9990	2.00	-7.987	0.9990	10.00
-3.228	0.9900	"	-5.888	0.9900	"
-1.690	0.9000	"	-3.233	0.9000	"
-0.798	0.7000	"	-1.646	0.7000	"
-0.376	0.5000	"	-0.855	0.5000	"
-0.135	0.3000	"	-0.356	0.3000	"

where $\lambda = \dfrac{\ast(J_i - J_e)}{(\ast J_i + J_e)}$

with the boundary conditions

$$F_w^2 = -2 s_w \ast \ , \quad F' = 0 \text{ and } F'' = \qquad \text{at } s = s_w (t = 0) \qquad (A38)$$

$$F \longrightarrow -\frac{\lambda}{s} \qquad\qquad\qquad\qquad \text{as } s \rightarrow s_o (t = 1) \qquad (A39)$$

Equations (A37) to (A39) are of an identical form to those obtained for spherical electrostatic probes by Cohen (56) who solved them numerically by initially choosing a point (F_w, s_w) at the conductor surface and adjusting the value of λ until the integral curve was found which satisfied relation (A39).

Cohen's values of s_w and λ have been used to provide values of G_w and J_i in equation (A33) for a range of J_i/J_e, $\ast$ and p^2 using equations (A35) and (A36) re-written in the following form,

$$-J_i = (1 + \lambda/\ast)(1 - \frac{\ast(-J_i)}{\ast + \lambda}^{2/3} \frac{s_w \ast^{1/3}}{((1 + \ast)p^2)^{1/3}}) \qquad (A40)$$

$$-J_e = (1 - \lambda)(1 - \frac{\ast(-J_i)}{\ast + \lambda}^{2/3} \frac{s_w \ast^{1/3}}{((1 + \ast)p^2)^{1/3}}) \qquad (A41)$$

and $G_w = p^{2/3} F_w \left[-(J_i + \frac{J_e}{\ast}) \right]^{1/3}$ \qquad (A42)

A summary of Cohen's numerical results is shown in Table 6.

A1.3 The Thickness of the Non-convective Sheath

The three parameters p^2, η_o and m_o (cf equations (A32) and (A12c)) define the thickness of the non-convective sheath, and are evaluated by matching the electric field strengths (E), the charge particle densities (N) and the fluxes (I), in each region at the common boundary.

For ambipolar diffusion the equations of continuity for ions and electrons (cf. equations (A1) and (A2)) at the common boundary of region become, neglecting convection effects,

$$D_i \, e \, \frac{dN}{d\xi}\Big|_{\xi=\xi_0} - \frac{D_i \, e \, E N_o}{k \, \theta_i} = I_a \qquad (A43)$$

and

$$D_e \, e \, \frac{dN}{d\xi}\Big|_{\xi=\xi_0} + \frac{D_e \, e \, E N_o}{k \, \theta_e} = I_a \qquad (A44)$$

Eliminating $\frac{dN}{d\xi}\Big|_{\xi=\xi_0}$ between (A42) and (A43) gives,

$$\frac{I_a}{D_i} \left(1 - \frac{D_i}{D_e}\right) = \frac{e N_o E}{k \, \theta_e} \left(\frac{1}{*} + 1\right) \qquad (A45)$$

Equation (A45) is recognised as being identical in form to equation (A38) which defines the field strength in the non-convective sheath for $t \rightarrow 1$ and large values of p^2.

Continuity of the charged particle fluxes requires that the dimensionless variable J_1 is matched at the boundary and since,

$$m_o = \frac{N_o}{N f_o}$$

is the value at the boundary of the dimensionless variable, m, defined above, elimination of E between equations (A43) and (A44) gives

$$(1 + *) \, m'_o = \frac{J_i \, m_o}{\xi_o} \left(1 + \frac{D_i}{D_e}\right) \qquad (A46)$$

m'_o is obtained by differentiating equation (A21), and evaluating the dimensionless variable η at the boundary we get,

$$(1 + *)(1 - m_o) \, \eta_o \, \frac{|f''|^{Sca}}{\int_{\eta_o}^{\infty} |f''|^{Sca} \, d\eta} = J_i \, m_o * \left(1 + \frac{D_i}{D_e}\right) \qquad (A47)$$
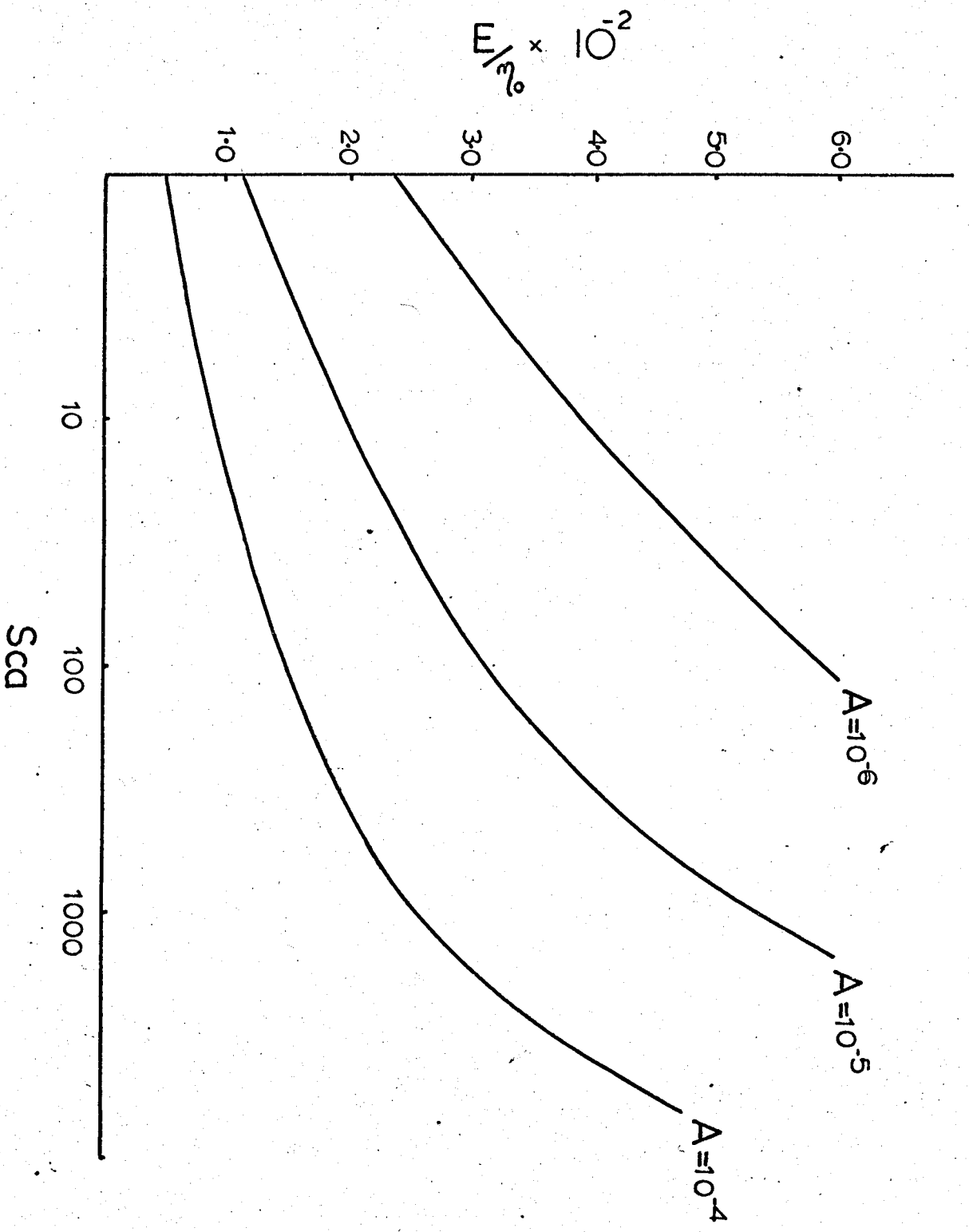
FIG.A.2 VARIATION OF 'E/η_0' WITH 'Sca' AND 'A'

Re-arranging (A47) and substituting for m_o from (A46) gives a corresponding relation solely in terms of η_o, i.e.

$$\left(\frac{\eta_o^2}{A p^2} - 1\right) \eta_o \frac{|f''|^{Sca}}{\int_{\eta_o} |f''|^{Sca}} = J_i \frac{\varkappa}{1 + \varkappa} \left(1 + \frac{D_i}{D_e}\right) \tag{A48}$$

where $A = \left[\dfrac{U_o}{2\nu_e} y(s)^2 \dfrac{\theta_e D \epsilon_o K}{\int_o^s (y(s))^2 ds\, e^2 Nf}\right]$

Equations (A47) and (A48) have been solved by an iterative procedure which satisfied simultaneously the conditions of. $p^2 \geqslant 10^3$ and $\frac{\partial f}{\partial \eta}$ (cf. equation (A13), which represents a measure of convection, > 0.8.

The dimensionless interfacial field strength G_w/η_o has then been calculated from equations (A42), (A47) and (A48). Some typical results are presented in Fig.(A2) as a function of the Schmidt number for $\varkappa = 1$, $J_i/J_e = 10^3$ and values of A equal to 10^{-6}, 10^{-5} and 10^{-4}. The latter value of A corresponds to the limiting values of p^2 and $\frac{\partial f}{\partial \eta}$ of 10^{-3}, 0.8 respectively. It is seen that the value of G_w/η_o progressively increases with Schmidt number. Beyond a value of about 10^2 equations reduce to a simple form in which $1/\eta_o$ is proportional to $Sca^{1/2}$. Under these conditions the interfacial field strength is most sensitive to variations in ambipolar Schmidt number.
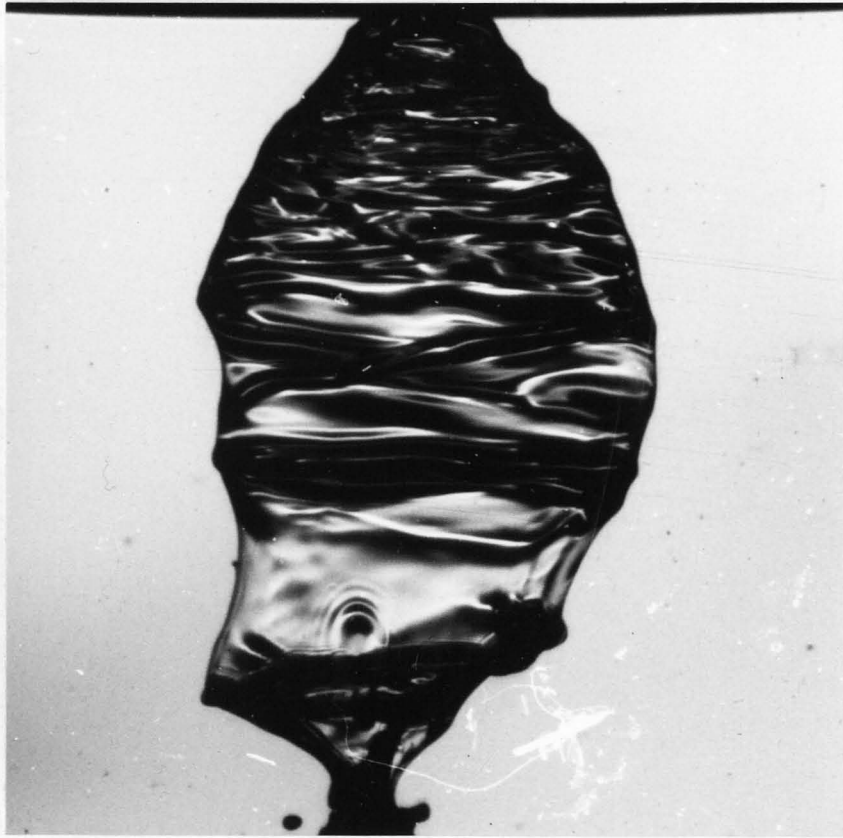
(a) Ambient gas temperature 20°C
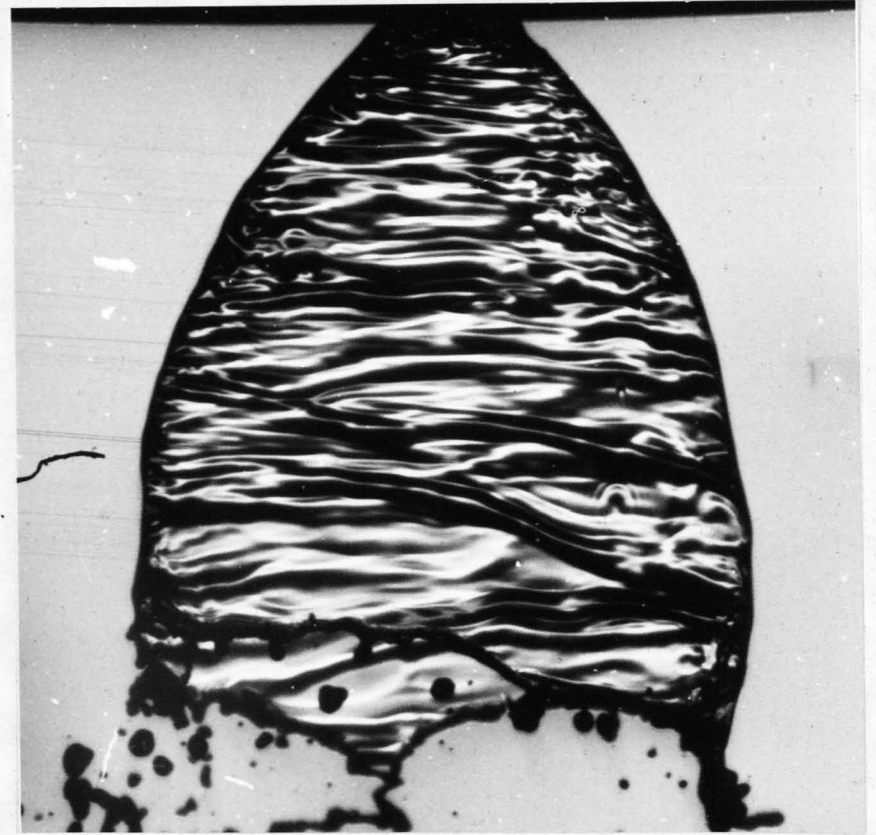
(b) Ambient gas temperature 940°C

Magnification   : x 16

Nozzle   : Danfoss D8./45

Differential Injection Pressure : 0.69 bar (10psig)

Fig. A.3   Typical Photographs of Conical Water Spray Sheets showing the change in profile when injected into a Hot Ionised Gas.
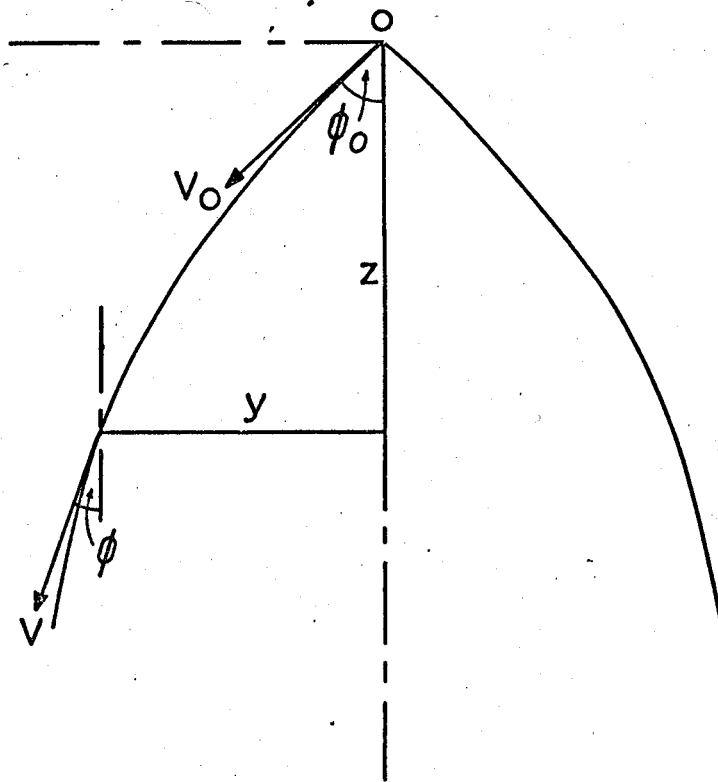
FIG. A4   PROFILE OF CONICAL SHEET

APPENDIX II

Estimation of the Field Strength at the Surface of a Liquid Sheet

in an Ionised Gas

As a result of surface tension a conical sheet initially

emerging into the atmosphere as a plane cone rapidly assumes a

curved profile.   When the sheet is injected into an ionised gas

the surface becomes charged by diffusion and, as a result of the

generated electrical stress, the sheet curvature becomes less con-

vex.   This is clearly demonstrated in Fig.(A3) which shows photo-

graphs of conical water sheets produced from nozzles at constant

injection velocity with the left hand one, (a), being formed at room

temperature, whilst the right hand one, (b), is formed in a hot ionised

gas.

It has been shown by Wolfsohn (54) that the profile of the

meridian section of a conical sheet produced under atmospheric

conditions, i.e. for the case of zero normal stress, is accurately

given by utilizing the equations derived by Taylor (59) for the

trajectory of a water bell.   In this section the equations are

solved for the more general case of an imposed stress normal to the

sheet.   The electrical stress is then calculated by matching the

observed and calculated profiles.

The model considered by Taylor, Fig.(A4), comprises an

inviscid liquid sheet projected in the form of a thin walled cone of

angle $2\phi_o$, with the x axis lying along the centre line.

Neglecting gravity, a momentum balance perpendicular to the

surface gives,

$$\frac{2T}{r_c} + \frac{2T \cos\phi}{y} - p - \frac{u^2 \rho_1 h}{r_c} = 0 \tag{A49}$$

where ϕ is the slope of the surface to the x axis, r_c the radius of

curvature of the meridian section and p is a normal imposed stress taken as the electrical stress, F, in the present case.

The equation of continuity is,

$$2 \pi y U_o h = Q \qquad (A50)$$

where Q is the volume of fluid projected per second. Equations (A49) and (A50) can be expressed in non-dimensional form as

$$- (1 - \frac{1}{Y}) \frac{d\phi}{dY} \sin\phi + \frac{\cos\phi}{Y} - \alpha = 0 \qquad (A51)$$

where $\alpha = \dfrac{U_o Q F}{8 \pi T^2}$

by setting,

$$\frac{R_c}{r_c} = \frac{X}{x} = \frac{Y}{y} = \frac{4 \pi T}{\mu Q U_o} = \frac{1}{R}$$

Equation (A51) can be integrated to give

$$(1 - Y) \cos\phi = C - \frac{\alpha Y^2}{2} \qquad (A52)$$

where C is a constant of integration which satisfies the condition $\phi = \phi_o$ when $Y = 0$.

Hence $(1 - Y) \cos\phi = \cos\phi_o - \frac{\alpha Y^2}{2}$

Since $\frac{dY}{dX} = \tan\phi$ equation (A52) gives

$$X = \int_0^Y \frac{\left\{ \dfrac{(\cos\phi_o - \frac{\alpha Y^2}{2})}{1 - Y} \right\}}{\left\{ 1 - \dfrac{(\cos\phi_o - \frac{\alpha Y^2}{2})}{1 - Y} \right\}^{1/2}} \, dY \qquad (A53)$$

In Section 2.3 the profile is required in terms of s, the arc length of a meridian section. This is obtained by expressing s in the non-dimensional form $S = \dfrac{s . 4 \pi T}{U_o Q}$

Thus, $\frac{dY}{dS} = \sin\phi$ and hence,

* From equation (2.140) $F = \epsilon_o^c E^2$
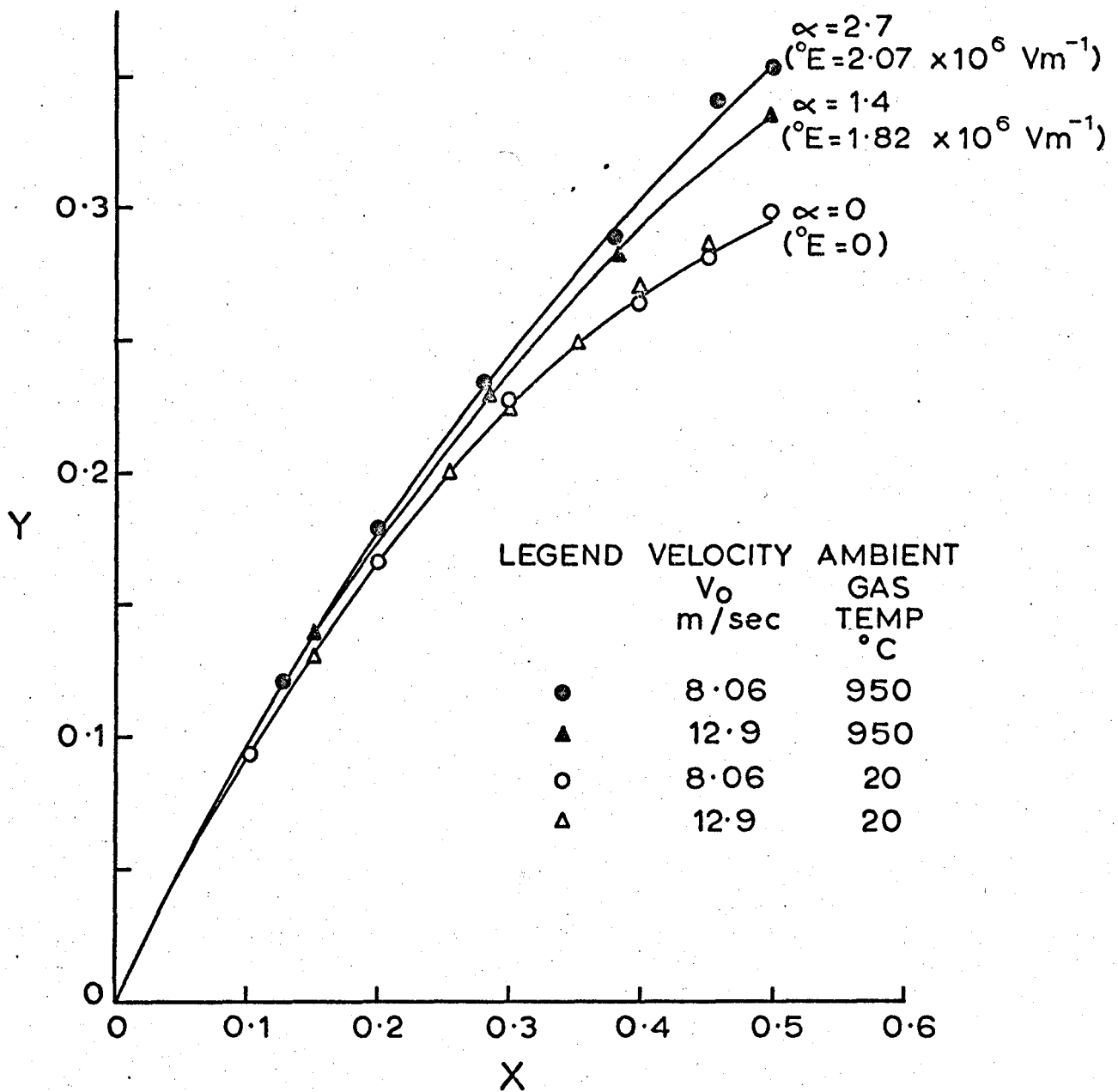
FIG.A.5 CALCULATED PROFILES OF CONICAL WATER SHEETS
WITH A DIFFERENCE IN NORMAL STRESS ACROSS
THE SURFACE (DANFOSS D8.45 NOZZLE)

$$\frac{dY}{dS} = \left\{1 - \frac{(\cos \phi_o - \frac{\propto Y^2}{2})}{1 - Y}\right\}^{1/2}$$

giving S explicitly as

$$S = \int_0^Y \frac{dY}{\left\{1 - \frac{(\cos \phi_o - \frac{\propto Y^2}{2})}{1 - Y}\right\}^{1/2}} \tag{A54}$$

Equation (A53) has been solved for a range of values of ϕ_o and $\propto$ by numerical computation based upon an R.K.M. procedure, and values of   selected to match the experimental and calculated profiles.   The results of calculations for two ejection velocities* are shown in Fig.(A5) together with the calculated values of the field strength $\overset{o}{E}$.   They demonstrate that the field strength is sensibly independent of sheet velocity and hence suggests that equilibrium is rapidly achieved.

*The velocities have been determined from the profiles of sheets emerging at room temperature, i.e. ($\propto$ = 0) by projecting images of the sheets on an X - Y plot and adjusting the magnification until the curves superimposed.   The value of the parameter $\frac{4\pi T}{U_o Q}$ is then given by the ratio of the image and abscissa magnifications.
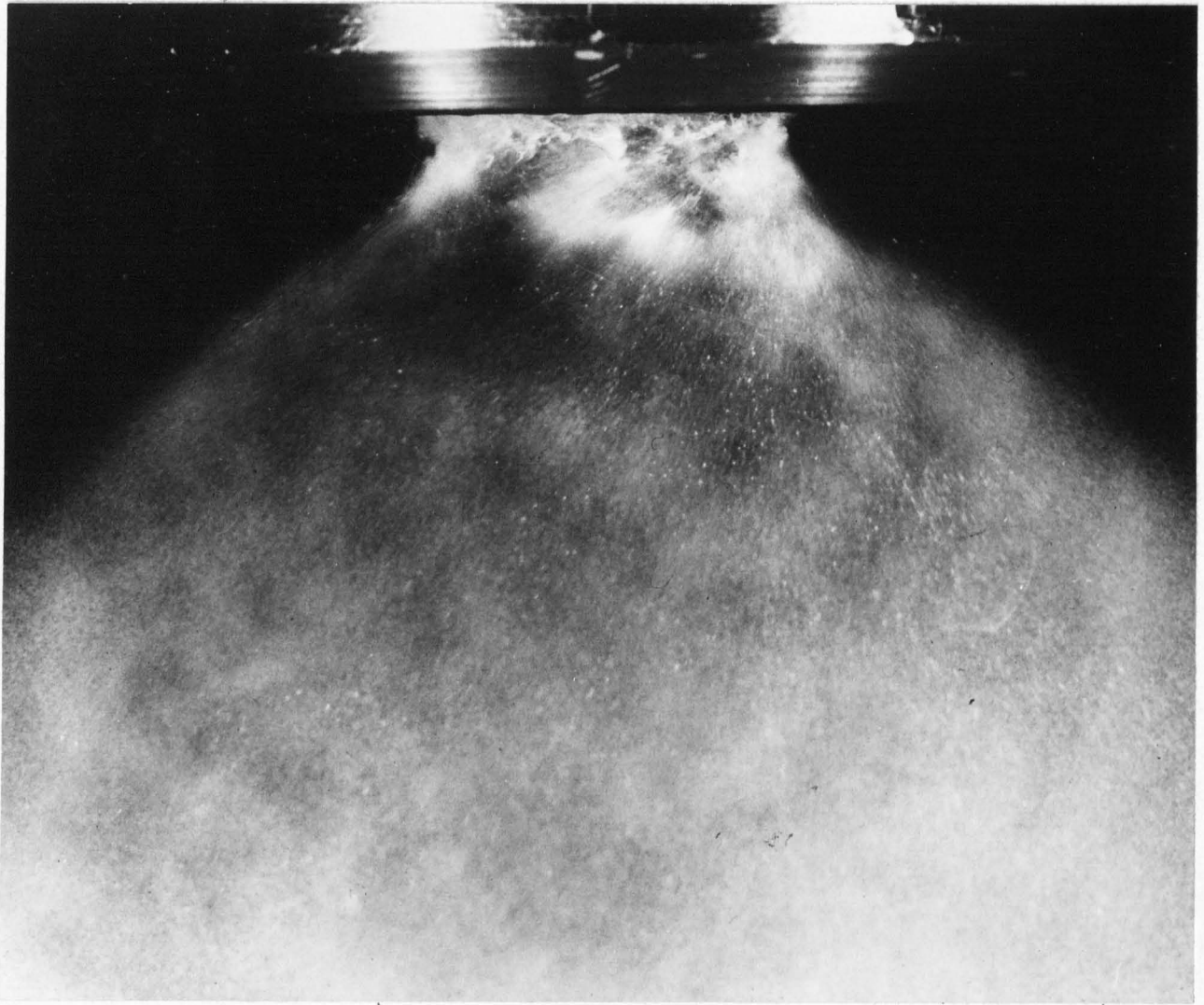
Fig.A7.   Formation of Drops from a Conical Sheet in a
High Velocity Air Stream
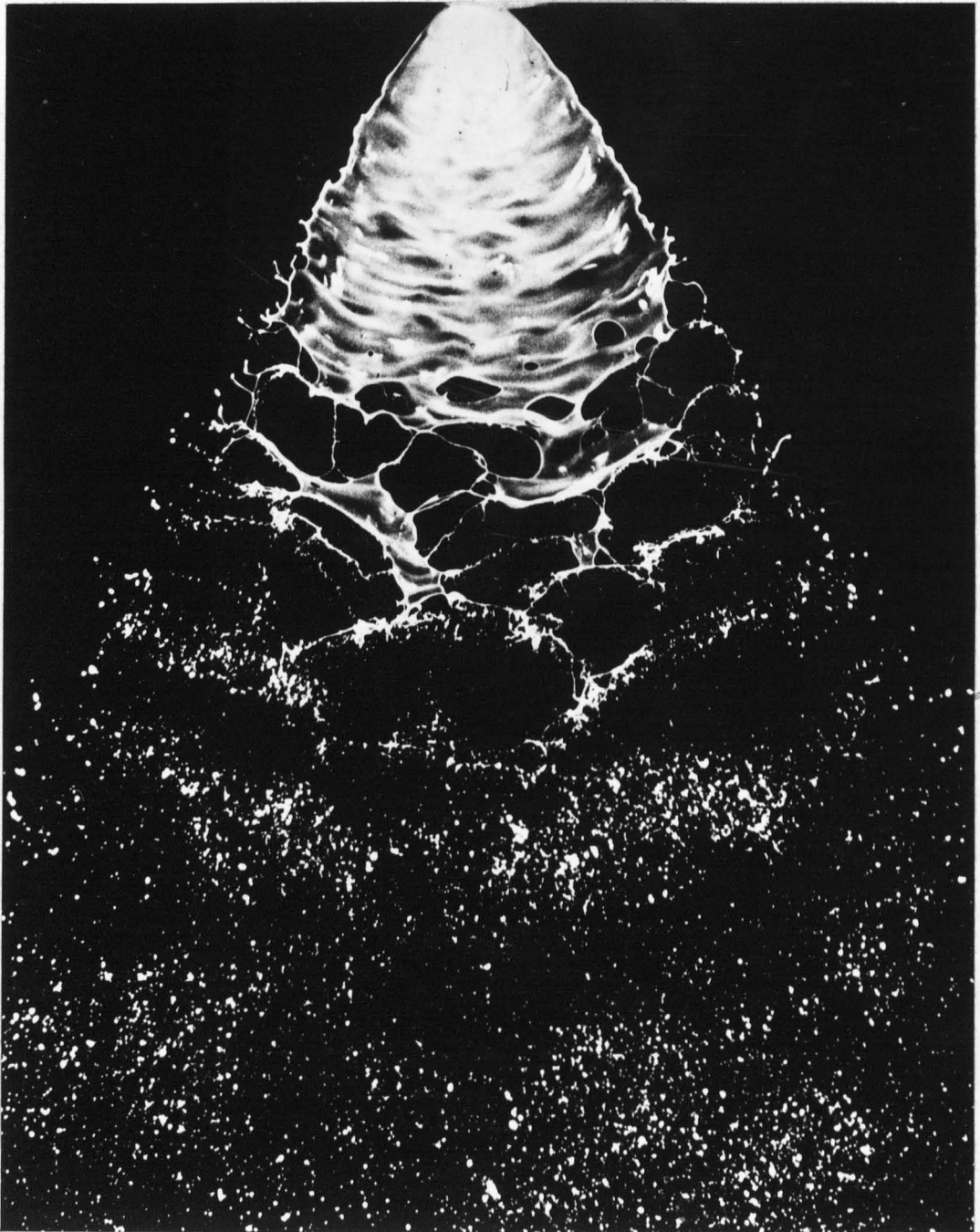
Fig.A6.   Formation of Drops from a Flat Sheet

Appendix III

Photographic Analysis of Sprays

Introduction

High speed photography affords a convenient means of assessing the drop-size distribution of a spray and has been widely used. The technique usually consists of taking double-exposure photographs to determine drop velocities and then weighting the number of drops found in each size range. This procedure is adopted, since drag creates a relative velocity between drops of different sizes, and the spatial distribution, as recorded by a single exposure, may be considerably different from that actually produced. The 'weighted' distribution is generally accepted as giving good correspondence (see for example ref. 60)), but it does not however seem to be realised that this implicitly assumes the drops to be moving in a continuous stream. In fact, the processes of drop formation usually occur in a periodic manner. This is demonstrated in figures(A6) and(A7), which show respectively examples of a flat sheet breaking down by aerodynamic wave motion in a quiescent atmosphere and a conical sheet of liquid atomised by a high velocity air stream. In each of these cases the spatial distribution, as represented by the first discrete band of drops, will clearly be identical to the temporal distribution of the spray, and it would thus be incorrect to 'weight' the drops even though they may be travelling at different speeds. It also follows that similar 'corrections' carried out further downstream where bands start to merge will also involve errors and a 'true' distribution will only be obtained where the drops are moving at their terminal velocities.

---

* The term "temporal distribution" is usually employed in the literature as a synonym for a weighted drop-size distribution. However, the former really describes the frequencies by which drops of various size ranges traverse a plane normal to the direction of flow. It is not possible to

a) NO DRAG

site of drop formation

sheet

liquid fragment

b) DRAG

sheet

DIRECTION OF DROP PROPAGATION
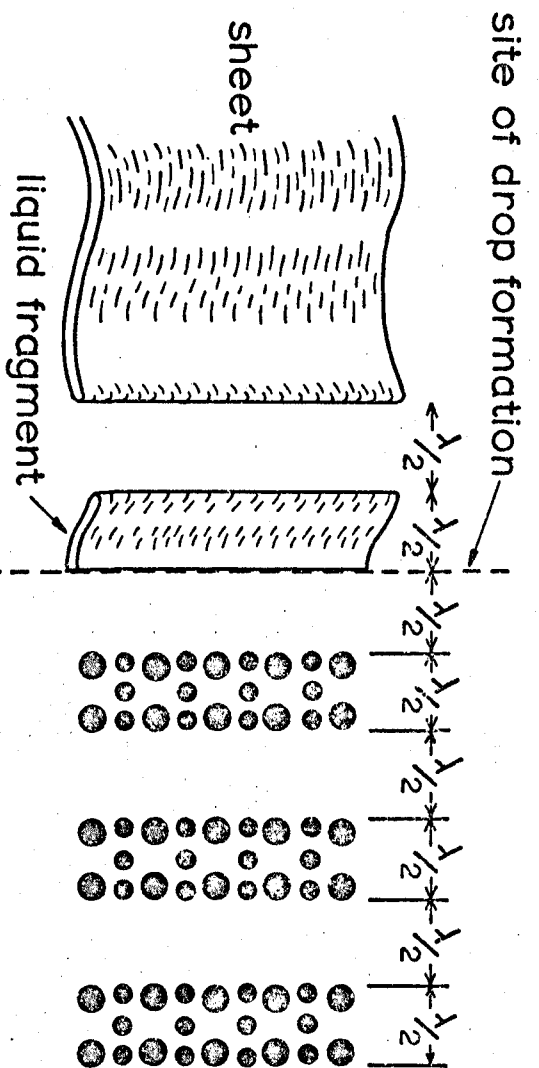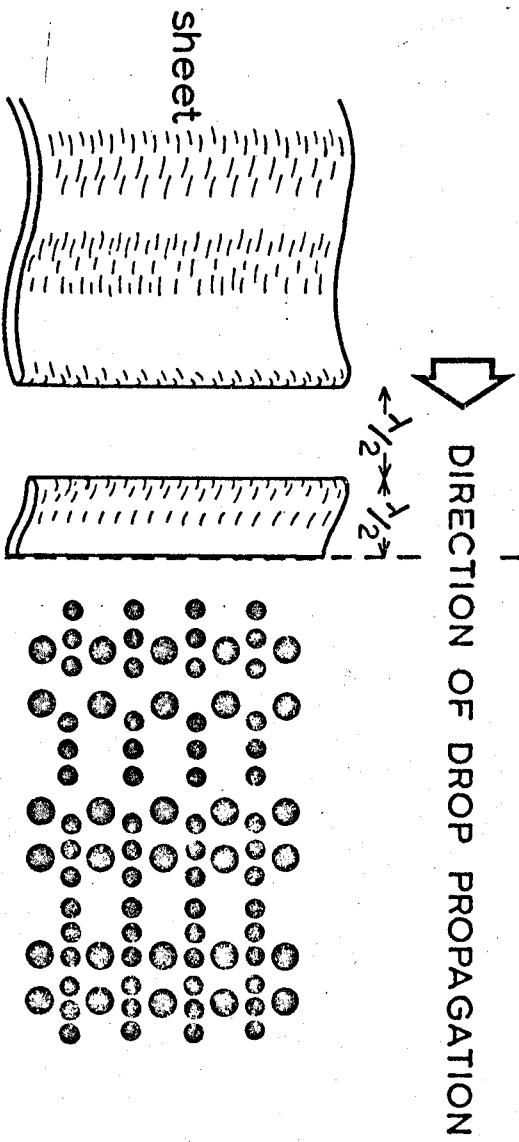
FIG.A8   PICTORIAL REPRESENTATION OF THE EFFECT OF DRAG ON SPRAY
DISTRIBUTION GENERATED BY PERIODIC SHEET BREAK-UP

Theoretical Considerations

A rigorous theoretical analysis of the relation between 'true' and 'weighted' drop-size distributions is not at present possible since it requires a knowledge of both the initial drop-size and velocity spectra. Drop formation is a complex process and occurs randomly from the free edges of fragments of liquid which are simultaneously being torn from the main stream in an irregular manner. When atomisation is complete, drops of all sizes will have been subjected to drag for different periods of time and their velocity will thus be unknown. Nevertheless, some appreciation of the effect of periodic disintegration on the likely errors which may arise by conventional 'weighting' can be adduced from the following simple model, where it is assumed that fragments are detached at regular intervals and subsequent drop formation occurs only at a fixed distance from the nozzle. It is further assumed that for a given drop size, the number of drops generated per unit area is constant, and that all drops are projected downstream with the same initial velocity. A pictorial representation of the spray pattern which would be observed as a result of this idealized process, both in the absence and the presence of drag, is shown for two drop sizes in Figs A8a and A8b respectively. In the absence of drag, drops are propagated downstream as a series of equispaced bands of constant width in which the concentration of drops is uniform. In the presence of drag, however,

---

derive this information from a double-flash photograph since there are insufficient image-pairs passing through any one plane. The size distributions which are obtained from these photographs are determined by weighting drops which extend over a relatively large area and they should be more accurately designated as 'weighted' or 'quasi-temporal' distributions.

drops immediately decelerate after formation with a consequent distortion
of the regular spray pattern.   The bands are preserved for each drop
size but become narrower and closer together to an extent which is
dependent in their decelerations, and as a result the bands merge with
a consequent loss of identity.   In order to describe this analytically
we shall first write the appropriate Fourier series for the square wave
spray pattern shown in Fig.A8a, noting that the length of a detached
fragment is equal to the distance between successive ones.
Thus

$$\frac{dN_j}{dx} = \frac{N_{jo}k}{2\pi} \left[1 + \frac{4}{\pi} \left[\sum_{m=0}^{\infty} \frac{\sin\ (k(2m+1)\ (x+\varepsilon))}{(2m+1)} \right] \right] \qquad (A55)$$

where N_{jo} is the initial number of drops of diameter D_j in an element dx,

k is the wave number $(2\pi/\lambda)$,

λ is the spatial period of the distribution, and

ε represents a phase difference which may vary between

$\varepsilon = 0$ and $\varepsilon = \lambda/2$ *

The effect of drag, as shown in Fig.A8b, is to cause a contraction
of the waves as they move progressively away from their origins.   The
appropriate expression describing this spray pattern is conveniently
obtained from equation A55 by introducing a new variable x' such that

$$\int_0^{x'} \frac{V_o}{V_j(x')}\ dx' = x \qquad\qquad (A56)$$

---

* $\varepsilon = 0$ corresponds to the conditions when a sheet fragment has just
disintegrated, while $\varepsilon = \lambda/2$ corresponds to the condition where
disintegration of the succeeding fragment begins, i.e. as shown in Fig.A8.
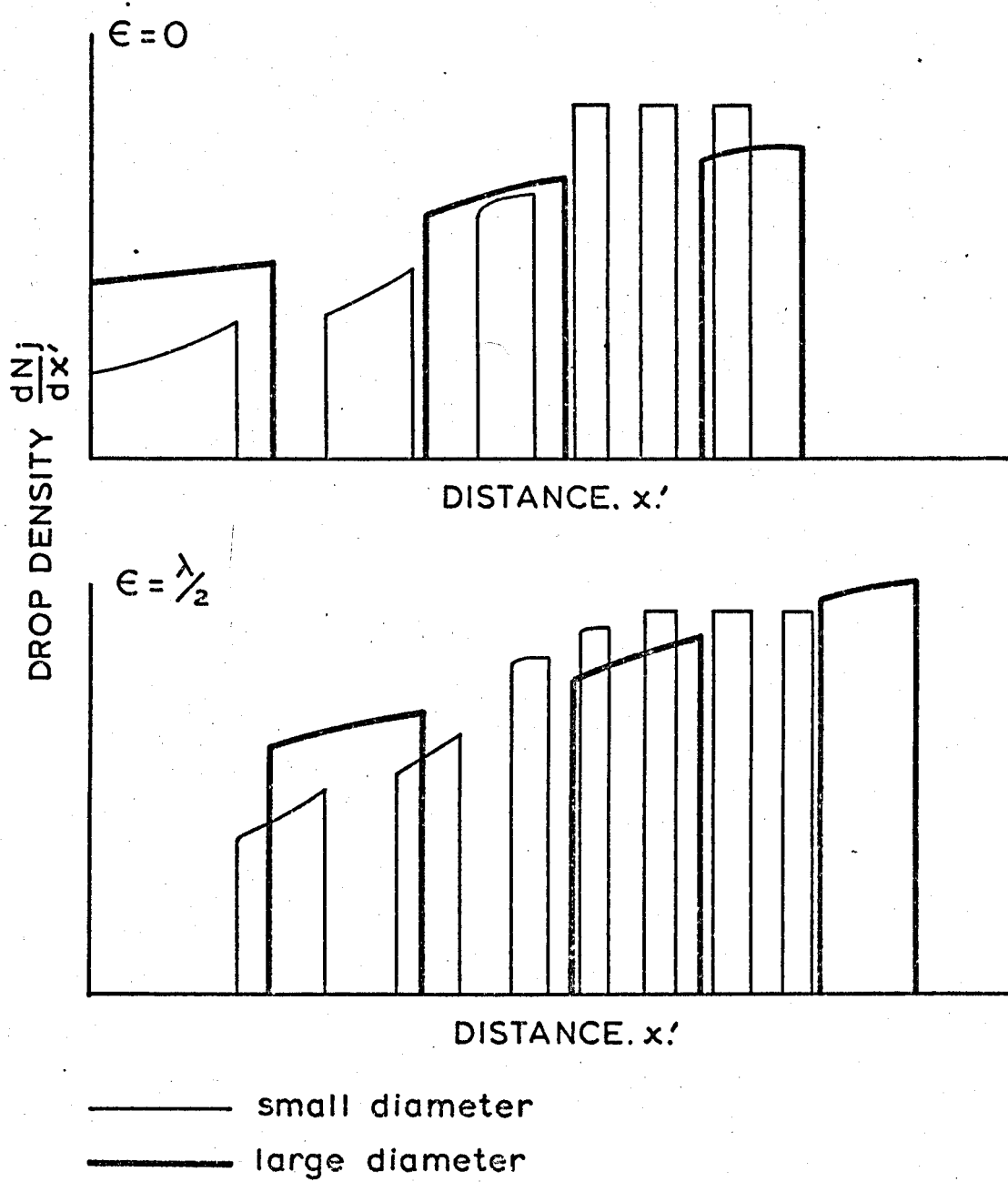
FIG. A9 PICTORIAL REPRESENTATION OF BAND HISTORIES FOR $\epsilon = 0$ and $\epsilon = \frac{\lambda}{2}$

where $V_j(x')$ is the velocity decay function of the drop D_j. In equation A56 x represents the distance travelled by a drop in time t in the absence of drag while x' corresponds to the distance the drop actually travels in the same time when decelerated by drag.

Substituting f or x in equation (A55) gives the number of drops in an element of length dx', i.e.

$$\frac{dN_j}{dx'} = \frac{V_o}{V_j(x')} \quad \frac{N_{jo}k}{2\pi} \left[1 + \frac{4}{\pi} \left[\sum_{m=o}^{\infty} \frac{\sin A}{B} \right] \right] \qquad (A57)$$

where $\quad A = k(2m+1) \left(\int_o^{x'} \frac{V_o}{V_j(x')} \, dx' + \epsilon \right)$

and $\quad B = 2m + 1$

A pictorial representation of equation A57 is given in Fig.(A9) which shows the histories of bands of drops comprising two widely differing drop sizes when $\epsilon = o$ and $\epsilon = \lambda/2$.

Integrating equation A57 gives the number of drops in an element of co-ordinates x'_1 to x'_2 i.e.

$$\triangle N_j = \frac{N_{jo}k}{2\pi} \left[\left[\int_{x'_1}^{x'_2} \frac{V_o}{V_j(x')} \, dx' - \frac{4}{\pi} \left[\sum_{m=o}^{\infty} \frac{\cos A}{k\,B^2} \right] \right]_{x'_1}^{x'_2} \right] \qquad (A58)$$

The weighted number of drops is obtained by multiplying the right-hand side of equation A57 by the normalised velocity decay function $V_j(x')/V_o$ and integrating between the limits x'_1 to x'_2.

Hence,

$$\triangle N_j^W = \frac{N_{jo}k}{2\pi} \int_{x'_1}^{x'_2} \left[1 + \frac{4}{\pi} \left[\sum_{m=o}^{\infty} \frac{\sin A}{B} \right] \right] dx' \qquad (A59)$$

For a poly-disperse system the possibility of an infinite number of drop sizes exists and consequently N_{jo} must be re-written as ΔN_{jo}, the initial number of drops of average diameter D_j in the size range. ΔD.   For the purpose of the illustration, calculations have been carried out for the following realistic example.   It is assumed that

(a)   the initial drop size spectrum varies from $12\frac{1}{2} - 262\frac{1}{2}\mu$, with a root-normal distribution, (61) viz

$$\frac{\Delta N_{jo}}{\Delta D} = \frac{1}{2s\sqrt{2D_j \pi}} \quad \exp - \frac{(\sqrt{D_j} - \sqrt{D_m})^2}{2s^2} \qquad (A60)$$

such that the standard deviation $s = \sqrt{5}$ and the

linear mean diameter $D_m = 100 \mu$. and

(b)   the drops are injected with an initial velocity of 10 m/sec.

vertically downwards into stagnant air, from fragments 5 mm in length.

It is further assumed that standard drag relations can be applied

to decelerating particles.   The drops thus move in the intermediate

flow regime according to the following relation (62).

$$V_j(x') \frac{dV_j}{dx'} = g - \frac{18\,\mu}{D_j^2 \rho_L} \left(1 + 0.15 \left[V_j(x') \frac{D_j \rho_a}{\mu}\right]^{0.687}\right) \qquad (A61)$$

Equations A58, A59 and A61 have been solved numerically for $\epsilon = \lambda/2^*$ and

$\underline{\Delta D = 25 \mu.}$

*Since drop formation is a random process, the value of ϵ recorded on a single flash photograph taken at any instant in time has an equal probability of lying anywhere in the range 0 to $\lambda/2$.   A value of $\lambda/2$ has been arbitrarily selected.
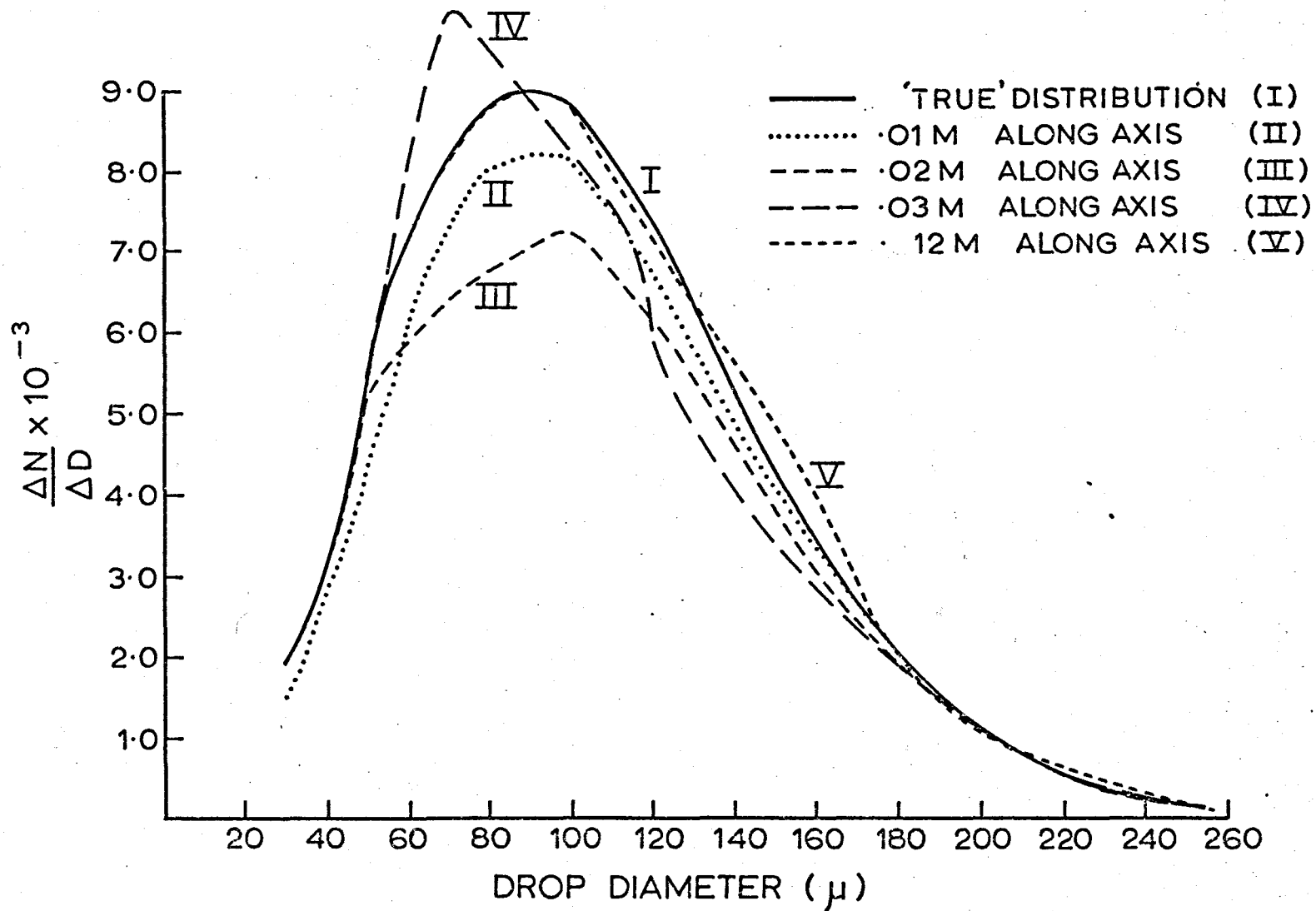
FIG. A.10 VARIATION OF 'WEIGHTED' SIZE-FREQUENCY DISTRIBUTION ALONG SPRAY AXIS
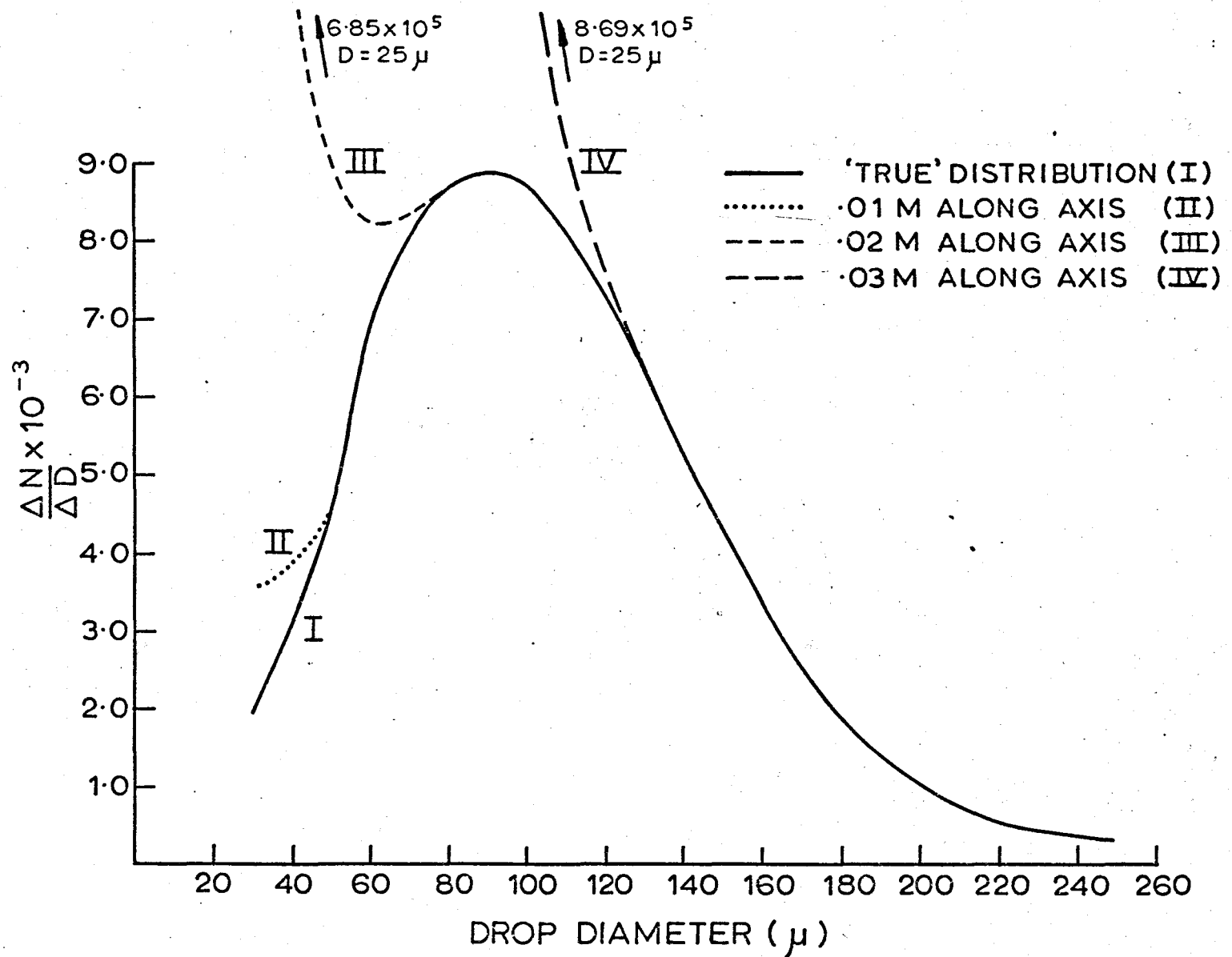
FIG. AJ1 VARIATION OF SPATIAL SIZE-FREQUENCY DISTRIBUTION
ALONG SPRAY AXIS
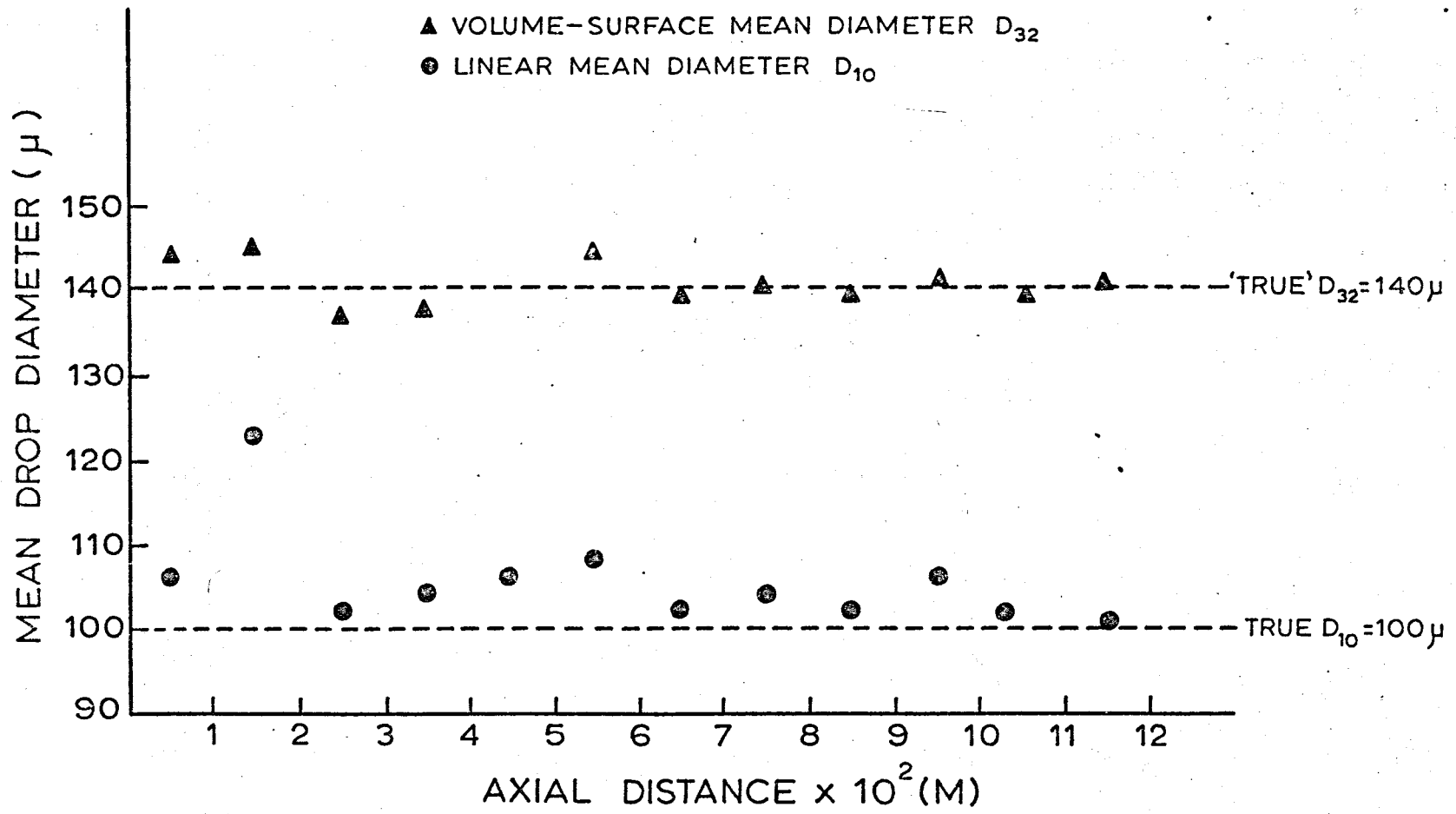
FIG. A.12 VARIATION OF WEIGHTED MEAN DIAMETERS WITH DISTANCE ALONG SPRAY AXIS
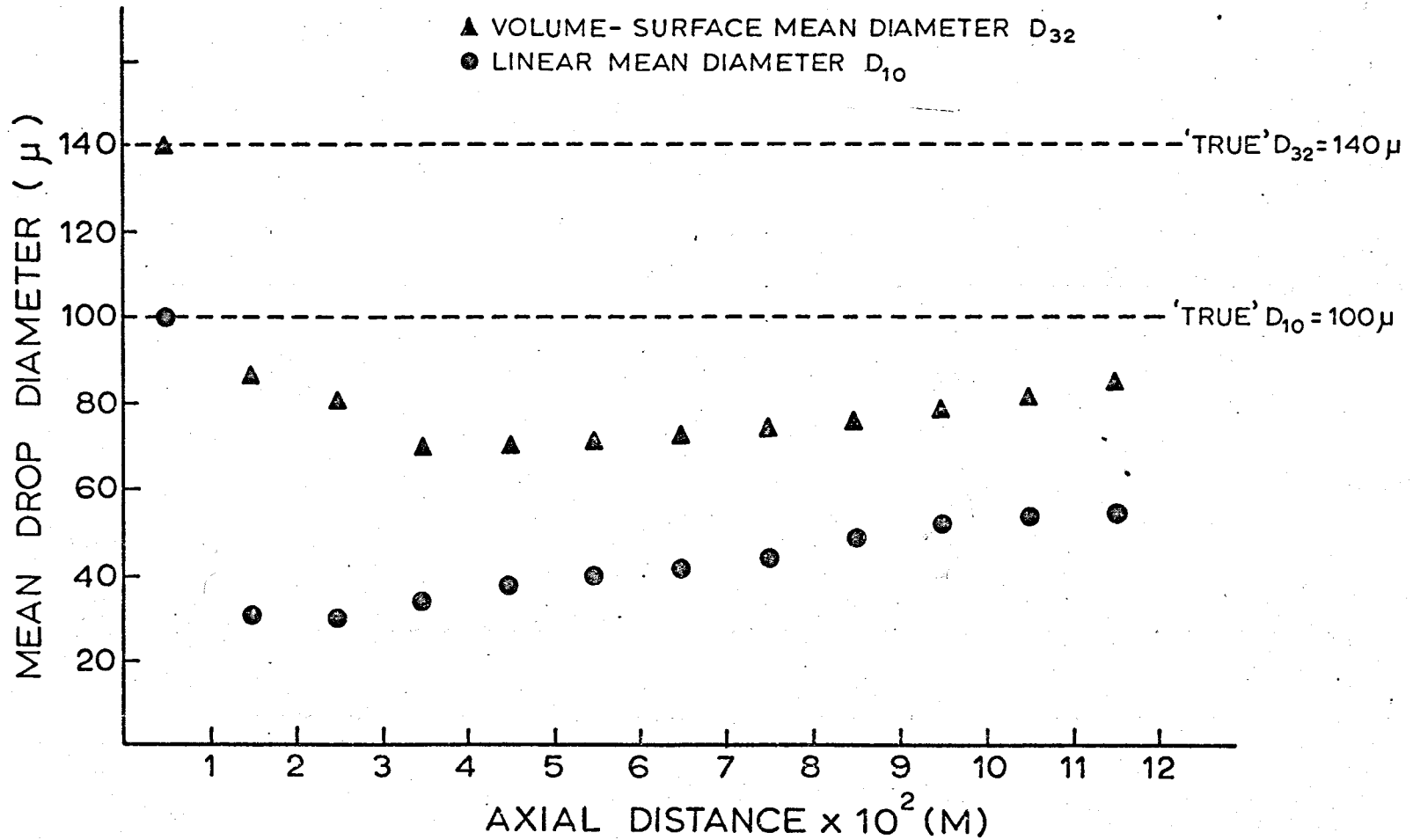
FIG.A.13 VARIATION OF SPATIAL MEAN DIAMETERS WITH DISTANCE ALONG SPRAY AXIS
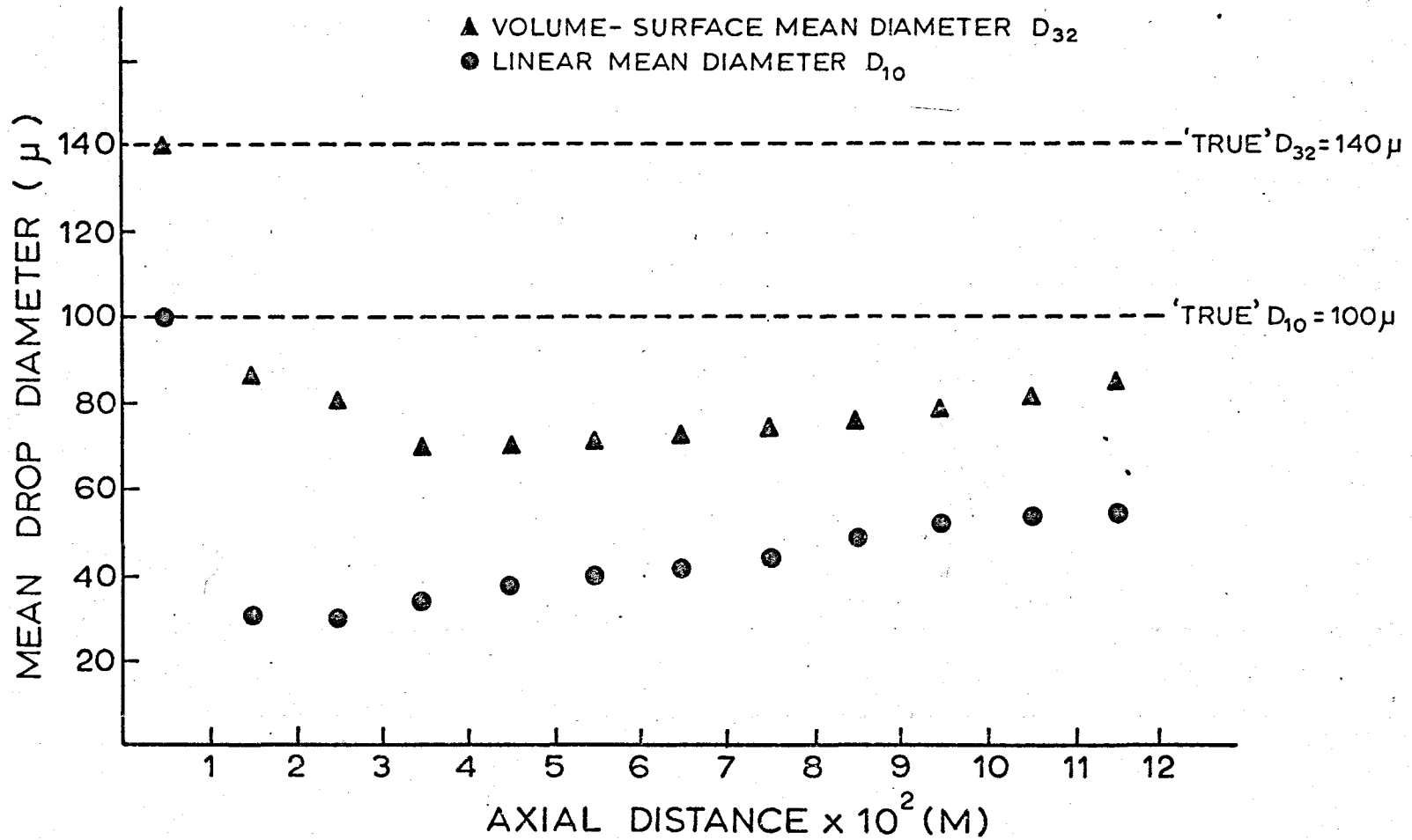
FIG.A.I3 VARIATION OF SPATIAL MEAN DIAMETERS WITH DISTANCE ALONG SPRAY AXIS

Results

Fig.A10 shows computed weighted size-frequency distributions (curves II to V) at various intervals down-stream of the site of drop formation compared with that initially produced (curve I). It is seen that, near the atomiser, marked differences exist, particularly around the peaks, and it is thus necessary to measure drop sizes some distance downstream (curve V) before congruence occurs between the measured and true distributions.

The corresponding spatial size-frequency distributions within the first three 0.01 m intervals are shown in Fig.A11. The curves demonstrate that the composition of the first band of drops (curve II) is practically identical to that of the original distribution (curve I), discrepancies only arising further downstream (curves III and IV).

Although the frequency distribution is essential for accurately defining the performance of a spray, it is often desirable in many transport processes to work with mean diameters. The input data has therefore been used to calculate two common mean diameters; namely, the volume-surface mean (D_{32}) and the linear mean (D_{10}).

Fig.A12 Compares the weighted and true mean diameters at various distances from the origin. It is seen again that discrepancies may occur near the region of disintegration, although these are less marked for the volume-surface mean diameters, which are least sensitive to variation in the smaller drop sizes. Fig.A13, on the other hand, demonstrates that while considerable errors arise from unweighted measurements obtained some distance away from the nozzle, very accurate results can be expected near the region of disintegration.

Discussion

The idealised model examined has shown that for specific types of sprays a weighting technique can result in significant disparities between the measured and true drop-size distributions. The size of these errors and the distance over which they persist are determined by the initial drop-velocity and size spectra, the band frequency, and the nature of the surrounding atmosphere. These conditions are effectively unknown in practice and hence except for regions where the drops approach their terminal velocities, it is not possible to relate a measured drop-size distribution to that originally produced.

Appendix IV.   Tabulated Results

Table 7

Measured and Theoretical Break-up lengths

(a) Flat sheets $\qquad\qquad h\eta_o = 10^{-8}$ (m)

Ambient gas temperature: 20°C. Liquid temperature : 20°C

Liquid : (i) Distilled Water.

Nozzle	$\left(\dfrac{\rho_l K_o T}{\rho_a^2 U_o^2}\right)^{1/3} \times 10^3$	Reynolds No.	Calculated break-up length, x (m) x 10^2	Mean of measured break-up lengths (m) x10^2
Y	1.38	7,350	1.37	2.8
	1.68	5,670	1.53	3.4
	2.38	3,340	1.90	4.0
X	1.79	13,500	1.79	2.6
	2.18	9,950	1.99	3.0
	2.86	6,400	2.47	5.4
W	1.99	16,900	1.98	2.7
	2.40	12,600	2.21	3.2
	3.17	8,300	2.74	4.6

(ii) Carbon Tetrachloride.

Nozzle		Reynolds	Calculated	Mean
Y	1.16	12,100	1.43	2.3
	1.41	9,350	1.51	2.7
	1.84	5,500	1.72	3.8
X	1.51	22,100	1.86	2.5
	1.83	15,400	1.97	2.9
	2.40	10,500	2.24	3.1

(iii) Acetone

Nozzle		Reynolds	Calculated	Mean
Y	0.88	18,200	1.13	2.0
	1.07	14,000	1.18	2.3
	1.40	8,300	1.23	3.2
X	1.15	33,400	1.46	2.0
	1.39	24,600	1.54	2.3
	1.83	16,000	1.73	2.8

Table 7 (cont.)

(iv) 50% Glycerin-water solution

Nozzle	$(\dfrac{\rho_1 K_o T}{\rho_a^2 U_o^2})^{1/3} \times 10^3$	Reynolds No.	Calculated break-up length (m) $\times 10^2$	Mean of measured break-up lengths (m) $\times 10^2$
Y	1.43	1,410	1.42	2.8
	1.73	1,090	1.58	3.7
	2.27	720	1.96	4.0
	1.85	2,500	1.84	4.2
X	2.25	1,840	2.06	4.7
	2.95	1,240	2.55	4.9

(b) Ambient gas temperature: 380°C.   Liquid temperature: 24°C

(i) Distilled water

Y	2.38	8,800	2.13	3.2
	2.88	11,000	2.50	3.5

Ambient gas temperature: 675°C.   Liquid temperature: 26°C

Y	2.92	11,400	2.56	3.7

(c) Conical sheets $\eta_o h = 3 \times 10^{-4}$ m

Ambient gas temperature: 20°C.   Liquid temperature: 20°C

(i) Distilled water

Danfoss D8/30	0.32		0.22	0.27
	0.34		0.22	0.30
	0.55		0.28	0.39
	1.08	Not given for conical sheets	0.49	0.49
Danfoss D25/45	0.67		0.31	0.33
	0.72		0.32	0.40
	1.12		0.41	0.46
	2.26		0.72	0.48
Danfoss D100/80	1.42		0.44	0.36
	2.26		0.57	0.49
	4.44		0.99	0.63

Table 8

Drop size distributions at various injection pressures and ambient

gas and liquid temperatures

Nozzle: Bray Unijet Y

Liquid: Distilled water

Differential injection pressure (bar)	1.72	1.59	3.58	3.58	6.35	1.72	1.72
(psig)	25	23	52	52	92	25	25
Ambient gas temp. ($^{\circ}$C)	380	380	380	380	380	675	675
Liquid temp. ($^{\circ}$C)	28	28	26	26	24	26	26
Volume surface mean diameter $(D_{32})(\mu m)$	170	150	85	81	70	125	165
Size range (μm)	ΔN	ΔN	ΔN	ΔN	ΔN	ΔN	ΔN
0-30	180	120	298	308	370	80	60
30-45	268	230	422	590	425	307	206
45-60	84	174	100	198	118	139	200
60-75	76	136	142	136	96	61	92
75-90	28	42	48	50	30	37	34
90-105	84	172	92	64	18	41	56
105-120	14	46	18	28	7	28	28
120-150	54	102	16	17	2	26	54
150-180	28	94	2	8	–	13	24
180-210	16	36	–	–	–	10	6
210-240	6	14	–	–	–	4	8
240-270	8	6	–	–	–	2	12
270-330	10	–	–	–	–	–	–
330-390	2	–	–	–	–	–	–

Table 8 (cont.)

Differential injection pressure (bar)	3.44	3.44	6.35	6.35	1.72	3.44	3.44
(psig)	50	50	92	92	25	50	50
Ambient gas temp. ($^{\circ}$C)	675	675	675	675	950	950	950
Liquid temp. ($^{\circ}$C)	25	25	24	24	24	23	23
Volume surface mean diameter (D_{32})(μm)	85	114	75	67	173	105	110
Size range (μm)	ΔN	ΔN	ΔN	ΔN	ΔN	ΔN	ΔN
0-30	110	90	141	135	60	88	50
30-45	526	263	459	447	300	390	308
45-60	320	160	178	161	203	312	218
60-75	122	61	65	37	61	80	86
75-90	66	33	40	25	36	122	49
90-105	64	32	21	12	43	60	22
105-120	32	16	7	3	11	18	14
120-150	54	30	7	2	31	28	17
150-180	8	4	1	2	24	12	6
180-210	6	3	-	-	16	10	8
210-240	-	-	-	-	9	2	1
240-270	-	-	-	-	8	-	1
270-330	-	-	-	-	6	-	-
330-390	-	-	-	-	1	-	-

Table 8 (cont.)

Differential injection pressure (bar)	90	1.72	1.59	1.72	1.65	1.59	1.72
(psig)	90	25	23	25	24	23	25
Ambient gas temp ($^{\circ}$C)	950	950	950	950	20	20	20
Liquid temp ($^{\circ}$C)	22	56	67	78	56	67	78
Volume surface mean diameter (D_{32})(μm)	81	157	185	165	115	111	100
Size range (μm)	ΔN	ΔN	ΔN	ΔN	ΔN	ΔN	ΔN
0-30	350	260	94	36	176	85	341
30-45	659	440	146	56	210	193	218
45-60	220	116	50	82	77	99	80
60-75	150	138	40	32	92	101	78
75-90	57	26	26	10	17	59	13
90-105	70	102	70	62	76	35	53
105-120	30	12	13	26	10	43	12
120-150	20	52	66	70	25	17	22
150-180	9	54	50	40	5	11	8
180-210	-	36	58	18	14	4	5
210-240	-	24	18	10	-	-	-
240-270	-	6	20	8	-	-	-
270-330	-	6	4	-	-	-	-
330-390	-	-	-	-	-	-	-

Table 8   (cont.)

Nozzle: Danfoss D8/45

Liquid: Distilled water

Differential injection pressure (bar)	6.9	3.44	3.44	3.44	1.38	1.38	0.69
(psig)	100	50	50	50	20	20	10
Ambient gas temp ($^{\circ}$C)	950	950	950	20	950	20	950
Liquid temp. ($^{\circ}$C)	25	26	26	20	27	20	27
Volume surface mean diameter (D_{32}) (μm)	100	95	93	49	125	188	165
Size range (μm)	ΔN	ΔN	ΔN	ΔN	ΔN	ΔN	ΔN
0-30	106	132	62	282	13	1	10
30-45	180	100	110	391	13	8	18
45-60	96	126	104	150	12	12	8
60-75	106	84	98	72	16	6	14
75-90	30	36	26	29	4	3	1
90-105	60	56	72	13	17	13	8
105-120	6	6	16	4	2	3	1
120-150	20	14	26	1	16	15	7
150-180	6	4	4	-	9	6	2
180-210	6	-	-	-	4	10	3
210-240	-	-	-	-	2	3	2
240-270	-	-	-	-	2	2	2
270-330	-	-	-	-	-	2	-

Table 8 (cont.)

Differential injection pressure (bar)	0.69		6.9
(psig)	10		100
Ambient gas temp. ($^{\circ}$C)	20		20
Liquid temp. ($^{\circ}$C)	20		20
Volume surface mean diameter (D_{32}) (μm)	210		38
Size range (μm)	ΔN	Size range	ΔN
0-30	14	0-10	321
30-45	8	10-18	141
45-60	16	18-28	101
60-75	21	28-38	40
75-90	5	38-48	19
90-105	14	48-58	8
105-120	3	58-68	6
120-150	17	68-78	1
150-180	15	78-98	1
180-210	5		
210-240	4		
240-270	5		
270-330	3		

Table 9. Sizes of Drops Formed at the Rims of Flat Spray Sheets

Liquid	Nozzle	U_o (m.sec^{-1})	$(\frac{T}{\ell_1})^{1/9}(\frac{K_o^2}{U_o})^{2/9}$ x 10^4	Mean Diameter (μ m)
Water	Y	11.9	1.19	310
		9.25	1.23	330
Water	X	6.75	1.86	404
		9.25	1.76	430
Water	W	6.75	1.98	475
		9.25	1.84	431
Carbon Tetrachloride	Y	14.1	0.98	185

APPENDIX V

Numerical Solution of Equations Describing Spatial and Weighted Drop-Size Distributions

Equations (A56), (A58) and (A59) have been solved numerically using a computer program written in Algol. Drop velocity - distance data obtained by solution of equation (A61) is provided in the form of the polynomial,

$$V(1) = a(1) + a(2) \, s + a(3) \, s^2 + a(4) \, s^3 \ldots . \, a(M+1) \, s^{M+1}$$

where the coefficients a(1) - a(M+1) have been obtained separately by the method of least squares.

The computed results are presented as a set of spatial and weighted drop size distributions and mean drop diameters at consecutive down-stream elements commencing at the region of drop formation. Because of the restricted choice of typewritten symbols it has not been possible to identify variables used in the program with the symbols appearing in the text. The following are, therefore, a list of equivalents.

$D_j = d(j)$

$D = deltad$

$D_{10} = d_m$

$D_{32} = SMD$

$x_1' = s_1$

$x_2' = s_2$

$x_2' - x_1' = ds'$

$N_{jo} = NO$

$N_j^w = INTND \, (2, \, j, \, r)$

$N_j = INTND \, (1, \, j, \, r)$

$$V = V(1)$$

$$\frac{dV}{dx} = V(2) \quad \text{etc.}$$

$$V_o = VO$$

$$s^2 = sd$$

Computer program

```
begin
real k,deltad,dm,sd,I,i,sl,VO,eps,deltas,totsum,SMD,Tv,Ts,s2,pi,A,B,Z,NO;
integer r,N,j,n,M,p,l,z,q,m,b;
open(20);open(70);
k:read(20);                        deltas:=read(20);
deltad:=read(20);                    N:=read(20);
dm:=read(20);                      n:=read(20);
sd:=read(20);                      p:=read(20);
VO:=read(20);                      b:=read(20);
begin array d,VOLDELTAN,AREADELTAN,Vstar(1:n),PARTSUM(0:n),a(1:20),
INTND(1:2 1:p), V(1:20);
for j:=1 step 1 until n do begin

                                d(j):=read(20);
end;
begin procedure summation(b,q);
value b,q;
integer q;
array b;
begin totsum:=0;
for j:=1 step 1 until q do begin PARTSUM(j):=0;end;
```

```
for j:=1 step 1 until q do begin

PARTSUM(j):=PARTSUM(j-1)+b(j);end;

totsum:=PARTSUM(q);

end;

real procedure function(s,X);

valueX;

real s,X;

begin

real F;integer p,o;

F:=0;

for z:=1 step 1 until M+1 do begin

V(z):=0;

if s  Ts then begin

for l:=z step 1 until M+1 do begin

p:=1;

if z≠1 then for o:=1 step 1 until z-1 do begin p:=px(l-o);end;

V(z):=V(z)+px(if l=z then a(z) else a(l)xs ↑ (l-z));

end;

end else

V(1):=Tv;

end;for z:=1 step 1 until M+1do begin for m:=1 step 2 until b do begin

F:=F+V(z)x4/pix(if z/2=z÷2 then (sin(mxkxX+pi))/(k↑zxm↑(z +1))x(if (z)/4=(z)÷

+4 then +1 else -1)else (cos(mxkxX+pi))/(k↑zxm↑(z+1))x(if (z+1)/4=(z+1)÷4 then

-1 else +1)) x (if z= 1 then + 1 else(V(1)↑ (z-1))/(VO↑(z-2))); end; end;

function:=F;.

end;

real procedure f(s);

real s;

begin
```

```
if s  Ts then begin

V(1):=0;

for l:=1 step 1 until M+1 do begin

V(1):=V(1)+(if l=1thena(1) else a(1)xs ↑ (1-1));end;

end else V(1):=Tv;

f:VC/V(1);

end;

        procedure simpson(a, b, f, I, i, eps, N);

        value a, b, eps, N;

        real a, b, I, i, eps;   integer N;   real procedure f;

        comment a procedure based upon simpsons rule;

        begin integer m, n;

        real d, h, ga, gb, gc, gd, ge, aa, ab, ac;

        real array s(1:N, 1:3);

            I:=0;   m:=n:=0;   i:=a;

            ga:=f(a);   gc:=f((a+b)/2);   ge:=f(b);

            aa:=(b-a)x(ga+4xgc+ge)/2;

        AA: d:=2 m;   h:=.25x(b-a)/d;

            gb:=f(a+hx(4xm+1));

            gd:=f(a+hx(4xm+3));

            ab:=hx(ga+4xgb+gc);

            ac:=hx(gc+4xgd+ge);

            if abs(ab+ac-aa) > epsxabs(ab+ac)

                then

                    begin m:=mx2;   n:=n+1;

                        if n>N then goto CC;

                        aa:=ab;

                        s(n, 1):=ac;

                        s(n, 2):=gd;

                        s(n, 3):=ge;
```

```
                                    ge:=gc;

                                    gc:=gb;

                                    goto AA

                          end

                else

                          begin I:=I+(ab+ac)/3

                          m:=m+1;

                          i:=a+mx(b-a)/d;

          BB:               if m=2x(m÷2) then

                                    begin m:=m÷2;

                                        n:=n-1;

                                        goto BB

                                    end;

                          if (m≠1) or (n≠0) then

                                    begin aa:=s(n, 1);

                                        ga:=ge;

                                        gc:=s(n, 2);

                                        ge:=s(n, 3);

                                        goto AA

                                    end

                end;

    CC:

    end of procedure simpson;

j:=0;

    pi:=3.142;

loop:               j:=j+1;

M:=read(20);

Tv:=read(20);

Ts:=read(20);
```

```
eps:=read(20);

for l:=1step 1 until M+1do begin
              a(l):=read(20);

end;

NO:=deltad/(2xsqrt(2xsdxpixd(j))xexp((sqrt(d(j))-sqrt(dm)) 2/(2xsd)))x1000;

write text (70,((3cl4s)Drop*size(c)));write(70,format((12s+d.dd_{10}+ndc)),d(j

write text (70,((3cl4s)Frequency(c)));write(70,format((12s+d.ddd_{10}+ndc)),NC

write text (70,((3cl4s)Axial*drop*density(c)));

write text (70,((3cl0s)Spatial(8s)Apparent*temporal(12s)Axial*distance(c)));

for r:=1 step 1 until p do begin

sl:=(r-1)xdeltas;

s2:=sl+deltas;

simpson(0,sl,f,I,i,eps,N);A:=I;

simpson(sl,s2,f,I,i,eps,N);B:=I;

Z:=0;

for m:=1 step 2 until b do begin

Z:=Z+(cos(mxkx(A+B)+pi))/m↑2xk)-(cos(mxkxA+pi))/(m↑2xk);end;

INTND(1,j,r):=NOxk/(2xpi)x(B-(4/pi)xZ);

INTND(2,j,r):=NCxk/(2xpi)x(function(sl,A)-function(s2,B+A)+VOxdeltas);end;

for r:=1 step 1 until p do begin

write (70,format((8s+d.dddd_{10}+nd)),INTND(1,j,r));

write(70,format((8s+d.dddd_{10}+nd)),INTND(2,j,r));

write(70,format((15s+d.dd_{10}+ndc)),(rxdeltas));

end; write text(70,((p))); if j n then goto loop;

for q:=1step 1 until 2 do begin

if q=1then

write text (70,((3cl0s))Spatial* drop *size * distributions*and*drop*sizes*

evaluated*at*equal*increments*along*the*spray*axis(c)) )
```

```
else write test (70,((3c10s) temporal*drop*size*distributions*and*drop*size

evaluated*at*equal*increments*along*the*spray*axis(c)));

for r:=1step 1 until p do begin for j:=1 step 1 until n do begin

VOLDELTAN(j):=d(j) 3xINTND(q,j,r);end;

summation(VOLDELTAN,n);

write text(70,((3c4s)Volume*percent*oversize(3s)Drop*size(c)));forj:=1step 1

until n do begin

Vstar(j):=100x(1-PARTSUM(j)/totsum);

write(70,format((12s+d.ddd_{10}+nd)),Vstar(j));

write(70,format((12s+d.ddd_{10}+ndc)),d(j));

end;

for j:=1step 1 until n do begin

AREADELTAN(j):=d(j) 2xINTND(q,j,r)/totsum;end;

summation(AREADELTAN,n);

SMD:=100/totsum;

write text (70,((3c4s)Sauter*mean*diameter(15s)Axial*distance(c)) );

write(70,format((14s+d.ddd_{10}+nd)),SMD);

write(70,format((15s+d.ddd_{10}+ndc)),rxdeltas);

end;write text(70,((p)));

end;

write text (70,((7c7s) order *of*approximation *to*a*square*wave*is*(2s)));

write(70,format((sdd)),b);

write text(70,((3c7s)Drop*number*density(7s)x-coordinate(c)));

for r:=1 step 1 until 20 do begin

sl:=rxdeltas/(20);

Z:=0;

for m:=1step 2 until b do begin

Z:=Z+(sin(mxkxsl+pi))/m;

end;
```

```
Z:=(1+(4/pi)xZ);

write (70,format((12s+d.ddd_{10}+nd)),Z);

write(70,format((12sd.dd_{10}+ndc)),sl);

end;

end;end;close(20);close(70);end
```

NOTATION

In order to use commonly accepted notation, duplication has been unavoidable; the notation used in each section is therefore listed separately.

2.1.1

A   cross sectional area of rim

C_q orifice discharge coefficient

d   width of orifice

f   distance of centre of pressure behind orifice

h   half sheet thickness

K_o sheet thickness parameter (= 2hr)

N   parameter ($\dfrac{2T}{U_o^2 K \rho_I}$)

Δp differential injection pressure

r   distance from centre of pressure to any point on the rim

s   distance along the rim

T   surface tension

U_o liquid velocity along any streamline within the sheet

U_t liquid velocity at any point along the rim

r_o distance from centre of pressure to initial point of thickening along the rim

$\theta, \theta_o, \omega, \sigma$ angles defined in Fig.(2.2)

ρ_I liquid density

2.1.2

a   effective equilibrium radius of perturbed cylindrical rim

a*   effective equilibrium radius of perturbed cylindrical rim at break-up

a_o	radius of unperturbed cylindrical rim
D	diameter of drops produced at a liquid rim
f	acceleration experienced by a liquid rim
H	time dependent amplitude of arbitrary surface disturbance
H_o	initial amplitude
I_m	modified Bessel function of order m
k	spatial frequency (wave number)
k_{opt}	spatial frequency corresponding to wave of maximum growth
K_o	sheet thickness parameter ($= 2hr$)
m	eigenvalue
P	parameter $(=(\frac{4K_o k^2}{3(\pi + \frac{1}{2})})^{\frac{1}{2}})$
S_1	kinetic energy per unit wavelength in perturbed state
S_o	kinetic energy per unit wavelength in unperturbed state
r	radial distance measured from jet axis (cf. Fig.2.6)
s	distance measured along rim arc (cf. Fig.2.7)
Q_1	potential energy per unit wavelength in perturbed state
Q_o	potential energy per unit wavelength in unperturbed state
t	time
T	surface tension
U_o	velocity along any streamline in a liquid sheet
x	distance co-ordinate measured along rim axis
ϕ	velocity potential
Φ	angle shown in Fig. (2.6)
θ	angle shown in Fig. (2.7)
ρ_T	liquid density
λ	wavelength

Subscripts

f   denotes potential energy term due to acceleration

s   denotes potential energy term due to surface area

m   denotes a time averaged quantity or order of Bessel function

t   denotes differentiation with respect to time

r   denotes differentiation with respect to r

2.2.1

$a_1 - a_4$ constants of integration

h   half sheet thickness

k   spatial frequency (wave number)

m   dimensionless parameter $(=(k^2 + \frac{i(n+U_ok)}{\nu_1})^{\frac{1}{2}})$

M   dimensionless parameter $(=(\frac{\rho_a n^2 - Tk^2}{\rho_1})^{\frac{1}{2}})$

n   complex temporal frequency

N   dimensionless parameter $(\frac{\nu_1 k^2}{N})$

t   time

T   surface tension

U   velocity vector

U_o zero order liquid velocity

U   x-component of perturbation velocity

V   y-component of perturbation velocity

x   distance co-ordinate along sheet axis

X   dimensionless parameter $(=(\frac{i(n+U_ok)+2\nu_1 k^2}{N}))$

y   distance co-ordinate normal to sheet axis

ψ stream function

ψ_j gaseous phase stream function

Φ_j separated variable in stream function

$\Upsilon_{\alpha\beta}$ Newtonian stress tensor

$\delta_{\alpha\beta}$	symmetric unit tensor
α	real part of temporal frequency
β	complex part of temporal frequency
β'	complex part of inviscid temporal frequency
ν	kinematic viscosity
η_j	Fourier component of arbitrary surface displacement
η_0	ratio of amplitude of initial surface displacement to sheet thickness ratio
ϵ	phase angle
ω	component of vorticity
ρ	density

Subscripts

a	gaseous phase
l	liquid phase
j	integer, (j=1) upper interface (j=2) lower interface
α,β	components of vector or tensor quantity with respect to rectangular Cartesian co-ordinates

2.2.2

a	second order complex temporal frequency
$\bar{a}$	conjugate of second order complex temporal frequency
A, B, C, D, E, F, G, H	constants of integration
P, Q, R	coefficients appearing in equation
h	half sheet thickness
k	spatial frequency (wave number)
n	first order complex temporal frequency
$\bar{n}$	conjugate of first order complex temporal frequency

t	time
T	surface tension
U_o	zero-order liquid velocity
x	distance co-ordinate along sheet axis
y	distance co-ordinate normal to sheet axis
$Y_{(s)}$	Laplace transform of ${}^{2}\psi_2$
ϕ	liquid phase velocity potential
${}^{r}\phi$	rth term in perturbation expansion of ϕ
ϕ'_j	gaseous phase velocity potential
${}^{r}\phi'_j$	rth term in pertubation expansion of ϕ'_j
η_j	Fourier component of arbitrary surface displacement
${}^{r}\eta_j$	rth term in perturbation expansion of η_j
η_o	amplitude of initial disturbance to sheet thickness ratio
ψ	separated variable in liquid phase velocity potential
${}^{r}\psi$	rth term in perturbation expansion of ψ
ψ_j	separated variable in gaseous phase velocity potential
${}^{r}\psi_j$	rth term in perturbation expansion of ψ_j
α'	real part of first order complex temporal frequency
α''	real part of second order complex temporal frequency
β'	imaginary part of first order complex temporal frequency
β''	imaginary part of second order complex temporal frequency
γ	ratio $\dfrac{{}^{r}\psi_1}{{}^{r}\psi_2}$
ρ	density
λ	wavelength

Subscripts

1	liquid phase
t	denotes differentiation with respect to t
x	denotes differentiation with respect to x

y	denotes differentiation with respect to y
j	integer, j=1 denotes upper interface, j=2 denotes lower interface
a	gaseous phase

2.2.3

h	half sheet thickness
h*	half thickness of undisturbed sheet at break-up
k	spatial frequency
K_o	sheet thickness parameter (=2hr)
t	time
t*	break-up time
T	surface tension
U_o	zero order sheet velocity
x	distance co-ordinate along sheet axis
x*	break-up length of a liquid sheet
β'	imaginary part of first order temporal frequency
β''	imaginary part of second order temporal frequency
η_j	Fourier components of initial surface displacement

Subscripts

n	denotes a time averaged value
j	integer j=1 denotes upper interface, j=2 denotes lower interface

2.3

a	amplitude of initial disturbance
$\bar{a}$	unit vector in y-direction
A	constant of integration
$\bar{b}$	unit vector in x-direction
B	constant of integration

D	dielectric constant
e	electronic charge
E_α	electric field strength vector
$\overset{o}{E}$	zero order component of electric field strength in y-direction
$\overset{1}{E}$	first order component of electric field strength in y-direction
F	function defined by
G	constant of integration in equation
G	dimensionless field strength
h	half sheet thickness
J_i	dimensionless ion current
J_e	dimensionless electron current
k	spatial frequency (wave number)
k'	dimensionless spatial frequency ($= k\,\xi_o$)
k_c	cut-off wave number
k_{opt}	wave number corresponding to wave of maximum growth rate
K	Boltzmann constant
$M_{\alpha\beta}$	Maxwell's stress tensor defined by equation
n_α	unit vector normal to liquid-gas interface
n_e	normalised electric density
n_i	normalised ion density
p	dimensionless parameter defined by equation
$'p_J$	perturbation value of liquid pressure
$'p_a$	perturbation value of gas pressure
q	dimensionless function. ($= \dfrac{d(n_i - n_e)}{d'R}$)
R	dimensionless electric potential ($= \dfrac{\phi_e\,e}{K\theta}$)
t	time
t	dimensionless distance ($\dfrac{y - h}{\xi_o}$)
T	surface tension
U_α	velocity vector

U_o zero order sheet velocity

V volume

x distance co-ordinate along sheet axis

x' dimensionless distance co-ordinate along sheet axis $(= \frac{x}{\zeta_o})$

$\varkappa$ ratio of ion and electron temperatures $(= \frac{\Theta_i}{\Theta_e})$

y distance co-ordinate normal to sheet axis

Y separated variable in electric potential

z dimensionless function $(= (\frac{3}{2} \int_{t_o}^{t} q^{1/2} dt)^{2/3})$

ϕ velocity potential

$^r\phi$ rth term in velocity potential perturbation expansion

ϕ_e electric potential

$^r\phi_e$ rth term in electric potential perturbation expansion

η_j Fourier component of surface displacement

$^r\eta_j$ rth term in surface displacement perturbation expansion

η_o amplitude of initial surface displacement to sheet thickness ratio

ϵ_o permittivity of free space

ρ density

ρ_f electric charge density

$^r\rho_f$ rth term in electric charge density perturbation expansion

$\delta_{\alpha\beta}$ symmetric unit tensor

$\epsilon_{\alpha\beta\gamma}$ alternating unit tensor

     vector differential operator $(= \frac{\partial}{\partial x_\alpha})$

ζ_o thickness of non convective sheath

σ_f surface charge density

Θ temperature

Φ separated variable in electric potential

Ψ separated variable in velocity potential

Subscripts

α, β, γ components of vector or tensor quantity with respect to

rectangular Cartesian co-ordinates

j   integer (j = 1) upper interface (j = 2) lower interface

t   differentiation with respect to t

t   differentiation with respect to t

x   differentiation with respect to x

y   differentiation with respect to y

o   denotes the value of the subscripted variable at the outer

edge of the non-convective sheath

w   denotes the value of the subscripted variable at the liquid

surface

3.3.1

e   emittance

h   heat transfer coefficient

L   height of test chamber

Nu   Nusselt number $\left(\dfrac{h \times \text{diameter of junction}}{\text{thermal conductivity}}\right)$

Pr   Prandtl number $\left(\dfrac{\text{specific heat} \times \text{viscosity}}{\text{thermal conductivity}}\right)$

Re   Reynolds number $\left(\dfrac{\text{velocity} \times \text{diameter of junction}}{\text{kinematic viscosity}}\right)$

R   heat transfer resistance

T   temperature

σ Stefans constant

Subscripts

a   denotes the value of the subscripted variable within the

surrounding air

j   denotes value of the subscripted variable at the thermo-

couple junction

o   denotes value of the subscripted variable at the outer wall

t	denotes the value of the subscripted variable within the gaseous phase at the thermocouple junction
w	denotes the value of the subscripted variable at the inner wall

<u>3.5</u>

D	length of light path in liquid sheet
K_o	sheet thickness parameter (Sx)
n, m	integers
s	sheet thickness
x	distance from centre of pressure to interface fringe
w	wavelength of light
θ, θ'	angles defined in Fig.(3.8)
μ	refractive index

Subscripts

r, n	integers

<u>3.7</u>

$$D_{32} \quad \frac{\int_0^{D_{max}} D^3 \frac{dn}{dD}\, dD}{\int_0^{D_{max}} D^2 \frac{dn}{dD}\, dD}$$

ΔD	drop size range
D	drop diameter
n	cumulative number of drops in the range 0 to D
ΔN	number of drops in ΔD
U	cumulative fraction volume oversize

Subscripts

max	denotes the maximum drop size in a spray
m	denotes the median diameter of a range
l	denotes the smallest diameter of a range

<u>4.3</u>

ki,kr	imaginary and real parts of a complex spatial frequency.

Appendix I

a_{1-n}	coefficients in power series expansion of $f(\eta)$
A_{1-n}	coefficients in power series expansion of (η)
c_{1-n}	coefficients in power series expansion of $F(\eta)$
D	dielectric constant
D_a	ambipolar diffusion coefficient
D_e	electron diffusion coefficient
D_i	ion diffusion coefficient
e	charge on an electron
^oE	zero order electric field strength
$f(\eta)$	transformed stream function
F	transformed variable $(=G\ p^{-2/3}(-(J_i + \frac{J_e}{\varkappa}))^{-1/3})$
$F(\eta)$	$\int_o^\eta f(\eta)\ d\eta$
G	dimensionless electric field strength $(= -\frac{dR}{dt})$
h_e	Debye attenuating length
I	ambipolar current
I_e, I_i	electron and ion currents respectively
J_e, J_i	dimensionless electron and ion current respectively
K	Boltzmann's constant
m	integer or dimensionless charge density in neutral region $(m = N/Nf_o)$
n	integer or dimensionless charge density $(= \frac{N}{N_o})$
n_e, n_i	dimensionless electron and ion charge densities $(= \frac{N_i}{N_o}\ , = \frac{N_e}{N_o})$
N	charge density in neutral region
N_e, N_i	electron and ion charge densities respectively in non-convective sheath

N_{fo} free stream charge density

P dimensionless perturbation parameter $(= \dfrac{h_e}{\xi_o})$

R dimensionless electric potential $(= -\dfrac{\phi_e e}{K\theta_e})$

S general ortlogonal co-ordinate along liquid surface

Sca ambipolar Schmidt number

t dimensionless distance

U velocity vector in gaseous phase

U_o liquid sheet velocity

U S - component of gas velocity

V ξ - component of gas velocity

x transformed variable $(= \int\limits_{o}^{s} (y(s))^2 \, ds)$

$\varkappa$ ratio of ion and electron temperatures $(= \dfrac{\theta_i}{\theta_e})$

$y(s)$ radius of curvative of surface measured from axis

s transformed variable $(= p^{2/3}(-(J_i + \dfrac{J_e}{\varkappa}))^{1/3}(ts - t)$

ϕ_e electric potential

ψ stream function

ξ generalised ortlogonal co-ordinate

Γ_i ion flux

Γ_e electron flux density

η similarity variable $(=(\dfrac{U_o}{2\nu_g x})^{1/2}\xi \, y(s))$

ν_g gas kinematic viscosity

$F(\eta)$

θ temperature

ϵ_o permittivity of free space

∇ vector differential operator $(= \dfrac{\partial}{\partial x_\alpha})$

Subscripts

o denotes the value of the subscripted variable at the outer

edge of the non-convective sheath

w } denotes the value of the subscripted variable at the
s } liquid surface

α, β components of vector or tensor quantity with respect to
rectangular Cartesian co-ordinates

Appendix II

C   constant of integration

^{o}E zero order electric field strength

F   electrical stress ($= \epsilon_o \, {}^{o}E^2$)

P   normal stress

Q   volume flowrate

R   dimensionless parameter ($= \dfrac{\rho_I \, QU_o}{4\pi T}$)

r_c radius of curvature of meridian section

R_c dimensionless radius of curvature of meridian section ($= \dfrac{r_c}{R}$)

s   arc length of the meridian section

S   dimensionless arc length of meridian section ($= \dfrac{S}{R}$)

T   surface tension

U_o liquid velocity

x   distance co-ordinate measured along the centre line

X   dimensionless co-ordinate along the centre line ($= \dfrac{x}{R}$)

y   distance co-ordinate measured normal to centre line

Y   dimensionless co-ordinate normal to centre line ($= \dfrac{y}{R}$)

α dimensionless stress ($= \dfrac{U_o \, QF}{8\pi T^2}$)

ϵ_o permittivity of free space

ϕ_o cone angle

ϕ slope of liquid surface to the x axis

Appendix III

A, B   see equation A57.

D_m number median diameter

$$D_{10} \qquad \frac{\int_0^\infty D \, \frac{dN}{dD} \, dD}{\int_0^\infty \frac{dN}{dD} \, dD}$$

$$D_{32} \qquad \frac{\int_0^\infty D^3 \, \frac{dN}{dD} \, dD}{\int_0^\infty D^2 \, \frac{dN}{dD} \, dD}$$

D_j drop size of type j

ΔD drop size range

k spatial frequency of square waves $(= \frac{2\pi}{\lambda})$

N_j number of drops of type j

N_{jo} initial number of drops of type j

ΔN_j total number of drops of type j in a given element

ΔN_j^w weighted number of drops of type j in a given element

m integer

s standard deviation

x distance co-ordinate in the absence of drag

x' distance co-ordinate in the presence of drag

V_j velocity of drops of type j

V_{jo} initial velocity of drops of type j

ϵ phase lag

μ air viscosity

ρ_a air density

ρ_l liquid density

λ wavelength

BIBLIOGRAPHY

1. Locklin, D.W.; "The A.P.I. Research Program for Distillate Fuel
    Combustion - Plans for 1961". A.P.I. Conference paper 61-2 (1961).

2. Fraser, R.P., Eisenklam, P. and Dombrowski, N.; Brit. Chem. Eng.
    2, 494, 496, 536, 610 (1957).

3. Fraser, R.P.; Plant Protection Conference. 237 (Butterworths
    London), (1956).

4. Dombrowski, N. and Munday, G.; Biochemical and Biological
    Engineering Science, Vol.2 (Academic Press), (1968).

5. Dorman, R.G.; "The Atomisation of Liquids in a Flat Spray".
    Brit. J. Appl. Phys. 3, 189, (1952).

6. Fraser, R.P., Dombrowski, N., Eisenklam, P. and Hassan, D.;
    "Drop Formation from Rapidly Moving Liquid Sheets". A.I.Ch.E.
    Journal, 8, 627, (1962).

7. Fraser, R.P. and Dombrowski, N.; "A Photographic Investigation
    into the Disintegration of Liquid Sheets". Phil. Trans. Roy.
    Soc. A247, 101, (1954).

8. Hasson, D. and Mizrahi, J.; "The Drop Size from Fan Spray
    Nozzles; Measurements by Solidifying Wax Techniques Compared
    with those Obtained by other Sizing Techniques". Trans. Inst.
    Chem. Eng. 39, 415, (1961).

9. Dombrowski, N. and Hooper, P.C.; "The Effect of Ambient Density
    on Drop Formation in Sprays". Chem. Eng. Sci., 17, 291, (1962).

10. Dombrowski, N., Hasson, D. and Ward, D.E.; "Some Aspects of Flow
    through Fan Spray Nozzles". Chem. Eng. Sci., 12, 35, (1960).

11. Dombrowski, N. and Johns, W.R.; "The Aerodynamic Instability
    and Disintegration of Viscous Liquid Sheets". Chem. Eng. Sci.,
    18, 203, (1963).

12. Lewis, D.J.; "The Instability of Liquid Surfaces, II". Proc. Roy. Soc., A <u>202</u>, 81, (1950).

13. Rayleigh, Lord; "On the Instability of Jets". Proc. London Math. Soc., <u>10</u>, (1879).

14. Basset, A.B.; "A Treatise on Hydrodynamics", Vol.2. Dover Publications New York), (1961).

15. Lamb, H.; "Hydrodynamics", 6th Edition. (Cambridge University Press), (1932).

16. Rayleigh, Lord; "Investigations of the Character of Equilibrium of an Incompressible Heavy Fluid of Variable Density". Proc. London Math. Soc., <u>14</u>, 170, (1883).

17. Taylor, G.I.; "The Instability of Liquid Surfaces when Accelerated Perpendicular to their Planes". Proc. Roy. Soc., A <u>20</u>, 192, (1950).

18. Bellman, R. and Pennington, ; "Effects of Surface Tension and Viscosity on Taylor Instability". Quarterly Applied Mathematics, <u>12</u>, 151, (1954).

19. Keller, J.B. and Kolodner, I.; "Instability of Liquid Surfaces and the Formation of Drops". J. Appl. Phys., <u>25</u>, 918, (1954).

20. Ingraham, R.L.; "Taylor Instability of the Interface Between two Superposed Fluids - Solution by Successive Approximations". Proc. Phys. Soc., LXVII, 748, (1954).

21. Chang, C.J., Emmons, C.T. and Watson, B.C.; "Taylor Instability of Finite Surface Waves". J. Fluid. Mech., <u>7</u>, 177, (1960).

22. Yuen, M.; "Non-linear Capillary Instability of a Liquid Jet". J. Fluid Mech., <u>33</u>, 151, (1968).

23. Melcher, J.; "A Comparative Study of Electrohydrodynamics and Magnetohydrodynamic Surface Waves". (M.I.T. Press), (1963).

24. Squire, H.B.; "Investigation of the Stability of a Moving Liquid Film". Brit. J. Appl. Phys., 4, 167, (1953).

25. Hagerty, W.W. and Shea, J.F.; "A Study of the Stability of Plane Fluid Sheets". J. Appl. Mech., 22, 509, (1955).

26. Van Dyke, M.D.; "Perturbation Methods in Fluid Mechanics". In Applied Mathematics and Mechanics (Academic Press), (1964).

27. Rosenlead, L.; Proc. Roy. Soc., A 134, 170, (1931).

28. Pfeiffer, R.J.; "Parametric Studies of Electrohydrodynamic Spraying". Charged Particle Research Laboratory, Report No. CPRL-4-65, Engineering Research Station, University of Illinois, (1965).

29. Schnieder, J.M., Linblad, N.R., Hendricks, C.M. and Crowley, J.M.; "Stability of an Electrified Jet". Journal of Applied Physics, 38, 2599, (1967).

30. Raco. R.; "Some Aspects of Electrostatic Atomisation". A.P.I. Conference Paper No. CP64-2, (1964).

31. Crowley, J.M.; "Growth of Waves on an Accelerated Jet". Physics of Fluids, 11, 2172, (1968).

32. Langer, P. ; Trans. Am. Math. Soc., 33, 23, (1931). (Referred to in Meskyn (57)).

33. Gaydon, A.G. and Wolfhard, H.G.; "Flames, their Structure, Radiation and Temperature". (Chapman and Hall), 311, (1960).

34. Kaskan, W.E.; Sixth Symposium (Int.) on Combustion. (Chapman and Hall), 134, (1957).

35. Fristrom, P.M. and Westernberg, A.A.; "Flame Structure". (McGraw-Hill, London), (1959).

36. Hinze, J.O. ; "Turbulence". (McGraw-Hill, London), (1959).

37. Coulson, J.M. and Richardson, J.F.; "Chemical Engineering". 2nd Edition, (Pergamon Press, London), 220, (1964).

38. Eckert, E.R.G. and Drake, R.M.; "Heat and Mass Transfer". 2nd Edition, (McGraw-Hill, Tokyo), 372, (1963).

39. "Scott's Standard Method of Chemical Analysis". 6th Edition, Vol.1, 784.

40. Hooper, P.C.; Ph.D. Thesis, London University, (1959).

41. Heywood, H.; Proc. Inst. Mech. Eng., 125, 383, (1933).

42. Wilson, H.A.; Rev. Mod. Phys., 3, 156, (1931). (Referred to in Gaydon and Wolfhard (33), p.318).

43. Calcote, H.F.; "Ion Production and Recombination in Flames". Eighth Symposium (Int.) on Combustion. (Williams and Wilkins, Baltimore), 184, (1962).

44. Calcote, H.F.; "Ion and Electron Profiles in Flames. 9th Symposium (Int.) on Combustion (Academic Press), 622, (1963).

45. Colburn, A.J. and Heath, H.H.; N.G.T.E. memo. No. 1486, (1950).

46. Talbot, L.; Physics of Fluids. 3, 289, (1960).

47. Bloom, S. and Margeneau, H.; "Ion Clustering". Phys. Rev., 85, 670, (1952).

48. Munson, J.R. and Hoselitz, K.; Proc. Roy. Soc., A17, 43, (1939).

49. Weinberg, F.J. and Lawton, J.; "Electrical Aspects of Combustion". (Clarendon Press, Oxford), 114, (1969).

50. Loeb, L.B.; "Fundamental Processes of Electrical Discharge in Gases". (Wiley, New York), (1939).

51. Cobine, J.D.; "Gaseous Conductors". (Dover, New York), (1958).

52. Dombrowski, D. and Briffa, F.E.J.; "Entrainment of Air in a Liquid Spray". A.I.Ch.E. Journal, 12, 708, (1966).

53. Briffa, F.E.J.B.; Ph.D. Thesis, London University, (1968).

54. Wolfsohn, D.L.; Ph.D. Thesis, Leeds University, (1970).

55. Chung, P.M. ; "The Electrical Characteristics of Couette and Stagnation Boundary Layer Flow of Weakly Ionised Gases". Physics of Fluids, $\underline{6}$, 1479, (1963).

56. Cohen, I.; "Asymptotic Theory of Electrostatic Probes in a Slightly Ionised, Collision Dominated Gas". Physics of Fluids, $\underline{6}$, 1479, (1963).

57. Meskyn, D.; "New Methods in Laminar Boundary Layer Theory". (Pergamon Press), (1961).

58. Howarth, L.; Appendix to (59).

59. Taylor, G.I.; "The Dynamics of Thin Liquid Films". Proc. Roy. Soc., $\underline{A253}$, 289, (1959).

60. Mellor, R., Chigier, N.A. and Beer, J.M.; A.S.M.E. Reprint, 70-GT-101, (1970).

61. Schiller, L. and Naumann, A.; Z. ver. Dtsch. Ing., $\underline{77}$, 318, (1933).

62. Tate, R.W. and Marshall, W.R.; Chem. Eng. Progress, $\underline{49}$, 169, (1953).